



Intensity-Modulated Spectroscopy Instrument and its Applications

By
Krisna Adhitya

*A thesis submitted for the degree of
Doctor of Philosophy
in Physics*

The University of Sheffield
Faculty of Science
Department of Physics and Astronomy

August 2016

Acknowledgment

First and foremost, I would like to thank my wonderful parents for their patience, understanding, and love without which I may not be able to follow through this process. My Thanks also to both of my siblings which for their kind assistance and understanding, especially during the early years of my PhD program. I would also very grateful to my wife without her patience and understanding this journey might be unnecessarily difficult. Thank you for being with me.

My very sincerest thanks and gratitude to Dr. Martin Grell and Prof. Richard Tozer for their kind and understanding supervision all throughout this program. Your valuable insight and input in my research undertaking have been very valuable throughout the program. Once again thank you very much. I would also like to send my gratitude to past C14 lab members, Antonius, Lee Hague and Abdullah Al Naim for their assistance in helping me to settle down during the first year of my PhD. I would also like to thank for their technical advice and shared experience which are very much needed in the beginning of my PhD program. My thanks also to Saud Al-Garni and Talal Al-Thagafi for sharing a wonderful three years in the lab. I have learned so much from you guys and I am grateful for that. Special thanks to Abraham and Abbad for your assistance in my day to day lab work. Thank you also for Steve Collins for your assistance in technical clearance in lab operation. There are a lot more people that I would like to thank you, but I do not have the chance. To all of those that have not been mentioned here, my sincerest thank you for all of you.

Finally, I would like to thank my superior and my coworker in Indonesia for their support and understanding during my PhD work.

Abstract

We have successfully built and tested an intensity-modulated spectroscopy (IMS) instrument that is centered around a commercial lock-in amplifier, which can be used to perform intensity-modulated spectroscopy (IMS) up to a frequency of 250 kHz. We have tested our instrument on a commercial CdS-based light dependent resistor (LDR), a device with well-known physical properties. We found that the dynamic characterizations results of the CdS-based LDR agree with an already well-established knowledge on its physical properties. We have also performed IMS on a state-of-the-art bulk heterojunction (BHJ) organic photovoltaics (OPV) and introduced a new mode of IMS operation where photovoltaic cells operate under a finite load, including at its maximum power point. From our IMS results on BHJ OPV, we have established IMS at maximum power point as the optimum operating condition for IMS on photovoltaics, a much better alternative to the traditional IMS operation, i.e. intensity-modulated photocurrent spectroscopy (IMPS) and intensity-modulated photovoltage spectroscopy (IMVS). By using IMS under finite load, we have managed to identify a high-frequency feature that was previously invisible under both IMPS and IMVS. We also found that this feature is ageing-related and is more pronounced after long-term storage. We have also managed to find the origin of this aging feature in the diffusion of indium ions that are etched by a PEDOT layer. In addition, with IMS, we are able to determine the BHJ capacitance of a BHJ OPV without absolute calibration of light intensity. We have also performed IMS on a similar BHJ device but with V_2O_5 as the hole extraction layer. We found that by using V_2O_5 as a hole extraction layer in OPV, we have avoided the problem of indium ions diffusion into the BHJ. We have also managed to perform IMS on an OLED and able to identify the causes of low-frequency “hook” feature in an OLED IMS results. This feature is attributable to the presence of parallel resistive- and capacitive-like components in the OLED’s emissive layer, which is also caused by the diffusion of indium ions into the OLED’s emissive layer. In addition, by using IMS, we have managed to determine carrier mobility in an OLED, though only an average mobility in the device. Finally, in the aging study of OLED device with IMS, we found that carrier transit time decreases as the device ages.

Keywords: Intensity-Modulated Spectroscopy, IMS under finite load, Bulk heterojunction organic photovoltaics, Organic light emitting diode.

Table of Contents

Acknowledgment	i
Abstract	ii
Table of Contents	iii
Chapter 1 Introduction	1
1.1 Introduction and Overview	1
1.2 Thesis Structure.....	3
1.3 Impedance Spectroscopy (IS)	5
1.4 Intensity-Modulated Spectroscopy (IMS).....	12
Chapter 2 Theory and Fundamental Concepts	20
2.1 Structure of Organic Semiconductors	20
2.1.1 Hybrid Orbitals and Conjugated Molecules.....	22
2.1.2 Polarons and Excitons in Conjugated Molecules.....	25
2.1.3 Light Emission from Conjugated Molecules	29
2.2 Carrier Transport in Organic Semiconductors	34
2.2.1 Injection/Contact-Limited Transport.....	36
2.2.2 Bulk-Limited Transport.....	39
2.3 Bulk Heterojunction (BHJ) Organic Photovoltaic (OPV) Devices.....	42
2.4 Organic Light-Emitting Diode (OLED).....	49
2.5 Light-Dependent Resistor (LDR).....	56
2.6 Alkaline Battery	57
Chapter 3 Preparation of Organic Semiconductor Devices	60
3.1 Preparation and Characterization of Organic Photovoltaic (OPV) Devices	60
3.1.1 Preparation of BHJ OPV with PEDOT:PSS HEL	60
3.1.2 Preparation of BHJ OPV with V ₂ O _{5-x} HEL.....	62
3.1.3 Current Density-Voltage (J/V) and Power Density-Voltage (P _D /V) Characterizations of OPV with PEDOT:PSS and V ₂ O _{5-x} HEL	64
3.2 Preparation and Characterization of Organic Light-Emitting Diode (OLED) Devices.....	71
3.2.1 Current Density-Voltage (J/V) and Luminance-Voltage (L/V) Characterizations of OLED Devices.....	73
Chapter 4 Intensity-Modulated Spectroscopy (IMS) Instrument	76
4.1 History of Intensity-Modulated Spectroscopy (IMS) Instrument	76
4.2 Development of A Bespoke Intensity-Modulated Spectroscopy (IMS) Instrument..	83
4.3 Development of A New Mode of IMS Operation.....	86
4.4 Development of The IMS Instrument Bespoke Software	88
4.5 Intensity-Modulated Spectroscopy (IMS) Instrument Calibration	94
4.6 Development of A Bespoke IMS Instrument for IMS on Organic Light-Emitting Diode (OLED).....	96

4.7	Intensity-Modulated Spectroscopy (IMS) Instrument Setup for Light-Dependent Resistor (LDR) Characterization.....	101
4.8	Intensity-Modulated Spectroscopy (IMS) Instrument Setup for Alkaline Battery Characterization	105
Chapter 5 IMS Characterizations of Commercial CdS-Based Light-Dependent Resistor (LDR).....		107
5.1	Results from IMS Characterizations on Commercial CdS-Based Light-Dependent Resistor (LDR).....	107
5.2	Summary of Results from IMS on Commercial CdS-Based LDR	112
Chapter 6 IMS Characterizations of Organic Photovoltaic (OPV) Devices.....		113
6.1	Results from IMS on OPV with PEDOT Hole Extraction Layer under Finite Load Resistance R_L	114
6.2	Results from Ageing Study on OPV Device with PEDOT Hole Extraction Layer.	123
6.3	Determination of Bulk Heterojunction (BHJ) Capacitance on OPV Device with PEDOT Hole Extraction Layer	126
6.4	Summary of Results from IMS on OPV with PEDOT:PSS HEL under Finite R_L .	128
6.5	Results from IMS on OPV with V_2O_{5-x} Hole Extraction Layer at Maximum Power Point Voltage (V_{MPP}).....	130
6.6	Summary of Results from IMS on OPV with V_2O_{5-x} HEL at Maximum Power Point Voltage (V_{MPP}).....	142
6.7	Results from Ageing Study on OPV with V_2O_{5-x} Hole Extraction Layer	143
6.8	Summary of Ageing Study Results on OPV with V_2O_{5-x} Hole Extraction Layer ...	152
Chapter 7 IMS Characterization of Organic Light-Emitting Diodes (OLED) Devices and Alkaline Battery		154
7.1	Results from IMS Measurements on OLED Devices with Different DC Voltage Bias.....	155
7.2	Results from IMS Measurements with Different Optical Filters on OLED Devices	164
7.3	Results from OLED Device Ageing Study with IMS.....	171
7.4	Summary of IMS Results on OLED Devices	177
7.5	Results from IMS Characterizations on an Alkaline Battery.....	178
7.6	Summary of IMS Characterizations on Alkaline Battery	181
Chapter 8 Overall Conclusions and Future Work.....		182
8.1	Overall Conclusions	182
8.2	Proposed Future Work	183
References		185
Lists of Tables		193
List of Figures		194
List of Abbreviations.....		206
Publication and Presentation		208

Chapter 1

Introduction

1.1 Introduction and Overview

This thesis describes the author's contribution to the field of optically-driven, dynamic characterizations of organic semiconductor devices. The main scope of this research is the development of an intensity-modulated spectroscopy (IMS) instrument and a new mode of IMS operation for dynamic characterizations of organic semiconductor devices, which is organic photovoltaic (OPV) and organic light-emitting diode (OLED) devices in our work. Organic semiconductor devices are devices that use organic materials as the semiconducting component, with the organic materials being conjugated polymers or small organic molecules. Examples of organic devices are; organic photovoltaics (OPV), organic light-emitting diode (OLED), organic thin film transistor (OTFT) and organic bistable memory devices [1]. In recent years, interest in organic semiconductor devices has risen to an unprecedented level of growth that is not seen in its inorganic counterparts [1]. Organic photovoltaic (OPV) devices, for example, have emerged as an alternative to the more established inorganic crystalline (silicon) photovoltaics technology in recent years [2]. While research on organic light emitting diode (OLED) is also growing due to their future potential as flat panel displays and lighting applications. In fact, up to 2014, OLED-based active matrix displays have gained a rapidly growing share of the display market [3, 4].

There are of course several reasons for recent growing interest in organic semiconductor devices. These are most importantly, the semiconductor's ability to be made in a fast and simple manner, and especially through low-temperature solution processing with low energy cost, good scalability for large-area applications, good versatility and design flexibility since the semiconductor's structure can be tailored and modified easily, and finally its ability to be made from an abundant supply of source materials. However, organic semiconductor devices also have their own drawbacks. Organic photovoltaics (OPVs) for instance have disadvantages in terms of device efficiency and stability, especially compared to inorganic PVs. As of 2014, the best-recorded power conversion efficiency (PCE) for an OPV is 10% [5], much lower when compared to that of a crystalline silicon PV with $PCE > 25\%$ [6]. Here, PCE is a measure of how efficient a solar cell converts sunlight into electricity. In addition, poor device efficiency and stability is also caused by the susceptibility of OPVs to chemical and physical degradation from contact with the ambient environment [7, 8]. Another drawback of OPVs is their low carrier mobilities compared to that of inorganic PVs [9, 10]. As for organic light-emitting diodes (OLEDs), among their drawbacks are that

the OLED's electrodes are susceptible to oxidation in air which can then lead to device degradation, and that OLED has a much lower carrier mobility compared to inorganic ones, since typical electron or hole mobility in an OLED is 10^{-8} - 10^{-2} $\text{cm}^2/\text{V s}$ [11], compared to electron mobility of $5000 \text{ cm}^2/\text{V s}$ for a doped n-type Gallium Arsenide (GaAs) LED and hole mobility of $300 \text{ cm}^2/\text{V s}$ for a doped p-type Gallium Arsenide (GaAs) LED at room temperature [12]. To add, in a bilayer OLED, interdiffusion between the OLED's organic layers can degrade the device through the formation of dark spots or nonemissive areas seen in the OLED [13-15].

To characterize an OPV and OLED performance, a DC current density-voltage characterizations (J/V) on OPV and both J/V and luminance-voltage (L/V) characterizations on OLED are usually performed on the device under test [14, 15]. However, the disadvantage of DC characterizations is that it cannot accurately determine the exact cause or nature of degradation, especially in devices with complex structure [16, 17]. Dynamic OPV and OLED characterizations, e.g. impedance spectroscopy (IS) and intensity modulated spectroscopy (IMS), offers a more accurate way of characterizing a PV's performance and degradation compared with the DC method [16, 18, 19]. In IS, we characterize the measured system impedance $Z(\omega)$ as a function of frequency ω by applying to the system, a stimulus voltage (V_s) in the form of $V_s = V + \Delta V \sin(\omega t)$, which is a combination of small, AC voltage $v(t) = \Delta V \sin(\omega t)$ that is superimposed on a larger DC voltage V . We then measured from the system, a current response (I_{res}) of $I_{res} = I + \Delta I \sin(\omega t + \theta)$ with I being the DC current response, $i(t) = \Delta I \sin(\omega t + \theta)$ is the AC current response, and θ the phase difference between the AC voltage stimulus $v(t)$ and AC current response $i(t)$. Alternatively, we can also apply to the system, a current stimulus (I_s) and obtained a voltage response (V_{res}) in return [20, 21]. Another dynamic characterization method that is similar to IS but uses different characterization stimulus is intensity-modulated spectroscopy (IMS). In IMS, we apply to the system a stimulus illumination $L(t)$ in the form of $L(t) = L + \Delta L \sin(\omega t)$, where L is the steady-state light intensity and ΔL being the modulation amplitude, hence, in other words, IMS is limited to photosensitive materials, e.g. OPV. We then measure the system's current density response $J_{ph}(t)$, in the form of $J_{ph}(t) = J + \Delta J \sin(\omega t + \varphi)$. Where J is the steady-state photocurrent density response, ΔJ and φ being the modulated photocurrent density amplitude and phase. Alternatively, we can also apply stimulus illumination $L(t)$ and measured a voltage response $V_{ph}(t)$ instead [16, 22]. The advantage of IMS is that, like impedance spectroscopy, it is able to distinguish or accurately assign a measured system's parameter to a specific internal dynamics that occurs within the system itself. Another advantage is that IMS, as well as IS, can also be done automatically, thus improving the method's accuracy while also reducing any potential for errors [16, 21, 22]. The distinctive advantage of IMS, especially over IS, is that since light is the sole source of stimulus, in the case of photovoltaics characterizations, we can perform

IMS at one of the solar cell operating conditions in its J/V characteristics, i.e. either at the cell's short-circuit condition, which is called intensity-modulated photocurrent spectroscopy (IMPS) or at the cell's open-circuit condition, which is intensity-modulated photovoltage spectroscopy (IMVS) [23].

In this work, we have developed a portable, optically-driven/intensity modulated spectroscopy (IMS) instrument that is capable of performing IMS measurement at any point in a solar cell's J/V characteristics, while at the same time being more affordable compared to commercial IMS instruments and impedance analyzers. We also proposed a new mode of doing IMS, i.e. IMS under finite load, in which we can realistically characterize the solar cell at its normal working condition and under which we can obtain the largest current/voltage response signal from the cell, which was not possible previously under traditional modes of IMS measurement, i.e. IMPS and IMVS. We first tested our instrument setup by conducting IMS on a commercial light-dependent resistor (LDR), and we then perform IMS under finite load on a bulk heterojunction (BHJ) OPV. We continue by adapting our instrument to perform IMS on an organic light emitting diode (OLED), and then adapting it (instrument) to conduct load modulation on an alkaline battery.

1.2 Thesis Structure

This thesis is divided into 7 chapters. The chapters are sequenced from an overview of our research scope, introduction and basic concepts of impedance spectroscopy (IS) and intensity-modulated spectroscopy (IMS), followed by the basic concepts, materials, properties and operation of organic semiconductor devices (OLED and OPV). To add, we also describe the materials and properties of a light-dependent resistor and alkaline battery that we characterize in our work. We proceed by describing the development of our intensity-modulated spectroscopy (IMS) instrument and then present our new mode of IMS operation for photovoltaic characterizations. We tested our IMS instrument setup by performing IMS on a commercial light-dependent resistor (LDR), and we then proceed by performing IMS under finite load on a bulk heterojunction (BHJ) OPV. We finally adapt and use our instrument to perform IMS on an organic light emitting diode (OLED), and then set the instrument to conduct load modulation IMS on an alkaline battery. Descriptions of each chapter are as follows:

1. Chapter I gives an overview of our research work, early history and basic introduction to impedance spectroscopy (IS) as a dynamic characterization method which has also been used ubiquitously for electrochemical device characterization, including for OPVs. We then discuss the basic concepts behind IS, along with its advantages and disadvantages compared to other methods. We then introduce intensity modulated spectroscopy (IMS) as a dynamic characterization method similar to IS but using modulated light to dynamically characterize a

device, and with an advantage over IS, especially in solar cell characterizations. Here, IMS, as well as IS, is introduced to address the weaknesses of steady-state/DC characterization. We then discuss the basic concepts behind IMS and its advantages and disadvantages with respect to other methods.

2. Chapter II gives the basic theory and concepts behind organic semiconductors and organic semiconductor devices with its advantages and drawbacks as an application, especially compared to its inorganic counterpart. We also discuss an organic semiconductor structure/chemistry, conjugated molecules, light emission in conjugated molecules, carrier transport and mobility in the organic semiconductor. We then describe device operations and carrier transport in a BHJ OPV and OLED as organic semiconductor devices that we characterize in this work. To add, we also discuss DC characterizations, i.e. J/V and L/V characteristics (for OLED) on organic semiconductor devices as an integral part of device operation. We then give a basic introduction on a light-dependent resistor (LDR) and an alkaline battery that we also characterize with IMS in our work. To add, we also discuss the basic structure, operation, and materials of LDR and alkaline battery, together with their advantages and drawbacks as an application.
3. Chapter III describes the preparation of organic semiconductor devices, i.e. the OPV and OLED in this work, which was done by someone else prior to our (IMS) characterizations. This chapter also gives the DC characterization results of the OPV and OLED sample in this work.
4. Chapter IV is split into two main parts, the first part describes the history of IMS instrument development, and IMS mode of operations prior to our work. In the second part, we first describe the development, setup and characterization source of our IMS instrument, which we use to perform IMS on an OPV. We then propose, also in the second part, a new mode of IMS operation that we use for OPV characterizations, i.e. IMS under finite load, which is different and more advantageous compared to the traditional IMS mode of operation (IMPS and IMVS). Following this, we also present and discuss the bespoke IMS software that we have developed to operate the IMS instrument in OPV characterizations. We then give the calibration results of our IMS light source and instrument setup in OPV characterizations. After the IMS on OPV calibration results, we then proceed to describe the adaptation/setup of our IMS instrument to characterize an OLED, along with the modification of our bespoke IMS software for OLED characterizations. We then go on to describe the adaptation/setup of our IMS instrument to characterize a commercial LDR. Finally, we also give the calibration results of an IMS light source and instrument setup for LDR characterization.

5. Chapter V gives and discusses the results of IMS characterizations on a commercial LDR as a test characterization of a device with widely known characteristics, by using our IMS instrument setup.
6. Chapter VI gives and elaborates the results of IMS characterizations on OPV with PEDOT and vanadium pentoxide (V_2O_{5-x}) hole extraction layer (HEL) along with the aging of both OPV types, and also the bulk heterojunction (BHJ) capacitance determination in OPV with PEDOT HEL. Along with the results, we also interpret and discuss all the IMS results in the context of OPV physical and equivalent-circuit model.
7. Chapter VII gives and discusses the results of IMS characterizations on an OLED for the purpose of carrier transit time, type and mobility determination, followed by IMS results from different light dynamics comparison in an OLED and also on the OLED aging itself. In addition, we also interpret and discuss all of the IMS results in the context of the OLED physical and equivalent-circuit model.
8. Chapter VIII gives the summary/conclusions from the development of our IMS instrument for both OPV and OLED characterizations, the introduction of a new mode of IMS operation that we use for OPV characterizations, and finally, the result of IMS characterizations on organic semiconductor devices in this work (i.e. OPV and OLED); and also describes the adaptation/setup of our IMS instrument for the purpose of conducting a load modulation experiment with a commercially available alkaline battery, as a potential future work.

1.3 Impedance Spectroscopy (IS)

Impedance spectroscopy (IS), or also known as electrochemical impedance spectroscopy (EIS), is a powerful and widely used dynamical characterization method that investigates material's electrical properties, their interface interactions with electronically conducting electrodes, dynamics of bound/mobile carriers in bulk or interfacial regions of any type of solids and liquid materials; e.g. ionic, semiconducting, mixed electronic-ionic, and insulators/dielectrics. To add, IS can also be used to characterize any type of solid electrolyte materials, either amorphous, polycrystalline or single crystals. Most importantly, IS has also been used to characterize the operational mechanism of different type of solar cells, from dye-sensitized solar cells (DSSC), organic photovoltaics (OPV) and inorganic or silicon solar cells [21, 24].

Impedance spectroscopy (IS) as an electrical characterization method has a rather long history. Although it has been used as an electrochemical analysis tool since at least the early 20th century, the concept of electrical impedance itself has already been well established ever since Oliver Heaviside first introduce the concept in the late 19th century, and followed after by A.E. Kennelly and C.P.

Steinmetz further developing its mathematical formalism (vector diagrams and complex representation) in the same period [25, 26]. By 1925, IS has already been used to characterize polarization across biological cell membranes [24]. In 1941, an important milestone was reached when Cole and Cole managed to plot ε' and ε'' from dielectric systems into a complex plane plot, which is known now as the Cole-Cole plot [27]. This plot is basically a further adaption to dielectric systems applications of an electrical engineering circle diagram developed in 1925. By the end of world war II, with the development of solid state batteries as rechargeable high-power-density energy storage devices, revolution in high-temperature electrochemical sensors in environmental and industrial efficiency control along with the introduction of fuel cells, there was a rapidly growing trend to abandoned electrolyte-based electrochemical systems/energy source away from using corrosive aqueous solutions and moving towards the development of solid state technology. As such characterization of systems with solid-solid, solid-liquid interfaces then became a major research concern for scientists and electrochemists [21]. Consequently, because of this development, a growing interest in impedance spectroscopy characterization then ensued. From at least 1947, Randles, Jaffé and Chang have used Z as a concept of electrical impedance in theoretical calculations of semiconductor and ionic systems properties and behavior [28-30]. While in the experimental field, Randles and Somerton uses IS in 1952 to characterize fast reactions in supported electrolytes, which was followed by Macdonald using the concept of impedance to analyze experimental results on photoconductive alkali halide single crystals [31, 32]. By 1957, Schrama introduced the concept of modulus function $M = \varepsilon^{-l}$ which were then used extensively by McCrum et al. and Macedo et al. in the 1970s [21, 33]. In the 1960s, Sluyters managed to plot for the first time an impedance plot in an impedance plane in his efforts to characterize aqueous electrolytes [34]. This was followed by Sluyters and Oomen using IS to characterize the same material [35]. After this period (the 1960s), IS has been used theoretically and experimentally to approach many research problems, and by 1980s the method and technology have already been well-established [20, 24]. Today, as mentioned before, IS has been used for many applications and purposes, and also for various materials/systems [21].

In impedance spectroscopy, as in 1.1, we measure the impedance $Z(\omega)$ as a function of frequency ω by applying to the characterized system, a stimulus voltage V_s in the form of $V_s = V + \Delta V \sin(\omega t)$, which is a combination of small, AC voltage $v(t) = \Delta V \sin(\omega t)$ that is superimposed on a larger DC voltage V . We then measured from the system, a modulated current response $I_{res} = I + \Delta I \sin(\omega t + \theta)$ with I being the DC current response, $i(t) = \Delta I \sin(\omega t + \theta)$ is the AC current response, and θ the phase difference between the AC voltage stimulus $v(t)$ and AC current response $i(t)$ [20, 24]. Here, $\theta = 0$ for resistive behavior, V and I are in V and A respectively, ΔV and ΔI are respectively the AC voltage and current amplitude (in V_{peak} and I_{peak}), with $\omega = 2\pi f$. The units for ω is rad/s and f

is in Hz. We then varied the voltage stimulus with respect to frequency ω , as such, the modulated component of current response or ΔI will also be a function of frequency ω . To add, since phase response θ depended on the current stimulus, θ will also be a function of ω . Hence, we then measure the system's resulting impedance $Z(\omega)$ from its AC current response with respect to the AC voltage stimulus, with ΔV , ΔI and θ a function of frequency ω . Since $Z(\omega)$ is a frequency-domain function and the AC current and voltage is first a time-domain function, we can convert the sinusoidal voltage stimulus and current response by using Fourier transform so that $Z(\omega)$ is then defined by equation (1) [21, 24, 36].

$$Z(\omega) = \frac{F\{v(t)\}}{F\{i(t)\}} \quad (1)$$

with $Z(\omega)$ in Ω , and F [37] operator is the Fourier transform. We can also state $Z(\omega)$ in the complex form as $Z(\omega) = Z' + jZ''$, where Z' and Z'' are respectively the real and imaginary part of $Z(\omega)$ [21, 24]. Both Z' and Z'' can be stated in Cartesian terms via equation (2).

$$\text{Re}(Z) = Z' = |Z| \cos(\theta) \quad \text{and} \quad \text{Im}(Z) = Z'' = |Z| \sin(\theta) \quad (2)$$

with phase angle θ defined by equation (3) below:

$$\theta = \tan^{-1} \frac{Z''}{Z'} \quad (3)$$

we can then plot equation (2) in an Argand diagram or complex plane as depicted in Fig. 1-1, taken from Macdonald et al [21].

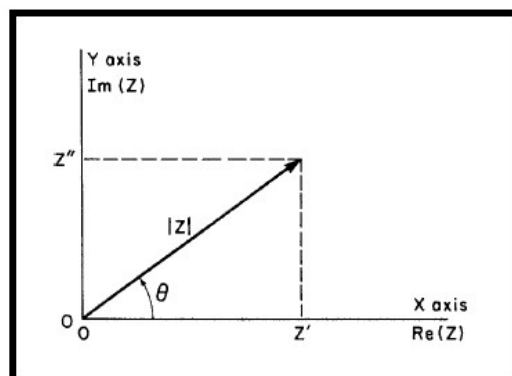


Fig. 1-1. An Argand diagram of equation (2) taken from Macdonald et al [21].

From Fig. 1-1, the modulus of $Z(\omega)$ is then defined by equation (4).

$$|Z| = \left[(Z')^2 + (Z'')^2 \right]^{1/2} \quad (4)$$

In polar form $Z(\omega)$ can also be written as $Z(\omega) = |Z| \exp(j\theta)$. Here we make use of the Euler formula $e^{j\theta} = \cos \theta + j \sin \theta$. Alternatively in IS, we can also measure the impedance $Z(\omega)$ by applying instead a stimulus current I_s to the characterized system, in which $I_s = I + \Delta I \sin(\omega t)$, thus I_s is a combination of a small, AC current $i(t) = \Delta I \sin(\omega t)$ that is superimposed on a larger DC current I . In turn, we can then measure from the system, a modulated voltage response $V_{res} = V + \Delta V \sin(\omega t + \theta)$ with V being the DC voltage response, $v(t) = \Delta V \sin(\omega t + \theta)$ is the AC voltage response, and θ the phase difference between the AC current stimulus $v(t)$ and AC voltage response $i(t)$. We then proceed to vary the current stimulus with respect to frequency ω , so that the modulated component of the voltage response or ΔV will be a function of ω . To add, the voltage phase response θ from the current stimulus will also be a function of ω . Hence, we again measure the system's resulting impedance $Z(\omega)$ from its AC voltage response with respect to the AC current stimulus, with ΔV , ΔI and θ a function of frequency ω [20, 21].

As a prerequisite in every IS measurements, it is necessary to have the AC modulation voltage or current smaller than that of the DC bias voltage/current. This is because nonlinear systems, i.e. most real systems, will only respond linearly/in proportion to the stimulus voltage/current if it is stimulated with such (very small) AC voltage/current magnitude, in which the AC component itself needs to be smaller than the system's thermal voltage $V_T = kT/e$, where k is the Boltzmann constant $= 1.38 \times 10^{-23}$ J/K, and T is the absolute temperature (in K) and e is the elementary charge $= 1.6 \times 10^{-19}$ C. In an IS experiment, the typical frequency range that we use is from 1 mHz to 1 MHz [20, 21]. In Fig. 1-2 we then present the flow diagram of general characterization procedure in IS taken from Macdonald et al [21].

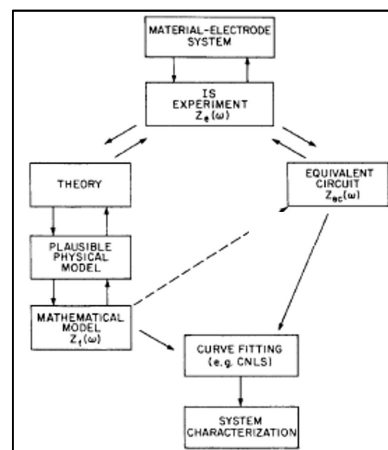


Fig. 1-2. A flow diagram of general characterization procedure in IS taken from Macdonald et al [21].

So from Fig. 1-2, we first characterize the material-electrode system with the stimulus voltage from our IS instrument and then measure the resulting current from the system as discussed previously. After the previous step, we can then analyze the resulting experimental data via two different ways; one is by analyzing the results based on a physical theory that predicts an exact theoretical impedance $Z_T(\omega)$, or the other way is by analyzing the results with a relatively empirical equivalent circuit model whose impedance predictions is designated as $Z_{EC}(\omega)$. From both ways/methods we can estimate the experimental impedance parameters, and thus we can then compare the resulting $Z(\omega)$ data with simulated $Z_T(\omega)$ and $Z_{EC}(\omega)$ from both methods. We can then fit either of the simulated impedance from both methods with CNLS or complex nonlinear least square fitting to accurately match the resulting $Z(\omega)$ data. As an example, for the analysis of charge transport processes in a characterized systems, an equivalent circuit with ideal resistors and capacitors will likely be needed, even with inductors in some instances. From the equivalent circuit, we can then calculate the resulting impedance in terms of the circuit parameters. To add, from the circuit's behavior and its impedance response as we change the experimental condition, we can then characterize the system's impedance behavior which in turn leads to an estimation of other microscopic parameters, such as mobility, carrier concentrations, etc. Note also that the parameters that we derive from an IS measurement can be divided into two, one is a parameter that is related to the system under test, such as conductivity, dielectric constant and mobility, and the other one is a parameter that is related to an electrode material interface, such as adsorption reaction rate constants and capacitance of the interface region [21, 24]. The procedure described in Fig. 1-2 can also be applied to intensity-modulated spectroscopy (IMS) characterizations, and we later use the second procedural approach for our IMS results analysis.

Once we obtain the resulting $Z(\omega)$ data, as an example, we can then model the result with the second method according to Fig. 1-2 procedure. To do this we start with the most simple equivalent circuit which has a resistor R and capacitor C equivalent component and can be used to model equivalent circuit behavior of many electrode-material systems. Since impedance $Z(\omega)$ can be represented as a complex function (from equation (2)), we can then plot the $Z(\omega)$ result from an IS measurement in the form of a Nyquist plot. This plot has two axis, the first one is the real axis or Re axis, which is parametric with the scanning frequency and the second one is the imaginary axis or Im axis. We then depict two examples of the equivalent circuit with their respective $Z(\omega)$ estimation in the form of simulated Nyquist plots in Fig. 1-3(a), (b), (c) and (d), taken from Macdonald et al [21].

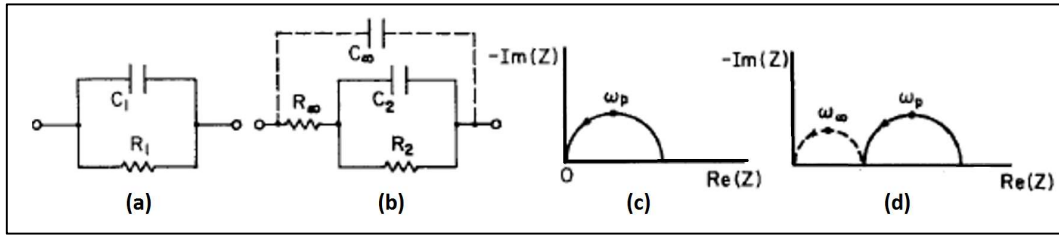


Fig. 1-3. (a) and (b) Examples of two RC circuit with R and C components in parallel and in different configurations, with their respective (c) and (d) Nyquist plot results of $Z(\omega)$. The direction of increasing frequency is from right to left/anti-clockwise, taken from Macdonald et al [21].

From Fig. 1-3(c) and (d) Nyquist plots, we can see that the plots form a perfect semicircle with a single peak for each R and C component in (a) and (b) circuits. So two RC element in a circuit will then result in two semicircle peaks in the Nyquist plot. This RC factor is the time constant τ of Fig. 1-3(a) and (b) equivalent circuit. The time constant τ can be derived from the AC equation $\tau = RC$. The time constant is the maximum peak in the Nyquist semicircle and it can be derived from the frequency where the resulting phase or θ from the phase measurement = 45° . This frequency is then called the corner frequency f_c , and τ can be derived from f_c via the equation $f_c = 1/2\pi\tau$. In a physical context for this example, τ represents the dielectric relaxation time of the measured system. It is typically the smallest time constant in an IS experiment. In addition to the above plots, impedance results can also be depicted with the Bode amplitude and phase plots, which are respectively the plots of impedance amplitude and phase with respect to measurement frequency and is depicted in Fig. 1-4, taken from Macdonald et al [21].

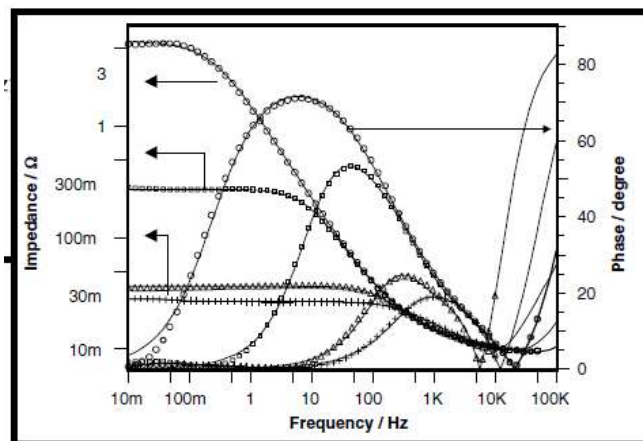


Fig. 1-4. Example of a Bode amplitude (arrow pointing left and in Ω) and phase (arrow pointing right and in $^\circ$) plot of an impedance measurement with respect to frequency f (in Hz), taken from Macdonald et al [21].

So from Fig. 1-4, we see that the Bode amplitude and phase plot are just another way of presenting impedance measurement results. In fact, we can derive the corner frequency f_c in the Bode amplitude plot as the frequency where the impedance phase $\theta = 45^\circ$, or where the impedance has dropped

equivalent to -3 dB of its previous value [21]. We then proceed to depict a typical impedance measurement setup in Fig. 1-5, taken from Park et al [38].

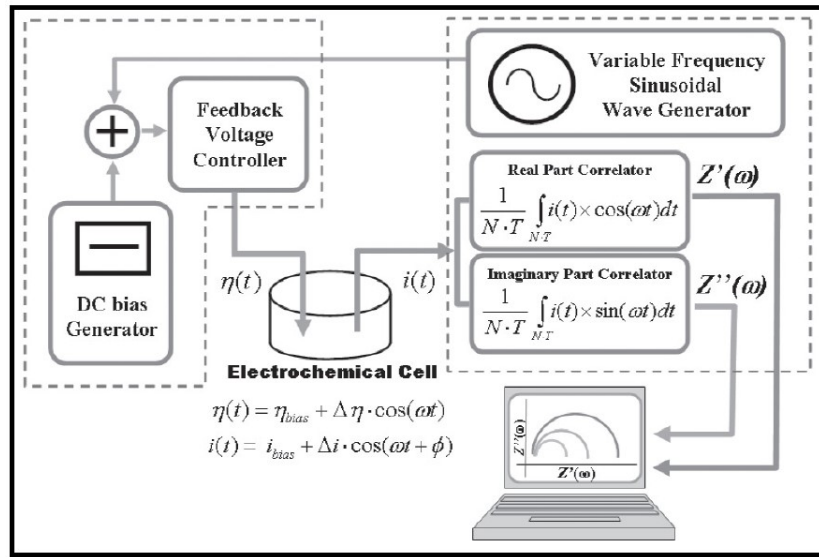


Fig. 1-5. An example of a typical impedance spectroscopy setup. Here, $\eta(t)$ is the total voltage applied to the cell, including the modulated component $\Delta\eta$. While $i(t)$ is the total current response from the cell, including the modulated component Δi , taken from Park et al [38].

From Fig. 1-5 example, a voltage stimulus $\eta(t)$ with a modulating component $\Delta\eta$ is applied to an electrochemical cell. Here the η_{bias} or voltage bias comes from the DC bias voltage generator and the modulating voltage component $\Delta\eta$ originate from the variable frequency sinusoidal generator. The $\Delta\eta$ is superimposed on the η_{bias} with the feedback voltage controller. After we apply the voltage stimulus $\eta(t)$, we then obtain a current response $i(t)$ with the modulating component Δi and an added phase ϕ . The response current $i(t)$ is then converted into a frequency-based parameter by the correlator and then into an impedance $Z(\omega)$ with respect to the stimulus voltage $\eta(t)$. In the response current conversion, the current is also turned into a real impedance $Z'(\omega)$ and imaginary impedance measurement $Z''(\omega)$ in the complex plane. The resulting real and imaginary impedance is then plotted and recorded in a computer with the entire impedance parametric with frequency f [38]. Further, an impedance analyzer can also be used as the DC and AC voltage generator, and also as the current or voltage response converter similar to the correlator in Fig. 1-5. To add, in terms of dynamic characterization, aside from measuring impedance, we can also measure other AC functions, such as admittance Y , which is the inverse of impedance or $Y = 1/Z$, with Y itself also a complex quantity.

Several advantages of IS compared to other analytical tools in the characterization of a material's electrochemical properties are as follows; first is that the measurement process is relatively simple, non-destructive in nature and that any parametrical results obtained from IS can be ascribed to specific dynamic processes occurring in the system. In addition, from the impedance interpretation,

we can also predict the fundamental processes/phenomenon occurring in the system. Thus IS is a multifunctional technique that can be used for various electrical/electrochemical studies, e.g. it can be used to study charge carrier dynamics in interfacial regions of all types of materials, membrane behavior in living cells, conductivity determination, and many others, and finally, the measurements itself can be fully automated. While the disadvantage of using IS lies in the ambiguity of results interpretation, since sometimes a measured parameter/dynamics can be ascribed to one or more processes in the system. Finally, modeling IS results via an electrical equivalent circuit also has its limitation in that a circuit with a certain amount of R and C components may not be able to adequately explain the measured impedance results [21, 24].

1.4 Intensity-Modulated Spectroscopy (IMS)

Intensity-Modulated Spectroscopy or IMS is also a dynamic characterization method similar to IS, but instead of applying a modulated voltage or current to the characterized system, we apply a slightly perturbed but larger steady-state illumination intensity to the system under test, and then measure the resulting perturbed voltage/current response from the system [16, 23, 39, 40]. In this method, we illuminate the system from an optically transparent contact, and then we measure the system's response from another contact, which is called the collecting contact. So from the transparent contact, carriers are generated and then travel towards the collection contact, thus generating photocurrents from the system [16, 40]. In IMS, depending on the characterization systems, a number of light sources can be used as the stimulus signal, for example, LED, laser, and Xenon short arc lamps [16, 39, 41]. The use of LED stimulus, in particular, is relatively advantageous compared to another light source because of the relative ease in modulating a LED with a drive current, in addition also to its (LED) ability in which it can be modulated at a very high frequency ($f > 1$ MHz), thus extending the measurement bandwidth to higher frequencies [41]. Also, in an IMS, it is necessary that the light intensity modulation amplitude is set to be much smaller than the steady-state light. This is because, in order to obtain a linear response from a nonlinear system, we have to stimulate the system with a small (and harmonic) perturbative stimulus, which is represented by the small and perturbative light intensity in an IMS experiment [22, 23, 39]. Then, the frequency range in a typical IMS experiment is the same as that in IS, i.e. from 1 mHz to 1 MHz [16]. As a technique, IMS has been used to measure rate constants for interfacial charge transfer and surface recombinations in photoelectrodes and then to study the dynamics of electron and holes in semiconductors, and also the dynamics of inorganic, organic and dye-sensitized solar cells. However, this technique is not as widely used as IS, as this technique is also limited to photosensitive devices, since without light input, there would not be any charge generation in the characterized

device/systems. Intensity-modulated spectroscopy as a technique is almost as old as IS, with the method first developed in 1925, when Foote and Mohler describe it in their paper entitled “*Photo-Electric Ionization of Caesium Vapor*” [42]. In 1976, the method was introduced for the first time by Green et al. as an “optogalvanic spectroscopy” [43]. By 1980, the method (IMS) itself has seen a widespread use in spectroscopic studies of materials and electrodes [44]. In 1981, Oheda et al. was among the first to report the use of IMS in studying semiconductor properties [45]. Several years later, IMS has been used to study reaction kinetics in photoelectrochemical systems, electron-hole recombination, anodic thin films and electron transport in disordered semiconductors. By 1990, this method has already been well-established [16]. As of today, the method has been used for various purposes, and especially for the purpose of characterizing various photosensitive materials/systems [21].

There are basically two different modes of IMS operation, one is intensity-modulated photocurrent spectroscopy or IMPS, where we apply a slightly modulated light intensity to the characterized system, and then measure the perturbed photocurrent response due to modulated light. While the other one is the intensity-modulated photovoltage spectroscopy or IMVS, where we instead measure perturbed photovoltage response from the modulated light intensity. In both methods, from the resulting photocurrents or photovoltage, we can then measure a function that compares the electrical response with respect to the modulated illumination. This function is not impedance but it has the same role as impedance does in IS. This function is called the transfer function $H(\omega)$ and it is dependent on frequency ω , with $\omega = 2\pi f$. Here, the units for ω is rad/s and f is in Hz. So first in IMPS, we apply to the system a stimulus illumination $L(t)$ in the form of $L(t) = L + \Delta L \sin(\omega t)$, where L is the steady-state light intensity (usually in photons $\text{cm}^{-2} \text{s}^{-1}$) and ΔL being the (light) modulation amplitude. After this step, we then measure the system’s current density response $J_{ph}(t)$, in the form of $J_{ph}(t) = J + \Delta J \sin(\omega t + \varphi)$. Where J is the steady-state photocurrent density response, ΔJ and φ being the AC photocurrent density amplitude and phase respectively. The current response here is usually measured with respect to an illuminated area, so I is stated in terms of current density J or current per unit area. We then vary the light stimulus modulating frequency ω which makes the current density ΔJ and phase φ a function of ω . In other words, because the modulated light component is a function of ω , modulated carrier generation in the system will also be a function of ω . As such, when generated carriers travel to the electrodes as photocurrents, the modulated part of the photocurrent will also be a function of frequency ω or $\Delta J(\omega)$. To add, since the resulting currents are phase-shifted with respect to $L(t)$, the resulting phase shift will then be a function of ω or $\varphi(\omega)$. Hence, we can then obtain the transfer function $H(\omega)$ from the system’s ΔJ with respect to ΔL , which is defined by equation (5).

$$H(\omega) = \frac{\Delta J(j\omega)}{\Delta L(j\omega)} \quad (5)$$

with $H(\omega)$ being dimensionless and $j = (-1)^{1/2}$. In IMPS, carriers are extracted out from the system and in photovoltaic applications, the cell has to be under a short-circuit condition since we are measuring photocurrents from light [16, 21, 39]. Alternatively, we can also present IMPS characterization results in the form of ΔJ only instead of $H(\omega)$, since from Eqn. 5, $H(\omega)$ is proportional to ΔJ , with ΔJ a function of frequency ω [21].

In intensity-modulated photovoltage spectroscopy or IMVS, we measure a transfer function $H(\omega)$ from the system by applying to it, $L(t) = L + \Delta L \sin(\omega t)$ and measuring the modulated photovoltage response due to light. Following this, we then measure the total voltage response $V_{ph}(t)$, in which $V_{ph}(t) = V + \Delta V \sin(\omega t + \varphi)$. Where V is the steady-state photovoltage response, ΔV and φ being the AC photovoltage amplitude and phase [23, 40, 46]. Because here modulated light intensity is varied with respect to frequency ω , the modulated rate of generated carriers will be a function of ω . As such, when generated carriers travel to the collecting contact, the modulated photovoltage across the contacts will also be a function of frequency ω or $\Delta V(\omega)$. To add, since the resulting voltage phase is shifted with respect to $L(t)$, the voltage phase shift will be a function of the modulating light frequency ω or $\varphi(\omega)$. We can then obtain the transfer function $H(\omega)$ from ΔV with respect to ΔL , which is defined by equation (6) [40, 46].

$$H(\omega) = \frac{\Delta V(j\omega)}{\Delta L(j\omega)} \quad (6)$$

with $H(\omega)$ dimensionless and $j = (-1)^{1/2}$. In IMVS, especially for photovoltaic applications, carriers are not extracted from the system, and the cell has to be under an open-circuit condition since we are measuring photovoltage from light [23, 40, 47]. To add, we can also present IMS characterization results in the form of ΔV instead of $H(\omega)$, since from Eqn. 6, $H(\omega)$ is proportional to ΔV , with ΔV a function of frequency ω [5]. Note also that since we are measuring voltage responses, no references to the area of illumination are needed. We then depict an example of IMPS and IMVS instruments setup in Fig. 1-6 taken from Metrohm Autolab application note on IMPS and IMVS [48]. In Fig. 1-6, both the IMPS and IMVS setup uses a LED as the characterization light source.

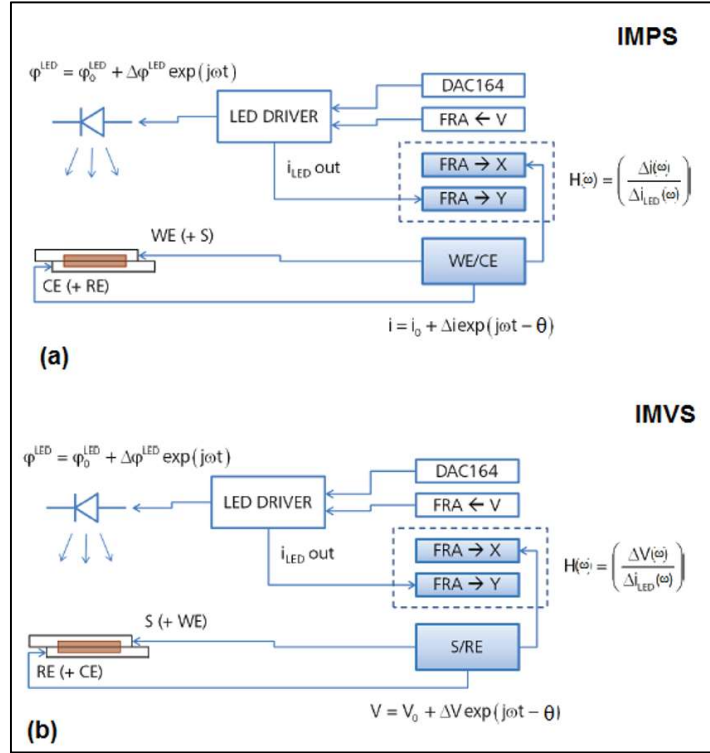


Fig. 1-6. Example of an (a) IMPS (top) and (b) IMVS (bottom) setup. For (a) and (b), transfer function $H(\omega)$, ΔV , Δi and Δi_{LED} is a function of frequency ω . Also the LED DC current is in proportion to the DC light intensity, taken from Metrohm Autolab application note [48].

From Fig. 1-6(a) example, in an IMPS setup, we drive and modulate an LED with a total driving current i_{LED} , through an LED driver that combines the i_{LED} 's current bias i_{DC} (not shown) from a bias provider (DAC164) and its (i_{LED}) modulating component Δi_{LED} from a frequency analyzer device (FRA). The LED will then emit a total light intensity (φ^{LED}) of $\varphi^{LED} = \varphi_0^{LED} + \Delta\varphi^{LED} \exp(j\omega t)$, with φ_0^{LED} being the steady state illumination, the $\Delta\varphi^{LED}$ is the modulated intensity component, and $\Delta\varphi^{LED}$ a function of frequency ω . Since the LED's $i_{DC} \sim \varphi_0^{LED}$, then its $\Delta i_{LED} \sim \Delta\varphi^{LED}$. We then apply the resulting illumination φ^{LED} to the system under test. The system is set under a working electrode (WE) and common electrode (CE) contact. Here, the WE contact acts as the anode while the CE act as the cathode. We then proceed to measure the resulting photocurrent i from the illumination through the WE/CE module, in which the photocurrent response $i = i_0 + \Delta i \exp(j\omega t - \theta)$ is taken and fed to a different frequency response analyzer (FRA) device. Here, i_0 is the photocurrent DC component, Δi is the AC photocurrent component and θ is the phase response from the system. We then compare the resulting photocurrent's Δi as a function of frequency ω with the LED's Δi_{LED} that is also channeled to the same FRA device in which we fed the photocurrent. This is done to obtain a transfer function $H(\omega)$, where $H(\omega) = \Delta i(\omega) / \Delta i_{LED}(\omega)$.

Whereas in an IMVS setup, as shown in Fig. 1-6(b), we again drive the LED with a total driving current i_{LED} , through a LED driver that combine the i_{LED} 's current bias i_{DC} from a bias provider

(DAC164) and its Δi_{LED} from a frequency analyzer device (FRA). The LED will then emit again a total light intensity φ^{LED} as before (in IMPS), with φ_o^{LED} being the steady state illumination, $\Delta\varphi^{LED}$ is the modulated intensity component, and $\Delta\varphi^{LED}$ a function of frequency ω . Because the LED's $i_{DC} \sim \varphi_o^{LED}$, then its $\Delta i_{LED} \sim \Delta\varphi^{LED}$. The total illumination φ^{LED} is then applied to the characterized system. The system is set under a source electrode (S) and reference electrode (RE) contact. In this setup, we measure a voltage response in the source electrode (S) with respect to the reference electrode (RE). We then measure the resulting photovoltage V from the illumination through the S/RE module, in which the photocurrent response $V = V_o + \Delta V \exp(j\omega t - \theta)$ is taken and channeled to another frequency response analyzer device. Here, V_o is the photovoltage DC component, ΔV is the AC photovoltage's component and θ is the phase response from the system. We then compare the resulting photovoltage's ΔV as a function of frequency ω with the LED's modulating component (Δi_{LED}), which is also fed to the same FRA device. This is done to obtain a transfer function $H(\omega)$, where $H(\omega) = \Delta V(\omega)/\Delta i_{LED}(\omega)$ [48].

The transfer function $H(\omega)$, similar to IS in 1.3., can also be represented in the form of Bode amplitude and phase plot, in which $H(\omega)$ amplitude and phase θ are plotted with respect to frequency ω . An example of these plots is shown in Fig. 1-7(a) and (b), which are respectively taken from the Bode amplitude and phase plot of a BHJ OPV's transfer function in Luther et al [49].

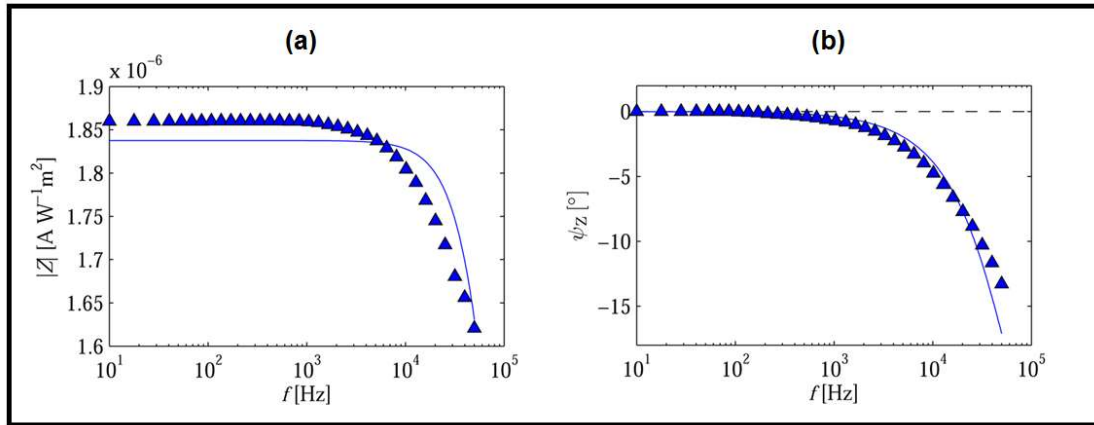


Fig. 1-7. Example of a transfer function Bode amplitude (a) and phase (b) plot with respect to frequency f (in Hz). The transfer function in (a) is represented by Z and the amplitude of Z in units of $A \text{ m}^2/W$. The phase (represented by ψ) plot in (b) presents the transfer function phase difference as a negative value, thus the plot location in the 4th quadrant. Both plots are taken from Luther et al [49].

In Fig. 1-7(a) amplitude plot, the transfer function is represented by Z , with the amplitude of Z in units of $A \text{ m}^2/W$. While in Fig. 1-7(b) phase plot, the transfer function phase is represented by ψ , in units of ($^\circ$), with the plot's phase difference taken as a negative value. In the case of impedance spectroscopy Bode plots, we can determine the corner frequency f_c from Fig. 1-7(a) Bode amplitude plot, as the frequency where the transfer function amplitude dropped to an equivalent of -3 dB from

its previous value. This f_c is also defined as a frequency where the transfer function phase $\psi = 45^\circ$ in Fig. 1-7(b) [21, 49]. From the f_c , we can determine a time constant τ , through the equation $f_c = 1/2\pi\tau$ [16, 23]. This time constant τ represents the time constant of a specific internal dynamic that occurs in the characterized system [23]. To add, we can also present IMS results in the form of Bode amplitude and phase of ΔJ or ΔV with respect to frequency ω [40, 50].

We can also plot the transfer function $H(\omega)$ as a complex quantity in a Nyquist plot, i.e. $H(\omega) = H' + jH''$, with H' and H'' being the real and imaginary part of $H(\omega)$ respectively. An example of the $H(\omega)$ Nyquist plot for IMPS mode of operation is depicted in Fig. 1-8, taken from Metrohm application note of a dye-sensitized solar cell (DSSC) IMPS result [48].

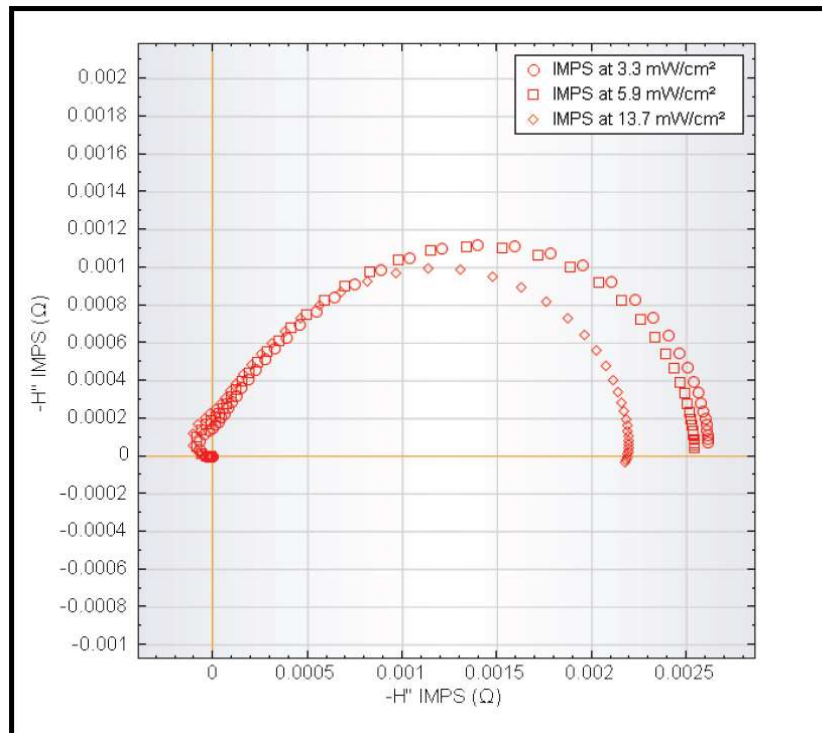


Fig. 1-8. An example of several $H(\omega)$ Nyquist plot result from a dye-sensitized cell under an IMPS mode of operation. The plot is taken at different DC light intensity ϕ_o^{LED} , with $-H'$ parametric with frequency ω . The $H(\omega)$ plot here is presented as an inverted plot, with the plot's real (H') and an imaginary axis (H'') under a (-) sign. Thus, the plot actually lies in the 4th quadrant with the extended part running into the 3rd quadrant, instead of lying in the 1st quadrant with the extended feature running into the 2nd quadrant. Note also that H' and H'' are in Ω . Here, the direction of increasing frequency is anti-clockwise, with the units of both H' and H'' in Ω [48].

From Fig. 1-8, we can see that the $H(\omega)$ plots resemble a semicircle with a single peak, with frequency increasing in the anti-clockwise direction. In literature, phase value in a Nyquist plot's is taken as negative value as a convention [16, 50, 51], so the H'' values in Fig. 1-8 H'' axis would be in the negative H'' axis, hence the plot typically lies in the 4th quadrant instead of the 1st. However in Fig. 1-8, the H'' axis is presented as $-H''$, hence the H'' values will be in the positive axis and the entire plot would lie in the 1st quadrant. Note also that H' and H'' in Fig. 1-8 example is stated in Ω , but in

reality, they are dimensionless according to (5) and (6). We also notice that the plots in Fig. 1-8 extend to the 2nd quadrant (3rd quadrant for an inverted plot) or in other words to negative values at the high-frequency region. This feature has also been observed in other IMPS characterizations in the literature [47, 50], in the case of bulk heterojunction OPV, it is attributed to the finite transit time of carriers between exciton splitting at the heterojunction and extraction at the contacts [47]. In addition, from Fig. 1-8 semicircle peak, we can also determine the time constant τ that is similar with the Bode plot's τ in Fig. 1-7. This time constant can be derived from the frequency f at the semicircle's maximum peak in Fig. 1-8. This frequency f is actually the corner frequency f_c that we correspondingly determine from the Bode amplitude and phase plot in Fig. 1-7. The f_c in Fig. 1-8 is also the frequency where the transfer function phase $\theta = 45^\circ$. So again, from the f_c we can derive τ via $f_c = 1/2\pi\tau$ [22, 39]. With the time constant τ again representing the characterized system specific internal dynamic [22, 39].

As for the example of a transfer function $H(\omega)$ Nyquist plot for IMVS mode of operation, this is depicted in Fig. 1-9, taken from Metrohm application note of a dye-sensitized solar cell (DSSC) IMVS result [48].

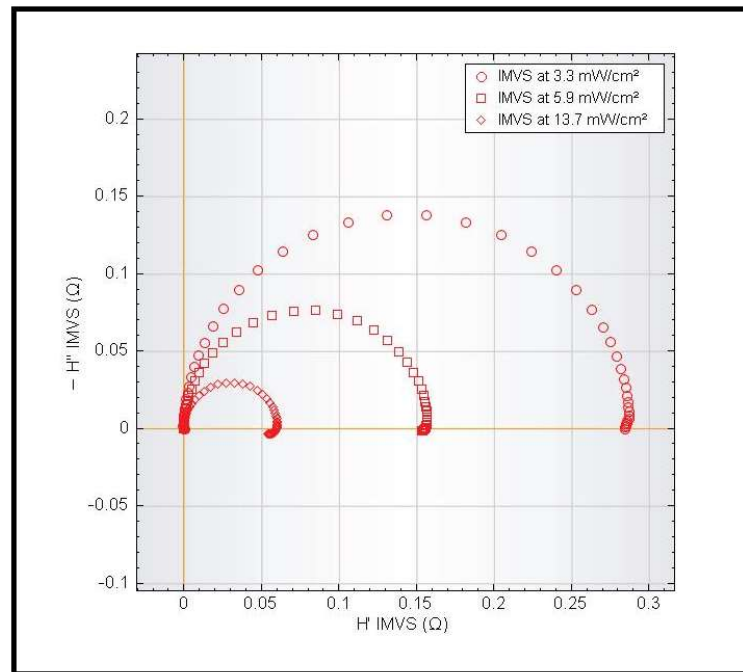


Fig. 1-9. Example of several $H(\omega)$ Nyquist plot result from a dye-sensitized cell under an IMVS mode of operation. The plot is taken at different DC light intensity φ_o^{LED} , with $-H''$ parametric with frequency ω . The $H(\omega)$ plot here is also presented as an inverted plot, with the plot's real (H') and imaginary axis (H'') under a (-) sign. Note also that H' and H'' are in Ω . Here, the direction of increasing frequency is anti-clockwise, with the units of both H' and H'' in Ω . [48].

From Fig. 1-9, we can see that the plots form perfect semicircles, each with a single peak, with frequency increasing in the anticlockwise direction. The $H(\omega)$ plots in Fig. 1-9 are also presented as

inverted plots, with the plot's real (H') and imaginary axis (H'') under a (-) sign. As in Fig. 1-8, we can also determine the time constant τ from the frequency f at the semicircle's maximum peak in Fig. 1-8. This is done through $f_c = 1/2\pi\tau$ [23, 40]. With the time constant τ again representing the characterized system specific internal dynamic [23, 40]. In addition, we can also present the Nyquist plot results in both IMPS and IMVS as the plot of real vs imaginary part of ΔJ and ΔV respectively [39, 40]. Later in this work, we introduce a new mode of operation that is neither IMPS or IMVS for organic photovoltaic (OPV) applications. This mode is called IMS under finite load and in the case of OPV characterizations, this operational mode is neither IMPS nor IMVS but instead lies between both modes of operation.

Finally, as in 1.1., several advantages of IMS compared to other methods are that any parameters obtained from IMS can also be assigned to specific dynamics inside the system. To add, IMS, as well as IS, can also be done automatically, thus improving the method's accuracy while also reducing any potential for errors [16, 21, 22]. The distinctive advantage of IMS, especially over IS, is that since light is the sole source of stimulus, in the case of solar cell IMS, we can perform IMS at one of the solar cell operating conditions in its J/V characteristics, i.e. either at the cell's short-circuit condition, which is called intensity-modulated photocurrent spectroscopy (IMPS) or at the cell's open-circuit condition, which is intensity-modulated photovoltage spectroscopy (IMVS) [40]. Another advantage of IMS over IS is that because light is the sole source of stimulus in an IMS, the resulting electrical response in an IMS experiment would solely be determined by the illumination intensity of the light source, and not due to any external electrical contacts. This meant that instead of applying voltage or current through an electrode or any electrical contacts as is the case in IS, IMS light stimulus can be directly applied to the characterized system, hence minimizing any series resistance effect from external electrical contacts. To add, IMS is also very suitable for BHJ OPVs and DSSCs dynamic characterizations as carrier transport is much slower in these type of devices, hence it is more susceptible to IMS frequency range with the advantage of light as its main characterizing signal [23, 40, 50]. However, the drawback of this method is it's limited to photosensitive devices characterizations [16, 23, 39, 40].

Chapter 2

Theory and Fundamental Concepts

2.1 Structure of Organic Semiconductors

Organic semiconductors are semiconductors that are made of molecules where the backbone of the molecular structure is formed by pi-conjugated orbitals [1, 9, 52]. This structure will then result in the energy difference of < 4 eV between the molecule's highest occupied molecular orbital (HOMO) and its lowest unoccupied molecular orbital (LUMO), hence the material semiconducting nature [1, 9, 52]. This formation will then define the semiconductor's optical and electrical properties. Examples of organic semiconductors are, thiophenes (P3HT, PCPDTBT, PDTBPBT, PTB7), PPV polymer (MEH-PPV, MDMO-PPV) and TPD polymer (PBDTTPD). A depiction of these semiconductor structures, along with their energy gap are shown in Fig. 2-1, taken from Saunders et al [53].

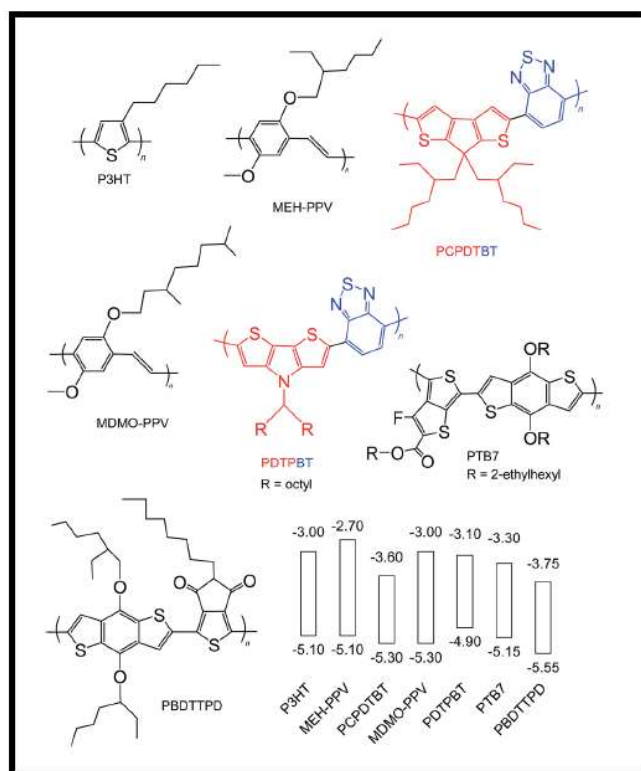


Fig. 2-1. Several examples of organic semiconductors along with their structures and energy gap [53].

Meanwhile, organic semiconductor devices are devices that use organic materials as the semiconducting component, with the organic materials being conjugated polymers or small organic molecules. Examples of organic devices are organic photovoltaics (OPV), organic light-emitting diode (OLED), organic thin film transistor (OTFT) and organic bistable memory devices [1, 54].

Interests in organic semiconducting material research started in the 1960s with investigations on the optical and electronic properties of acenes as model organic molecules [41]. By late 1970s and into the 1980s, organic semiconductor research gained a significant momentum when highly pure small organic molecules with tailored structure and properties were made and processed at room temperature and later deposited into thin films by using a physical vapor deposition technique [9]. At the same time, conjugated polymers research also gained significant interest after the popularization of conductive polymers by Heeger, MacDiarmid and Shirakawa [55]. Another significant milestone was achieved when Tang reported the development of a bilayer organic photovoltaic (OPV) with a power conversion efficiency of $\sim 1\%$, thus heralding the rise of OPV as an alternative PV technology to silicon PV [14]. By the 1990s, with the availability of highly pure conjugated polymers, OPV fabrications can be achieved through low-temperature solution processing, which is a highly desirable property in organic semiconductors and puts them in an advantage over their inorganic counterparts [56]. There are several reasons for recent growing interest in organic semiconductor devices. These are most importantly, the semiconductor's ability to be made in a fast and simple manner, especially through low-temperature solution processing with low energy cost and good scalability for large-area applications [1, 8]. In addition, organic semiconductors can also be used with flexible plastic substrates for low-cost and flexible form application, e.g. plastic solar cells [9]. Finally, in the case of OPV, the device can be made from an abundant supply of source materials [8]. However, organic semiconductor devices also have their drawbacks, especially compared to inorganic ones. These are, poor device efficiency and stability, as the device is susceptible to chemical and physical degradation from exposure to the ambient environment, and low carrier mobility. The semiconductor's low mobility will also limit the device thickness, thus reducing its active area size and its performance [1, 8, 57].

The main characteristics of organic semiconductors are that the optical absorption and charge transport within the semiconductor molecular structure is dominated by delocalized pi- and conjugated pi orbitals, and then, any excitations that occur in an organic semiconductor will be localized within the semiconductor's molecule, because the strength of intermolecular electronic couplings between adjacent molecules is weaker than the overlap of pi-orbitals within the molecule itself [1, 9, 52]. As a consequence of the localized nature of any excitations in an organic semiconductor, transport will occur via thermally assisted tunnelling or "hopping" of polarons from one molecule to another at room temperature. With a polaron being an excitation state in an organic semiconductor where a charge carrier is either removed from/added to the semiconductor molecular backbone, which is also accompanied with lattice deformation or relaxation within the backbone [1, 9]. In addition, this weak intermolecular coupling between molecules and the localized nature of the

excitation will then result in the semiconductor's lower mobilities (10^{-7} to 10 $\text{cm}^2/\text{V s}$) when compared to inorganic semiconductor mobility (10^3 to 10^4 $\text{cm}^2/\text{V s}$) [1, 9, 52]. Another main characteristic of organic semiconductors is the presence of diagonal disorder phenomenon that is also caused by the localized nature of any excitation [1, 9]. To add, most organic semiconductors can only transport either hole polaron or electron polaron due to the presence of traps for the other carrier type, hence the presence of another localized carrier will then cause it to fall into a trap that is also localized [1]. Finally, the absorption length of organic semiconductors is quite small, i.e. in the order of 100 nm, this is in addition to their narrow absorption width (i.e.~200-300 nm) with respect to the absorption edge [2]. In the following subchapters, we elaborate more on organic semiconductor's pi-conjugated orbital structure and charge transport, including the role of polarons and excitons, types of carrier transport and carrier mobilities. We then describe luminescence/light emission in organic semiconductors, i.e. fluorescence and phosphorescence. Following this, we perform IMS on bulk heterojunction (BHJ) OPV and OLED and will elaborate more on both BHJ OPV and OLED structure and operations.

2.1.1 Hybrid Orbitals and Conjugated Molecules

To better understand organic semiconductor's structure, we first examine the structure of carbon and how chemical bonding develops between carbon atoms. A carbon atom has 6 protons and 6 neutrons in its nucleus and 6 electrons located on its orbitals. In the ground state, the 6 carbon electrons are arranged as shown in Table I.

TABLE I. ELECTRON ARRANGEMENTS WITHIN THE ORBITALS OF A CARBON ATOM AT GROUND STATE

Orbital	1s	2s	2p _x	2p _y	2p _z
No. of Electrons	2	2	1	1	0

From Table I, the electronic configuration of a carbon atom is written as $1s^2 2s^2 2p^2$. Here, with regards to 1s, 1 is the principle quantum number of an electron shell and s is the electron subshell within that shell. Also for 1s, the orbital quantum number, designated by l, is 0, and that its magnetic quantum number, represented by m, is also 0. While for 2p, the orbital quantum number $l = 1$ and the magnetic quantum number $m = 1$. The s subshell itself can accommodate a maximum of 2 electrons, with the p subshell able to accommodate as much as 6 electrons, hence the $1s^2 2s^2 2p^2$ configuration in Table I. As in most elements, (chemical) bonding in the form of a covalent bond will take place between the carbon atom outer shell orbital with another atom's outer/valence electrons. In carbon,

however, bonding occurs via first a “promotion” process, which is then followed by “hybridization” process. The first process, i.e. “promotion” occurs when carbon “promotes” one electron from subshell 2s to the empty p_z orbital, which then results in the electronic configuration $1s^2 2s^1 2p^3$. After “promotion”, a “hybridization” process then follows, in which carbon will combine/“hybridizes” the remaining 2s electron with the 2p electrons such that three possible (orbital) combinations may occur. These combinations are called “hybrid orbitals”, and these are designated as “ sp^3 ”, “ sp^2 ” and “ sp ” hybrid orbitals [58, 59].

The first type of hybrid orbitals, i.e. “ sp^3 ”, occur when the 2s electron fills and then “hybridizes”/combine with three 2p orbitals and one 2s orbitals to form “ sp^3 ” hybrid orbitals. In the case of “ sp^3 ” hybrid, the 4 “ sp^3 ” will form a tetrahedron structure, with the 4 orbital “arms” pointing outwards into space symmetrically and forming tetrahedron corners with neighbouring atoms outer orbitals. The angle between the “arms”/bonds that form the (tetrahedron) structure is 109.5° . Now when bonding happens between two atoms having “ sp^3 ” hybrid structure, one of the “ sp^3 ” orbitals can form a strong σ (sigma) bonds of the same length and strength with adjacent atoms or with neighboring atom’s “ sp^3 ” orbitals. This σ bond between a “ sp^3 ” orbital and another atom is called a single bond (C-C). Note also that a carbon structure that consists of/forms 4 σ bonds with its “ sp^3 ” orbitals is said to be “saturated”. An example of a carbon backbone in other substances which has a “ sp^3 ” hybrid structure is ethane (C_2H_6) [58, 59].

The next type of hybrid orbitals, i.e. “ sp^2 ”, occur when the 2s electron fills the remaining 2p orbitals but only “hybridizes” with two of the 2p orbitals, while leaving one 2p orbital “unhybridized” so that a total of 3 “ sp^2 ” hybrid orbitals are formed. In “ sp^2 ” hybrid, the 3 “ sp^2 ” orbital will form a trigonal-planar structure, with the 3 orbital “arms” having the same (bond) length and located within one plane while the “unhybridized” 2p orbital is perpendicular with respect to the (trigonal) plane. The angle between the “arms”/bonds that form the trigonal structure is 120° . To add, a “ sp^2 ” hybrid molecule can also be formed by atoms having the same hybrid structure. So first, the two “ sp^2 ” orbitals forms “ sp^2 ” bonds (each having the same bond length) with adjacent atoms non-“ sp^2 ” orbitals, with the one “ sp^2 ” orbital forming a σ bond with another atom’s “ sp^2 ” orbital. The “unhybridized” 2p orbital will then form a much weaker π or pi-bond (compared to σ bond) with another “unhybridized” 2p orbital in the neighboring atoms. So in total, 1 σ and 1 π bond will then exists within the “ sp^2 ” hybrid structure, and this bond combination is then called a double bond ($C=C$). Note that in this case (bonding between atoms with the same hybrid), since the π bond is much weaker in nature, the resulting orbital structure will be “delocalized” between two atoms due to the much further position the “unhybridized” 2p occupies from the central carbon atom. An example of a substance which has “ sp^2 ” hybrid structure is ethene (C_2H_4) [58, 59].

Finally, the third type of hybrid orbitals, i.e. “sp” hybrid, occur when one of the 2s electron goes to the remaining 2p orbital and the remaining 2s hybridizes with one of the 2p orbitals, leaving two 2p orbital “unhybridized” so that a total of 2 “sp” hybrid orbitals are formed. The “sp” hybrid orbital will then form a linear structure, with the 2 orbital “arms” having the same length and are located in-line with each other, while the two “unhybridized” 2p orbitals are perpendicular with respect to the linear structure. Again, we can also form a “sp” hybrid molecule between atoms with “sp” hybrid structure. In this case, an atom “sp” orbital will form a σ bond with the other atom’s “sp” orbital and one of the “unhybridized” 2p orbital in an atom will form a π bond with another atom’s “unhybridized” 2p orbital. While another “unhybridized” 2p orbital that is located at 90° with the first “unhybridized” 2p will also form a π bond with another atom’s “unhybridized” 2p. So in total, 1 σ and 2 π bond will exist within the “sp” hybrid structure, and this is then called a triple bond ($C\equiv C$). An example of a substance with this structure is acetylene (C_2H_2) [58, 59]. A depiction of “sp³”, “sp²” and “sp” hybrid orbitals structure is shown in Fig. 2-2.

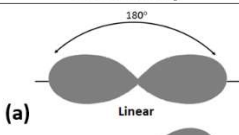
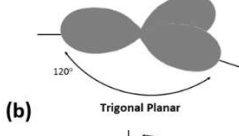
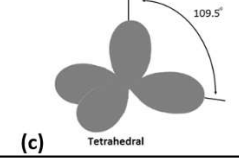
Atomic Orbital	Hybrid Orbital	Geometry
s p	Two sp	 <p>(a) Linear</p>
s p ²	Three sp	 <p>(b) Trigonal Planar</p>
s p ³	Four sp	 <p>(c) Tetrahedral</p>

Fig. 2-2. The three different carbon hybrid orbitals (a) The “sp” hybrid orbitals with 2 “sp” forming a linear structure, (b) The “sp²” hybrid orbitals with 3 “sp²” forming a trigonal-planar structure and (c) The “sp³” hybrid orbitals with 4 “sp³” forming a tetrahedron structure The respective hybrid orbital’s angle is also given in the figure.

An important structure commonly found in a conjugated molecule is the benzene ring structure. A benzene ring comprises 6 “sp²” hybrid orbitals that form a planar hexagonal structure, with a 120° angle between the “sp²” hybrid bonds such that each hexagon vertices will be occupied by a carbon nucleus. In the benzene structure, each carbon atoms uses two “sp²” hybrids to form a σ bond with other carbon’s “sp²”, while the remaining “sp²” hybrid is then used to bond with the outer orbitals of hydrogen (H) atoms. So here, the hexagonal sides are formed by “sp²” hybrid bonds between the carbon atoms. The remaining 2p orbital will then overlap with other atom’s 2p orbital to form a π bond, so a carbon atom’s 2p orbital in the hexagon vertices will have one π bond though it is not clear

with which neighboring carbon's 2p orbitals [60]. As a result of this structure, the planar hexagonal structure will then consist of alternating double and single bonds as depicted in Fig. 2-3.

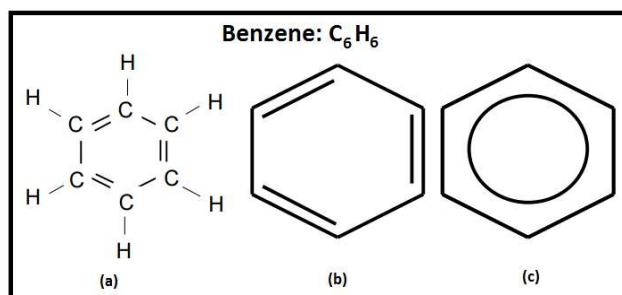


Fig. 2-3. Three different depictions of the benzene ring structure. These are (a) The benzene ring structure with the complete atomic labels. (b) The alternate single and double bonds depiction of the ring structure and (c) another depiction of the benzene ring structure that shows the influence of 2p orbital's delocalization within the structure.

As we can see from Fig. 2-3(a) and (b), it is not clear where the location of the π bond should be within the structure. In reality, one depicts the π electrons (from the π bonds) in Benzene as delocalized throughout the ring structure, where the π electrons spread throughout the π bonds in the (ring) structure. Note that the length of the hexagonal sides in Fig. 2-3(c) structure = 1.39 Å [60].

The delocalization of the π electrons between the carbon atoms π bonds in the same molecule is the defining feature of a conjugated molecule. Any organic molecules that have this feature are called a conjugated molecule. The energy difference between the molecule's highest occupied molecular orbital (HOMO) and its lowest unoccupied molecular orbital (LUMO) is determined by the degree of the π electron's delocalization in that molecule. The more π electrons are delocalized in an organic molecule, the more conjugated the molecule will be, and as the molecule conjugation increases, the energy gap between the molecule's HOMO and LUMO will also decrease to a few eV, thus classifying conjugated molecules as organic semiconductors [60-62].

2.1.2 Polarons and Excitons in Conjugated Molecules

For a semiconductor to be useful for applications, it must be excited from its ground state. Here, we will discuss two fundamental excitations in conjugated molecules, i.e. excitons and polarons. When an organic semiconductor molecule is in its ground state or lowest energy state, the molecule's HOMO will be fully occupied with electrons while its LUMO is left vacant. If an electron is removed completely from the HOMO and the entire molecule itself or is added into the LUMO with the HOMO fully occupied, the resulting molecule then becomes a polaron or also called a radical ion. The term "radical" here refers to the molecule's net spin due to the presence of an unpaired electron when an electron is either removed from the molecule's HOMO or added into its LUMO. If an electron is removed from the HOMO, the radical ion is then called a radical cation or hole polaron, since the

removal of the electron (from HOMO) will cause the molecule to have a net positive charge. On the other hand, if an electron is added into the LUMO but with the HOMO fully occupied, the radical ion will become a radical anion or electron polaron, as the molecule will have a net negative charge.

Here, the removal or addition of a carrier is also accompanied by the molecule's structural deformation, where the structure's orbitals are affected and as a result, bond distances and angles also changes. The underlying cause behind this deformation is the localized character of excitations or strong electron-vibration coupling in an organic semiconductor, which is very different compared to carrier behavior in a conduction band (CB) or valence band (VB) of a crystalline semiconductor. After a carrier is either removed or added into an organic molecule structure, the entire structure will be relaxed into a position of minimum energy [9, 62, 63]. An illustration of hole and electron polaron formation in an organic semiconductor structure, along with both polarons formation in terms of spin, is shown in Fig. 2-4(a) and (b) respectively. In Fig. 2-4(a) we use PPV (polyphenylene vinylene) as the organic semiconductor example.

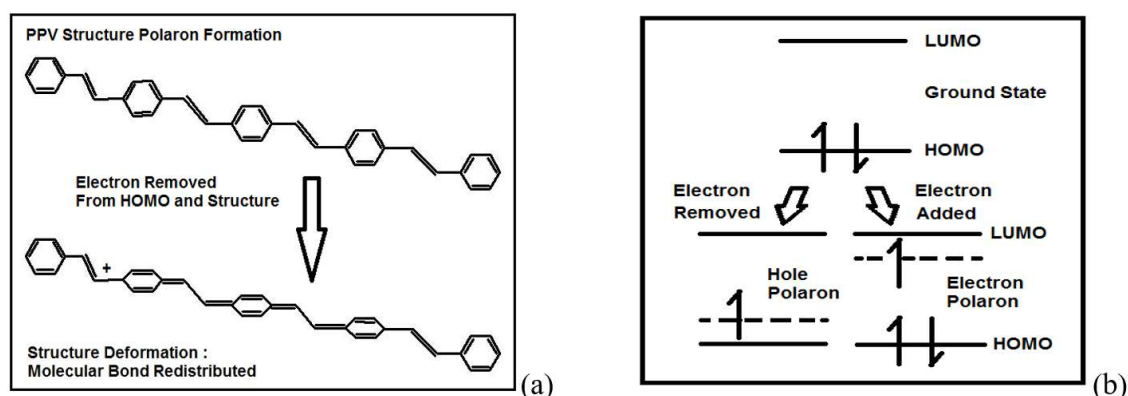


Fig. 2-4 (a). Illustration of polaron formation in a PPV structure. Shown here is a hole polaron formation, i.e. when an electron is removed from the molecule's HOMO. This then results in the molecule's structure experiencing a deformation due to the strong electron-vibration coupling in an organic semiconductor. After electron removal, the semiconductor's structure relaxes to the minimum energy position but with different bond lengths and angles due to bond redistributions. (b). In terms of spin, the molecule's HOMO will be fully occupied with no net spin at the ground state. If an electron is removed, a net spin will be present from an unpaired electron with the electron transitioned to a lower energy level due to strong electron-vibration coupling. On the other hand, if an electron is added, a net spin will be present and the added electron will gain more energy than the LUMO, with the electron transitioning to a lower energy level.

From Fig. 2-4(a), we can see that polaron formation is accompanied by structural deformation that causes changes in bond lengths due to strong electron-vibration coupling in the semiconductor (PPV in Fig. 2-4 example). The polaron showed in Fig. 2-4(a) is a hole polaron which is formed when an electron is removed from a semiconductor molecule's HOMO. In Fig. 2-4(b), in terms of spin, if an electron is removed from the HOMO, a hole polaron will be formed with the presence of an unpaired electron with a net spin. This unpaired electron, in turn, will transition to an energy level higher than the HOMO. On the other hand, if an electron is added into the LUMO, with the HOMO fully occupied, an electron polaron will be formed with the presence of an unpaired electron and a net spin.

The added electron will transition to an energy level lower than the LUMO. In addition, because of the strong electron-vibration coupling in an organic semiconductor, removing an electron in the structure will cost less in energy than the HOMO level, while electron added into the LUMO will gain more energy than the LUMO level, as illustrated in Fig. 2-5 [63].

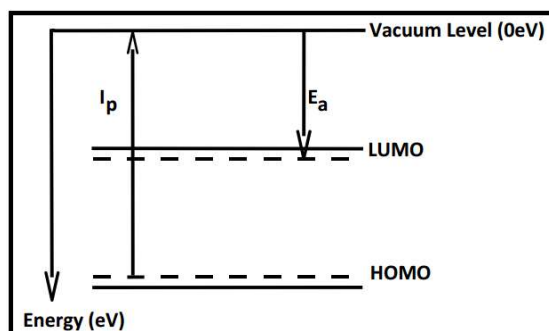


Fig. 2-5. Because of the strong electron-vibration coupling in an organic semiconductor, removing an electron from the molecule will cost less in energy than the HOMO level, with the energy needed by the molecule to remove an electron from the HOMO being the ionization potential or I_p (in eV). On the other hand, an electron added into the molecule will gain more energy than the LUMO level, with the energy gained by the molecule called the electron affinity or E_a (in eV).

From Fig. 2-5, the energy needed by the molecule to remove an electron from the HOMO is called the ionization potential or I_p (in eV). While the energy gained by the molecule when an electron is added into the LUMO is called the electron affinity or E_a (in eV) [63].

The other type of excitation which can be found in many organic semiconductor applications is called an exciton. In an organic semiconductor molecule, if an electron is removed from the molecule's HOMO and is excited into its LUMO, an exciton state will then be formed. This state is electrically neutral as there is a presence of an unpaired electron in the LUMO and a hole in the HOMO. Exciton formation usually occurs when a photon is absorbed by an organic semiconductor. In addition to an exciton being electrically neutral, it is also accompanied by structural deformation due to strong electron-vibrational coupling as was the case of a polaron. The affected orbitals in the deformed structure then become π^* orbitals and are called antibonding orbitals, because the affected orbitals overlap in a destructive manner such that it would result in the molecular orbital having a higher energy compared to individual atomic orbital [59, 62]. The molecular structure itself will still be intact during π^* orbital formation due to the presence of strong σ -bonds in the molecule. An illustration of exciton formation in an organic semiconductor structure, along with its depiction in terms of spin is shown in Fig. 2-6(a) and (b) respectively. To add, in Fig. 2-6(a) we again use PPV as an example.

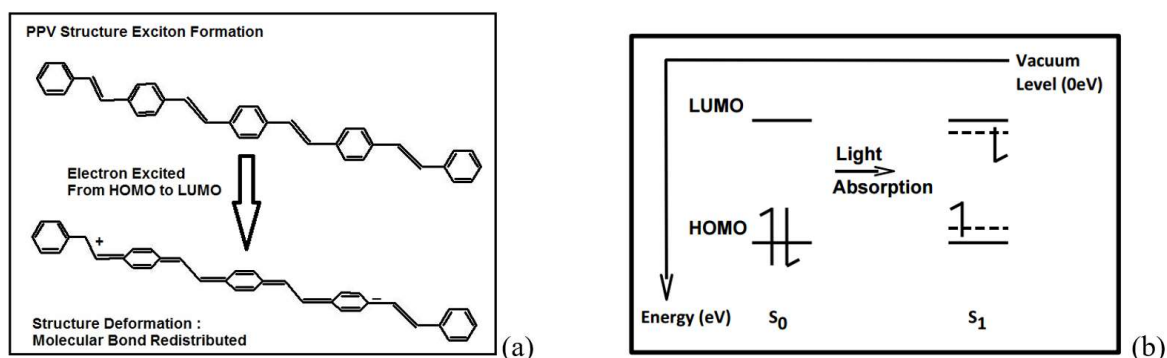


Fig. 2-6 (a). Exciton formation in a PPV structure. Here, an electron is excited from the molecule's HOMO into its LUMO which results in the molecule's structure experiencing a deformation due to strong electron-vibration coupling. Exciton formation usually occurs when a photon is absorbed. After formation, the excited structure will have different bond lengths due to the strong vibration coupling (b). In terms of spin, the molecule's HOMO will be fully occupied with no net spin in the ground state, which is called the S_0 state. Now if an electron is excited from the HOMO into the LUMO by photon absorption, the S_0 state will be excited into a singlet exciton state or S_1 . At S_1 state, the excited electron transitions to an energy level lower than LUMO while the unpaired ones in the HOMO transition to a higher energy level than the HOMO.

From Fig. 2-6(a), we can see that exciton formation is also accompanied by structural deformation that leads to different bond lengths due to strong electron-vibration coupling in an organic semiconductor (PPV in Fig. 2-6(a)). In addition, because of this strong electron-vibration/phonon coupling, an exciton is by nature a strongly bound electron-hole pair, in which the bond is a coulomb-type bond. As a result, the exciton binding energy (E_b) is high, ranging from 0.5-1 eV. Because of this strong bond, the size of an exciton in the organic semiconductor is about 10 nm. This means that the exciton in organic semiconductors is classified as a Frenkel or localized exciton because it occurs/localized in a single conjugated molecule which is reflected in its size. This is contrary to a Wannier exciton or delocalized exciton, which occurs in a band and are usually found in inorganic semiconductors, with the exciton binding energy being much lower than that of Frenkel exciton. Finally, in the case of an exciton, the semiconductor molecule's energy gap (E_g) can be defined from Fig. 2-6(b), as either the difference between the ionization potential and the electron affinity or $E_g = I_p - E_a$, or as the difference between the exciton binding energy E_b and ionization potential - electron affinity difference, or $E_g = (I_p - E_a) - E_b$. Examples of organic semiconductor devices that uses excitons in their operations are organic photovoltaics (OPV) and organic light-emitting diodes (OLED) [2, 9, 62, 63].

In quantum mechanics, an exciton by its nature is represented by a wavefunction which has both a spin and a spatial component. In the ground state, the molecule's HOMO will be fully occupied with no net spin, which is usually called the S_0 spin state as we can see in Fig. 2-6(b). Once an exciton is formed due to photon absorption, the molecule's S_0 state will then be excited into an S_1 singlet exciton state as seen also in Fig. 2-6(b). An S_1 singlet exciton, is formed when there is a presence of

antiparallel spins from an unpaired electron with spin up and an unpaired holes with spin down that lies in an energy level higher than the HOMO, and another unpaired electron with spin down with an unpaired holes with spin up that lies at an energy level lower than the LUMO, which together results in a total spin = 0. In terms of the wavefunction, the spin part of a singlet exciton wavefunction is antisymmetric, i.e. its wavefunction changes sign under an exchange of particles. In general, there are three combinations of electron and hole spin that will result in an overall symmetric spin part in the wavefunction, in which the wavefunction does not change sign under an exchange of particles. There is one combination that will result in antisymmetric spin part in the wavefunction, i.e. wavefunction changes sign in an exchange of particles. These symmetric and antisymmetric electron and hole spin combinations can be represented by a ket notation as shown in Table II [2, 63].

TABLE II. POSSIBLE ELECTRON AND HOLE SPIN COMBINATIONS IN A WAVEFUNCTION IN TERMS OF A KET NOTATION

Spin state Ket	Total Spin S	Symmetric (+) / Antisymmetric (-)
$ \uparrow\uparrow\rangle$	1	+ (Triplet)
$ \downarrow\downarrow\rangle$	1	+ (Triplet)
$1/\sqrt{2}(\uparrow\downarrow\rangle + \downarrow\uparrow\rangle)$	1	+ (Triplet)
$1/\sqrt{2}(\uparrow\downarrow\rangle - \downarrow\uparrow\rangle)$	0	- (Singlet)

From Table II, we can see that the three symmetric spin combinations will result in a total spin = 1, where the wavefunction does not changes sign under an exchange of particle. This three symmetric combination is called the triplet exciton state (T_1). The spin combinations that result in a singlet exciton state has its wavefunction changes sign (-) under an exchange of particles as seen also in Table II. Hence, we can see that when a photon is absorbed, an organic semiconductor will be excited from its S_0 spin state into an S_1 singlet exciton state as seen in the antisymmetric spin combinations in Table II. However, in order to form a triplet exciton state T_1 , we need to combine an electron and hole polaron together to form a symmetric spin combinations as seen also in Table II [63].

2.1.3 Light Emission from Conjugated Molecules

From 2.1.2., when a photon is absorbed by an organic semiconductor molecule, the molecule is then excited from its ground S_0 state to form a singlet S_1 exciton state. Alternatively, the reverse can also happen, so a molecule that is excited into a singlet S_1 state can also decay into the ground state S_0 , and in doing so accompanied by light emission from the molecule itself. This decay process is then called fluorescence. In other words, fluorescence will only be produced from the decay of a singlet S_1 exciton state into the ground state S_0 [62-64]. An illustration of this process, and later

phosphorescence light emission in terms of spin states is shown in Fig. 2-7, taken from Clegg et al [64].

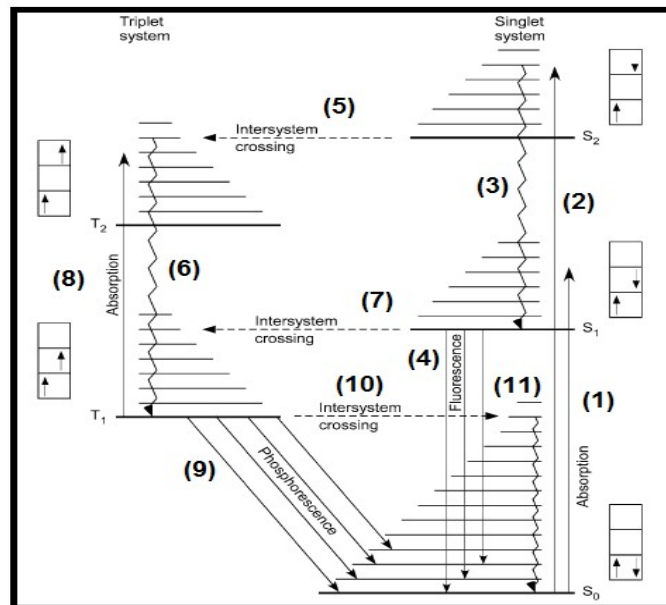


Fig. 2-7. An illustration of fluorescence and phosphorescence processes in an organic semiconductor molecule. First, a photon is absorbed by the molecule which then excites the molecule (electron) from the ground state S_0 with no net spin into (1) the first singlet exciton state S_1 , where there is a net spin, or (2) into a much higher singlet exciton state S_2 which has a net spin at a higher energy state. Once the molecule has been excited into S_2 , it will always decay to S_1 (3) due to interaction with the outside environment and internal vibrations. When it arrives at S_1 , the molecule can further decay into the ground state S_0 , accompanied by light emission from the semiconductor (4). This process is called fluorescence and the resulting light spectra are broad since the decay from S_1 to S_0 can occur from a lower S_1 energy level to different vibrational levels of S_0 . In addition, if a molecule is excited into an S_1 or S_2 state, it can decay from these states to another energy states which are lower, i.e. the triplet T_1 and a higher T_2 state via intersystem crossing (ISC) mechanism in (5) and (7). However this ISC decay process is very rare and triplet excitons are most commonly found in electrically driven devices. If the molecule transitions to higher T_2 state, the molecule can decay into the lower T_1 state due to internal vibrations (6). Also, photon absorption can occur when the molecule is already in the T_1 state, which can then excite the molecule into the T_2 state (8). When a molecule has already decayed into the T_1 state, two decays pathways are possible, one is that the molecule decays directly into the ground state S_0 , which is called the phosphorescence process (9), in which there must be an interaction/coupling between the singlet and triplet states. While the other decay pathway for T_1 state molecule is through intersystem crossing mechanism to higher S_0 state (10) at which it can then decay into the S_0 state (11) [64].

From Fig. 2-7, the process occurs as follows, first, as in 2.1.2., the molecule's HOMO will be fully occupied with no net spin at the ground state S_0 . Then, when a photon is absorbed by the molecule, the molecule (electron) will be excited from the S_0 to the different vibrational levels of S_1 (1) and even higher to the S_2 state (2). The absorption spectrum in (1) and (2) will be broad because of the strong electron-vibration coupling in the molecule itself. Once the molecule has been excited into S_2 , it can decay/relax back to S_1 (3) due to interaction with outside environment and internal vibrations in the S_2 level. When the molecule has decayed back to the S_1 state, it can further drop/decay from the lower level of the S_1 state into the higher level of the ground state S_0 (and the ground state level itself) and is also accompanied by light emission from the semiconductor (4). This decay process is then called fluorescence and the resulting light spectra are typically broad since the decay from S_1 to

S_0 occurs from the lower S_1 energy level to different higher levels of S_0 , including S_0 itself. The underlying reason behind the broad emission spectra is also the strong electron-vibration coupling in the molecule itself. So from the process (1) to (4), step (4) will result in light emission/fluorescence and step (3) will result in a nonradiative decay [64]. A typical fluorescence process happens on a time scale of 10^{-10} to 10^{-8} s [4, 64].

Also in Fig. 2-7, when a molecule is excited into an S_1 or S_2 state, it can also experience a transition into the lower triplet states T_1 and T_2 via an intersystem crossing (ISC) mechanism in (5) and (7). An ISC mechanism is caused/driven by a coupling interaction between the S_1 , S_2 , and T_1 , T_2 states which are called the spin (S)-orbit (L) or LS coupling interaction. Earlier in this chapter, and from the discussion of the process (1) to (4), when a photon is absorbed, this process will only generate a singlet exciton S_1 , with the generated singlet excitons capable of decaying as fluorescence. So the transition for the absorption process is called the $S_0 \rightarrow S_1$ transition. In the absorption process, each photon carries with it an orbital angular momentum L , with the S_0 and S_1 orbital quantum number differing by one. Thus, the photon will then provide an angular momentum for the $S_0 \rightarrow S_1$, while in fluorescence, when the transition becomes $S_1 \rightarrow S_0$, this transition will provide an angular momentum for light emission. Thus, the fluorescence transition ($S_0 \rightarrow S_1$) is dipole allowed as it fulfils the selection rule of $\Delta\ell=1$. However, the transition from the first triplet state T_1 to S_0 or $T_1 \rightarrow S_0$ is dipole forbidden since both T_1 and S_0 have the same angular momentum quantum number = 1. Thus, $\Delta\ell=0$ for the $T_1 \rightarrow S_0$ transition, as the transition cannot provide an angular momentum for photon emission, and therefore cannot emit a fluorescence light. This also applies for the $S_1 \rightarrow T_1$ and $S_2 \rightarrow T_2$ transitions (T_2 the higher triplet exciton state) which are also dipole forbidden [64, 65]. However, a triplet exciton also has an angular momentum component, although it is in the form of spin instead of orbital angular momentum. Several molecules can convert this spin into an orbital angular momentum. This (spin \rightarrow orbital angular momentum) is achieved by facilitating the weak link between the spin and orbital angular momentum component in the triplet through the interaction of magnetic fields that are generated by both the spin and orbital angular momentum. This interaction between the magnetic fields will then be proportional to the product of the triplet's spin and orbital angular momentum, and thus known as the spin (S)-orbit (L) or LS coupling interaction. To produce a strong LS coupling, we can add atoms into our molecule atoms that will fill the molecule's atomic shells with an orbital quantum number = 1. Typically, this is done by adding atoms with high atomic numbers Z , i.e. higher than that of carbon, into the molecule. An example of such atom is phosphorus [64, 65]. Thus, it is very rare for an ISC decay to occurs without this coupling interaction.

So again in Fig. 2-7, a molecule excited into an S_1 or S_2 state is able to transition into the lower triplet states T_1 and T_2 via an ISC mechanism in (5) and (7), due to the LS coupling interaction between

S_1 , S_2 , and T_1 , T_2 states. If a molecule in the T_1 state is excited to a higher T_2 state, the molecule can decay into the lower T_1 state due to internal vibrations (6). In addition, if photon absorption occurs when a molecule is in the T_1 state, the molecule can be excited into the T_2 state, as in (8). If a molecule already decays into the T_1 state, two main decay pathways are possible, one is by the molecule decaying directly into the ground state S_0 while also emitting light, which we then called phosphorescence (9). Thus, phosphorescence is the emission of light from the decay of T_1 to S_0 that is facilitated by the LS coupling between the T_1 and S_0 states in the form of ISC. While the other pathway is taken with the molecule transitioning via ISC from the T_1 state to higher S_0 state (10) at which point it can then drop/decay into the S_0 state without emitting any light, i.e. it is nonradiative by nature (11). So from the process (5) to (11), step (9) will result in light emission, i.e. phosphorescence, while step (6) and (11) will result in nonradiative decay [64]. In addition, a typical phosphorescence process is slower than fluorescence, because of the weak nature of LS coupling, with phosphorescence timescales of the order of μs to s [4, 64].

Also, the exciton that is produced from the combination of an electron and a hole polaron, as is the case in organic light-emitting diode (OLED), is different compared to the exciton that is produced when a photon is absorbed by an organic molecule. Whereas photon absorption will only generate singlet or S_1 excitons, electron and hole polaron injection in an OLED will produce a triplet or T_1 excitons as seen in Table II in 2.1.2. The light emitted from these (electrically generated) triplet excitons is then called electroluminescence (EL). When excitons are electrically generated, 1 out of 4 excitons will be in a singlet state, while the other 3 will be in a triplet state. This is because there are three ways to combine an electron and hole spin together, with only 1 way to combine the electron and hole polaron into a singlet state S_1 in a molecule, as seen in Table II in 2.1.2. Thus, in organic electroluminescence, the majority of produced excitons are triplet in nature and does not emit light at all [64, 65].

To further illustrate the coupling between the transition states and molecular vibration in an organic semiconductor structure, we use a potential energy diagram in Fig. 2-8 which show transition states that are involved in an absorption, fluorescence and phosphorescence process, taken from Clegg et al [64].

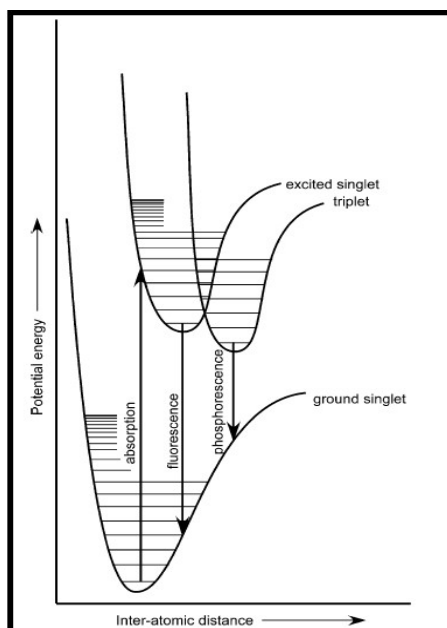


Fig. 2-8. A potential energy diagram that shows transitions and excitations between electronic states in an absorption, fluorescence and phosphorescence process with respect to inter-atomic distance in an organic semiconductor molecule [64].

From Fig. 2-8, we can see that in an organic semiconductor, both the ground and excited states are split into different energy levels due to the presence of discrete molecular vibrations components within each (ground and excited) states. Then, between the states in Fig. 2-8, several transitions will be allowed and these (transitions) are differentiated by the generated amount of molecular vibrations from absorption or emission processes. Transitions from the lowest vibrational level in the ground singlet state to the lowest vibrational level in the excited (singlet) state are called the 0-0 transition (not shown). An example of this transition is if the molecule is excited/transitioned from the lowest level of S_0 (ground singlet state) to the lowest level of S_1 (excited singlet state). While further transitions, such as 0-1 and 0-2, or sometimes 0-3 clearly results in molecular vibrations in either absorption or emission processes, and are called the vibronic satellites as we will see later in Fig. 2-9. Examples of these transitions are transitions from the molecule's lowest S_0 state to the first higher S_1 state, and again from the lowest S_0 state to the second higher S_1 state, with respect to the lowest S_1 state energy level. These transition states are separated in terms of their energy level by about 0.1 eV difference, with the (energy) spacing differences between transition states being the vibronic spacing. These vibronic spacing differences will then lead to a broad emission and absorption spectrum from a semiconductor molecule. The relative intensity of the transition states that results in molecular vibration are measured by a quantity called the Franck-Condon (FC) factor. This parameter is used as a measure of a transition state intensity in a spectrum plot. Hence, the same FC factor that occurs in both absorption and fluorescence spectrum, will then result in a mirror image property between

both spectra [64, 65]. As an example, a perylenediimide (PDI) molecule absorption-emission spectrum is shown in Fig. 2-9, taken from Fron et al [66].

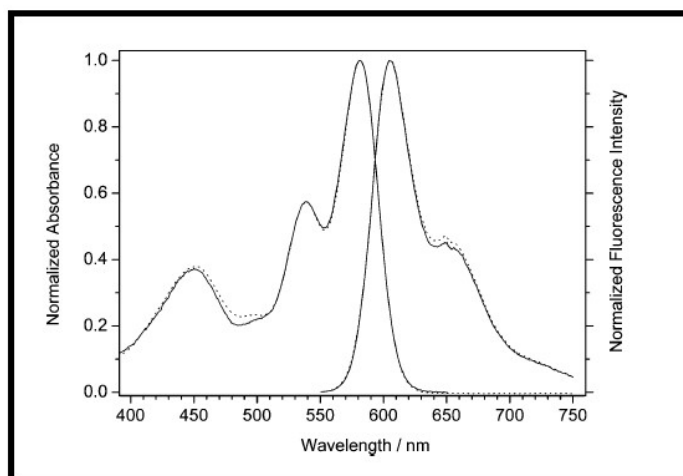


Fig. 2-9. A mirror plot of Anthracene absorption and emission (fluorescence) intensity spectra for an unspecified number of transition states with respect to the states wavelength (in nm) [66].

From Fig. 2-9, we can see the well expressed ‘mirror image’ symmetry between absorption and fluorescence, albeit this is often blurred in more flexible molecules, e.g. conjugated polymers. The spectra in Fig. 2-9 are symmetric around their intersection at ~ 600 nm. We also observe that the central or the 0-0 transition in the spectra has the highest intensity as it has the largest vibronic spacing. In addition, the 0-0 transition absorption peak is not always located at the same position with the 0-0 emission peak. In most cases and as seen in Fig. 2-9, the 0-0 emission peak is shifted by several nm (~ 5 - 10 nm) with respect to the 0-0 absorption peak. This shift is known as a Stokes shift, and it is caused by the interaction between the organic molecule and the surrounding environment. Hence, we can now determine the definition of an excited organic semiconductor band gap with much certainty from Fig. 2-9 plot example. The band gap, or the optical gap in Fig. 2-9 is defined as the beginning/’foot’ of the molecule’s 0-0 absorption spectrum, or it can also be defined as the intersection between the molecule’s absorption and emission spectrum [64, 65]. Finally, an example of an organic semiconductor application that utilizes both fluorescence and phosphorescence emission is an organic light-emitting diode (OLED) [4, 64].

2.2 Carrier Transport in Organic Semiconductors

As elaborated in 2.1, carrier transport in organic semiconductors will be determined by the semiconductor molecular structure which is dominated by delocalized pi- and conjugated pi orbitals, and also the overlap of pi-orbitals within the molecule itself. In addition, the semiconductor’s large electronic transition-molecular vibration couplings and diagonal disorder will also influence carrier

transport within the semiconductor. Carrier transport in the semiconductor itself happens via thermally assisted tunneling or a “hopping” process at room temperature. Transport occurs through polarons that hop from molecule to molecule or between one localized states to another in an organic semiconductor [1, 9, 52]. In discussing carrier transport, we first elaborate on carrier injection in organic semiconductors. A typical organic semiconductor device structure usually consists of one or more layers of active organic semiconductor that are sandwiched between two metal electrodes. Thus, efficient carrier transfer or injection at the interface between the metal-organic semiconductor is one of the most important factors in the performance of an organic semiconductor device, for example in an OLED and organic field-effect transistors (OFET). Carrier injection in an organic semiconductor, or in an organic semiconductor device, is the promotion of a carrier (electron or hole) from the device metal electrode(s) into an organic semiconductor molecule’s HOMO or LUMO. Therefore, charge injection will be strongly dependent on the metal-organic interface and the energy barrier that needs to be overcome by carriers at that interface. Specifically, the injection will be dependent on the energy difference/relationship between the metal electrode(s) Fermi level and the organic semiconductor LUMO and HOMO level, where the Fermi level is the energy level that separates the filled and empty electron states in a metal [67, 68]. While the energy needed to remove an electron from a metal is called the work function (Φ) [67]. To illustrate this relationship and to depict both electron and hole injection between metal-organic interfaces, we use the example of carrier injection on an organic semiconductor device, in which the semiconductor is sandwiched between two metal electrodes (e.g. OLED), with one electrode being the cathode, which injects electrons into the semiconductor, and the other being the anode, that injects holes into the semiconductor [67, 68]. This illustration is shown in Fig. 2-10, with PPV or polyphenylene vinylene as the organic semiconductor example, indium tin oxide (ITO) as the anode due to its high work function and a calcium-aluminium (Ca/Al) layer as the cathode due to the layer low work function.

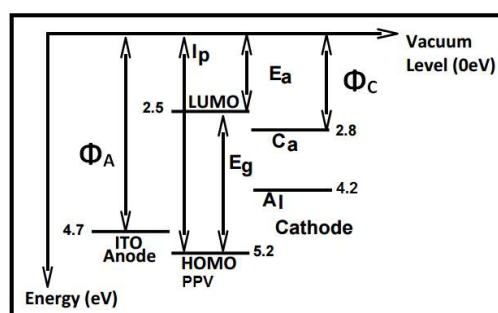


Fig. 2-10. An energy level illustration of an organic semiconductor device, in which the semiconductor is sandwiched between two electrodes, where one is an anode due to its high work function and the other being a cathode due to its low work function. In the above example, PPV is the organic semiconductor, ITO is the anode and the Ca/Al layer is the cathode. In the above illustration, E_g is the energy gap between the semiconductor’s HOMO and LUMO, I_p and E_a are respectively the ionization potential and electron affinity of the semiconductor, while Φ_A and Φ_C are respectively the anode and cathode work function. The respective energy levels of the anode, cathode, and the semiconductor’s LUMO and HOMO are also given. Finally, the vacuum level in the above is taken at 0 eV.

In Fig. 2-10, E_g is the energy gap between the semiconductor's HOMO and LUMO, I_p and E_a are respectively the ionization potential and electron affinity of the semiconductor, while Φ_A and Φ_C are respectively the anode and cathode work function. We have also assumed in Fig. 2-10 and in our discussion hereafter that the organic semiconductor is not doped, there is no interface potential at the metal-organic interface, there are also no carriers in the semiconductor at the beginning, and that there are no chemical reactions between the semiconductor and the metal electrode [67, 68]. As for carrier injection into the organic semiconductor itself, it is categorized into two different categories based on whether or not carrier injection from the electrodes to the semiconductor is easier than transport within the semiconductor structure. These categories are injection/contact-limited and bulk-limited transport [67-69].

2.2.1 Injection/Contact-Limited Transport

In injection/contact-limited transport, injection from the metal contact/electrodes into the semiconductor becomes the limiting factor in carrier transport or in the flow of current within an organic semiconductor device. Thus, carrier injection into the semiconductor will be controlled by the metal electrode work function Φ with respect to the semiconductor's electron affinity (E_a) in the case of electron injection, and with respect to the ionization potential (I_p) for hole injection [67, 68, 70]. From Fig. 2-10, if we inject/transfer carriers into the metal-organic semiconductor interface by applying a voltage bias on the semiconductor, an electric field will then be generated within the semiconductor and as a result, the energy level structure in Fig. 2-10 will be tilted as shown in Fig. 2-11.

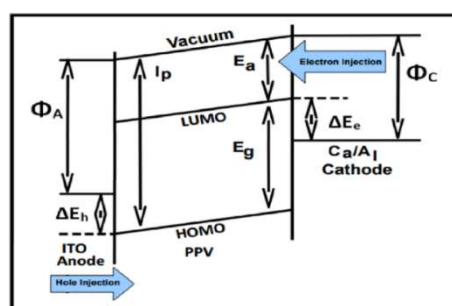


Fig. 2-11. An energy level illustration of the sandwiched organic semiconductor device under an applied voltage bias (the bias is not shown here). Here, as in Fig. 2-10, PPV is the organic semiconductor, ITO is the anode and the Ca/Al layer is the cathode. Because of the applied bias, an electric field will be generated in the semiconductor and the energy levels will be tilted. The tilt is uniform since the generated field will be uniform across the semiconductor due to our earlier assumption that there are no carriers beforehand in the semiconductor. Under an applied bias, electrons will be injected from the Ca/Al layer cathode into the LUMO and will encounter an electron injection barrier ΔE_e , while from the opposite side, holes will be injected into the HOMO and will encounter a hole injection barrier ΔE_h . As in Fig. 2-10, E_g is the energy gap between the HOMO and LUMO, I_p is the ionization potential, E_a is the electron affinity of the semiconductor, while Φ_A and Φ_C are respectively the anode and cathode work function. The vacuum level is taken at 0 eV.

From Fig. 2-11, the tilt in the energy level is constant since the generated field will be uniform across the semiconductor due to our earlier assumption that there are no carriers beforehand in the semiconductor. So under an applied voltage bias, electrons will be injected from the Ca/Al layer cathode into the LUMO and will roll downwards to the LUMO. However, the injected electrons will encounter an electron injection barrier ΔE_e , as much as 1.7 eV from the Al layer into the PPV LUMO (Fig. 2-10). In addition, holes will be injected from the ITO anode into the HOMO and will roll upwards to the HOMO. But the injected holes will also encounter a hole injection barrier ΔE_h , where holes need to overcome as much as 0.5 eV energy barrier from the ITO into the PPV HOMO (Fig. 2-10). If however, we tried to inject electrons from the ITO side, electrons will encounter an injection barrier of 2.2 eV that comes from the combination of injection barriers in the ITO and Ca/Al side. This means that the use of electrodes from different metals in the device will define the device forward and reverse bias condition under an applied voltage bias, due to the cathode and anode different work functions. So to define a forward bias condition in our device, we choose a low work function metal as the cathode, and a high work function metal as the anode, thus minimizing barriers for both electron and holes injection. On the other hand, we define a reverse bias by choosing a high work function metal as the cathode and a low work function metal as the anode, hence maximizing barriers for both electron and holes injection [67, 68, 70].

In Fig. 2-11, both holes, and electrons still need to overcome the injection barriers under a forward bias condition. To do this, carriers undergo a tunneling mechanism in the injection process. There are two classical carrier tunneling models that describe carrier tunneling in the form of current density J with respect to an applied voltage bias V , where $J = I/A$, with I being the tunneling current and A the area size. These are Fowler-Nordheim tunneling and the other is Richardson-Schottky thermally activated injection [71, 72]. In the Fowler-Nordheim model, tunneling is achieved through an external electric field, with the tunneling current density called Fowler-Nordheim current density J_{FN} and is defined in equation (7) [71].

$$J_{FN} = \frac{C}{\Delta V} \left(\frac{V_{bias}}{d} \right)^2 \exp \left[- B \frac{d \Delta V^{3/2}}{V_{bias}} \right] \quad (7)$$

where ΔV is the size of the injection barrier (in eV), B is a constant that is defined as $B = 8\pi\sqrt{2m^*}/(2.96 eh)$, where m^* is the carrier effective mass, e is the elementary electron unit charge = 1.6×10^{-19} C, h is the Planck constant = 6.6×10^{-34} J/s, k is the Boltzmann constant = 1.38×10^{-23}

J/K , V_{bias} is the applied voltage (in V) and d is the injection distance from the metal to semiconductor or in other words the metal/semiconductor interface thickness. While in the Richardson-Schottky thermally activated injection, i.e. a thermally-assisted tunneling, the tunneling current density is called the Richardson-Schottky current density J_{RS} and it is defined by equation (8) [72].

$$J_{RS} = aT^2 \exp \left[- (\Delta V - V_m(E))/kT \right] \quad (8)$$

where T is the absolute temperature (in K) and a is a constant that is defined as $A = 4\pi emk^2/h^3$, where m is the electron rest mass $= 8.2 \times 10^{-14} \text{ J/C}^2$ and $V_m(E)$ is a field-dependent parameter that describes the lowering of the injection barrier due to injection carrier attraction with its opposite charge carrier. Here, $V_m(E) = (eE/4\pi\epsilon\epsilon_0)^{1/2}$, where E is the electric field in the metal-organic semiconductor interface due to applied voltage (in V/m^2), ϵ is the semiconductor's permittivity and ϵ_0 being the vacuum permittivity $= 8.8 \times 10^{-12} \text{ F/m}$. However, both the Fowler-Nordheim and Richardson-Schottky model and equations were originally developed for carrier injection at a metal/vacuum interface, and not carrier injections through metal/organic semiconductor interface. Thus to address this weakness, in 1999, Scott and Maliaras introduced a modified version of the Richardson-Schottky equation (8) which results in the Scott and Maliaras tunneling current density J_{SM} defined by equation (9) [72, 73].

$$J_{CSM} = 4\psi^2 N_0 e \mu E \exp(-\Delta V/kT) \exp f^{1/2} \quad (9)$$

where N_0 is the density of chargeable sites in the semiconductor, μ is the electron mobility (in cm^2/Vs) and E is the electric field at the metal-semiconductor interface. Also, f is the reduced electric field and $f = eEr_c/kT$, where T is the absolute temperature (in K) and r_c is the Coulomb radius. The Coulomb radius is defined as $r_c = e^2/4\pi\epsilon\epsilon_0kT$. Finally, $4\psi^2$ is an injection barrier factor and is a function of the electric field E [73]. From all the models represented in equations (7)-(9), the tunneling current density is affected or decreases exponentially with injection barrier height and the current density will also depend on the applied voltage bias V and the semiconductor thickness d , from $E = V/d$. So in injection limited transport, the dependence of current density J on E or on injection barriers is a hindrance, since applied bias will be used primarily to inject carriers first into the semiconductor. Therefore, several steps are usually taken to overcome this issue, for example, using a semiconductor with lower ionization potential or higher electron affinity, selecting electrodes with suitable work functions as we see in Fig. 2-10 or doping a semiconductor, so that the metal-semiconductor energy level will experience band bending and form a Schottky contact at the metal-semiconductor interface [69]. If an injection barrier is eliminated or overcome, then equation (7) injection barrier $(\Delta V) = 0$ and

the tunneling current will be infinite. However this is physically impossible, what happens is that the injected carriers/transport will instead be limited by the bulk semiconductor film properties.

2.2.2 Bulk-Limited Transport

In general, under an applied bias, carriers in a semiconductor will move in the direction of the generated field arising from the bias. As a result, there are two possible ways carrier can move within the semiconductor, one is through coherent/band-like movement which is described by a wave vector k and the other is through incoherent/thermally-assisted tunnelling (“hopping”) mechanism. In an organic semiconductor at room temperature, carrier transport always happens via the “hopping” mechanism, where carriers or hole and electron polarons tunnel from one molecule to another. Thus, it is very rare for carriers in an organic semiconductor to move in a band-like manner. In general, under an applied voltage bias, carriers will move with an average velocity v that is defined in equation (10) [69, 74].

$$v = \mu E \quad (10)$$

where E is the generated electric field from the applied bias, and is defined as $E = V/d$, with E in V/cm and d being the semiconductor film thickness (in cm), while μ is the carrier mobility (in $\text{cm}^2/\text{V s}$) and average velocity v is in cm/s. In an organic semiconductor, carrier mobility μ is an important characteristic. As described in 2.1., typical organic semiconductors mobility ranges widely from 10^{-7} to $10 \text{ cm}^2/\text{V s}$, all under hopping-type transport. This range of mobility is much lower compared to those in inorganic semiconductor and metal, which can range from 10^3 to $10^4 \text{ cm}^2/\text{V s}$ [1, 9, 52]. If we look back at equation (10), average carrier velocity v is not strictly proportional to the electric field E . This is because carrier mobility in (10) depends on temperature T and carrier concentration p aside from the electric field E . In the case of hopping transport in an organic semiconductor, in 1993 Bässler proposed a model of carrier mobility within the hopping transport regime that takes into account the mobility dependence on both applied field and temperature. In the model, he assumed that the HOMO levels within the semiconductor are not equal in energy but instead display a Gaussian distribution around an average HOMO level. This Gaussian distribution of energy is called the diagonal disorder and is characterized by a variance σ^2 , or through a dimensionless quantity $\sigma^\wedge = \sigma/kT$, where σ is the standard deviation of a carrier energy level from the average HOMO level. In addition, in the model, the mobility, or the hopping transport is also dependent on the positional or off-diagonal disorder factor that is represented by another variance quantity Σ^2 . The off-diagonal disorder is the

distribution of carrier position within the organic molecule. The model is represented by equation (11) [75].

$$\mu(E, T) = \mu_0 \exp \left[- (2\hat{\sigma}/3)^2 \right] \begin{cases} \exp \left[\left(\hat{\sigma}^2 - \Sigma^2 \right) \sqrt{E} \right], \Sigma < 1.5 \\ \exp \left[\left(\hat{\sigma}^2 - 2.25 \right) \sqrt{E} \right], \Sigma \geq 1.5 \end{cases} \quad (11)$$

where the carrier mobility μ is a function of both field E and absolute temperature T with μ_0 being the carrier mobility before we account for the field and temperature dependence [75]. More recently, Pasveer et al. have modified Bässler's equation to account for the dependence of carrier mobility μ on the carrier density p . Their equation cannot be deduced into an analytical form, but their model can be approximately modeled by equation (12) [76].

$$\mu(T, p, E) = f(T, E) \mu(T, p) \quad (12)$$

where p is the carrier density, and $f(T, E)$ is a dimensionless function that is independent of p . For small or near-zero p , Pasveer equation will approach that of Bässler in equation (11), however, in the case of high p , Pasveer equation predicts that the mobility value can increase by several orders of magnitude as predicted by the experimental results [77]. Again, μ in hopping transport is always lower than that of band-like transport.

We then proceed to use equation (10) to determine the current density in bulk-limited transport, which is defined in equation (12) [74, 78].

$$J_{\Omega} = qn v = qn \mu E = \sigma E \quad (13)$$

where J_{Ω} is the bulk-limited transport carrier density (in A/cm²), q being the charge per carrier and it can be positive/negative, n is the carrier density (in number of carriers/cm³), v is the carrier velocity (in cm/s), and $\sigma = qn\mu$ is the semiconductor's conductivity (in Ω cm) [69, 74, 78]. However equation (13) does not give us the carrier density n and it also assumes that the electric field E on each carrier at any position within the semiconductor is equal/has the same strength with externally applied electric field. So equation (13) still assumes the flat band condition we see in Fig. 2-11. However, as there are now injected carriers in the semiconductor, the conditions seen in Fig. 2-11 no longer hold. So in the case of an undoped semiconductor where the only current flowing is due to injected carriers, carriers that are already injected into the semiconductor will screen the strength of the externally

applied electric field. These carriers are then called space charge carriers. As a result, the electric field E in the semiconductor will vary depending on location/position. Thus, bulk-limited carrier transport will be a competition between the externally applied electric field that moves the carrier and the screening of that external field by the same carriers that it (ext. field) moves. The resulting current in this type of transport is known as space charge limited current (SCLC), and for the case of one type of injected carriers from one electrode, the SCLC current density J_{SCLC} is given by equation (16).

$$E(x) = -\frac{3}{2}V\sqrt{\frac{x}{d^3}} \quad (14)$$

$$n(x) = \frac{\frac{3}{4}\epsilon_r\epsilon_0V}{q\sqrt{xd^3}} \quad (15)$$

$$J_{SCLC} = \frac{9}{8}\epsilon_r\epsilon_0\mu\frac{V^2}{d^3} \quad (16)$$

where $E(x)$ and $n(x)$ are the position-dependent field E and carrier density n respectively, x is a position coordinate, and the electrodes are located at positions $x = 0$ and $x = d$ respectively, J_{SCLC} is in A/cm^2 , d is the semiconductor film thickness (in cm), μ is the carrier mobility (in $cm^2/V\ s$) and V is the externally applied voltage (in V). Equation (16) is also known as Child's law [79]. Note also that $J_{SCLC} \sim E(x)$ and $n(x)$. But J_{SCLC} itself is not dependent on the position x as J_{SCLC} is the resulting current from the competition between external field and injected carriers within the semiconductor that screen the field. In addition, the space charges will screen the external field so there will not be an electric field at the injecting electrode, or in other words we have to assume an ohmic injection condition. To add, J_{SCLC} itself does not depend entirely on the external electric field [74, 78]. In reality, however, real semiconductors are always doped to an extent, hence we cannot always assume that the semiconductor is undoped, which is the case in SCLC. Doping-induced carriers in a semiconductor will be balanced by counter ions from injected carriers, but unlike injected carriers, the doping will not introduce space charge into the device. As such, there will be an ohmic contribution from a current density $J_o \sim V$ which will dominate transport for highly doped semiconductor at the low external field, but at the high external field or in a very pure semiconductor, J_{SCLC} will instead dominate [74, 78]. Usually for organic semiconductor devices with a sandwiched structure as seen in Fig. 2-11 with semiconductor thickness ~ 50 nm, SCLC current will dominate transport more than the ohmic current contribution. However in a planar device architecture, where there are more electrodes that layer the semiconductor film (high d), transport will be dominated by

the ohmic contribution [69, 74]. In the following subchapter, we will elaborate more on the organic semiconductor device, i.e. OPV and OLED that we characterize in this work.

2.3 Bulk Heterojunction (BHJ) Organic Photovoltaic (OPV) Devices

A bulk heterojunction (BHJ) organic photovoltaic (OPV) is a PV device that is made of a mixture of two phase-separated organic semiconductors, in which one is an electron-donating polymer that absorbs light strongly and acts as the cell's carrier source, and another one being an electron-acceptor fullerene derivative which is added to improve carrier separation in the semiconductor. Examples of donor polymers are, poly(3-hexyl thiophene) or P3HT and poly(2-methoxy-5-(2-ethyl-hexyloxy)-1,4-phenylene vinylene) or MEH-PPV. While a soluble fullerene derivative, [6]-phenyl-C₆₁ butyric acid methyl ester or PCBM is usually used as an acceptor polymer [2]. As mentioned in 2.1, the first bilayer/heterojunction OPV with a power conversion efficiency (PCE) of ~ 1% was reported by Tang in 1986 [14]. In 1992, Hiramoto et al. reported the first bulk heterojunction (BHJ) OPV that is made from a mixture of perylene (PTC) and phthalocyanine (Pc) pigments, which has a PCE = 0.44% [80]. Ever since then, interest on BHJ OPV has been growing rapidly as mentioned in 1.2., and at the same time device efficiency (PCE) has increased dramatically as well, from 0.44-1% in its early years to PCE > 10% in 2014 with a BHJ mixture of PffBT4T-2OD donor polymer and traditional PCBM acceptor [5]. Current use of OPV includes, but not limited to printed/roll-to-roll solar cells, portable solar cells for charging small devices and power installations in buildings due to its suitability for large-area applications [2, 57]. The reason for growing interest in BHJ OPV includes its characteristics, has been outlined in 2.1. Compared to other types of OPV, the rising interest in a BHJ OPV structure is due to several reasons. These are, as in 2.1., its ability to be fabricated via low-temperature solution processing with low energy cost, it is also able to be manufactured on flexible plastic substrates, and compared to a bilayer PV structure, it has a larger photoactive area due to the BHJ interface between the donor and acceptor polymer in the cell. Higher interface area means that carrier generation will occur more often in a BHJ structure, and as such overall device efficiency will also be higher. However, the BHJ OPV also has its own drawbacks. These are, as in 2.1., its vulnerability to ambient environment, its low (carrier) mobility, the cell's relatively narrow optical absorption bandwidth compared to the solar spectrum which limits its photocurrent, device thickness limitations due to low carrier mobility, and that carrier transport is highly dependent on temperature due to the disordered structure and "hopping"-type transport [1, 3].

A depiction of a BHJ OPV device structure and operation, including examples of donor-acceptor material that are typically used in an OPV, are shown in Fig. 2-12(a), (b) and (c) respectively, with the illustrations taken from Brabec et al., Nelson and Huang et al [1, 2, 52].

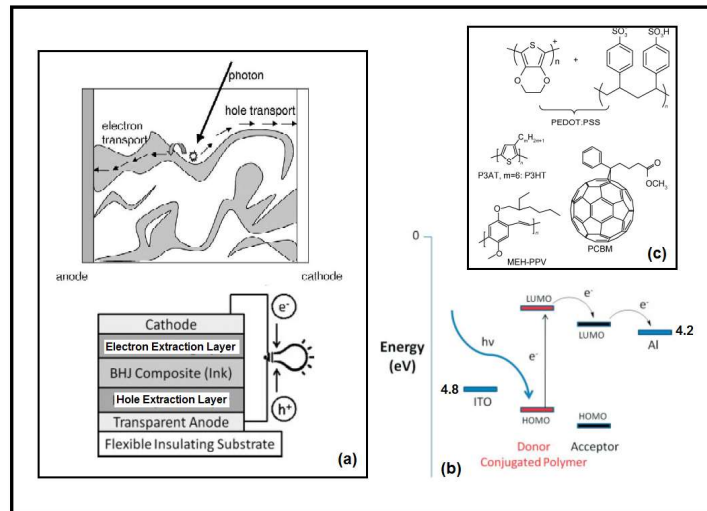


Fig. 2-12 (a). A typical BHJ OPV structure with a microscopic diagram that describes charge generation/operational process inside the BHJ (b). Energy level diagram of photon absorption, exciton generation and dissociation into free charge carriers inside the OPV's BHJ layer. (c). Chemical structure of a typical donor polymer (P3HT and MEH-PPV), acceptor (PCBM) and hole extraction materials (PEDOT:PSS) used in BHJ OPV [1, 2, 52].

A typical BHJ OPV structure is depicted in Fig. 2-12(a), along with a microscopic diagram that describes BHJ operation from photon absorption until carrier generation from the OPV. In a BHJ OPV device, the BHJ layer will be sandwiched between a cathode and an anode layer which have different work functions, with the cathode work function lower than that of the anode. This difference in work function is necessary to improve charge extraction once free carriers are generated from the BHJ, as we will see later. The OPV's anode is usually made of a transparent conductive oxide (TCO) with high work function (e.g. indium tin oxide (ITO)) as the anode function is also to pass light through to the BHJ since it serves as the OPV front/"window" part. Whereas the OPV's cathode is usually made from low work function metals or combination of metals with low work function, e.g. aluminium (Al), lithium fluoride (LiF)/Al, calcium (Ca)/Al and barium (Ba)/Al. Both the anode and cathode layer are also covered with additional layers which are respectively, a hole extraction layer (HEL) and an electron extraction layer (EEL). The EEL is usually made from an n-type metal oxide (e.g. zinc oxide (ZnO), titanium dioxide (TiO₂)) that helps with electron extraction from BHJ but also protecting the BHJ from unwanted reaction with the cathode material and ambient atmosphere. While the HEL is usually made from a conductive polymer such as poly(3,4-ethylenedioxythiophene) polymer doped with poly(styrenesulfonate) (PEDOT:PSS), as seen in Fig. 2-12(c). However, one of the disadvantages of using PEDOT as an HEL is that it is susceptible to degradation from the ambient environment, especially from water due to its hygroscopic nature [57]. In addition, the acid in PSS can also trigger the etching of the ITO electrodes in an OPV, which then liberates indium ions from

the ITO and cause it to diffuse across the HEL into the BHJ layer, thus degrading the OPV structure and its performance [57, 81, 82].

Another example of a material that can be used as an HEL and has been shown to have the same or better performance as HEL compared to PEDOT is vanadium pentoxide or V_2O_5 [83-85]. In 2006, Shrotriya et al. found that by utilizing V_2O_5 as a HEL in an organic solar cell structure, they managed to prevent the chemical reaction that usually occur between the cell's ITO electrode and the organic semiconductor layer, where cells with the V_2O_5 as its HEL has similar and even better performance in terms of *PCE* compared to cells with PEDOT as their HEL [83-85]. In addition, as with PEDOT, another advantage of using V_2O_5 as an HEL in an OPV is that it can be deposited on the cell via solution processing, thus enabling a low-temperature OPV fabrication that will not damage the OPV's semiconductor layer [85]. In the context of low-temperature processing of V_2O_5 as an OPV's HEL, recently Alsulami et al. have utilized a solution-processed V_2O_{5-x} as the HEL of a BHJ OPV and investigate the effect of thermal annealing on the V_2O_{5-x} layer [86]. In their research, they compare the performance of a BHJ OPV in which the V_2O_{5-x} layer was annealed before the BHJ deposition with an OPV where its V_2O_{5-x} layer was unannealed [86]. They found that the thermal annealing of V_2O_{5-x} HEL in the OPV does not improve performance significantly in terms of *PCE* when compared to the unannealed devices. Further, they also found that there are no significant *PCE* differences between devices with annealed and unannealed HEL and that as the V_2O_{5-x} HEL is annealed at a higher temperature, the performance of devices with the annealed V_2O_{5-x} HEL decreases as evident from the decrease in their *PCE* [86]. As for the OPV organic semiconducting layer or its BHJ layer, it is usually made from a mixture of P3HT: PCBM, or MEH-PPV:PCBM as seen in Fig. 2-12(c). The P3HT polymer is chosen as the donor polymer due to its high hole mobility that comes from its high degree of molecular ordering (regioregularity/head-to-tail molecular arrangement). While PPV and its derivatives (MEH-PPV) is also chosen as a donor polymer in other literature as it can be made conductive via doping and that it is abundantly available. Finally, PCBM is chosen as the electron acceptor due to its high electron mobility and good miscibility with the OPV's conjugated polymer [52, 57].

As depicted in Fig. 2-12(a) and (b), the BHJ OPV operate as follows; incoming photons will first pass through the cell's "window" (the TCO) and transparent anode before arriving in the BHJ layer. Once in the layer, photons will be absorbed by the donor polymer and an electron in the donor's HOMO will be excited into its LUMO as in 2.1.2., thus forming an exciton or an excitation state within the donor. By themselves, these excitons will not dissociate due to strong coulomb bonding between the excited electron-hole pair. The exciton will then diffuse along the polymer chain but will not separate into free carriers at the same time. Because of the exciton's low mobility and short

lifetime, its diffusion length will be limited to ~ 10 nm. Since the donor forms an interface with the electron acceptor in a BHJ, and if the distance from the exciton generation site to the interface is less than 10 nm, then the probability of the exciton traveling to/arriving at the donor-acceptor interface will increase. Once the exciton arrives at the donor-acceptor interface, the exciton will dissociate by the electron affinity (E_a) differences between the donor and acceptor layer. With the right selection of donor and acceptor material (in terms of their bandgap), the donor-acceptor electron affinity difference will be bigger than the exciton binding energy. As such, the cell differences will be sufficient to drive carrier separation or transfer the electron and hole from the interface to the acceptor's LUMO and the donor's HOMO respectively, thus transforming the carrier into an (electron) and hole polaron as seen in Fig. 2-12(a) and (b) [1, 2]. In terms of spin, the generation of the exciton and its final separation at the interface, followed by the respective hole and electron transfer into the donor and acceptor is depicted in Fig. 2-13, taken from Kippelen et al [9].

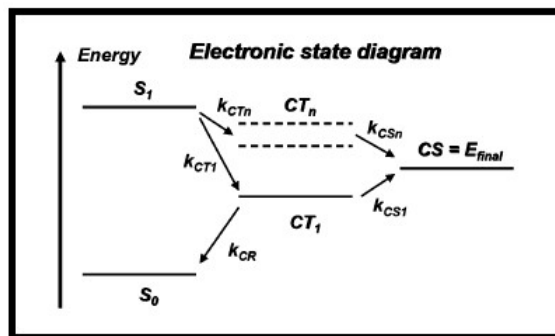


Fig. 2-13. An electronic state diagram depicting the BHJ spin states, starting from the ground state (S_0) to the first state after excitation or the exciton state (S_1). This state is then followed by charge-transfer (CT) states, which is where the electron and hole are separated at the donor-acceptor interface. Here, there are multiple CT states that can be formed during charge transfer from donor to acceptor. These possible states are represented by the lowest (CT_1) to the highest (CT_n). These CT states are also an intermediate transition state before the carrier is separated in the final charge-separated state (CS). The different rate constants k_i represents different competing transfer rates in the whole process [9].

From the spin picture in Fig. 2-13, when the BHJ's donor electron is in its ground state, it is in a singlet state (total spin 0) represented by S_0 . Now when a photon or a single photon is absorbed in the donor, the electron will be excited into its first and lowest singlet excited state, represented here by S_1 . Then, after the exciton diffused into the donor-acceptor interface, (hole and electron) carriers will separate due to the donor-acceptor electron affinity differences. At this point, carriers will be transferred from S_1 to the lowest intermediate state, which is called charge transfer CT_1 , with the accompanying transfer rate k_{CT1} . Actually, at CT_1 , the electron and hole are still under the influence of coulomb attraction though the electron and hole are already in the acceptor's LUMO and the donor's HOMO respectively, thus CT_1 having lower energy. At this state, there are 2 possibilities that could happen. One is that the electron/hole can experience a geminate recombination and then decay back to S_0 with recombination transfer rate k_{CR} , or the other possibility is that, the carriers will proceed

to dissociate further to the final free carrier state, which is designated as the charge-separated state CS with the separation transfer rate k_{CSI} . Here, k_{CSI} is bigger than k_{CR} due to possible disorder at the interface. In addition, there is also another possibility that can happen once carriers move into the charge transfer state. This possibility is that the carrier could be transferred to a higher CT state, which is called the CT_n states with accompanying transfer rate k_{CTn} . This can happen when electrons/holes diffuse further away from the interface, thus resulting in higher energy CT. Then from this higher CT state, carriers thus proceed to totally separate and transfer to the final CS state with a higher separation transfer rate k_{CSn} compared to k_{CSI} [9].

So once electron and hole polaron have been formed in the acceptor's LUMO and the donor's HOMO, both carriers must now be transported into the cell's respective electrodes in order to generate photocurrent. This is achieved through the presence of a built-in potential V_{bi} due to the difference between the anode (Φ_A) and cathode work function (Φ_C) [87, 88]. From 2.2.1, work function differences will be present in an organic device where the organic semiconductor is sandwiched between two different metal electrodes. If carriers are already present in the semiconductor, carriers will redistribute to achieve an energy level alignment with the respective electrodes Fermi level. As a result, the semiconductor will experience a band bending at the metal-organic interface which then will lead to a build-up of built-in potential V_{bi} within the semiconductor [67, 88]. The V_{bi} itself can be determined from equation (17) [67, 68].

$$V_{bi} = \frac{\Phi_A - \Phi_C}{e} \quad (17)$$

Where Φ_A and Φ_C are respectively the anode and cathode work function. Thus, the V_{bi} will effectively separate carriers, and carriers will then travel via thermally assisted tunneling/"hopping" mechanism into the respective electrodes [87, 88]. So the electron will move from the fullerene acceptor and on to the EEL until finally arriving in the cathode. The hole meanwhile, will move from the donor polymer, towards the HEL and on to the anode. Thus photocurrents are generated from the electrodes [9]. In order to characterize any solar cell performance, we usually obtain the cell's DC current density-voltage or J/V characteristics [89] as depicted in Fig. 2-14, taken from Grossiord et al [57]. We first do this by illuminating the cell with an air mass (AM) 1.5 light at an active area A . An AM 1.5 illumination is a (white) light standard that matches the sun spectral intensity distribution as it is received on the earth's surface at an angle of 48.2° to the normal direction. We then measure the cell's current density J (A/m^2) by sweeping the cell's voltage V from highest to lowest V under AM 1.5 light which then leads to the DC current-density or J/V characterization sweep as seen in Fig. 2-14.

The current density J here is the cell's measured current with respect to the cell's AM 1.5 illuminated active area A [57, 89].

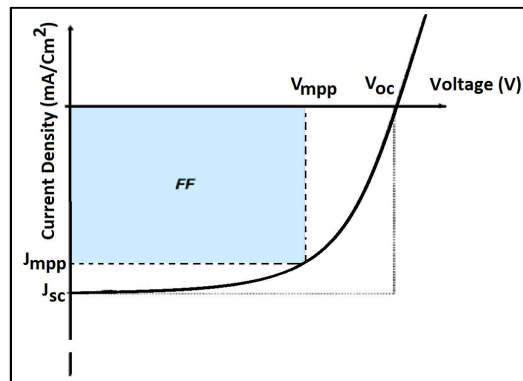


Fig. 2-14. A solar cell's DC current density-voltage or J/V characteristics under AM 1.5 light that depict several of the cell's DC parameters, i.e. V_{oc} , J_{sc} , V_{MPP} , J_{MPP} and fill factor or FF [57].

In addition to the J/V characteristics, we can also obtain the cell's power density-voltage (P_D/V) characteristics by multiplying the measured current density J under AM 1.5. light with the cell's sweeping voltage V to construct a power density P_D (in W/m^2 or mW/cm^2) profile [90]. An example of this profile is depicted in Fig. 2-15, taken from Zhan et al [91]. The P_D here is the power density with respect to illuminated area A .

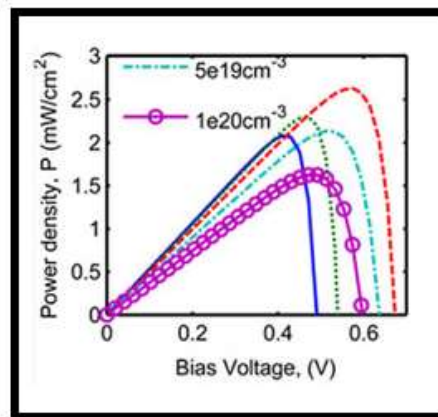


Fig. 2-15. A solar cell's several DC power density-voltage or P_D/V characteristics under AM 1.5 light, where each P_D/V curve depicts a maximum peak, which is called the maximum power point (MPP), and the voltage and current density at that point being V_{MPP} and J_{MPP} respectively [91].

From Fig. 2-15, we then obtain the cell's power density-voltage characteristics from the lowest to the highest voltage under AM 1.5 light. Here the P_D/V curve has a maximum point which is called the maximum power point (MPP), in which the current density and voltage is at its maximum point, i.e. at J_{MPP} and V_{MPP} respectively. The MPP point also corresponds to the point in Fig. 2-14 J/V characteristics where J_{MPP} and V_{MPP} intersect [90]. Therefore from Fig. 2-14 and 2-15, we obtain several DC parameters that can be used to assess the cell's DC performance. These are; its open-

circuit voltage or V_{oc} (V), short-circuit current density or J_{SC} (A/m², more often mA/cm²), V_{MPP} (V), J_{MPP} (A/m² or mA/cm²), fill factor or FF , power conversion efficiency or PCE (in %), external quantum efficiency η_{EQE} , absolute series resistance R_s (Ω) and shunt resistance R_{sh} (Ω), and also specific series and shunt resistance, i.e. R_{s-spec} (Ωcm^2) and $R_{sh-spec}$ (Ωcm^2) respectively. The V_{OC} is the cell's voltage under an open-circuit condition or when current density $J = 0$ at Fig. 2-14. In an OPV, V_{oc} is determined by the difference between the donor's HOMO and the acceptor's LUMO and is also a function of temperature. While J_{SC} is the cell's current density under a short-circuit or when $V = 0$ at Fig. 2-14. Finally, FF is the ratio of the maximum cell's power to maximum theoretical power output, which is defined by equation (18) below:

$$FF = \frac{V_{MPP} J_{MPP}}{V_{OC} J_{SC}} \quad (18)$$

where V_{OC} (V), J_{SC} (A/m²), V_{MPP} (V) and J_{MPP} (A/m²) have been elaborated before. The FF is represented by the shaded blue area in Fig. 2-14. and it represents the quality of carrier extraction from the cell. In other words, FF is dependent on the cell's intrinsic properties with respect to carrier extraction. The OPV's overall power conversion efficiency (PCE) is defined by equation (19) below:

$$PCE = \frac{V_{OC} J_{SC} FF}{P_{in}} \quad (19)$$

where P_{in} is the incident light power (in W) and PCE is in %. Then, the OPV's external quantum efficiency η_{EQE} is defined by equation (19) below:

$$\eta_{EQE} = \eta_A \eta_{ED} \eta_{CC} \quad (20)$$

The OPV's external quantum efficiency η_{EQE} is actually the sum of the OPV's entire micro processes efficiencies, e.g. photon absorptions, exciton dissociation at the donor-acceptor interface and carrier transport to the cell's electrode. In other words, it represents the number of photons that are really converted into electrical current. While η_A is the light absorption efficiency and represents the probability of photon absorption, η_{ED} being the exciton diffusion efficiency, representing the excitons that are able to arrive in the donor-acceptor interface and η_{CC} being the carrier collection efficiency, which is the probability of a liberated carrier reaching the cell's electrode. To add, $R_{sh-spec}$ or specific shunt resistance (in Ωcm^2) can be determined from the inverse of the J/V characteristics slope near

V_{OC} in Fig. 2-14. Meanwhile, R_{s-spec} or series resistance (in Ωcm^2) can be found from the inverse of the J/V characteristics slope near J_{SC} in Fig. 2-14. Also, R_{sh} or absolute shunt resistance (in Ω) is the cell's shunt resistance without reference to the cell's illuminated active area A , with $R_{sh} = R_{sh-spec}/A$. While, R_s or absolute series resistance (in Ω) is the cell's series resistance that is also without reference to the cell's A , with $R_s = R_{s-spec}/A$. Hence the shunt resistance R_{sh} represents carrier losses or current leakage within the cell that can occur due to the presence of short circuit connection or carrier recombination. Whereas R_s represents the cell's layers and contact resistance. In addition, the $R_{sh-spec}$ and R_{s-spec} represent the cell's R_{sh} and R_s with respect to its illuminated active area. Therefore, both R_{sh} and R_s will influence the OPV's FF . As we will see later, R_{sh} and R_s can be modeled as electrical resistances in an OPV-equivalent circuit. Thus in the circuit, it is desirable to have $R_{sh} \gg R$ so as to prevent carriers from recombining/leaking within the cell and reducing the overall OPV's photocurrents.

So the drawback from the cell's DC J/V characteristics and its measured parameters is that the change in one parameter can be ascribed to different causes and phenomenon, similar to what we observe with R_{sh} and R_s [16, 92]. Hence, the dynamic characterization in the form of intensity modulated spectroscopy (IMS) offers the potential to accurately assign the changes occurring in a measured parameter to a specific phenomenon/dynamics in the cell [16, 50, 92].

2.4 Organic Light-Emitting Diode (OLED)

Another organic semiconductor devices that will be discussed in this work are organic light-emitting diodes (OLED). An OLED is a light-emitting diode/electroluminescent device in which the emissive semiconductor/component is made of small organic molecules and conjugated polymers. Examples of emissive materials from small molecules are, tris(8-hydroxyquinoline) aluminium(III) or Alq_3 as a green emitter, tetraphenyl dibenzoperiflanthene or DBP as a red emitter and 9,10-bis(3'5'-diaryl)phenyl anthracene or DPA as a blue emitter. While examples of emissive materials from conjugated polymers are, poly(9,9-dihexylfluorenyl-2,7-diyl) as a blue emitter, poly(p-phenylene vinylene) or PPV as a green emitter and poly(2,5-di(hexyloxy)cyanoterephthalylidene) or CN-PPV as a red emitter. Hence from the examples, an OLED's colour depends entirely on its organic material band gap [93-95]. The first electroluminescent device made from anthracene crystals was reported in 1963 by Pope et al [96]. By 1969, Dresner et al. had developed the first practical electroluminescent device with anthracene as the organic material [97]. In another milestone, in 1987 Tang and VanSlyke fabricated the first modern (thin film) multi-layer OLED as we know it today by using Alq_3 as the emissive material [98]. This OLED was reported to have a $\eta_{EQE} \sim 1\%$ and a power efficiency ~ 0.46 m/W. In 1990 Bradley et al. developed the first OLED device that used conjugated

polymer, i.e. PPV as the emissive material [99]. This OLED's η_{EQE} was reported to be $\sim 8\%$. As recently as 2015, Song et al. reported an OLED that is made from an anthracene derivative organic material with a $\eta_{EQE} \sim 14.8\%$ [100].

As mentioned before in 1.1, research on OLED is growing rapidly due to their future potential as flat panel displays and lighting applications [4]. The reason for this interest in OLED and its characteristics, especially with regards to its potential in display and lighting applications are as follows, first, its ability to be fabricated via low-temperature solution processing with low energy cost and that it can be made on top of a flexible substrate [4, 95]. In addition, as a display, the OLED has the advantage of being flat and lighter in weight, having a higher (display) resolution, good brightness, good contrast and colour variation and also its ability to operate at a very low voltage [95]. However, the OLED also has its own drawbacks. These are, as in 1.1., its vulnerability to the ambient environment, its low carrier mobility, low emission efficiency and its broad emission spectrum due to the organic nature of the OLED's emissive layer [95]. A depiction of an OLED device structure and operation, including examples of the emissive layer (small organic molecules and conjugated polymers) that are typically used in an OLED, are shown in Fig. 2-16(a),(b) and Fig. 2-17(a),(b) respectively, with the illustrations taken from Brütting et al., Kalyani et al., Shinar et al., So et al. and Kan et al [95, 101-103].

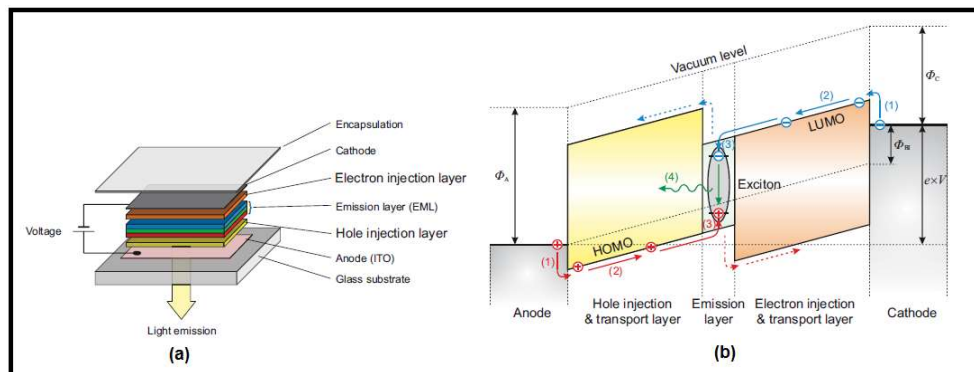


Fig. 2-16 (a). A typical multi-layer OLED structure with (b). an energy level diagram that describes charge generation/operational process inside the OLED's organic materials [103].

From Fig. 2-16(a), the emissive layer will be sandwiched between a cathode and an anode layer which have different work functions, with the cathode work function (Φ_C) lower than that of the anode (Φ_A). From 2.2.1., this difference in work function is necessary to increase charge injection into the emissive layer, because it will define the OLED forward bias condition by minimizing the injection barrier in both electrodes [68]. The OLED's anode is usually made of a transparent conductive oxide (TCO) with high work function (e.g. ITO), where its (the anode) function is to inject holes into the emissive layer. In addition, the anode will later serve to channel light out from the

emissive layer, since it (anode) is basically the OLED "window" part. Whereas the OLED's cathode is usually made from low work function metals or a combination of metals with low work function, e.g. aluminium (Al), lithium fluoride (LiF), silver (Ag), LiF/Al and calcium (Ca)/Al. Here, the cathode function is to inject electrons into the emissive layer. Both the anode and cathode layer are also covered with additional layers which are respectively, a hole injection layer (HIL) and an electron injection layer (EIL). The EIL is usually made from small organic molecules, e.g. 2,2',2''-(benzene-1,3,5-triyl)-tris(1-phenyl-1*H*-benzimidazole) or TPBi, that helps with electron injection to the emissive layer and blocks hole flowing into the cathode. An EIL material must have a good electron injection and hole blocking efficiency, and also high glass transition temperature T_g which results in a material with high thermal stability. The HIL is also made from small organic molecules such as copper phthalocyanine or CuPc and PEDOT:PSS, that helps with hole transport and blocks electrons flowing into the anode. An HIL material needs to have a good hole transport and electron blocking properties, and also high T_g so that the material will have a high thermal stability. Note that the HIL must also be transparent like the anode and also transparent in the red, blue and green wavelength range to channel the light emission out of the emissive layer [54, 95, 103]. Also, the EIL and HIL chemical structure can be found in Fig. 2-17(b). An OLED uses either small organic molecules or conjugated polymers as the emissive layer. In terms of colour, an OLED typically emits either a white colour from the combination of slower colours or a single colour from the emissive material. There are two ways an OLED can combine different colours to emit white light. First, the OLED can combine red, green and blue emitters in a lateral manner or two, the OLED can combine a blue emitter and a yellow phosphorescence material in a stacked manner within the emissive layer as illustrated in Fig. 2-18(a). and (b) respectively from So et al [93].

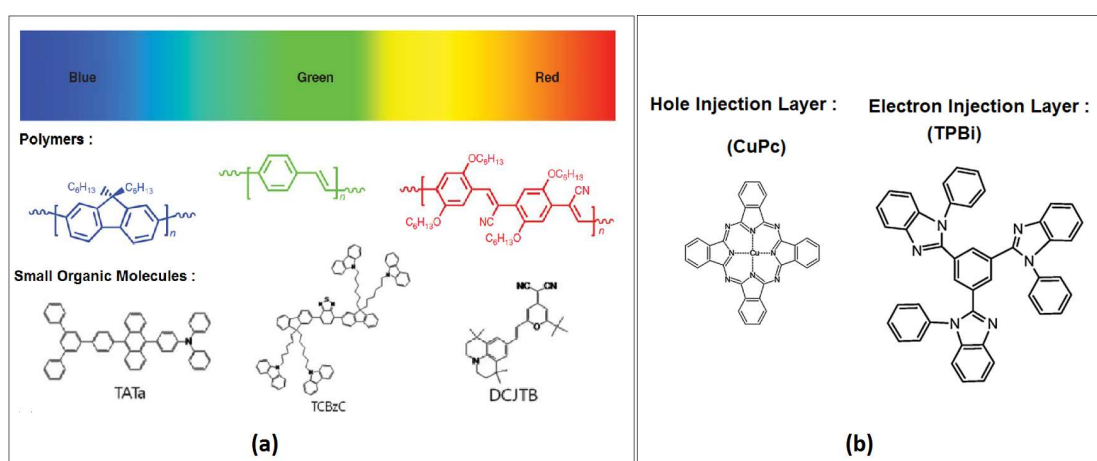


Fig. 2-17. Chemical structure of a typical (a) polymer and small organic molecules fluorescence emitter, and (b) hole injection layer (CuPc) and electron injection layer (TPBi) materials that are used in an OLED. Note that the colour emitted from the polymer and small molecules examples follows the colour spectrum identifier above them, e.g. DPA and DBP are respectively, a blue and red emitter [95, 101-103].

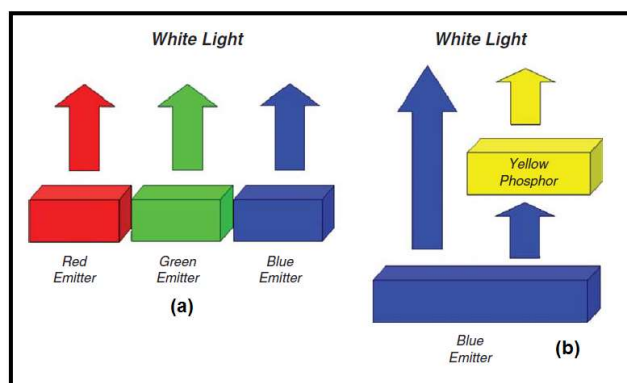


Fig. 2-18. An OLED can emit white light from (a). the lateral configuration of red, green and blue emitters or (b). stacked configuration of the blue emitter and yellow phosphor in the emissive layer [93].

In Fig. 2-18 scheme, a single colour emitter can act as a host organic material while the other colour/other two colours act as a dopant material. Continuing, the OLED emissive layer can be made from a mixture of host 4-(10-(3',5'-diphenylbiphenyl-4-yl)anthracen-9-yl)-N,N-diphenylaniline or TATA molecules doped with a carbazole derivative, TCBzC as a green dopant and 4-(dicyanomethylene)-2-t-butyl-6(1,1,7,7-tetramethyljulolidyl-9-enyl)-4H-pyran or DCJTB as a red dopant, which will results in a white emission from the OLED. Thus, the TATA, DCJTB, and TCBzC were chosen due to them being a blue, red and green emitter respectively. Also, the OLED emissive layer can be made from either poly(9,9-dihexylfluorenyl-2,7-diyl) as a blue emitting polymer, or from poly(*p*-phenylene vinylene) (PPV) as a green emitting polymer, or from poly(2,5-di(hexyloxy)cyanoterephthalylidene) (CN-PPV) as a red emitting polymer [93, 94]. The chemical structure of all the small organic molecules and polymers emitters in this paragraph can be found in Fig. 2-17(a).

From Fig. 2-16(b), an OLED operate as follows; first, an external voltage of a few volts is applied across the OLED so that both electron and holes will be injected from opposite electrodes, with electrons injected from the cathode and hole from the anode (represented by step no. 1 in Fig. 2-16(b)). Here, the injection is similar to that describe in 2.2.1. The two free carriers will then travel first towards the the EIL (for electrons) and HIL (for holes), before finally meeting each other in the emissive layer. As they (carriers) travel, a built in voltage V_{bi} will appear in a similar process as described in 2.3 due to the work function differences between the OLED electrodes, the V_{bi} can also be determined from equation (17) [67]. Therefore, the applied external voltage V must be set to overcome this built-in voltage so that both carriers can flow into the OLED. Further, if we apply more V bias, we will obtain more current and consequently, brighter OLED. Both electrons and holes will travel by way of thermally assisted tunneling/"hop" from one localized state to another in the OLED. In other words, both carriers transform into electron and hole polarons that are traveling towards the

emissive layer from opposite sides (represented by step no. 2 in Fig. 2-16(b)). Once both carriers meet each other in the emissive layer, exciton formation will then occur and both carriers become an electron-hole (bound) pair (represented by step no. 3 in Fig. 2-16(b)). Finally, the newly formed exciton can then decay/recombine with each other and emit light (represented by step no. 4 in Fig. 2-16(b)). Note that for the small molecules based emissive layer, the carrier recombination area is narrower than that of polymer-based ones [103]. We can also depict the OLED's light excitation process in terms of spin as illustrated in Fig. 2-19 [104].

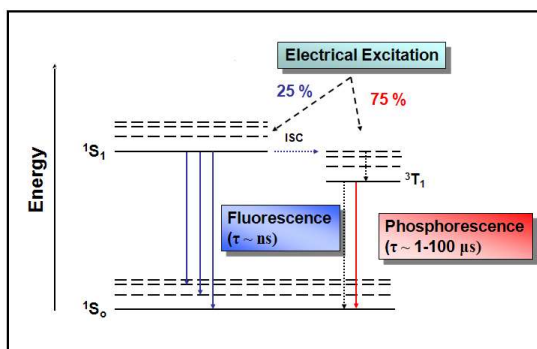


Fig. 2-19. An electronic state diagram depicting OLED operation in terms of carriers spin. To begin with, both carriers started from the excitation/exciton state (1S_1). Then from 1S_1 carriers can decay into the ground state (1S_0) through several pathways, one is through fluorescence (in blue), the other is via phosphorescence (in red) with triplet exciton (3T_1) and intersystem crossing and then finally third, through fluorescence quenching (not shown) [104].

From the spin picture in Fig. 2-19, both carriers will first be in their singlet excited state, as represented by 1S_1 . Carriers can then decay to the ground state/singlet state 1S_0 through several ways, one is through fluorescence (in blue), the second is via phosphorescence (in red) and then third, through fluorescence quenching (not shown). As in 2.1.3. when carriers decay via fluorescence, it is from the singlet excited state 1S_1 to the singlet (ground) state 1S_0 . The time scale τ for this process is $\sim ns$. Again as in 2.1.3., if carriers choose to decay via the phosphorescence route, they will first decay via the intersystem crossing mechanism (ISC) into a triplet state 3T_1 which is then followed by the decay of 3T_1 to 1S_0 . The ISC of course very rarely happens by itself, and it usually occurs through LS interaction by adding atoms with high atomic numbers Z [64, 65]. The time scale τ for phosphorescence is, of course, longer, hence $\tau \sim \mu s$. Finally, carriers can also decay in a non-radiative manner from 1S_1 to their ground state (1S_0) without emitting any light. Also as in 2.1.3, the majority of excitons that are produced in OLED or devices where both electrons and holes are injected, will be triplet (3T_1) excitons, with the remaining being a singlet exciton (1S_1). This is because excitons in these devices will be a combination of both electron and hole polaron, and from Table II in 2.1.3 there are three ways to obtain a triplet exciton but there is only one way to obtain a singlet exciton. Thus in OLEDs, roughly 3 (75%) out 4 excitons will be triplet, while the rest (25%) will be singlet [64, 65].

To characterize any LED performance, we first obtain the cell's DC current density-voltage or J/V characteristics by applying a voltage V to the OLED, from the lowest to the highest, and then measure its current density J at active area A within the applied voltage range [105] as in Fig. 2-20 example, taken from Chung et al [106].

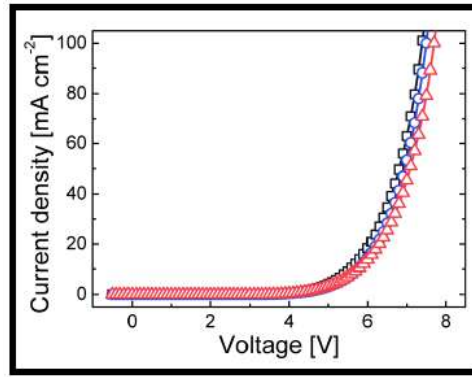


Fig. 2-20. Example of an OLED's DC current density-voltage or J/V characteristics [106].

From Fig. 2-20, we can then obtain several DC parameters from the cell's J/V characteristics that can be used to assess its DC performance. These are its turn-on voltage or V_{on} (V), turn-on current density or J_{on} (A/m^2 , more often mA/cm^2), and differential resistance R_{diff} (Ω). The V_{on} is the voltage where the OLED's current started to rise exponentially in Fig. 2-20. So in the above picture, we can see that $V_{on} \sim 5.7$ V for all three plots. Also, J_{on} is the current density at V_{on} . The differential/dynamic resistance (R_{diff}) is a measure of how much the OLED's current density will change if we vary the voltage by a very small amount. In other words, R_{diff} is an intrinsic property of the OLEDs, i.e. its intrinsic resistance. R_{diff} can be found from the slope of the J/V curve near the V_{on} point [105-107].

In addition, we also characterize an OLED light intensity or luminance L with respect to its applied voltage V . In order to do this, we measure the cell's DC luminance-voltage or L/V characteristics by applying a voltage V to the OLED, from the lowest to the highest, and then measure its luminance L at that voltage range by using a luminance/light meter. Then, we can plot the L/V characteristics as seen in Fig. 2-21 example, taken from Abedi et al [37].

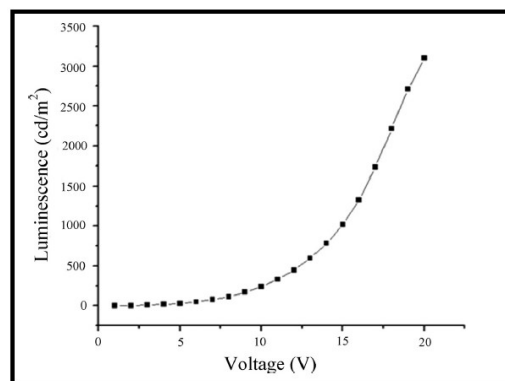


Fig. 2-21. An example of an OLED's DC luminance-voltage or L/V characteristics [37].

From Fig. 2-21, we can then obtain the OLED's turn-on luminance or L_{on} (cd/m²). The L_{on} is, of course, the OLED's luminance at V_{on} or the point where the luminance starts to change in slope. At Fig. 2-21 plot, for example, $L_{on} \sim 500$ cd/m² at $V_{on} \sim 11$ V. Also, to determine an OLED's turn-on voltage (V_{on}) and luminance (L_{on}), we can alternatively plot both the OLED's J/V and L/V characteristics in a semi-log manner. For example, we can plot both J and L measurements from an OLED logarithmically with respect to the applied voltage V . This is shown in an OLED J/V and L/V plot example in Fig. 2-22, taken from Bange et al [108].

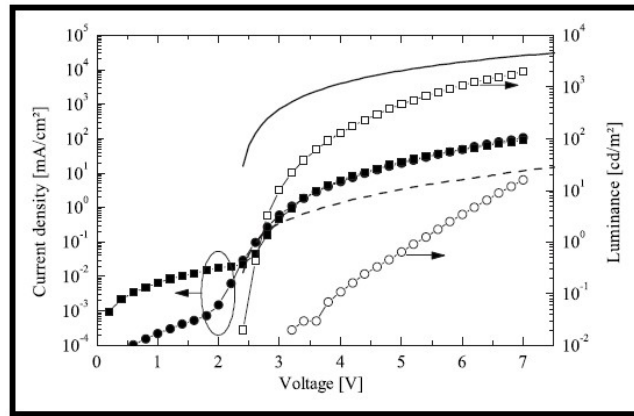


Fig. 2-22. An example of an OLED's DC J/V and L/V characteristics plot in a semi-log manner. The left-pointing arrow refers to J/V plot, while the right-pointing ones refer to the L/V plot [108].

From Fig. 2-22, we can see that both J and L are presented in a semi-log manner with respect to the applied voltage V . We can then define the OLED's turn-on voltage (V_{on}) and luminance (L_{on}) from Fig. 2-22 as the voltage where respectively the J/V and L/V plots intercepted the x/voltage axis. Hence, from Fig. 2-22, the $V_{on} \sim 0.5$ V and $L_{on} \sim 0.01$ cd/m².

Finally, we can also determine the OLED's external electroluminescence quantum efficiency η_{EQE} , which is defined by equation (20).

$$\eta_{EQE} = \gamma \eta_{S/T} q_{eff} \eta_{OUT} \quad (21)$$

where γ is the carrier balance factor, which describes whether or not there are an equal number of electron and holes injected into the OLED, and also how many of those carriers then bounded together to become excitons. While $\eta_{S/T}$ is the fraction of excitons that manages to decay radiatively according to theoretical calculations. In addition, q_{eff} is the actual fraction of excitons that do manage to decay radiatively. Also, η_{OUT} is the actual fraction of generated photons produced by the OLED [103]. The drawback from an OLED's DC J/V and L/V characteristics is that similar to DC characteristics on OPV, changes in one parameter can be ascribed to changes in different OLED parameters. Further,

the DC parameters that we can get from a J/V and L/V plot is much less compared to that of an OPV's I/V characteristics [109]. Thus, intensity modulated spectroscopy (IMS) offers the potential to characterize an OLED and accurately assign a measured parameter to a specific OLED dynamics.

2.5 Light-Dependent Resistor (LDR)

In this work, we will also characterize a commercial light-dependent resistor (LDR), i.e. a cadmium sulfide (CdS)-based LDR to test our IMS instrument setup. A light dependent resistor (LDR)/photoresistor is a resistor that can reduce its resistance when illuminated by light. An LDR is made from a light-sensitive semiconductor, in which the resistance is high under dark and decreases under illumination. Examples of semiconductors used in LDR are cadmium sulfide, lead sulfide, germanium, silicon, and gallium arsenide. Here, we will discuss CdS-based LDR as these constitute the majority of commercial LDR that are widely available in the market today. Photoresistance or photoconductivity was first discovered by W. Smith in 1873 when he observed that the electrical resistance of selenium (Se) varied considerably with the amount of light on it. Ever since then, different varieties of photoresistor device have been made. By 1920, T.W. Case has already conducted intensive investigations to search for a new material candidate for a photoresistor device [110]. Thus by this time, the device technology has been very well-established. Today, LDRs have been used for many applications, to name a few, LDR or CdS-based LDR have been used for smoke detectors, card readers, photographic light meter and lighting controls for street lamps. This ubiquitousness is due to its attractive properties such as they are cheap and widely available, having a simple structure and also rugged characteristics [111]. However LDR properties also vary greatly depending on the constituent materials properties, and that it is also an inaccurate measurement component. A depiction of an LDR device structure, top view and the CdS structure used as LDR is depicted in Fig. 2-23(a), (b), and (c) respectively [110].

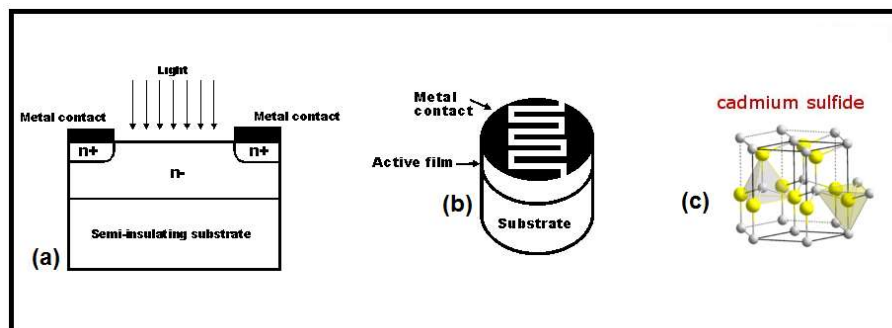


Fig. 2-23. A depiction of (a) LDR device structure, (b) top view and (c) the CdS crystal structure in LDR [110].

The semiconductor (represented by (“n-“ in Fig. 2-23(a)) is slightly doped to improve conduction, and it is placed between two metal contacts. In Fig. 2-23(b) top view, the semiconductor is placed on top of an insulating substrate. Also, the semiconductor area between the contacts is in the form of an interdigital pattern to maximize the exposed area and keep the contact distance small to minimize carrier resistance. Meanwhile CdS in Fig. 2-23(c) has a hexagonal (wurtzite) structure for LDR application, with CdS a direct band gap semiconductor with a band gap = 2.42 eV. Further, this structure also depends on the CdS manufacturing method and temperature [110]. Normally CdS LDRs are made from sintering, with the electrodes added later after CdS fabrication [110]. Also, an LDR itself always operates under a DC voltage bias (V_{bias}). Under dark condition, the LDR resistance will be very high, hence, currents from the applied V_{bias} that flows in the LDR will be very small [111]. But when light falls upon the semiconductor, the LDR resistance will decrease rapidly, thus allowing much larger current from the V_{bias} to flow through the LDR. So here we can see an opportunity to characterize the LDR with light modulation-based characterization due to its light-sensitive properties. In addition, intensity modulated spectroscopy (IMS) offers the potential to characterize an LDR parameter and accurately assign a specific internal dynamics occurring within the LDR.

2.6 Alkaline Battery

Aside from conducting IMS on organic devices and CdS-based LDR in this work, we also perform IMS characterization on a 1.5 V alkaline battery. A battery or an electrochemical cell is basically a device that operates by converting chemical energy into electrical energy through electrochemical discharge reactions. Batteries usually consist of one or more cells, with each cell having an anode, cathode, separator and electrolyte. Further, there are two types of cells, one is primary and the other is secondary. Primary cells are non-rechargeable batteries and must be replaced once reactants are depleted inside the battery. Secondary cells are rechargeable and need a DC current source to restore reactants to their fully charged state. Examples of primary cells are, carbon-zinc, alkaline-manganese and lithium cells. While those of secondary are, lead-lead dioxide, nickel-cadmium, and lithium-ion. Batteries are assessed in terms of their nominal voltage and ampere-hour capacity. The voltage rating is based on the number of cells connected in series in a battery and the nominal voltage of the individual cell (e.g. 1.2 V for nickel-cadmium). Ampere-hour (Ah) capacity is a fully charged battery parameter that depends strongly on the battery temperature, discharge rate and age [112]. In this work, we will only discuss the alkaline-manganese type/alkaline battery.

In 1800, Alessandro Volta discovered the first true battery known as the voltaic pile. It consists of pairs of copper and zinc discs piled on top of each other and separated by a layer of cloth soaked

by saltwater. By 1836, John Frederic Daniell had invented the first practical battery that consisted of a copper pot filled with a copper sulfate solution, where an earthenware pot is filled with sulfuric acid and a zinc electrode. The earthenware barrier was designed to be porous so ions can pass but kept the copper sulfate and sulfuric acid from mixing with each other. Then in 1886, Carl Gassner invented the first dry cell battery without liquid electrolyte. This was called the zinc-carbon battery. Finally, in 1955, Lewis Urry invented the first alkaline battery that consists of a manganese dioxide cathode, a powdered zinc anode and an alkaline electrolyte [113]. A cutaway of an alkaline battery structure is depicted in Fig. 2-24 [114].

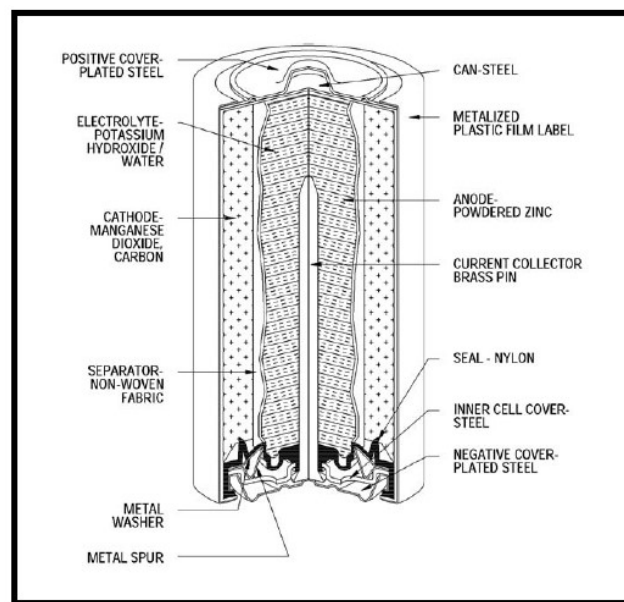
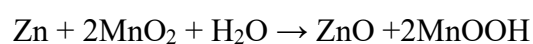
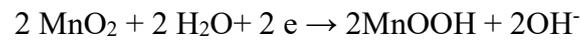


Fig. 2-24. A cutaway of an alkaline battery [114].

Whereas the negative cover/cathode is the nail-shaped object that extends to the battery center. This object function is to “collect” currents from the electrolyte and connect it to the cathode bottom part. The electrolyte is a mixture of potassium hydroxide, water, and other chemicals. The electrolyte envelops the brass nail while a mixture of carbon and manganese dioxide surrounds the electrolyte. This outer layer (carbon-manganese) is separated from the electrolyte by a thin polyester fabric layer. The outer case being just a simple metal case without any significance [114]. A battery is designed to keep the cathode and anode separated to prevent a reaction from occurring. The battery will only operate if we complete the connection between the cathode and anode with an external circuit [114]. In this event, the manganese dioxide cathode is then reduced and the zinc anode becomes oxidized, according to the following reaction [114]:



During this reaction, water is consumed and a hydroxyl ion (OH⁻) is produced by MnO₂ cathode under the following reaction [114]:



At the same time, the anode consumes the hydroxyl ions and produced water as well:



The electrons (e) generated in the last reaction are then used to power devices. The reaction rate is dependent on the quality of the raw materials and availability of water and hydroxyl ions during the reaction. The stronger attraction for electrons by the manganese dioxide will pull electrons from the zinc anode electrode through the wire in the circuit to the cathode electrode. This flow of electrons will then be the electricity produced by the battery. Here, we see an opportunity to characterize chemical reaction dynamics in the battery with IMS and then assign the measured parameter in IMS to a specific chemical reaction [115].

Chapter 3

Preparation of Organic Semiconductor Devices

3.1 Preparation and Characterization of Organic Photovoltaic (OPV) Devices

As elaborated in 1.1, we perform IMS characterization on two different organic semiconductor devices, one is a bulk heterojunction (BHJ) OPV device and the other is an organic light-emitting diode (OLED). Two types of BHJ OPV devices were characterized, one is a BHJ with poly(3,4-ethylenedioxythiophene) polystyrene sulfonate (PEDOT:PSS) hole extraction layer (HEL) and the other is a BHJ with vanadium pentoxide (V_2O_{5-x}) HEL, with both types having the same BHJ mixture. In view of the disadvantages of using PEDOT as the HEL in an OPV as described in 2.3, here, we also characterize BHJ OPV devices with V_2O_{5-x} as an alternative HEL to PEDOT in an OPV device. In addition, we also characterize such OPV (OPV with V_2O_{5-x} HEL) to investigate its dynamics and the effect of thermal annealing on the V_2O_{5-x} HEL before the BHJ deposition. Hence, we varied the devices with V_2O_{5-x} HEL were varied by HEL annealing/non-annealing before preparation. We perform IMS on OPV with non-annealed, 100, 200, 300 and 400 °C annealed HEL before preparation. All OPV BHJ with PEDOT:PSS and V_2O_{5-x} HEL were prepared and provided by Mr. Abdullah Alsulami, University of Sheffield, Sheffield UK. All OLEDs were prepared and provided by Mr. Thomas Routledge, also from The University of Sheffield, Sheffield, UK. In total for our IMS characterizations, 2 OPV devices with PEDOT:PSS, 4 OPV devices with V_2O_5 HEL and 3 OLEDs were prepared. In addition, DC characterizations on all the prepared OPV were conducted and provided by Mr. Abdullah Alsulami, University of Sheffield, UK. While DC characterized on all the OLED were conducted and provided by Mr. Thomas Routledge, University of Sheffield, UK. In this chapter, we will briefly describe OPV preparation and DC characterization results, while OLED preparation and DC characterization results will be given in the next chapter.

3.1.1 Preparation of BHJ OPV with PEDOT:PSS HEL

First, a BHJ OPV with PEDOT:PSS HEL was prepared. For the OPV's BHJ layer a blend of the low bandgap, hole transporting, PFDT2BT-8 donor polymer, and an electron accepting C_{70} derivative, PC₇₀BM, was prepared. The BHJ donor-acceptor materials and illustration of the OPV structure are depicted in Fig. 3-1 taken from Waters et al., Huang et al. and Griffin et al [52, 116, 117].

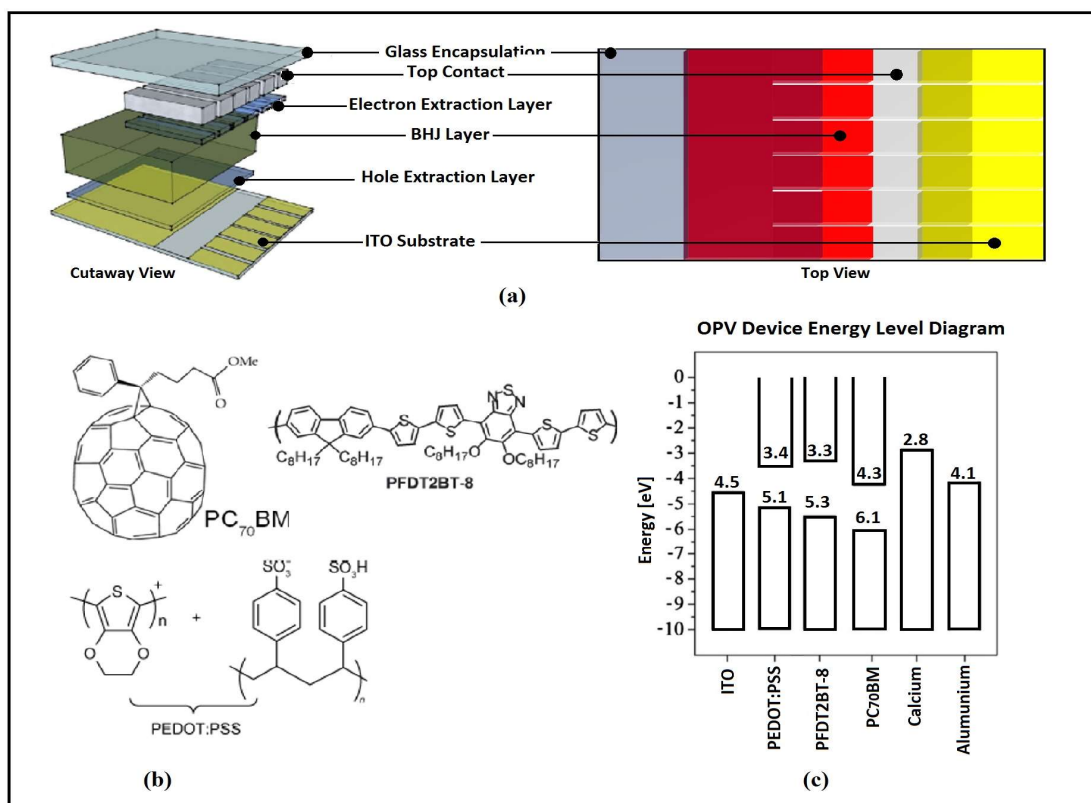


Fig. 3-1 (a). A cutaway and top view of the prepared BHJ OPV device, with (b) the BHJ's donor-acceptor and the cell's hole extraction layer material and (c) The energy level diagram of the device constituent layers. Here, PFDT2BT-8 is poly[9,9-dioctylfluorene-4,7-alt-(5,6-bis(octyloxy)-4,7-di(2,2'-bithiophen-5-yl)benzo[c][1,2,5]thiadiazole)-5,5-diyl], PC₇₀BM is [6,6]-Phenyl-C71-butyl acid methyl ester and PEDOT:PSS is poly(3,4-ethylenedioxythiophene) polymer doped with poly(styrenesulfonate) [52, 116, 117].

From Fig. 3-1(a) and (b), each device consists of 6 individual OPV cells which are called pixels. Here, a total of 1 device (or 6 pixels/cells) was prepared for IMS characterizations. We later perform IMS on 1 cell from the prepared device. The OPV structure, as depicted in Fig. 3-1(a) and (b), consists of a BHJ layer that is sandwiched between two electrodes, one is an Al/Ca top contact and the other is an indium tin oxide (ITO) coated substrate, with both electrodes having different work functions. This difference in work function is necessary to improve charge extraction once free carriers are generated from the BHJ, as mentioned in 2.4. From Fig. 3-1(c) energy level diagram, the OPV's anode, i.e. ITO has a higher Fermi energy level compared to that of the OPV's cathode, i.e. calcium (Ca)/Al layer. As a consequence, there will be a difference in work function between both electrodes, with the PEDOT:PSS work function being higher than that of the Aluminium's. Hence, electrons will flow towards the direction of the Aluminium electrode and holes towards the ITO electrode. Further, between the electrodes and the BHJ layer, charge extraction layers were inserted to improve carrier transport and protect the BHJ from reaction with the electrodes. Hence, an electron extraction layer (EEL) is deposited between the cathode and BHJ, and a hole extraction layer (HEL) is deposited between BHJ and the anode. Here, as seen in Fig. 3-1(c), PEDOT:PSS is used as the HEL since it has

a higher HOMO level compared to that of the PFDT2BT-8:PC₇₀BM (BHJ) layer. While the Ca layer is used as the EEL as its high Fermi energy prevent holes from flowing towards it, but at the same time allowing electrons to flow to it from the BHJ layer. Also, the OPV's front part is the ITO coated substrate, which means that the device follows standard BHJ OPV structure as described in Fig. 2-12(a).

For OPV preparation, PEDOT:PSS was purchased from Ossila Ltd, while PFDT2BT-8 was synthesized in the Department of Chemistry at the University of Sheffield via a previously reported method, and had a molecular weight of 91.6 kDa and a polydispersity index (PDI) of 1.47 [116]. Also, PC₇₀BM was purchased from Ossila Ltd with a purity of 95% (5% PC₆₀BM). The BHJ layer solution was prepared by mixing PFDT2BT-8 and PC₇₀BM at a weight ratio of 1:4 in chloroform with an overall concentration of 20 mg/mL. Subsequently, the solutions were placed onto a hot plate at 55 °C for a few hours before they were filtered through a 0.45- μ m PTFE filter. All devices were fabricated onto 15 x 20 mm² of pixellated cathode design glass substrates that were supplied by Ossila. These substrates are sold pre-patterned with a 100 nm layer of Indium Tin Oxide (ITO). Prior to use, the substrates were sonicated in a warm cleaning solution of either NaOH (10 wt% in water) or Hellmanex (2 wt%) from Hellma Analytics GmbH & Co. KG, Germany, for 10 minutes and then deionised in water for 5 minutes followed by warm IPA for 5 minutes. Finally, they were dried with nitrogen gas PEDOT:PSS film with (30 nm \pm 3 nm) thickness was spin cast in ambient conditions and then was annealed at 130 °C for 30 minutes in glove box environment. The PEDOT:PSS annealing temperature was set to 130 °C since it is known from literature that PEDOT will degrade/becomes unstable if heated at temperatures above 150 °C [118]. The active semiconductor layer was prepared by spin casting the solution onto a substrate at a spin speed of 3000 rpm in order to obtain an active film with a thickness of 70 nm \pm 3 nm. The bi-layer cathodes of Ca (5 nm) and Al (100 nm) were evaporated at a rate of 3 Å/s and 10 Å/s. Here, Al/Ca layer is chosen as the cathode due to its low work function while ITO is chosen as the anode because of its high work function. The entire active device area $A_D = 2.86$ mm² is defined by the overlapping of the individual metallic top contact and the single ITO square. Finally, the central area of each substrate was encapsulated by using a glass slide and light-curable epoxy. The light-curable epoxy used here is the E131 Encapsulation Epoxy from Ossila Ltd., UK. The encapsulation was done to prolong the cells lifetime for characterizations and storage.

3.1.2 Preparation of BHJ OPV with V₂O_{5-x} HEL

For our characterization, five varieties of BHJ OPV with V₂O_{5-x} HEL were prepared. The OPVs were varied by having the V₂O_{5-x} HEL annealed/unannealed before preparation. These variations are:

OPVs with non-annealed, 100, 200, 300 and 400 °C annealed V_2O_{5-x} before preparation. We use the V_2O_{5-x} as the HEL in this research besides PEDOT:PSS to find an alternative HEL that would not degrade the OPV and its organic semiconductor layer, adaptable to the different type of solar cells and has similar or even better performances compared to PEDOT HEL in an OPV [57, 83]. In addition, we vary the devices V_2O_{5-x} HEL annealing temperature before the BHJ deposition, in order to investigate the effect of thermal annealing on the respective OPVs dynamics and compare these (dynamics) to that found in OPV with unannealed V_2O_{5-x} HEL. Also, the devices use the same BHJ mixture, i.e. PFDT2BT-8:PC₇₀BM, and the same OPV structure and electrodes as those in 3.1.1. Hence, a total of 5 devices (or 30 pixels/cells) were prepared for IMS characterizations. We later perform IMS on 1 pixel/cell (5 pixels in total) from each prepared device. From 2.3, the V_2O_{5-x} was used as an alternative HEL to PEDOT since it has been shown that cells with the V_2O_5 as its HEL have similar and even better performance in terms of *PCE* compared to cells with PEDOT as their HEL [83-85]. In addition, the advantage of using V_2O_5 as an HEL is that it can be deposited on the cell via solution processing, thus enabling a low-temperature OPV fabrication that will not damage the OPV's semiconductor layer [85].

For the organic photovoltaics preparation, vanadium (V) oxytriisopropoxide or $(OV(OCH(CH_3)_2)_3$ was purchased from Sigma-Aldrich (Dorset, UK) and was blended with isopropanol/IPA (99.5%) at a 1:250 volume ratio to obtain a solution with 4 mg/mL⁻¹ concentration. PEDOT:PSS was purchased from Ossila Ltd., Sheffield, UK, while aluminium (99.99%) and calcium (99%) were purchased from Sigma-Aldrich (Dorset, UK). Also, PFDT2BT-8 as a donor polymer was prepared at the University of Sheffield via a previously reported method and had a molecular weight of 91.6 kDa and a polydispersity index (PDI) of 1.47 [116]. In addition, PC₇₀BM was also purchased from Ossila Ltd with a purity of 95% (5% PC₆₀BM). The BHJ layer solution was prepared by mixing PFDT2BT-8 and PC₇₀BM at a weight ratio of 1:4 in chloroform, with a total solution concentration of 20 mg/mL. All OPV devices were then fabricated into pre-patterned ITO coated glass substrates purchased from Ossila Ltd (Sheffield, UK). Before use, the substrates were sonicated in a warm cleaning solution of either NaOH (10 wt% in water) or Hellmanex (2 wt%) from Hellma Analytics GmbH & Co. KG, Germany, for 10 minutes at 70 °C. After sonication, the substrates were then washed with de-ionized (DI) water. After washing, they were then placed in isopropanol and sonicated again for 10 min at 70 °C. The substrates were then dried with nitrogen gas. After drying, thin films (~5 nm) of V_2O_{5-x} were deposited via spin coating on to cleaned ITO substrates in ambient atmosphere. After deposition, the V_2O_{5-x} films were annealed in ambient condition before spin coating the active layer at previously mentioned temperature variations. All of the substrates were then transferred into a dry glove box environment for BHJ layer deposition. The BHJ films were

prepared by spin casting the BHJ solution on to a substrate with a spin speed of 3000 rpm to obtain a BHJ layer with a thickness of $70 \text{ nm} \pm 4 \text{ nm}$. The substrates were then transferred to the glove box to a high-vacuum system (10^{-7} mbar) to thermally evaporate the cathodes. In this process, bi-layer cathodes of calcium (5 nm) and aluminium (100 nm) were evaporated at a rate of 3 \AA/s and 10 \AA/s , respectively. Here, the BHJ OPV area size = 2.86 mm^2 as defined by the overlapping of the individual metallic top contact and the single ITO square. Finally, the central area of each substrate was encapsulated by using a glass slide and light-curable epoxy, which was also done to extend the OPV's lifetime for characterization and storage purposes [116]. The light-curable epoxy used here is the E131 Encapsulation Epoxy from Ossila Ltd., UK.

3.1.3 Current Density-Voltage (J/V) and Power Density-Voltage (P_D/V) Characterizations of OPV with PEDOT:PSS and V_2O_{5-x} HEL

After fabrications of all BHJ OPV with PEDOT:PSS and V_2O_{5-x} HEL, DC characterization in the form of current density-voltage (J/V) and power density-voltage (P_D/V) characteristics were then performed on all OPVs. For the J/V characterizations, OPV devices were measured under ambient atmosphere by using a Keithley 2400 source meter (Tektronix Ltd., Bracknell, UK) and a Newport 92251A-1000 AM 1.5 solar simulator (Newport Co., Didcot, UK). In addition, the J/V characteristics were done by illuminating the characterized cells while sweeping their voltage V from 1 to -1 V with a decrement of 0.2 V, and then measure the resulting current density J (mA/cm^2). The entire (J/V) process was controlled by a bespoke software based on MATLAB© that was also developed by Mr. Abdullah Alsulami. In addition, a National Renewable Energy Laboratory (NREL)-calibrated silicon diode was used to calibrate the power output at 100 mW/cm^2 . The OPV's measured J from AM 1.5 light were defined with respect to an illumination area $A = 2.6 \text{ mm}^2$. This was done by placing a shadow mask with the same area size ($A = 2.6 \text{ mm}^2$) on top of the characterized device. Note that A here is the OPV's active area that is limited by the shadow mask and illuminated by AM 1.5. A_D in 3.1.1. is the OPV's entire active area in an individual cell. After J/V characteristics, a power density-voltage (P_D/V) characteristic was constructed from the J/V plot. This was done by multiplying the measured J under AM 1.5. with the voltage V from the J/V plot, which then leads to the measured OPVs P_D/V characteristics plot. First, we depict the J/V and P_D/V characterization results from OPVs with PEDOT HEL and then followed by those with V_2O_{5-x} HEL. We then derived both type of OPV DC J/V and P_D/V parameters which consists of short-circuit current density J_{SC} , open-circuit voltage V_{OC} , maximum power point voltage V_{MPP} and current density J_{MPP} , maximum power density P_{D-MPP} , absolute series and shunt resistance (R_s and R_{sh} respectively), specific series and shunt resistance (R_{s-spec} and $R_{sh-spec}$ respectively), fill factor FF and power conversion efficiency/ PCE (in %). These

parameters were then used to assess both cell's DC performances. The J/V and P_D/V plots for OPV with PEDOT HEL are depicted together in Fig. 3-2, with J in mA/cm^2 , P_D in mW/cm^2 and V in V.

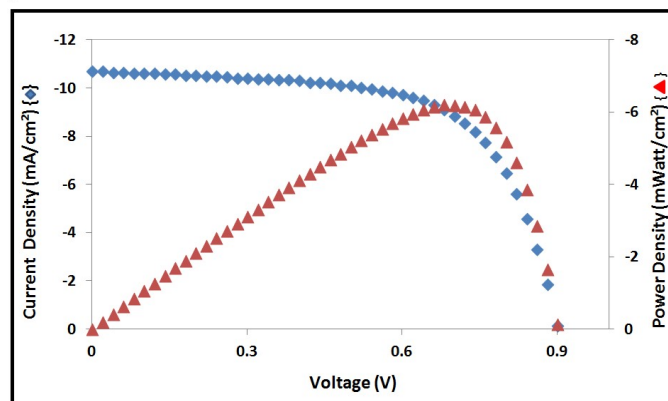


Fig. 3-2. The J/V (in blue) and P_D/V (in red) characteristics of BHJ OPV with PEDOT:PSS HEL. Here the BHJ mixture is PFDT2BT-8:PC₇₀BM.

From J/V and P_D/V plots in Fig. 3-2, we obtained $J_{SC} = -10.7 \text{ mA}/\text{cm}^2$, $V_{OC} = 902 \text{ mV}$, $V_{MPP} = 680 \text{ mV}$, $J_{MPP} = -9.13 \text{ mA}/\text{cm}^2$, maximum power density $P_{D-MPP} = 6.2 \text{ mW}/\text{cm}^2$, $FF = 64$ and $PCE = 6.2\%$. Also, from the J/V plot, we derived a specific serial resistance $R_{s-spec} = 12.6 \Omega\text{cm}^2$ and specific shunt resistance $R_{sh-spec} = 1820 \Omega\text{cm}^2$ for an active device area $A = 2.6 \text{ mm}^2$. This translates to absolute shunt and series resistance of $R_{Sh} = 70 \text{ k}\Omega$, and $R_S = 485 \Omega$ respectively. In addition, a J/V and P_D/V characterization for OPV with PEDOT HEL after 30 days of storage under dark and ambient conditions, were also conducted with the same setup as mentioned before. These J/V and P_D/V characterization results were later used in OPV with the PEDOT HEL aging study with IMS. The J/V and P_D/V plots for OPV with PEDOT HEL are depicted together in Fig. 3-3, with J in mA/cm^2 , P_D in mW/cm^2 and V in V.

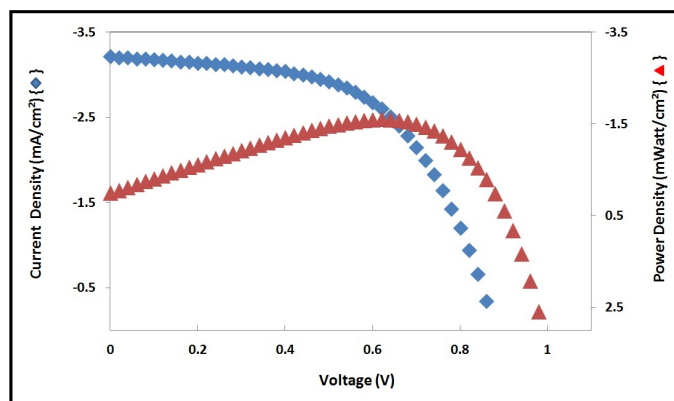


Fig. 3-3. The J/V (in blue) and P_D/V (in red) characteristics of BHJ OPV with PEDOT:PSS HEL after 30 days of storage under dark and at ambient conditions.

From J/V and P_D/V plots in Fig. 3-3, we obtained $J_{SC} = -3.2 \text{ mA/cm}^2$, $V_{OC} = 879 \text{ mV}$, $V_{MPP} = 620 \text{ mV}$, $J_{MPP} = -2.6 \text{ mA/cm}^2$, maximum power density $P_{D-MPP} = 1.6 \text{ mW/cm}^2$, $FF = 57$ and $PCE = 1.6\%$. Also, from the J/V plot, we derived a specific serial resistance $R_{s-spec} = 3.1 \text{ } \Omega\text{cm}^2$ and specific shunt resistance $R_{sh-spec} = 62 \text{ } \Omega\text{cm}^2$ for an active device area $A = 2.6 \text{ mm}^2$. This translates to absolute shunt and series resistance of $R_{Sh} = 2.4 \text{ k}\Omega$, and $R_S = 120 \text{ } \Omega$ respectively. Thus, there is, of course, a decreasing trend in all J/V and P_D/V parameters in Fig. 3-3 after 30 days of storage. In addition, we also conducted J/V and P_D/V characteristics for OPVs with unannealed, 100, 200, 300 and 400 °C annealed V_2O_{5-x} HEL before BHJ deposition. We first present together with the J/V plots of all 5 varieties of OPVs with V_2O_{5-x} HEL in Fig. 3-4, which is then followed by the P_D/V plots of those 5 cells in Fig. 3-5 together.

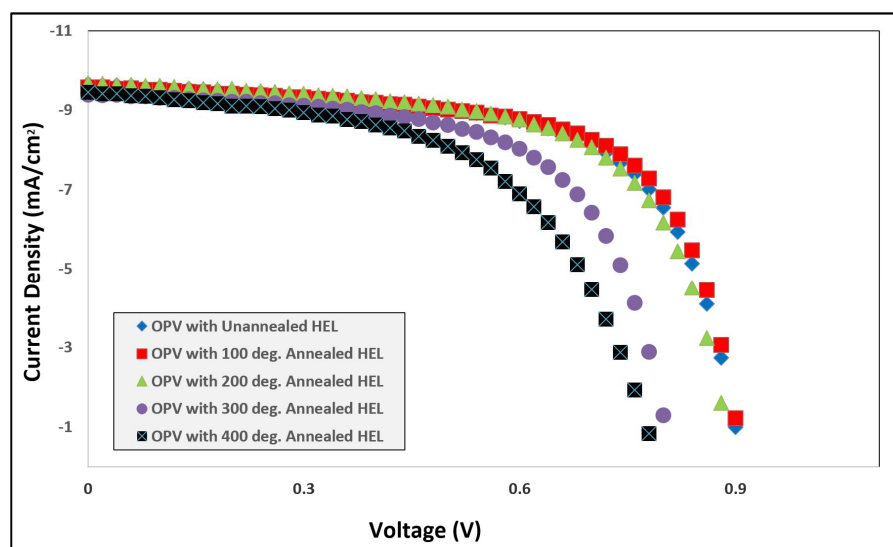


Fig. 3-4. The J/V characteristics of 5 varied OPV with V_2O_{5-x} HEL. Here, the OPVs were varied by preparing OPV with unannealed, 100, 200, 300 and 400 °C annealed V_2O_{5-x} HEL before BHJ deposition (shown in colour inset).

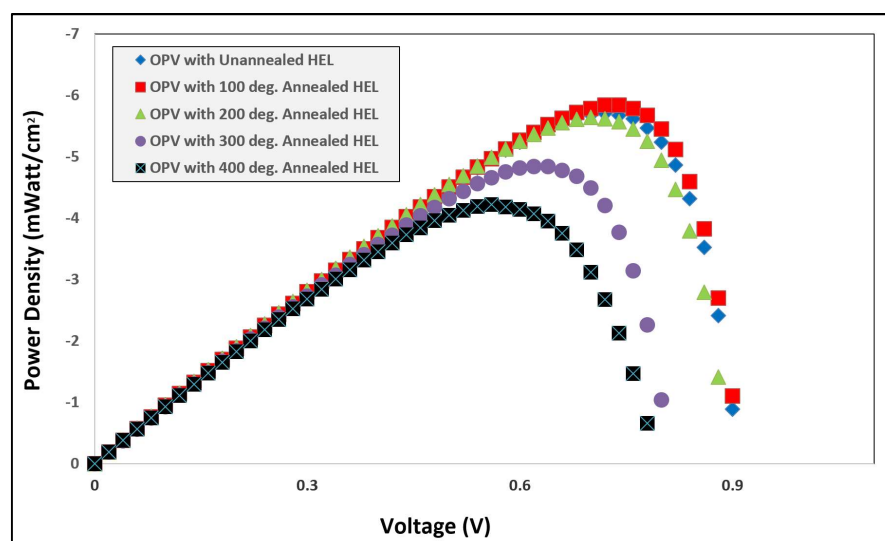


Fig. 3-5. The P_D/V characteristics of 5 varied OPV with V_2O_{5-x} HEL. Here, the OPVs were varied by preparing OPV with unannealed, 100, 200, 300 and 400 °C annealed V_2O_{5-x} HEL (shown in colour inset).

From J/V and P_D/V plots in Fig. 3-4 and 3-5 respectively, we can then obtain several DC parameters from both plots for all OPV varieties, these are; J_{SC} , V_{OC} , V_{MPP} , J_{MPP} , P_{D-MPP} , R_{s-spec} , $R_{sh-spec}$, R_{Sh} , R_S , FF , and PCE . We then list all of the parameters together with the OPV varieties in Table III.

TABLE III OPV Varieties, J_{SC} , V_{OC} , J_{MPP} , V_{MPP} , P_{D-MPP} , R_{s-spec} , $R_{sh-spec}$, R_{Sh} and R_S FROM FIG. 34. AND FIG 35.

OPV Varieties	J_{SC}	V_{OC}	J_{MPP}	V_{MPP}	P_{D-MPP}	R_{s-spec}	$R_{sh-spec}$	R_S	R_{Sh}	FF	PCE
[Non/Annealed]	[mA/cm ²]	[V]	[mA/cm ²]	[V]	[mW/cm ²]	[Ω cm ²]	[k Ω cm ²]	[Ω]	[k Ω]		[%]
Non-Annealed	-9.67	0.91	-7.93	0.72	5.71	15	833	577	32	65	5.7
Annealed-100 °C	-9.58	0.91	-8.11	0.72	5.84	15	926	577	36	67	5.8
Annealed-200 °C	-9.68	0.90	-8.10	0.70	5.65	15	910	577	35	65	5.6
Annealed-300 °C	-9.40	0.81	-7.81	0.62	4.84	15	910	577	35	63	4.8
Annealed-400 °C	-9.50	0.80	-7.54	0.56	4.22	21	513	810	20	56	4.2

From Table III, we clearly observe that by annealing the OPV's V_2O_{5-x} at 300 and 400 °C before BHJ deposition, its (DC) performance decreased further compared to those that were unannealed, 100 and 200 °C annealed, as seen from the significant decrease of J_{MPP} , P_{D-MPP} , FF and PCE values. We can also see that the DC performances of OPVs with unannealed V_2O_{5-x} , and also 100 and 200 °C annealed V_2O_{5-x} are almost the same as evident from their J_{MPP} , P_{D-MPP} , FF and PCE values. To add, we see that annealing the V_2O_{5-x} HEL at 400 °C practically degrade the device further than at any other temperatures, as seen by the sharp decrease in $R_{sh-spec}$ and R_{Sh} , and the high increase in R_{s-spec} and R_S . Despite best attempts to achieve identical processing conditions for both BHJ OPVs with PEDOT and V_2O_{5-x} HEL, not all cells performed with the same standard, e.g. with $PCE \sim 6\%$ for OPV with PEDOT HEL. In order to illustrate the performance statistics for sample devices that consist of 9 devices with PEDOT HEL, or 54 pixels in total (with 6 pixels in each device), in terms of their power conversion efficiency (PCE), we then plot the PCE data in the form of a box plot.

A box plot is a plot that depicts and grouped the plot's data based on their quartiles, i.e. the data's minimum, lower quartile (25th percentile), median (50th percentile), upper quartile (75th percentile) and maximum value [119, 120]. The box plot is a way of displaying a set of data without any assumptions on the data's underlying statistical distribution [119, 120]. Among the advantages of using box plots are that it is easy to compute, easily explained by the plot's user and that it provides detailed information on the data's minimum and maximum value in that we can observe the maximum or minimum data's spread with respect to the data set's median or its quartile values [120]. Here, the box plots are constructed as follows; we use Microsoft Excel © to first obtained pixels with the lowest (minimum) and the highest (maximum) PCE value from among the individual pixel's PCE of OPV/device number 1. We do this by using Excel's MIN and MAX function which will sort out the

maximum and minimum *PCE* value out of the 6 pixels *PCE* in device No. 1. We then use the Excel's PERCENTILE function to obtain the 25th, 50th (median) and 75th percentile *PCE* value out of those 6 pixels. To do this, Excel will first determine the percentile rank (represented by *R*) of the 25th, 50th and 75th percentiles by using equation (22), which is generally used in percentile statistics [121, 122].

$$R = \frac{P_n}{100} (N + 1) \quad (22)$$

where *N* = the total number of sample and *P_n* = the percentiles taken. Thus, *P_n* = 25, 50 and 75 for the 25th (*P₂₅*), 50th (*P₅₀*) and 75th (*P₇₅*) percentiles respectively. Here, *N* = 6, as there are 6 pixels in a device. If *R* is not an integer, *R* will then be rounded up to the nearest integer by Excel. As an example, equation (22) will give us an *R* = 1.75 as the 25th percentile rank, as such, Excel will round up *R* = 2 for the 25th percentile rank. Hence, for the 50th and 75th percentile, their rank would be *R* = 3 and *R* = 5 respectively. Once the rank of a particular percentile is taken, Excel will then calculate the value of that percentile (represented by *x_{P_n}*) from the data set with equation (23), which is typically used to determine *x_{P_n}* in percentile statistics [121, 122]. Here, *x_{P_n}* = *x₂₅*, *x₅₀* and *x₇₅* for the 25th, 50th and 75th percentiles value respectively.

$$x_{P_n} = (f)(x_{i+1} - x_i) + (x_i) \quad (23)$$

where *f* = *P_n*/100 and is the fractional part of the percentile, *x_i* is the data point in which the percentile rank is located and *x_{i+1}* is the data point immediately after *x_i*. Thus, *f* = 0.25, 0.5 and 0.75 for the 25th, 50th and 75th percentiles value respectively. As an example of percentile value determination, if we have a data set that consists of (after ordering) 2, 2, 3, 5, 5, 6 and we want to determine the data's 25th percentile value, we would first find the data's 25th percentile rank, which is *R* = 2. This *R* then correspond to 2 in the data set with the data point after it being 3, hence the 25th percentile value is *x₂₅* = (0.25)(3-2) + (2) = 2.25. An exception, however, applies for the 75th percentile value calculation. If the *x_{i+1}* is equal to the data set maximum value, or the maximum *PCE* value, in this case, Excel will assign the *x_{i+1}* point to the data point immediately before the maximum value, with the *x_i* also shifted following the *x_{i+1}* point. In other words, Excel will not include the maximum data point in the 75th percentile value determination with equation (23) [123].

After we found all the percentiles, maximum and minimum value out of the 6 pixels *PCE* in device No. 1, we then repeat the same procedure (percentiles determination) to the 6 pixels *PCE* data from other devices (No. 2-9). When we have completed the pixel's *PCE* percentiles calculation on all of the sample devices, we proceed to construct the box plot data spread from the resulting

percentile data. We first do this by subtracting the median data/*PCE* value with the 25th percentile value to obtain the plot's lower data spread/difference for device No.1. We then subtract the 75th percentile *PCE* value with that of the median value to obtain the plot's upper data spread/difference for that same device. We then use Excel to add error estimations on the upper and lower data spread in device No. 1 in the form of an upper and lower vertical error bars. After we add the error bars, we then repeat the same procedure to obtain the percentile data spread and error estimations to the other 8 devices. Once we have obtained the percentile data spread and error estimations for all 9 devices, we then plot them as a box plot with the 6 pixels *PCE* of each numbered devices as the y-axis and the OPV device number on the x-axis. In addition, we also plot the individual pixel's *PCE* in a sample OPV/device with respect to that device designated number. This plot is called the grouped point plots and we use it to compare the individual pixels *PCE* data grouping/spread with that of the box plot spread. The grouped point plots are simply constructed by plotting the *PCE* (in %) data from 9 OPV devices, and then plot the individual pixel's *PCE* from each device as the y-axis with respect to the devices designated number as the x-axis. Finally, we superimpose the grouped point plots on top of the resulting box plots with the resulting plots depicted in Fig. 3-6.

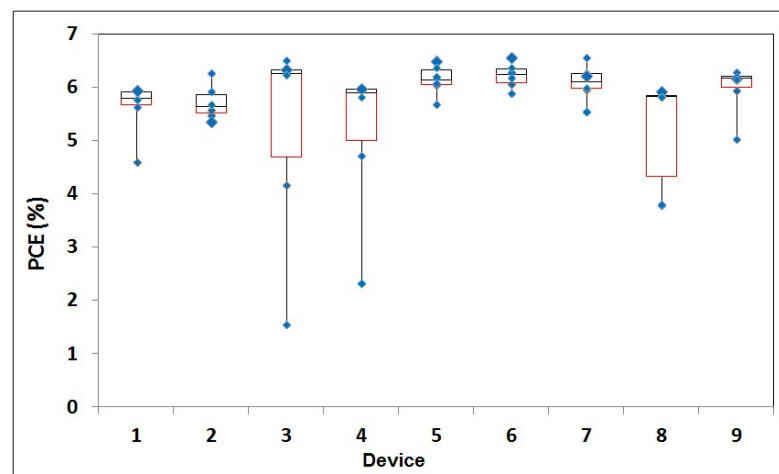


Fig. 3-6. Box plots for OPVs with PEDOT HEL. Here, the *PCE* statistics are for 9 devices (or 54 pixels in total), in which the average maximum *PCE* ~ 6%. The *PCE* is represented by the blue points in the plots.

In Fig. 3-6, the grouped point plots are depicted by the blue-coloured points that are superimposed on the box plots, with respect to the device number in the y-axis. While the box plots are depicted by the red and black box in each numbered devices, with an upper and lower vertical error bars (sometimes called whiskers [119, 120]) that extend outside of the boxes. The red boxes in each device are the lower *PCE* data spread, while the black ones are the upper data spread. To add, the upper error bars is located above the box plot's upper spread, while the lower bars is located below the plot's lower spread.

From Fig. 3-6, we can clearly see that there is a large difference among pixel qualities in device No. 3, 4 and 8, as evident from the large lower spread and large *PCE* grouping distance in those devices. On the other hand, the majority of the devices seems to have the same qualities in that they relatively have the same *PCE* value as seen from how both the box plot and group plot has the same spread/grouping distance in device No. 1, 2, 5, 6, 7 and 9. From Fig. 3-6, we see that most of the OPVs (with PEDOT HEL) have a *PCE* ~ 6%. Further, this value is also the average maximum *PCE* of all devices in the same plot. Hence, cells with that *PCE* (~ 6%) can be said as “good” cells in terms of *PCE* performance as a parameter window, while those with lesser *PCE*s can be said as “bad” cells/pixels. Therefore, for OPV with PEDOT HEL, since we have chosen a device with *PCE* = 6.2% for our IMS characterizations, we have therefore selected a “good” representative of this OPV type.

In addition to the box plots of OPV with PEDOT HEL, we have also constructed a *PCE* boxplot and grouped points plot for OPV with unannealed, 100, 200, 300 and 400 °C annealed V_2O_{5-x} HEL before BHJ deposition. The box and grouped points plots for these OPVs are also constructed and plotted with the same procedure as described for OPVs with PEDOT HEL. The difference is that there are now 5 different OPV types that we plot (i.e. OPV with unannealed, 100, 200, 300 and 400 °C annealed V_2O_{5-x} HEL before BHJ deposition), with each type represented by 2 sample devices (so in total 12 pixels for each OPV types and 60 pixels for all of the types). We depicted the resulting box and grouped point plots in Fig. 3-7(a), (b), (c), (d) and (e).

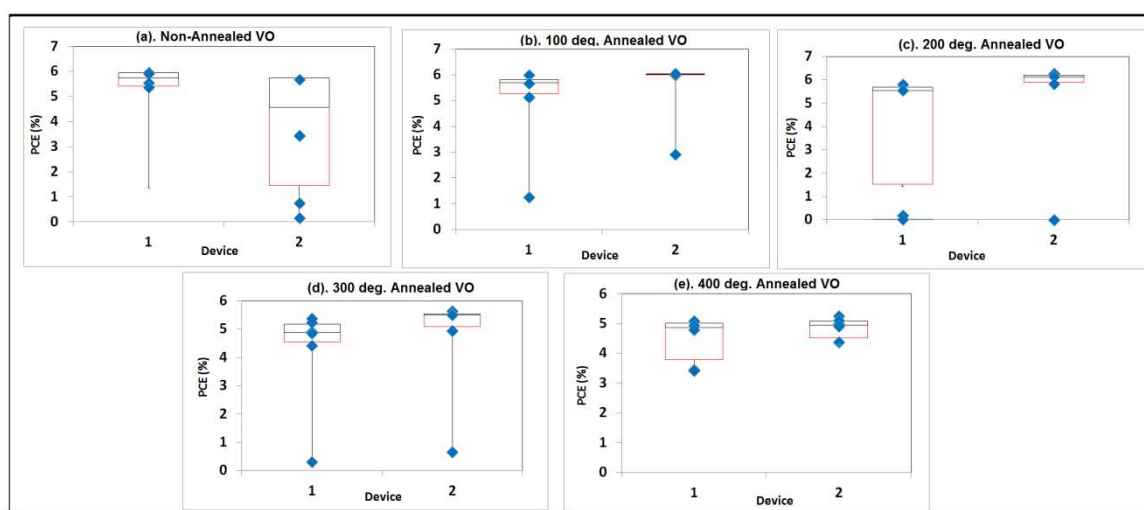


Fig. 3-7. Box plots for OPVs with their V_2O_{5-x} HEL (a). unannealed, (b). 100 °C annealed, (c). 200 °C annealed, (d) 300 °C annealed and (e). 400 °C annealed before BHJ deposition. Here, the *PCE* statistics are for 2 devices (or 12 pixels in total), in which ~ 5.8%. The *PCE* is represented by the blue points in the plots.

From Fig. 3-7(a), (b), (c), (d) and (e), we can first observe that there are quality differences in terms of *PCE* value among the pixels in almost all of the OPV types. These are evident from the differences between the minimum value and the lower box plot spread as shown by the lower error bars in almost

all of the device types. The only exception is the PCE value spread of OPV with the 400 °C annealed V_2O_{5-x} HEL before BHJ deposition, as can be seen from the OPV's box plot spread and its PCE value locations in the grouped points plot. On the other hand, we can see that the average maximum PCE $\sim 5.8\%$ for OPVs with their V_2O_{5-x} HEL unannealed, and also for OPVs with 100, 200 °C annealed V_2O_{5-x} , as evident from the respective OPVs same maximum pixel's PCE value. While for OPVs with 300 and 400 °C annealed V_2O_{5-x} HEL, the average maximum PCE are respectively ~ 5.2 and 5%. Therefore, for our IMS experiment, we have chosen a representative of "good" cells for OPVs with unannealed, 100 and 200 °C annealed V_2O_{5-x} HEL, since these cells PCE $\sim 5.6-5.8\%$. The same thing (i.e. the "good" cells were chosen) can also be said for OPVs with 300 and 400 °C annealed V_2O_{5-x} HEL, as these cells PCE $\sim 4.2-4.8\%$. Finally, all PCE data for OPVs with PEDOT and V_2O_{5-x} HEL were also provided by Mr. Abdullah Alsulami, University of Sheffield, Sheffield, UK.

3.2 Preparation and Characterization of Organic Light-Emitting Diode (OLED) Devices

Organic light-emitting diode (OLED) devices were also prepared for our IMS characterizations. The prepared OLEDs emit white light by using a copolymer, i.e. W1100 made by Sumitomo Chemicals Co., Ltd, as the device emissive material. The W1100 is a block copolymer that emits white light from the (combination) ratio of red and blue emitter/chromophores within the polymer structure. By combining different emitters in such a way, the different (emitters) ratio within the structure will be kept fixed during polymer synthesis [124]. The W1100 electroluminescence spectrum is depicted in Fig. 3-8, taken from Pounds et al [124].

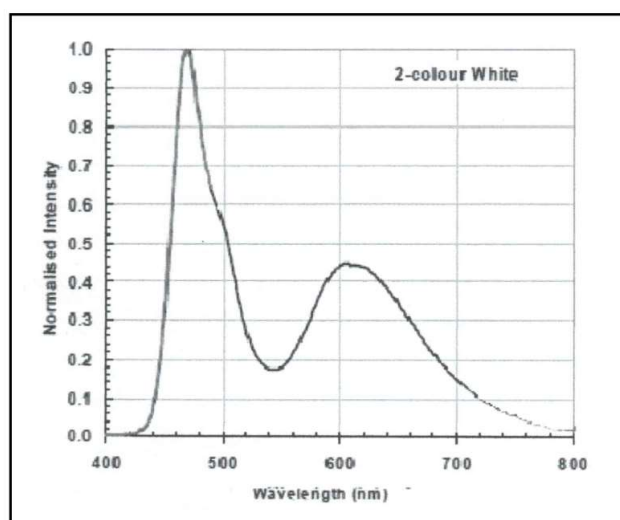


Fig. 3-8. Electroluminescence spectrum of a W1100 polymer. The total (white) spectrum is a combination of red and blue emitter/chromophores. Here we can observe two peaks, the highest peak, i.e. at the spectrum's blue part, has a full width at half maximum (FWHM) = 50 nm. While the smaller one, i.e. at the red part, has an FWHM = 120 nm [124].

From Fig. 3-8, two emission peaks are observed within the spectrum, the higher peak, with a full width at half maximum (FWHM) = 50 nm, lies between 450-500 nm and represents the emitted blue spectrum from the polymer. While the smaller peak, which lies between 560-680 nm with FWHM = 120 nm, represents the polymer's emitted red spectrum. An illustration of the OLED structure, along with its hole (HIL) and electron injection layer (EIL) material is depicted in Fig. 3-9, with the EIL and HIL structure depiction taken respectively from Huang et al [52].

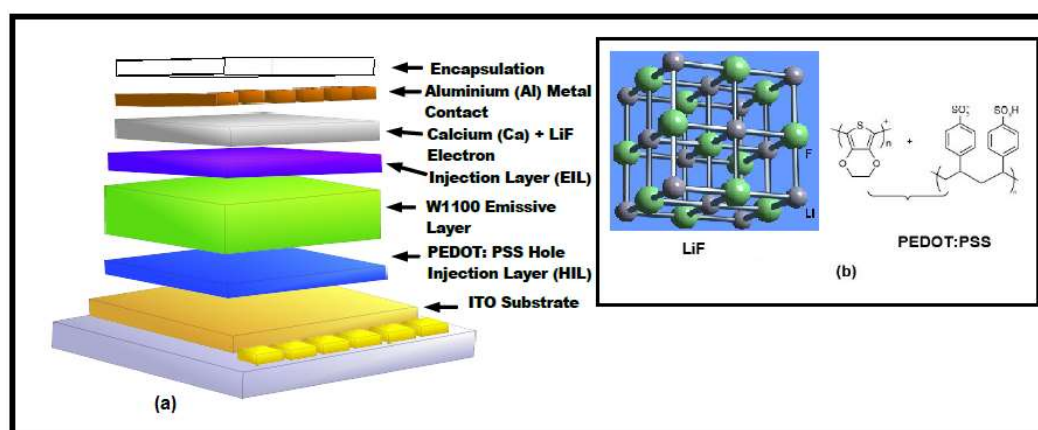


Fig. 3-9 (a). The prepared OLED structure and (b). PEDOT:PSS, calcium (Ca) and lithium fluoride (LiF) as the OLED's hole (HIL) and electron injection layer (EIL) respectively [52].

From Fig. 3-9(a), we see that the OLED structure is similar to those of OPV in 3.1.1. Here, each OLED device consists of 6 individual OLEDs which are also called pixels. So a total of 3 devices (or 6 pixels/OLEDs) were prepared for IMS characterizations. Later, we perform IMS on 1 pixel/OLED (3 pixels in total) from each prepared device. The OLED structure consists of an emissive layer that is made from a copolymer and is sandwiched between two electrodes, one is an aluminium top contact and the other is an indium tin oxide (ITO)-coated substrate. Further, between the electrodes and the emissive layer, charge injection layers were inserted to improve carrier transport towards the emissive layer while also protecting it from reaction with the electrodes. Hence, an electron injection layer (EIL) is deposited between the cathode and emissive layer, and a hole injection layer (HIL) is deposited between the emissive layer and the anode. The overlapping of individual metallic top contacts and the single ITO square define the pixel/OLED emissive area size. Also here, the OLED's front/window part is the ITO-coated substrate, where light is emitted from the emissive layer. In addition, aluminium is chosen as the cathode due to its low work function while ITO is chosen as the anode due to its high work function. Finally, an additional glass encapsulation is deposited on top of the metallic contacts to protect the cathode and the entire device from the ambient atmosphere.

For OLED preparation, W1100 copolymer was obtained from Sumitomo Chemicals Co., Ltd as the emissive layer material. A solvent, p-Xylene (with purity $\geq 99\%$) was purchased from Sigma-Aldrich as a dissolving agent for the W1100 polymer. A microbalance was then used to weigh the

W1100 polymer, after which it (the polymer) was put into vials that had been cleared before from particles with compressed air. The p-Xylene was then used to dissolve W1100 so that it will result in a W1100 solution with a total concentration of 13 mg/ml. Pre-patterned 6-pixel glass-ITO substrates were purchased from Ossila Limited. The substrates were then cleaned by sonication with Helmanex solution, then de-ionized (DI) water and finally isopropyl alcohol (IPA). After cleaning, the substrates were then dried with compressed air and placed on a hotplate at a temperature of 120 °C for 10 minutes before use. Also, PEDOT:PSS was obtained from HC Stark Clevios (batch number P VP AI4083, filtered through a 0.45 μm polyvinylidene fluoride (PVDF) filter). After filtration, PEDOT:PSS was spin cast, at 5000 rpm, on top of the cleaned substrates to form a hole injection layer with a thickness of 45 nm, which was then annealed in air at 120 °C for 10 minutes before usage. The reasoning behind the selection of PEDOT annealing temperature and time is the same as that in the selection of PEDOT HEL annealing temperature and time in 3.1.1. Thus, in general, the PEDOT annealing temperature must be set below 150 °C and for a shorter time at 150 °C, since above it (150 °C) and at a longer time, PEDOT will start to degrade/becomes unstable [118]. The PEDOT film-substrate was coated with the W1100/emissive polymer through spin coating. The spin coating was done at 2400 rpm in order to cast an emissive layer with a thickness of 85 nm. The remaining films in the electrodes were then wiped off by using appropriate solvents before the deposition of electron injection layer (EIL). After the spin coating process, Lithium fluoride (LiF) and calcium (Ca) as the EIL, and also aluminium (Al) as the OLED's cathode were thermally evaporated on top of the emissive layer in a vacuum chamber at a pressure between 10^{-6} and 10^{-7} mbar. Here, the thickness of the (evaporated) LiF, Ca layers and Al electrodes are respectively 3, 10 and 100 nm. Finally, prepared devices were encapsulated using a UV-treated epoxy (supplied by Ossila Ltd) and glass slides before any characterizations.

3.2.1 Current Density-Voltage (J/V) and Luminance-Voltage (L/V) Characterizations of OLED Devices

After fabrications of all OLED devices, DC characterization in the form of current density-voltage (J/V) and luminance-voltage (L/V) characteristics were performed. Both the OLEDs J/V and L/V characterizations were performed under dark, in a black box equivalent container and under ambient conditions. The OLEDs were placed in an OLED testing module/board that was obtained from Ossila Ltd [125]. Here, the electronic testing board function is to allow for separate/individual characterizations of pixels in an OLED. The J/V and L/V characterizations were first conducted by applying a voltage sweep V from 0 to 10 V with 0.2 V increments to the characterized pixels with a Keithley 2602 source meter. For J/V characteristics, the resulting current is then measured by this

source meter and the OLED's current density J is then defined with respect to an emissive area $A = 4 \text{ mm}^2$. While for L/V characteristics, the resulting luminance L from the OLEDs were measured using a Konica Minolta LS-110 luminance meter connected to the 2602 source meter. Both J/V and L/V characterizations results are recorded by using a bespoke LabView software made by Mr. Thomas Routledge. We first present all 3 OLEDs J/V characterization results in Fig. 3-10, followed by the L/V results in Fig. 3-11, with J in mA/cm^2 , L in mcd/cm^2 , and V in V. From the J/V and L/V plots, we can then derive the OLED's DC parameters such as, its turn-on voltage or V_{on} , turn-on current density or J_{on} , differential resistance R_{diff} and turn-on luminance or L_{on} . Also, since R_{diff} is in Ω , area-dependent R_{diff} from the J/V plots were converted to Ω by dividing it by $A = 4 \text{ mm}^2$. Finally, the derived parameters were, in turn, used to assess the OLED's DC performance.

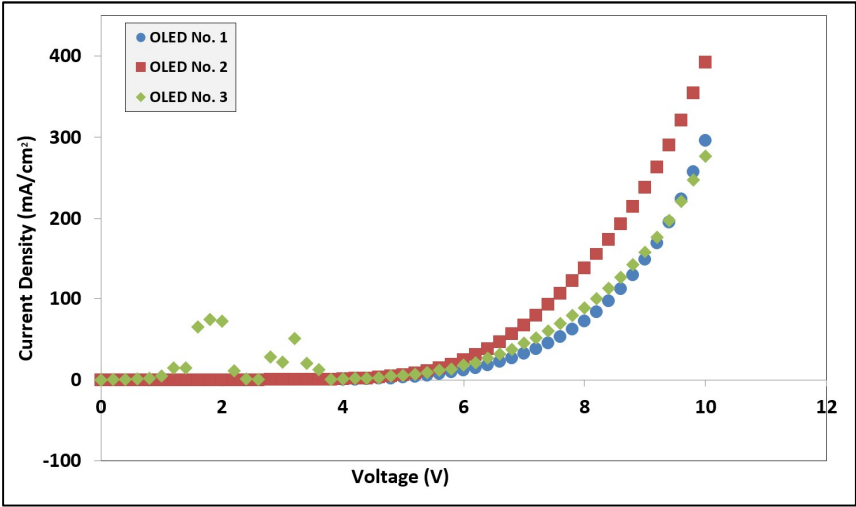


Fig. 3-10. The J/V characteristics of all 3 OLEDs. Here, OLED No. 1 to 3 is of the same structure and emissive materials.

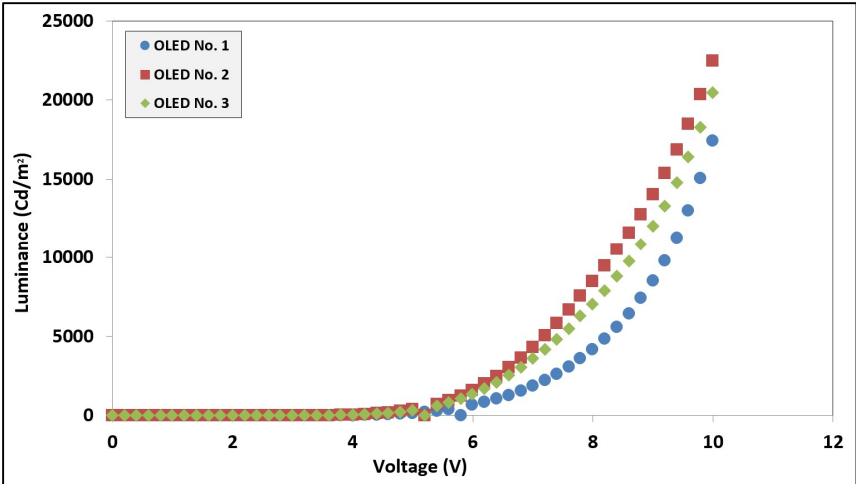


Fig. 3-11. The L/V characteristics of all 3 OLEDs.

The OLED numbering in both J/V and L/V plots are taken according to the order their IMS results are presented later in this work. So OLED No. 1 is the OLED from which the IMS results will be presented as the last in this work. While OLED No. 2 is the OLED which we presented just before OLED No.1 and so on. From Fig. 3-10 and 3-11 respectively, we then obtain several DC parameters from both plots for all OLEDs, these are; J_{on} , V_{on} , R_{diff} , and L_{on} . We then list all of the parameters together in Table IV.

TABLE IV OLED No., J_{on} , V_{on} , V_{bi} , R_{diff} and L_{on} FROM FIG. 40. AND FIG 41.

OLED No.	J_{on} [mA/cm ²]	V_{on} [V]	L_{on} [Cd/m ²]	R_{diff} [Ω]
1	3.4×10^{-5}	2.4	0.01	1227
2	4.1×10^{-4}	2.6	0.01	578
3	28	2.8	0.08	588

From Table IV, we see that OLED no 1 and 2 have similar DC performances, while OLED No. 3 has a very high J_{on} compared with the other two, this is despite similar processing steps and emissive material used in all 3 OLEDs. A possible cause can be seen from OLED No. 3 J/V plot in that the current density reading is already large at low OLED V_{bias} , or in other words, OLED No. 3 produces larger currents under the same voltage bias sweep. This can also be the likely reason why the OLED No. 3 J/V plot fluctuates at low OLED V_{bias} .

Chapter 4

Intensity-Modulated Spectroscopy (IMS) Instrument

4.1 History of Intensity-Modulated Spectroscopy (IMS) Instrument

An intensity-modulated spectroscopy (IMS) instrument is a dynamic characterization instrument that uses a modulated light intensity with the steady-state intensity being larger than the modulating component as the stimulus signal. It is applied to the characterized system, which is then followed by measuring the system's electrical response as a function of angular frequency ω . The instrument will then measure the transfer function $H(\omega)$ as the ratio of (system's) current/voltage-to-modulated light stimulus as in 1.4 [16, 40]. The IMS instrument itself can be operated at either two modes of operation, one is under intensity-modulated photocurrent spectroscopy (IMPS) and the other is under intensity-modulated photovoltage spectroscopy (IMVS) [16, 40]. In IMPS mode, the instrument applies a light stimulus with an intensity $L_T(t) = L + \Delta L \sin \omega t$ with $L > \Delta L$ to the characterized system, and it will then measure the system's current density response $J_{ph}(t)$ in the form of $J_{ph}(t) = J_{ph-DC} + \Delta J \sin(\omega t + \phi)$. The instrument then varies the modulating light ω , thus scanning the ΔJ and ϕ response with respect to frequency ω . Finally, the instrument measure the system's response in the form of $H(\omega) = \Delta J(\omega)/\Delta L(\omega)$, i.e. a ratio of $\Delta J(\omega)$ to $\Delta L(\omega)$ [16, 39]. Alternatively, the instrument can also operate under intensity-modulated photovoltage spectroscopy (IMVS), where the instrument applies the same light stimulus as IMPS and then measure a voltage response $V_{ph}(t) = V_{ph-DC} + \Delta V \sin(\omega t + \phi)$. As in IMPS, the instrument will then measure the system's response in the form of $H(\omega) = \Delta V(\omega)/\Delta L(\omega)$, i.e. as a ratio of $\Delta V(\omega)$ to $\Delta L(\omega)$ [40, 46]. In addition, an IMS instrument can also measure $\Delta J(\omega)$ or $\Delta V(\omega)$ with respect to frequency ω in place of transfer function $H(\omega)$ [41, 50].

Intensity-modulated spectroscopy was first developed as a technique by Foote and Mohler in 1925, for the purpose of measuring the photoelectric effect from an irradiated tungsten (W) filament in a cesium (Cs) vapour-filled container. From their work, it was found that thermionic currents from the heated filament inside the Cs vapour-filled container increased rapidly when irradiated with external light radiation from various sources. Further, when the irradiation rate is changed slightly or modulated slightly, photoelectric/photoemission detection from changes in thermionic currents improved dramatically, thus increasing the measurement sensitivity [42]. Hence, we can see how slightly modulated illumination in an IMS can be used to characterize a specific dynamic that originates from a system. In 1928, FM Penning also observed changes in electrical resistance that resulted from irradiation of a discharge neon lamp by another neon lamp, where resistance changes

can be used to measure the neon lamp irradiation effect in a similar manner as in previous literature (Foote 1925) [126]. By 1967, Carswell and Wood have applied this technique to measure gas discharge from a CO₂ laser. In their work, they used a chopper wheel to slightly modulate a higher laser intensity that interacts with the CO₂ gas discharge. In addition, they also measured the electrical response from the laser-gas discharge interactions as an impedance due to a modulated laser, which is similar to today's IMS setup measured parameters [127]. By 1976, the technique was introduced for the first time as “optogalvanic spectroscopy” by Green et al. At the time, Green et al. applied this technique to measure the electrical response from a gas discharge that was irradiated with a slightly modulated laser. A depiction of the setup that they used is shown in Fig. 4-1, taken from Green et al [43].

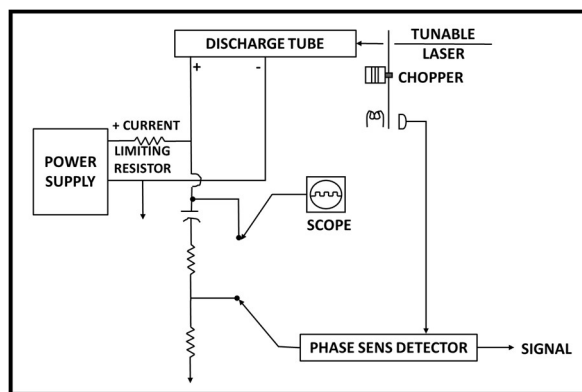


Fig. 4-1. A depiction of the “optogalvanic spectroscopy” setup that was used by Green et al. to measure the electrical response from a laser-irradiated gas discharge inside the tube [43].

In Fig. 4-1, a tunable dye laser as the source of stimulus is slightly modulated with a mechanical chopper at a certain frequency ω . The modulated laser is then used to irradiate a neon gas discharge inside the discharge tube. Here, applied voltage from the power supply is used to discharge/ionized the inert gas within the tube. As a result of modulated irradiation, the voltage across the discharge tube will be modulated by the modulated laser interaction with the inert gas inside the tube. This photovoltage is then channeled into a phase sensitive detector/lock-in amplifier, where the detector will compare the AC voltage component with respect to the modulated laser stimulus and then determine an equivalent transfer function from this ratio [43]. Note that in the Fig. 4-1 setup, the modulated laser component was kept separated from the measured voltage connection/setup. This configuration is also another characteristic of an IMS setup, which is that the modulated component is independent of the power supply voltage, thus changes in the supply voltage will not influence the modulated light and vice versa. By 1980, Stanciulescu et al. acknowledged and categorized the technique as similar to impedance spectroscopy but with a distinctive experimental procedure that measure modulated electrical response from a system due to modulated illumination [44]. By this

time, IMS had been used to investigate light absorption processes in material microstructures and atomic states. A year later, Oheda proposed a generalized theory that linked phase shift in modulated photocurrent response of an amorphous semiconductor to trap states within the semiconductor [45]. By 1990, Peter et al. have described this method as IMPS with a similar setup as we know it today, and use it to investigate semiconductor electrode properties/behavior. Their setup at the time is depicted in Fig. 4-2 taken from Peter et al [16].

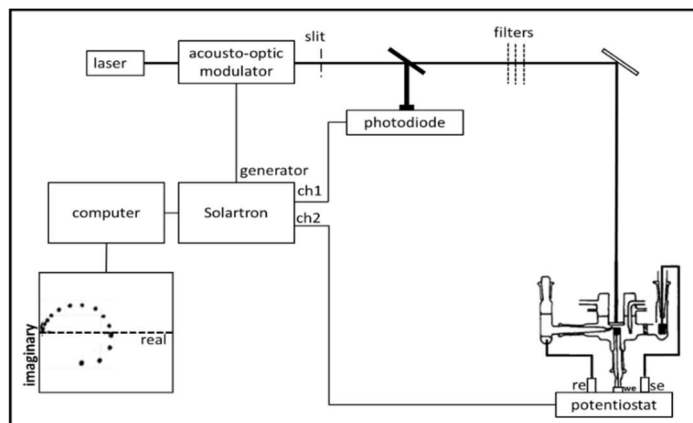


Fig. 4-2. The IMPS setup that was used by Peter et al. to measure photocurrent response of a semiconductor electrode that was illuminated by a modulated laser. Here re, we and se refers to reference, working and standard/counter electrode respectively in a potentiostat three-electrode setup [16].

In Fig. 4-2, a laser is used as the IMPS source of stimulus. Here, the laser is slightly modulated by a Solartron impedance analyzer through the modulator device. The modulated laser is then channeled through a slit and a series of filter in order to transmit only laser stimulus with the desired wavelength. The electrode sample is then illuminated by the modulated laser, and followed by measuring the sample's photocurrent response with a potentiostat in a three-electrode setup. Here, a potentiostat is used since in this setup a photocurrents response was measured from an electrode. This is because the function of a potentiostat in an electrochemical measurement is to apply a potential difference between the working electrode (WE), where the sample is, and the standard electrode (SE), an electrode that closes the circuit, such that current will flow between WE and SE, thus enabling WE characterization by measuring changes in current flowing out of WE. In addition, the function of the reference electrode or RE (placed near to WE) is to control the potential difference between WE and SE from the potential difference measurement between RE and WE. So if there are changes in potential between WE and SE, this can be adjusted by looking at the potential difference between RE and WE, i.e. whether RE-WE has been changed from the standard RE value. Hence, from the Fig. 4-2 setup, AC photocurrent will be measured from SE, as current flows from the measuring electrode in WE to the SE. This photocurrent response will be measured as a (transfer function) ratio to the modulated laser intensity which itself is obtained through a photodiode. The transfer function is then

displayed in a Nyquist plot plane. In 1997, Peter et al. also developed a theoretical framework of IMPS application on photoelectrode processes that involves surface-bound molecules [16, 92]. As recently as 2013, IMS has been used to characterize specific dynamics on different kinds of organic and inorganic solar cells, and also other photosensitive materials/systems [49, 128]. Also from 1.4, depending on the characterized systems, a number of light sources can be used as the stimulus signal, for example, LEDs, lasers and Xenon short arc lamps [16, 39, 41]. The use of LEDs in particular, has been relatively advantageous compared to other light sources because of the ease in modulating one with a drive current, in addition to its (LED) ability where it can be modulated up to a very high frequency ($f > 1$ MHz), thus extending the measurement frequency bandwidth [23, 41].

In addition to the two different modes of IMS operation, an IMS instrument/setup generally consists of 5 main components with different functions. These are, a light source which functions as a stimulus, a modulator device that modulates the light source intensity at a certain frequency, a voltage/bias adder that adds/decrease the light stimulus steady-state intensity, a sample measurement module that channels or converts the electrical (current/voltage) response from the sample to the IMS instrument and finally, a phase-sensitive detector (PSD)/lock-in device connected to the modulator device that “pick out” the sample’s AC current/voltage component due to the modulated illumination [39, 41]. On the other hand, a setup can also consist of only 3 main components, with the phase-sensitive detector function taken over by an impedance analyzer device, for example, which serve as the modulator device, a bias adder and a phase sensitive detector all together at the same time. Hence, the majority of IMS instrument/setups can be divided into two: IMS instruments/setups that use impedance analyzers in their operation [16, 47], and IMS instruments that do not employ one/a custom-made IMS instrument. The later setups instead use a phase sensitive detector/lock-in amplifier to both modulate the light stimulus and processed the sample’s electrical response from modulated light [52].

The first type of setup basically uses an impedance analyzer to modulate the light stimulus and to serve as a phase-sensitive detector or lock-in device that “picks out” the modulating electrical (current/voltage) component response from the sample due to the modulated light. This setup is one of the most commonly found IMS setup in the literature [16, 47, 50]. One example of this setup is already depicted in Fig. 4-2 from Peter et al [16]. A recent example, in this case, an IMS under IMPS, taken from Kasavoglu et al. is depicted in Fig. 4-3 [129].

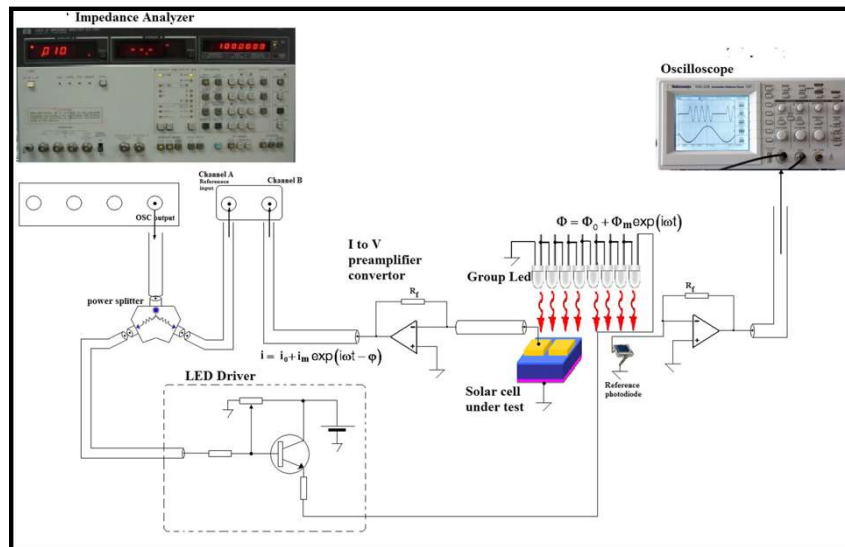


Fig. 4-3. The IMS setup under IMPS used by Kasavoglu et al. to measure photocurrent response from CIGS ($\text{Cu}(\text{In}_x\text{Ga}_{1-x})\text{Se}_2$) and porous Si solar cells. Here, the impedance analyzer controls the current modulation on the LED driver, with the DC current bias provided by the LED driver itself. The LED driver, in turn, modulates the LED group illumination intensity, which is then used to characterize the solar cell sample [129].

In Fig. 4-3, a LED group is used as a source of illumination in the characterization of a CIGS and porous Si solar cell sample. For this purpose, an impedance analyzer is used to apply a modulating voltage to a custom-made LED driver, which then results in the driver producing modulated currents to modulate the LED. A voltage driver is needed in order to combine modulating current from the analyzer and the bias current from the driver, so changes in bias current will not affect changes in the current modulation, which can be the case if an analyzer is used to supply both the bias and modulating voltage to the driver. So from Fig. 4-3, the LED driver will combine a DC voltage bias from itself and a modulating voltage from the analyzer to drive the LED group and produce a modulated illumination in the form of $\Phi = \Phi_0 + \Phi_m \exp(i\omega t)$. Where Φ_0 is the steady-state light intensity and Φ_m is the modulated intensity amplitude. This modulated LED intensity is then used to illuminate the sample. In Fig. 4-3, the sample will produce a photocurrent response in the form of $i = i_0 + i_m \exp(i\omega t - \phi)$, where i is the DC current, i_m is the current AC response and ϕ being the current's phase with respect to illumination. The process is then repeated again by varying the analyzer's modulating voltage frequency ω , thus scanning the photocurrent with respect to ω . This photocurrent is then converted into a voltage signal with an IV converter device and fed back into the analyzer. The IV converter here is used as to amplify the photocurrent into a voltage. The analyzer then "picks out" the voltage and phase of the IV converter and compares it with the analyzer's voltage stimulus frequency ω . Although the signal fed into the analyzer is a voltage from the IV converter, the converter input itself is the sample's photocurrent (with phase) response. Finally, a transfer function response as a ratio of voltage response-to-the analyzer's voltage stimulus is obtained from the sample. The

analyzer's voltage stimulus being the voltage that earlier modulates the LED group [129]. A photodiode is also illuminated with the same modulated illumination from the analyzer. This is only done to measure the group LEDs modulated light intensity by converting photodiode currents into a voltage with an IV converter and then measure the voltage in an oscilloscope. This measurement has no connection with signal processing from sample response [129].

Several advantages of this setup are that first it provides the user with more automation over the instrument's operation, which includes simplified control over the setup light stimulus, and also automated (sample) response acquisition and processing. The other advantage is that the instrument's automated operation will also allow for a more accurate, precise, simple and faster response acquisition and processing, while also reducing the amount of error in the measurement process. However, the drawbacks of this setup are, first is that since the current market price of a high-quality, commercial impedance analyzer is around £11.000-16.000, this would make the analyzer a very expensive choice of instrument in an IMS measurement [130]. The other drawback is that since most commercial analyzers are heavy and bulky in size, analyzers-based setup will be limited to lab-based measurements/applications [47, 50, 129].

Another type of IMS instrument setup is a custom-made, phase-sensitive detector (PSD)-based setup, where a PSD or a lock-in amplifier is used to modulate the light stimulus and process the electrical response from the sample due to the modulated light. In other words, the setup is centered on a lock-in/PSD device that has its own sinusoidal/modulating voltage signal. This type of setup is also quite common, but not as common as analyzer-based setups [52, 131]. A simple depiction of this setup, in this case, an IMVS setup, is shown in Fig. 4-4, taken from Huang et al [52].

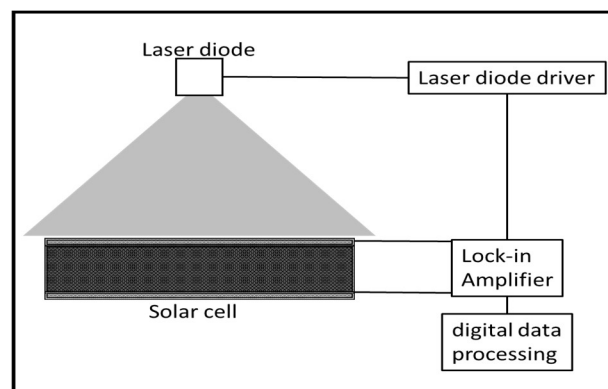


Fig. 4-4. The IMS setup used by Huang et al. to measure photovoltage response from dye-sensitized nanocrystalline TiO_2 solar cells (DSSC). Here, the setup is under IMVS mode and the lock-in modulates the illumination and measures the photovoltage response from the DSSC. Note that the digital data processing module above does not refer to the analyzer but it refers to further digital data processing from the lock-in [52].

In Fig. 4-4, a laser diode is used as a source of illumination in the characterization of a DSSC sample. For this purpose, a lock-in amplifier, which emits its own sinusoidal voltage signal, is used to

modulate a laser diode through a commercial laser diode driver, which then results in the driver producing modulated currents from the modulated voltage. Here, as in Fig. 4-3, the LED driver is also used to provide a DC bias current to drive the laser diode and to combine the modulating current component from the lock-in and bias current from itself, so that changes in bias current will not affect the modulating current component. So from Fig. 4-4, the LED driver will combine a DC voltage bias from itself and a modulating voltage from the lock-in to drive the laser diode and produce a modulated illumination of $L(t) = L + \Delta L \sin(\omega t)$. Where L is the steady-state light intensity and ΔL is the modulated intensity amplitude. This modulated LED intensity is then used to illuminate the sample. Because of Fig. 4-4 is under IMVS, a photovoltage response from the sample will instead be measured in the form of $V(t) = V + \Delta V \sin(\omega t + \varphi)$, where V is the DC voltage, ΔV is the modulated voltage and φ being the voltage phase with respect to illumination. This process is then repeated again by varying the analyzer's modulated voltage frequency ω , thus scanning ΔV with respect to ω . The photovoltage is then fed into a lock-in amplifier. The lock-in then "picks out" the ΔV and φ from the sample and compares it with the light stimulus or the lock-in's modulating voltage frequency ω . Finally, a transfer function response as a ratio of voltage response-to-the lock-in's voltage stimulus can be obtained for the sample with the lock-in's voltage stimulus being the voltage that modulates the laser diode [52]. In addition to this instrument setup, there is also another variation of lock-in based setup which is done by using a separate light source, so one source functioning as the steady-state illumination while another as the modulating light component [132].

Several advantages of a lock-in based setup, especially compared to the analyzer-based ones are that, it provides a much cheaper alternative to control light modulation and sample response processing, in addition to cheaper operational automation. Cheaper automation is achieved simply by using a software-controlled lock-in to regulate, automate and control the process at a fraction of an analyzer cost. Also, this setup offers the possibility of portable and easily modified applications due to the simple and custom-made nature of the setup. Finally, the setup gives us the same instrument capability in conducting IMS but with a much cheaper cost compared to an analyzer. The drawbacks of this setup, however, are that they are less precise and accurate compared to an analyzer-based setup since the setup's operational automation is custom-made compared to that of an analyzer. However, this can be rectified by deploying an error correcting mechanism/steps in the setup, to offset possible measurement errors [39, 41, 52]. Later in this work, we use the lock-in based IMS setup to develop our very own IMS instrument by using LED as a light stimulus.

4.2 Development of A Bespoke Intensity-Modulated Spectroscopy (IMS) Instrument

In this work, we have developed a portable, bespoke intensity-modulated spectroscopy (IMS) instrument that is based on a generic digital lock-in, which offers a far more affordable alternative to analyzers-based setup, with the instrument capable of performing IMS at any point of a solar cell's J/V characteristics. In addition, we have also introduced a new mode of IMS operation which is different from both the established IMVS and IMPS mode. We call this method IMS under finite load and we perform this mode by applying intensity-modulated light on a solar cell (OPV in our work) which are externally loaded with a finite load resistance R_L , including at the cell's maximum power point resistance R_{MPP} . In the next chapter, we will elaborate this new mode of operation further. Our bespoke instrument consists of a fast red LED (RC LED, peak wavelength $\lambda_p = 650$ nm, rise time $\tau = 3$ ns) as the source of light [133], a digital Anfatec USB 250 Lock-In amplifier that sourced its own sinusoidal voltage to modulate the LED intensity with this AC voltage [134], a bespoke voltage adder based on fast 2N2369 NPN transistors (rise time $\tau = 6$ ns) which adds and combines a DC bias voltage to the lock-in AC voltage to drive and modulate the LED, and finally, a PC with LabView software that is used to operate the (IMS) frequency scan on the sample. The instrument's bespoke voltage adder was designed and built by Prof. Richard Tozer, from the Department of Electronic and Electrical Engineering at The University of Sheffield, UK. A depiction of the IMS instrument setup and the voltage adder are given in Fig. 4-5(a) and (b) respectively.

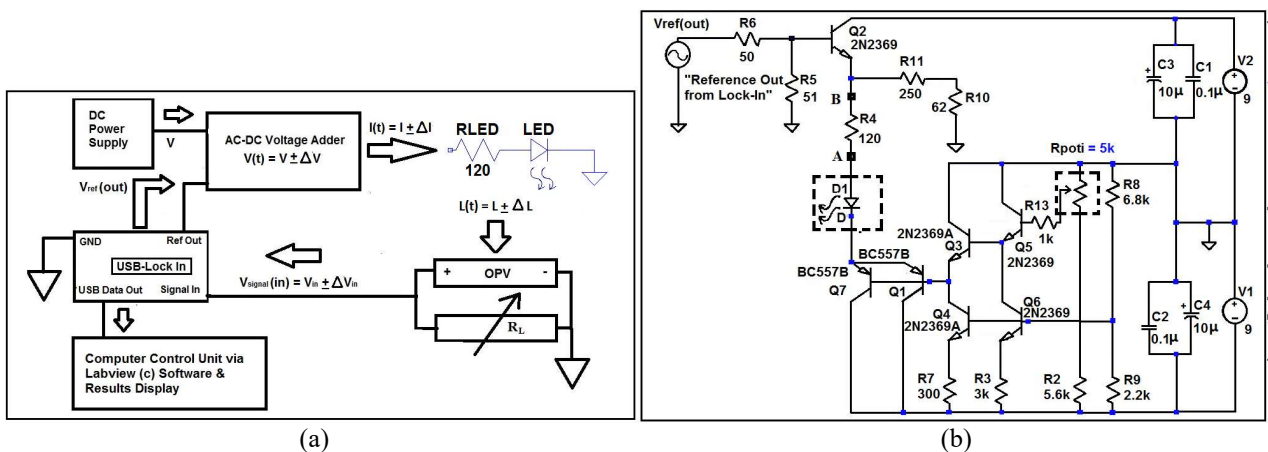


Fig. 4-5 (a). A block diagram of our IMS measurement setup, showing the PC running LabView software which controls the USB lock-in, a circuit driving a fast red LED by adding a DC offset voltage to the AC modulation voltage taken from the lock-in's reference output, the solar cell with its terminals connected via a variable load R_L , and the voltage across the load fed into the lock-in's measurement input. (b) A circuit schematic of the DC + AC adder circuit, that adds a DC bias to the AC lock-in reference output to drive the LED. The lock-in reference output is represented by a voltage source, top left. DC voltage supply is from 2 x 9 V batteries stabilized by capacitors (right). The level of DC bias is set by a 5 k Ω potentiometer (highlighted). The LED (D1) is also highlighted. As a performance test of the DC + AC adder, we fed the DC + AC signal directly into the lock-in measurement input, and found no measurable drop in AC amplitude, and less than 1° of added phase, up to 250 kHz.

In Fig. 4-5(a), we use an AC modulation voltage V_{AC} from the lock-in's reference output voltage and by using a bespoke voltage adder, superimpose the AC voltage on a larger DC bias voltage V from the voltage adder's power supply (9 V batteries). We set the V_{AC} amplitude by using a bespoke LabView software that we have developed to operate our IMS measurements. We also input the lock-in settings for the IMS scan by using our LabView software. These settings are; V_{AC} amplitude (in V_{rms}), input coupling, roll-off, frequency, input gain, phase offset and reference. For IMS on OPV in this work, we set the lock-in's input coupling to DC, roll-off to 24 dB/oct, dynamic to high, phase offset to 0 and the reference harmonic to 1. The time constants are set to 5 s at scanning frequency $f = 1-10$ Hz, 1 s at $f = 10-100$ Hz, 0.5 s at $f = 10-1000$ Hz, 0.1 s at $f = 1$ kHz-10 kHz and 0.05 s at $f > 10$ kHz. The software and the lock-in settings will be explained further in the next chapter. We then use the voltage adder to apply the previous (DC+AC) voltage to the fast D1 LED as V_{LED} with protective $R_{LED} = R4 = 120 \Omega$, where for all OPV characterizations $V_{LED} = (2.2 \pm 0.5)$ V so that the adder will drive/modulate the LED with a LED current $I_{LED} = (18 \pm 4)$ mA. Here, the LED DC current $I_{DC} = 18$ mA and its AC current $I_{AC} = 4$ mA. The modulated LED will then produce a modulated light intensity of $L_T = L + \Delta L \sin \omega t$. The light intensity here is not known in absolute terms, but it is significantly smaller than AM 1.5. However, since $L_T \sim I_{LED}$, then $\Delta L/L = \Delta I/I$. We then use the modulated LED to illuminate an OPV that is connected to a potentiometer as a variable load resistance R_L , and use our IMS software to perform an automatic frequency scan by varying the lock-in's voltage modulation frequency ω between 1 Hz and 250 kHz at 12 steps per decade.

Here, a total of 68 frequency points, or data points were taken between 1 Hz and 250 kHz, with $\omega = 2\pi f$. From the illumination, the photocurrent response from the cell is then measured as a voltage drop $V + \Delta V(\omega) \sin(\omega t + \phi(\omega))$ across R_L . R_L will later be varied in the OPV measurements depending on the experiment. Also, the $\Delta V(\omega)$ and $\phi(\omega)$ response is a function of ω since we varied the modulation frequency ω . The cell's voltage response is then fed into the lock-in voltage measurement input, without a current-to-voltage converter. Note that here, the lock-in can only receive voltage inputs but not current. The lock-in will then measure and "pick out" the cell's $\Delta V(\omega)$ by comparing it with the lock-in's ref out voltage frequency ω . As a result, we obtained the amplitude $\Delta V(\omega)$ and phase $\phi(\omega)$ from the voltage response and record these parameters as a function of $f = \omega/2\pi$. Later the amplitude $\Delta V(\omega)$ and phase $\phi(\omega)$ can be plotted as a Bode and Nyquist plot as seen in 1.4. So with this setup, we have the advantage of performing IMS at a fraction of the cost of an impedance analyzer, i.e. $\sim \text{£}3000$ (with the lock-in device) vs $\sim \text{£}16000$ (with an impedance analyzer) [134].

From Fig. 4-5(b), the bespoke adder circuit consists of two main parts, one is an AC part, which modulates the LED with the AC current from the lock-in and represented by the AC voltage source

and the $Q2$ transistor. While the other is the DC part, that provides a DC bias current to the LED and represented by $Q1$, $Q3$, $Q4$, $Q7$, $Q5$, $Q6$ and the circuit's 9 V power source. In an IMS measurement, we first apply an AC voltage to the circuit as represented by the AC voltage source in Fig. 4-5(b). Here, $R6 = 50 \Omega$ is the characteristic impedance of a coaxial cable that we use to connect the ref out voltage with the adder circuit. While $R5$ is a resistance that we placed in parallel to the circuit's input to match the coaxial cable characteristic impedance, thus minimizing any voltage signal reflection at the adder's input. The ref out voltage will then be a base voltage or V_{BE} to $Q2$ with respect to the emitter. As such, V_{BE} will apply this modulation to the intersection node between $R4$ and $R11$, thus modulating D1 LED through $R4$. So the measured AC modulation current I_{AC} can be determined from $I_{AC} = V_{AC}/R4$, with $V_{AC} = V_{BE}$ (in V_p) and I_{AC} in mA. Note that $R10$ and $R11$ were placed as a parallel branch with $R4$ and D1 LED so that we can monitor the V_{AC} amplitude and waveform from the node between R10 and R11, since monitoring V_{AC} between $R4$ and $R11$ directly may disturb the LED modulation and cause an additional phase to appear at point B.

As for the circuit's DC part, we use the -9 V connection from the battery to add the DC bias current to the LED, thus the voltage across $R4$ and $R_{poti} = -9$ V. Also note, the 2 pairs of 10 μ F electrolytic and 0.1 μ F ceramic capacitors in-parallel with the ± 9 V power sources were used to guard against voltage drop when we perform IMS at high frequency. This is due to charging and discharging effect in batteries at high frequencies. We use $R_{poti} = 5$ k Ω (highlighted in Fig. 4-5(b)) to set $Q5$ V_{BE} and drive it with a base current I_{BE} through $R13 = 1$ k Ω . The R_{poti} here will act as a voltage divider to the -9 V from the battery. The R_{poti} is actually used to tune the DC bias level of D1 LED, since by tuning R_{poti} manually, we can set $Q5$ V_{BE} and consequently $Q3$, $Q1$, and $Q7$ V_{BE} . So once we set the V_{BE} on $Q5$, the Darlington pair connection between $Q5$ and $Q3$ will result in a current gain I_{BE} that will drive $Q1$ and $Q7$ BC557B transistors. Because $Q1$ and $Q7$ will then drive the LED bias current, the emitter current I_E flowing out from $Q1$ and $Q7$ needs to be stable enough under high-frequency conditions. Note that the Darlington connection is used since the current gain of a 2N2369A model is not that large, hence the need for $Q5$ and $Q3$ pair to drive the bases of $Q1$ and $Q7$. In addition, we also use the -9 V battery connection to set a -9 V voltage across $R8$ and $R9$ and then use the voltage divider setup between $R8$ and $R9$ to apply a base voltage V_{BE} on $Q4$ and $Q6$. The $Q4$ and $Q6$ transistors are needed to define both $Q3$ and $Q5$ collector currents and their emitter resistances. So now, the $Q1$ and $Q7$ BC557B PNP transistors will drive the LED with a bias current in combination with the modulated current that runs through $R4$. Also, the DC input voltage applied to the LED can be measured by measuring the voltage V_E (in V) at $Q1$ emitter with respect to ground. While the LED bias current can be determined from $I = V_{R4}/R4$, with $V_{R4} = V_A - V_B$ (in V) and I in mA. Here, V_A and V_B are respectively the voltage at point A and B of Fig. 4-5(b) circuit. Note also that the $Q1$ and $Q7$

transistors are needed to reduce the effect of (static) series resistances in both transistors base-emitter connections.

4.3 Development of A New Mode of IMS Operation

From 1.4, traditionally, two modes of IMS operation exist, one is IMPS where we measured the system's current response with respect to modulated light and the other is IMVS where we measured the voltage response with respect to modulated light [16, 46]. For IMS under IMPS, the characterized system must be set at a short-circuit condition since we are measuring photocurrents [16]. While to operate IMS under IMVS, the system must be set at an open-circuit condition since we measure photovoltage instead [46]. In this work, we introduce a new mode of operation where we perform IMS neither at IMPS or IMVS, but instead between the two modes which also includes IMS at maximum power point (MPP) for solar cells characterizations. We called this method IMS under finite load, and we achieve this by externally connecting the characterized system, i.e. a solar cell, to a finite load resistance R_L . To further elaborate this method, we use IMS on a solar cell as an example. Practically, solar cells operate neither under open-circuit ('infinite' load resistor R_L) nor short-circuit (zero R_L) conditions, but under an electric load at maximum power point R_{MPP} that tunes the cell to its MPP voltage/ V_{MPP} , with R_{MPP} amplitude: $0 < R_{MPP} < \text{infinity}$. In this context, we can then perform IMS under finite load by connecting the illuminated cell to a finite load resistance R_L . An illustration of this new IMS mode, along with the mode representation in terms of a solar cell J/V characteristics, are shown in Fig. 4-6(a) and (b) respectively [135].

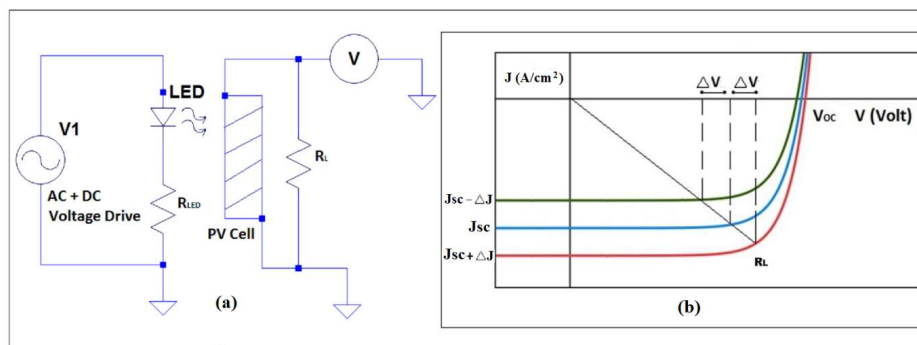


Fig. 4-6 (a). The schematic setup for IMS under finite load. R_L represents an external load resistance. (b) DC Current Density-Voltage (J/V) characteristic of a PV cell under modulation, which results in three different light intensities (L (blue); $L - \Delta L$ (green); and $L + \Delta L$ (red)). The ΔL is the intensity modulation in IMS. Here J_{sc} and V_{oc} are respectively, the cell's short-circuit current density and open-circuit voltage point. The load line (in black) represents the external load resistance R_L , which intersects the three lines at the characteristic midpoint. This midpoint is the cell's maximum power point. Also, ΔJ and ΔV are respectively the current density and voltage modulation due to the modulated light [135].

From Fig. 4-6(a), in the IMS under finite load setup, R_L can be varied so that we can perform IMS when the cell is in-between the short- (zero R_L) and open-circuit condition (infinite R_L), including at MPP (finite R_L). In our instrument, this setup is achieved by connecting the cell to a potentiometer

that functions as a variable resistor as depicted in Fig. 4-6(a). This then means that we can perform IMS on a solar cell at its realistic working condition, which is at its maximum power point, rather than at the short- or open-circuit point which is far from practical cell operation.

To understand finite load IMS, we also look at the cell's DC J/V characteristics under AM 1.5 as illustrated by the blue J/V curve in Fig. 4-6(b). Under modulated illumination/different light intensities, the J/V curve will rise and decrease as represented by the red and green curve respectively. For the cell's J_{SC} , if the light intensity increases/decreases, J_{SC} will also increase/decrease in proportion to intensity, while V_{OC} is near constant at different intensities [135]. In Fig. 4-6(b), we use a load line representation in the J/V curve to illustrate external R_L on a solar cell operation [36]. In the J/V characteristics, the load resistor R_L is represented by the black load line that intersects the three different intensities. The intersection of load line with the J/V curve and other intensities gives the resulting DC voltage V of a solar cell that is under illumination and loaded with R_L at the same time. We then call this V the 'voltage point' for a load R_L . As this point is the voltage measured across R_L due to illumination. Under light intensity modulation $\pm \Delta L$, the voltage point V will be modulated by $\pm \Delta V$. In the limit of the low modulation frequency, ΔV is the intersections of the same load line with the J/V characteristics for $L \pm \Delta L$ or different light intensities, as shown in Fig. 4-6(b). While at higher frequencies, the amplitude of ΔV will drop, and display a phase (ϕ) with respect to ΔL , leading to an IMS spectrum/modulated voltage response at finite load R_L .

In addition, Fig 4-6(b) also reveals the advantage of finite load IMS compared to both IMVS (R_L near infinity: load line parallel to voltage axis) and IMPS mode (R_L near 0: load line parallel to J axis). Since in both cases, the measured voltage modulation tends to be zero even at low frequency, leading to difficulties in practical measurement. For IMPS, this can be solved by measuring current instead of voltage, by using a current-to-voltage (IV) converter. On the other hand, since we use a finite load resistance R_L in finite load IMS, or choose an R_L similar to R_{MPP} , we will find a measurable, finite modulated voltage ΔV without the need of using an IV converter. This ability to measure finite ΔV is obviously a clear advantage in doing finite load IMS in addition to achieving this at the cell's normal (optimum) working condition. Later in our work on IMS on organic photovoltaic (OPV), we also run IMS measurements with a variety of added external load capacitors C_L at the order of 1 nF that are placed parallel to R_L . We do this in order to determine a bulk heterojunction (BHJ) OPV capacitance (C_{BHJ}).

4.4 Development of The IMS Instrument Bespoke Software

From 4.2., we have also developed a bespoke, LabView-based IMS software which we use to operate and control our IMS instrument and measurements. This software takes advantage of our lock-in's own interface software, which is also based on LabView. We use the interface software to set all of the lock-in settings or in other words the frequency scan settings. For our bespoke software, we integrate this interface software into a routine to run and automate the frequency scan. The LabView-based bespoke software was made and designed by Krisna Adhitya, Department of Physics and Astronomy, The University of Sheffield, UK. Here, we first describe general lock-in operation as our instrument/setup is a lock-in based setup. We then proceed to describe the lock-in interface software, its (lock-in) settings and the selection of settings used in our measurements. We then elaborate on how the interface software is integrated into our overall software routine.

A lock-in amplifier works by first amplifying and digitalizing the total ΔV response (which has a ϕ component) from the characterized sample. This is then followed by splitting the response into two components, one is the amplified ΔV and the other is the voltage phase response ϕ . The lock-in will then multiply both components with both the original ref out voltage and the 90° -phase shifted ref out voltage. This stage is where the lock-in “picks out” the modulated voltage and phase response with respect to ref out voltage or V_{AC} frequency ω . After multiplication, the resulting voltage and phase is then low-pass filtered to eliminate any random noise/ finally yield a ΔV result, which is the amplitude of an AC voltage signal that has the same frequency as the LED modulation frequency, in addition to producing a phase response ϕ with respect to ref out voltage [36]. A snapshot of the interface software that we use to set the lock-in settings is depicted in Fig. 4-7, taken from Anfatec Instruments AG [134].

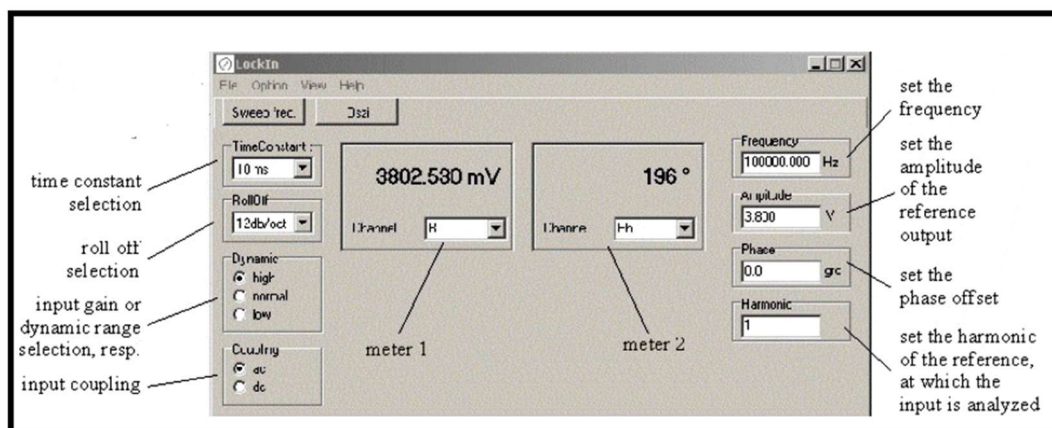


Fig. 4-7. A snapshot view of the lock-in's interface software menu page that shows the lock-in settings. These settings are; ref out voltage amplitude (in V_{rms}), input coupling, roll-off (in dB/oct), frequency f (in Hz), input gain, phase offset (in degrees) and reference harmonic [134].

In Fig. 4-7, we see that in the menu, there are 8 lock-in settings that have to be set to conduct a frequency scan [134]. These are the time constant (in ms), roll-off (in dB/oct), dynamic, coupling, frequency (in Hz), amplitude (in V_{rms}), phase (in degrees) and reference harmonic. The time constant setting is actually the lock-in's internal low-pass filter time constant. Note that the behavior of a low-pass filter can be represented by the Bode amplitude plot shown in Fig. 1-4 [36]. As such, its time constant can also be derived from such plot. Here, the time constant setting is the time taken to stabilize the ΔV output derived from the $V_{\text{signal}(in)}$ in Fig. 4-5(a) [36, 134]. This setting also corresponds to the filter's corner frequency f_c , i.e. $f_c = 1/\tau$, with τ being the filter's time constant. The time constant is set as high as possible at low scanning frequencies to allow as much time as possible for the ΔV output to stabilize at that frequency. This is because the ΔV output obtained at a low frequency is equivalent to the ΔV output obtained at a large time period in a time-based picture since $f = 1/T$ with f being the scanning frequency and T is the time period of that frequency [36, 134]. Therefore, at higher scanning frequencies, the time constant is set to lower values since the ΔV output will be obtained at a much smaller time period. While in a frequency-based picture, the filter's f_c is set to as small as possible value (i.e. large time constant τ) at low scanning frequencies to eliminate noises/fluctuations at higher frequencies, thus stabilizing the ΔV output at that frequency range. Whereas at higher frequencies, the filter's f_c is set to a large value (i.e. small τ) to stabilize the ΔV output. For our IMS on OPV experiments, we set the time constant to 5 s (the longest time available) at scanning frequency $f = 1-10$ Hz, 1 s at $f = 10-100$ Hz, 0.5 s at $f = 10-1000$ Hz, 0.1 s at $f = 1$ kHz-10 kHz and 0.05 s (the smallest time) at $f > 10$ kHz.

The next setting, the roll-off, is the lock-in's low-pass filter roll-off. Hence, the roll-off can also be derived from the Bode plot shown in Fig. 1-4. The roll-off settings allow us to control the low-pass filter attenuation slope immediately after the filter's corner frequency f_c [36, 134]. So the steeper the slope is, the better it will filter out noises after the f_c point. We typically set the roll-off to 24 dB/oct in our work to eliminate as much noise/fluctuations as possible. The next one, the dynamic setting, is used to set the response voltage input amplification once it is fed into the lock-in. So in this setting, a high dynamic setting means not amplifying the input or input x 1, while at a normal dynamic, the input is amplified by 10 times or input x 10, and finally, at a low dynamic, the input is amplified by 100 times, or input x 100. As this is related to coupling setting, and to understand the context of its use, we must discuss the coupling setting beforehand.

The coupling setting is the setting that allows us to process the response as a DC-coupled or an AC-coupled input. This means that a DC-coupled input will result in the processing of the entire response signal, including any DC parts, while the AC-coupled input will result in only the AC part being processed. Thus, if we use a DC coupling, we cannot amplify the voltage response because by

doing so we would exceed the instrument input limits. On the other hand, since in AC coupling, only the AC part is processed, we can obtain higher voltage response as we can pre-amplify the AC part of the signal. But with AC coupling we cannot perform a frequency scan at low frequencies since this coupling will discard the DC part/low-frequency parts. So ideally we set the coupling to AC and dynamic to low, in order to obtain the maximum signal response. However, for our IMS on OPV, we set the coupling to DC and dynamic to high (input x 1) since a DC input coupling will enable us to perform frequency scan in low frequencies which cannot be done in AC coupling. The next setting is the frequency or f setting, this is where we set the starting frequency for our IMS scan, and later in our routine, shows the frequency where the scan currently operates. We typically set our frequency scan to f values between 1 Hz and 250 kHz. After the f setting, the amplitude setting is where we set the ref out voltage/ V_{AC} amplitude that we use to modulate the LED. For all IMS on OPV, we set $V_{AC} = 0.5 V_p$. Following amplitude setting, the phase setting denotes any phase correction/offsets that need to be done after the phase response is produced. For our IMS on OPV, we set this to 0, as we do not need to correct the voltage phase response to any phase offsets/corrections. Finally, the harmonic settings designate the selection of ref out voltage harmonic that we use to evaluate the response voltage. For our IMS on OPV, we set this to 1, as we usually evaluate the response voltage at the 1st harmonic [134].

We then proceed to integrate and expanded the lock-in interface software in Fig. 4-7 into a longer routine so that we can automatically set and operate an IMS frequency scan at f between 1 Hz to 250 kHz. This routine is basically our bespoke software and it is called a virtual instrument (VI) in LabView. It consists of various LabView routine/functions, called a sub-VI, that needs to be used to operate the VI. In developing the software, we use a conventional sequential-stacking approach. Here, we first divide f between 1 Hz to 250 kHz into several frequency groups, with the groups varied from lowest to highest frequencies. The groups are also numbered with the lowest being the lowest frequency group, and so on to higher frequency groups. For all IMS characterizations in our work, the groups are, $f_1 = 1-10$ Hz, $f_2 = 10-100$ Hz, $f_3 = 10-1000$ Hz, $f_4 = 1-10$ kHz and $f_5 = 11-250$ kHz. The frequency groups are prepared in a Microsoft Excel tab-separated (spreadsheet) format which can be interfaced to the lock-in's software. For each group, we developed an individual VI to accommodate a different lock-in setting, i.e. different time constant setting for that particular group. The group frequency VI do this by using the interface software with selected lock-in settings to run a frequency scan and then process the response for that frequency group. A snapshot of our software menu page and the group frequency VI structure is depicted in Fig. 4-8(a) and (b) respectively.

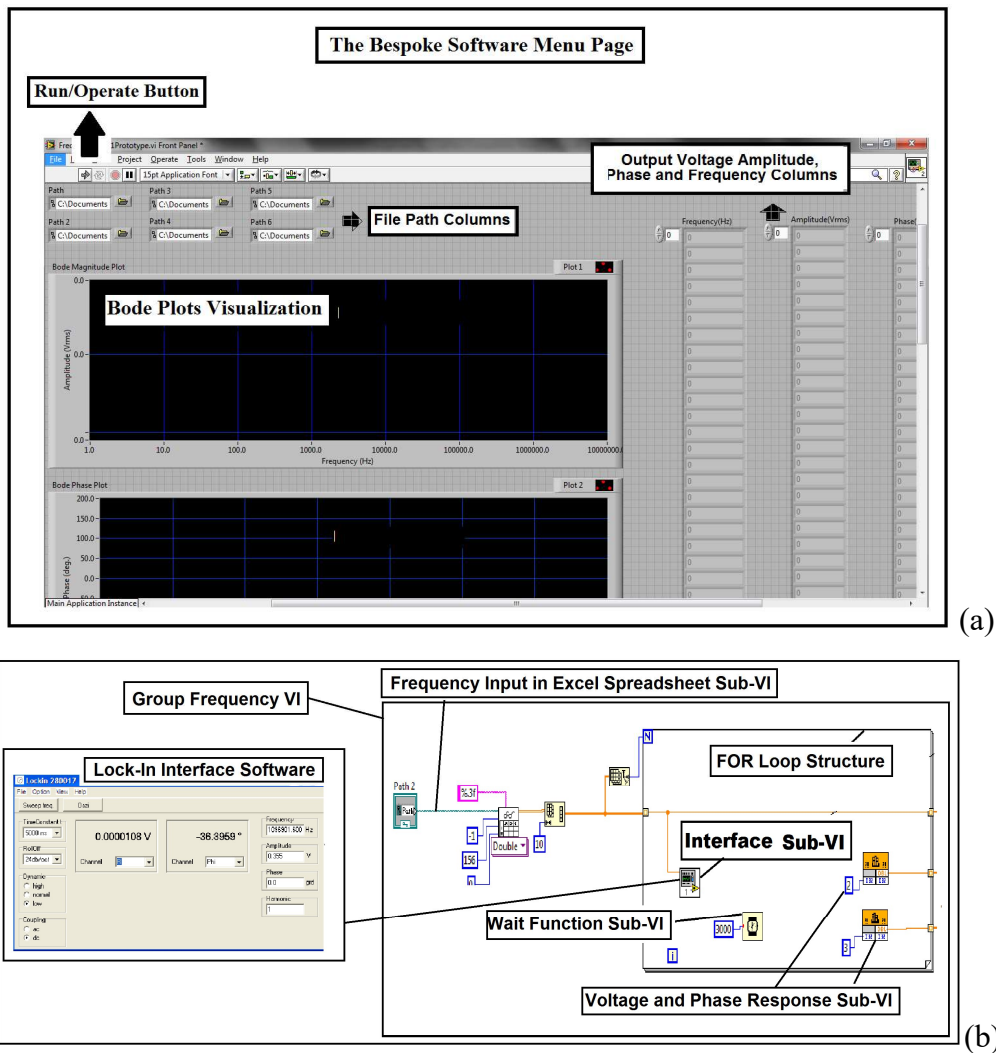


Fig. 4-8 (a). A snapshot of our frequency scan menu page. Depicted are the file path columns where we insert the frequency group’s spreadsheet, the response columns where we display the resulting voltage and phase response, and finally, the Bode plots visualization for the voltage response. (b) depicts the individual group frequency VI enclosed within a FOR loop structure which we use to build our software. Here, we can see the lock-in interface software which is used as a sub-VI in the routine, in addition to a spreadsheet frequency input sub-VI, voltage and phase response sub-VI and wait function sub-VI.

In Fig. 4-8(a), we can see in the software menu page, several file path columns in which we insert the frequency groups spreadsheets, the response columns where we display the voltage and phase response, and finally the Bode plots visualization for the voltage response. While in Fig. 4-8(b), we can see the group frequency VI that is enclosed within a FOR loop VI structure. The group VI structure in Fig. 4-8(b) operates as follows, first, the group VI will conduct the scan at a frequency f which is taken from the frequency input sub-VI. The lock-in sub-VI will then “pick-out” voltage and phase response with respect to modulating ref out voltage frequency ω and produce a voltage (amplitude) and phase response with the voltage and phase sub-VI. The scanning is then repeated for the next frequency in that group by a FOR loop structure. Hence, the number of group frequencies will be the FOR loop iteration number N . For example, if a group consists of 10 frequencies, then N

= 10, and so on. In addition, between each frequency scan, we also add a wait time sub-VI to add more time between each scan. This is to guard against random noise at each frequency in that group. After a group VI scan is finished our software will then move on to the next frequency group that we listed before. A flowchart diagram of how an individual group VI operates is depicted in Fig. 4-9.

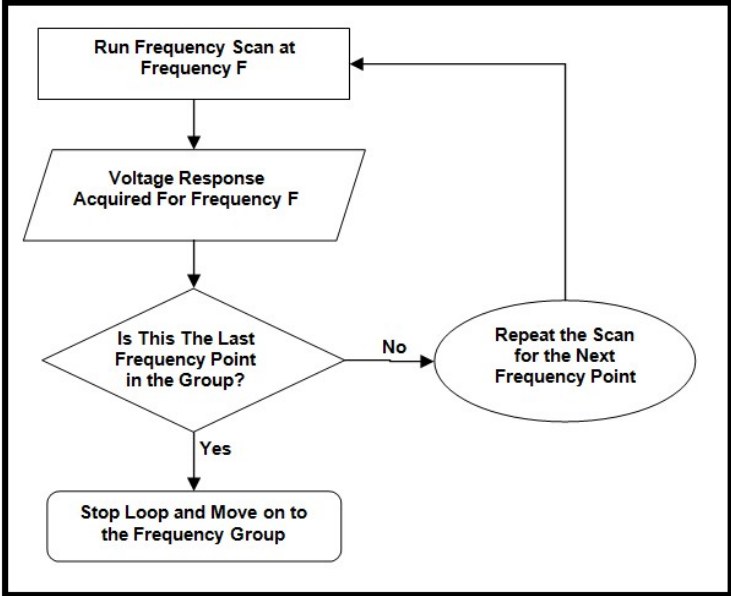


Fig. 4-9. A flowchart diagram that describes the frequency scan process in each frequency group VI.

In Fig. 4-9 diagram, we can see that the group VI will repeat the scan until the scan has been conducted at all frequencies in that group. After scan completion, the scan will then move on to the next group of frequencies and repeat the process in Fig. 4-9 for the new group. We then use a group frequency VI and integrate it with the other group frequencies VIs to form a sequential and accumulative processing VI, where the first group of frequencies will be scanned and after this is done, the scan will automatically move to the next frequency group while sending the previous group’s voltage and phase response to another sub-VI that will store and accumulate the results. This sub-VI will then plot a voltage and phase response in the form of Bode amplitude and phase plots only after all group frequencies have been scanned. Hence, through this expanded routine, we can obtain a Bode amplitude and phase plot for f between 1 Hz and 250 kHz. An overall depiction of our bespoke software/routine, including the scanning steps taken in the software, is depicted in Fig. 4-10.

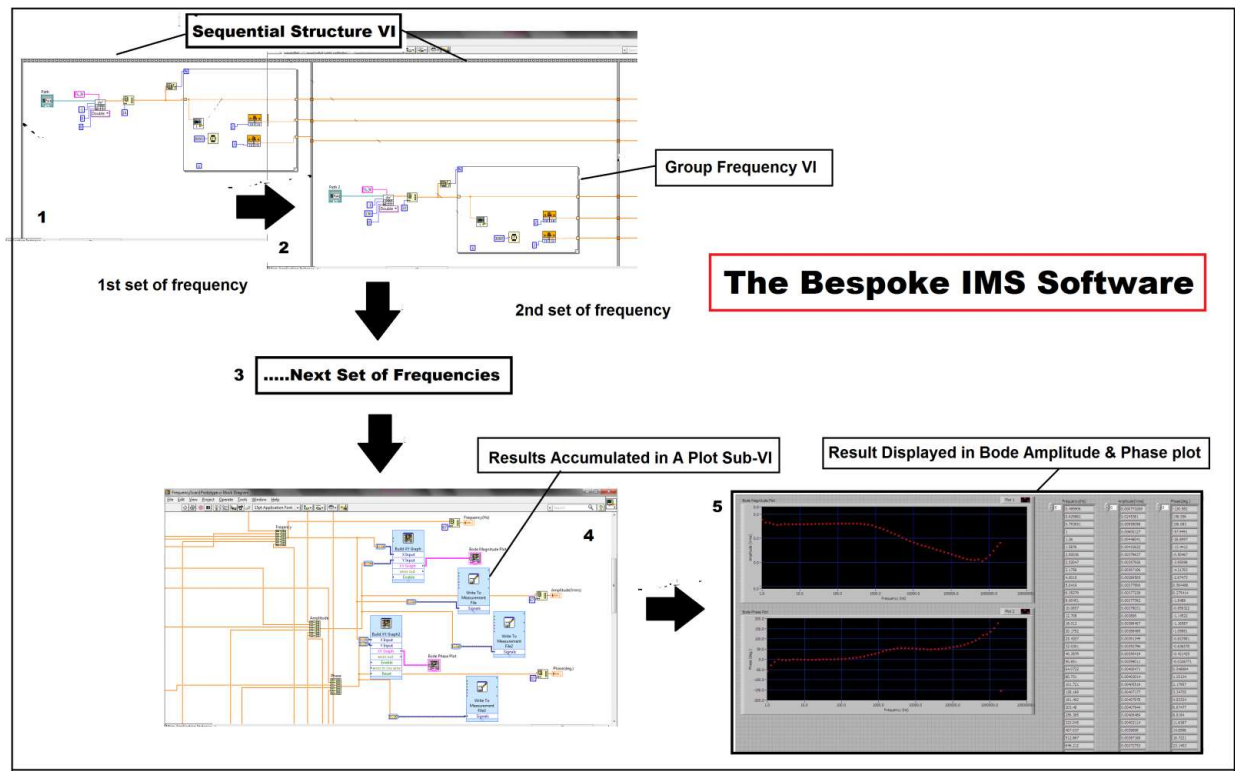


Fig. 4-10. An expanded view of our IMS software virtual instrument (VI), which depicts the software process flow, group frequency VIs, FOR loops and interface software together with the sequential structure that is used to build the software. The scanning process starts at (1), where we perform an IMS scan at the first frequency group by using that group VI. After the first group scan is finished, the results will be sent to a plot sub-VI which will then accumulate the results until all frequency groups have been completed. At (2), the sequential structure will continue the scan to the next group VI for the next frequency group. At (3), the scan will continue to the next group and so on, until all frequency groups have been scanned. Finally, at (4), the resulting voltage and phase is accumulated at the plot sub-VI and then at (5), the results are plotted and displayed in the menu page Bode amplitude and phase plots visualization.

From Fig. 4-10, in (1), after we set all the lock-in settings parameters, we perform the frequency scan at the first frequency group from our spreadsheet frequency data, which is followed by the acquisition of voltage and phase response from the first group. In (2), after the first group has been scanned, the sequential structure will automatically transition the scan to the next group to repeat the process. This is done while the structure sends the response from the previous scan to a plot sub-VI, which is to be accumulated with other frequency group data. After the second group scan is finished, the routine will continue on to the next frequency group (3) and conduct the same scan until all frequency groups have been exhausted. Note that at each group VI, a wait time sub-VI is used to make sure the voltage response does not fluctuate much at that frequency group. In addition, the wait time here is set much longer than each group's time constant setting. This is done so that there will be enough time available for the ΔV output to stabilize at each frequency/data point in each group. After all, groups have been scanned, the voltage and phase response at all frequencies were then accumulated (4) by a plot sub-VI and plotted into the Bode amplitude and phase plots displayed in the software menu page. Thus,

another advantage of using a lock-in-based IMS setup is that it offers us almost unlimited possibility in customizing our setup for any type of IMS measurements.

4.5 Intensity-Modulated Spectroscopy (IMS) Instrument Calibration

We have calibrated our IMS instrument setup that is depicted in Fig. 4-5(a). We do this by first replacing the solar cell in Fig. 4-5(a) setup with a fast and reverse-biased silicon photodiode (Centronic OSD5-5T, rise time $\tau = 9$ ns), with the photodiode reverse-bias voltage $V_{REV} = -13.2$ V [136]. We use the same setup, including the bespoke voltage adder and red LED in 4.2 to illuminate the photodiode, thus calibrating our setup with the photodiode. A depiction of our calibration setup is shown in Fig. 4-11.

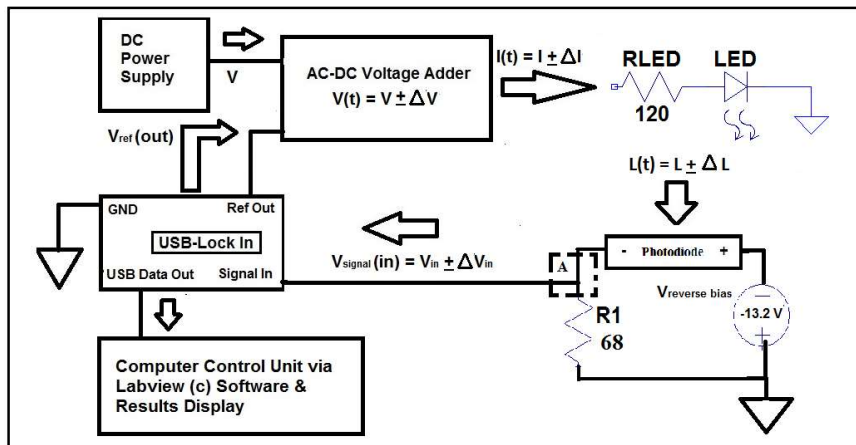


Fig. 4-11. A block diagram of the IMS calibration setup on the solar cell connections. The diagram along with other instrument setup is similar to 4.2, while also showing the -13.2 V reverse-biased silicon photodiode with voltage measurement at point A in-parallel with measurement resistance $R1 = 68 \Omega$.

In Fig. 4-11, we use a similar procedure as in 4.2. We use V_{AC} from the reference output voltage, and by using the same voltage adder, combine the V_{AC} with a larger bias voltage V from the adder's power supply. We use the modulated LED to illuminate the photodiode that is under a reverse bias voltage or $V_{REV} = -13.2$ V, and connected in-parallel with a load resistance $R1$, where $R1 = 68 \Omega$. We reverse-biased the photodiode as it will operate faster under a reverse-bias voltage in terms of its rise time τ [36]. For this photodiode, the maximum V_{REV} that we can apply is $V_{REV} = 15$ V. We proceed to use our IMS software to perform an automatic frequency scan by varying the lock-in's voltage modulation frequency ω to values between 1 Hz and 250 kHz in 12 steps per decade.

From the illumination, photocurrents response from the cell is then measured as a voltage drop $V + \Delta V(\omega) \sin(\omega t + \phi(\omega))$ at points A in parallel with $R1 = 68 \Omega$. The load resistance $R1$ function is to convert a photocurrent signal into a voltage at point A since the lock-in can only receive voltage input. The magnitude of resistance $R1$ is chosen to be 68Ω , so that the resistance will not be too high which

can then greatly reduce the photocurrents and the measured voltage signal at A but also not too small, so that the resulting photocurrents and the voltage signal at A can still be detected by the lock-in device. The $\Delta V(\omega)$ and $\varphi(\omega)$ response is a function of ω as we varied the modulation frequency ω . The cell's voltage response is then fed into the lock-in voltage measurement input, without IV converter. We then plot the amplitude $\Delta V(\omega)$ and phase $\varphi(\omega)$ response from the photodiode in a Bode amplitude and phase plot which are shown in Fig. 4-12(a) and (b) respectively.

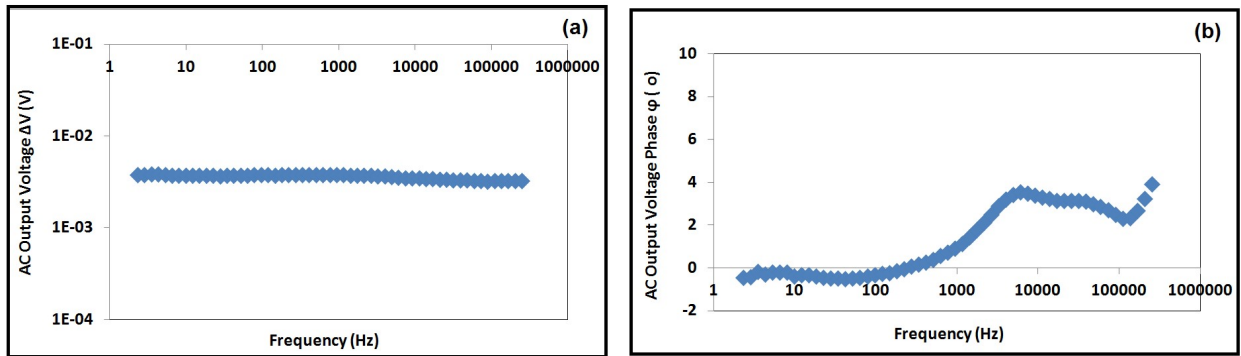


Fig. 4-12. Bode (a) amplitude, and (b) phase plots from an OSD5-5T photodiode under a red LED and reversed-bias at a reverse-bias voltage $V_{REV} = -13.2$ V. Here, the total LED drive current $I_{LED} = (18 \pm 10)$ mA.

From both Fig. 4-12(a) and (b), we observe that the setup, including the LED, does not add a significant phase to the fast photodiode. This is also evident from the amplitude plot since we cannot find any corner frequency f_c in the plot. With f_c being the frequency where ΔV amplitude from the photodiode starts to drop to its -3dB equivalent magnitude at phase $\varphi = 45^\circ$. While from Fig. 4-12(b), we observe that at the highest frequency, i.e. at 250 kHz, the ΔV phase is $\sim 4^\circ$, while from 2 to 100 Hz they are practically 0. There is indeed an incremental rise in phase starting from 100 Hz to 10 kHz, but these are very small, i.e. $\sim 1^\circ$ rise. Thus, because the photodiode is already very fast in terms of its rise time, any additional phase from the setup or the LED will add phase to the Bode plots in Fig. 4-12(a) and (b), which can then result in a noticeable drop in the photodiode ΔV amplitude at a certain frequency f or even f_c , and also higher phases in the Bode phase plot. In other words, the photodiode voltage and phase response serve as a baseline measurement for our IMS characterizations. Hence we can conclude that our IMS setup will not add a significant phase to our IMS measurements, with only 4° of the additional phase detected at the highest frequency (250 kHz) from calibration. To add, we can also conclude that the use of the ODS5-5T model is indeed suitable as a calibrating photodiode in our IMS work since its response will only add 4° phase at the highest frequency.

In addition, for photodiode-based measurements with the same setup, where we use the photodiode to characterized system response, we can easily use the calibrated photodiode ΔV

amplitude and phase to correct the measured system's ΔV amplitude and phase response. We can do this by dividing the real result with the photodiode's ΔV amplitude. While for phase, we can subtract the system's phase with the photodiode's output phase. Note that the corrections themselves can only be performed when both the system's response and the photodiodes measurement were taken under the same modulating light amplitude.

4.6 Development of A Bespoke IMS Instrument for IMS on Organic Light-Emitting Diode (OLED)

In addition to the bespoke IMS instrument in 4.2, we have also adapted and modified our IMS instrument for the purpose of IMS on an OLED. The modified IMS instrument that we have developed for IMS on OLEDs is basically the same as in Fig. 4-5(b), but here, the roles of IMS light source, and its light detector, are exchanged. Here, we use the OLED under test, rather than a fast inorganic LED, as the driven light source. On the other hand, we detect the modulated light emitted by the OLED with the same fast, reverse-biased Si photodiode (rise time $\tau = 9$ ns) in 4.5 rather than projecting it onto an experimental solar (i.e. organic photovoltaic) cell in 4.2. We then record the OLED's IMS spectrum as detected by the fast photodiode circuit. On a conceptual level, both the IMS instruments in Fig. 4-5(b) and the IMS setup for OLED can be seen as derivatives of the completely inorganic circuit that we used for the IMS instruments calibrations in 4.5. For the first IMS instrument in Fig. 4-5(b), we replace the fast, reverse biased Si-photodiode with an experimental OPV cell, while retaining the fast LED as light source. For the OLED IMS instrument, we retain the fast reverse biased Si photodiode but replace the fast red LED with an experimental OLED light source. However, the entirely inorganic 'parent' circuit serves no scientific purpose other than testing and correcting for unwanted artifacts. The instrument becomes a meaningful IMS spectrometer when either light source, or light detector, are replaced with an experimental sample rather than a fast inorganic stock component.

The modified instrument setup itself consists of an OLED sample as the light stimulus, a fast, reverse-biased OSD5-5T photodiode as the OLED light detector, a digital Anfatec USB 250 Lock-In amplifier that modulates the OLED intensity, a bespoke voltage adder based on fast 2N2369 and BC547C NPN transistors (rise time $\tau = 6$ and 3.3 ns respectively) that drive/modulate the OLED, an IV converter based on LM6171 op-amp with feedback resistor (R_f) and capacitor (C_f) of 4.7 k Ω and 4.7 pF respectively, and finally a PC with a modified version of the software in 4.4 to operate the frequency scan. The bespoke voltage adder is a modified version of the circuit in Fig 4-5(b). The modified voltage adder was also designed and built by Prof. Richard Tozer, from the Department of

Electronic and Electrical Engineering at The University of Sheffield, UK. The IMS instrument setup and the bespoke voltage adder are depicted in Fig. 4-13(a) and (b) respectively.

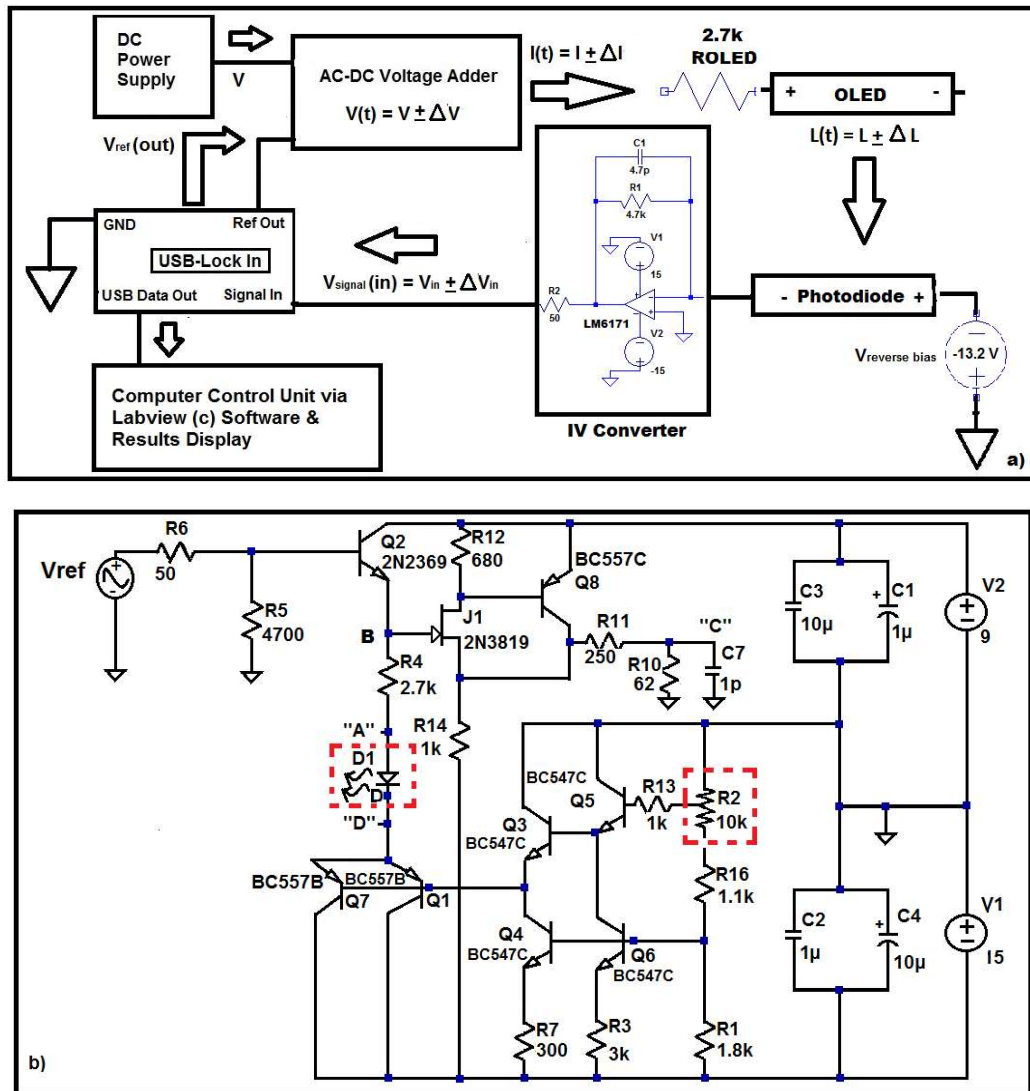


Fig. 4-13 (a). A block diagram of our IMS measurement setup, showing the PC running LabView software which controls the USB lock-in, a circuit driving the OLED by adding a DC offset voltage to the AC modulation voltage from the ref out, the OSD5-5T photodiode connected to an LM6171 op-amp with feedback resistor (R_f) = 4.7 k Ω and capacitor (C_f) = 4.7 pF, and the photodiode's current converted into voltage at the op-amp's output. This voltage is then fed into the lock-in's measurement input. (b) A circuit schematic of a modified DC + AC adder circuit in 4.2. which adds a DC bias to the AC ref out to drive the OLED. The lock-in ref out is represented by a voltage source, top left. DC voltage supply is a 9 V and 15 V DC power supply stabilized by capacitors (right). The level of DC bias is set by a 10 k Ω potentiometer (highlighted). The OLED (DI) is also highlighted. As a performance test of the DC + AC adder, we fed the DC + AC signal directly into the lock-in measurement input, and found no measurable drop in AC amplitude, and less than 1 $^\circ$ of added phase, up to 250 kHz.

In Fig. 4-13(a), we use V_{AC} from the reference out voltage, and with the modified bespoke voltage adder, we combine the lock-in's V_{AC} with a larger DC bias voltage V from the modified adder's 9 V and 15 V power supply. We then set V_{AC} amplitude by using a modified version of the software in 4.4 and also set the lock-in's input coupling to DC, roll-off to 24 dB/oct, dynamic to high, phase

offset to 0 and the reference harmonic to 1. The time constants are set to 5 s at scanning frequency $f = 1-10$ Hz, 1 s at $f = 10-100$ Hz, 0.5 s at $f = 10-1000$ Hz, 0.1 s at $f = 1$ kHz-10 kHz and 0.05 s at $f > 10$ kHz. As in 4.4, the time constant is set as high as possible at low frequencies and gradually reduced at higher frequencies to allow more time for the ΔV output to stabilize and to eliminate any possible noise/fluctuations. The roll-off is also set to 24 dB/oct with the same reasoning mentioned in 4.4, i.e. to eliminate as much noise/fluctuations as possible. The coupling is set to DC and dynamic to high (input x 1) since a DC input coupling will enable us to perform frequency scans at low frequencies that cannot be done in AC coupling. The frequency setting is where we set the start frequency for our scan, and later shows the frequency where the scan currently operates. The amplitude setting is where we set the ref out voltage/ V_{AC} amplitude that we use to modulate the OLED. The phase setting is set to 0, as we don't need to correct the voltage phase response to any phase offsets. Finally, the harmonic setting is set to 1, as we usually evaluate the response voltage 1st harmonic. We then use the adder to apply $V_{OLED} = (V_{DC} \pm V_{AC})$ V on the OLED with $R_{OLED} = R4 = 2.7$ k Ω so that the adder will modulate the OLED with $I_{OLED} = (I_{DC} \pm I_{AC})$ mA. The V_{OLED} and I_{OLED} will be given in the results chapter since we apply different V_{OLED} and I_{OLED} in IMS on OLED measurements. In addition, we also varied the input coupling and dynamic in one of the IMS on OLED measurement in this work.

The OLED will then produce a light intensity $L_T = L + \Delta L \sin \omega t$. We use the modulated OLED to illuminate a photodiode (same as 4.5) under a reverse bias voltage = -13.2 V. We then use the modified IMS software to perform an automatic frequency scan by varying the lock-in's voltage modulation frequency ω to values between 1 Hz and 250 kHz in 18 steps per decade. Here, a total of 90 frequency points, or data points were taken between 1 Hz and 250 kHz, with $\omega = 2\pi f$. From OLED illumination, the photodiode will then produce a current in the form of $I_{PD} = I_{PD-DC} + \Delta I_{PD}(\omega) \sin(\omega t + \phi(\omega))$. This photocurrent is then fed into an IV converter based on an LM6171 op-amp with $R_f = 4.7$ k Ω and $C_f = 4.7$ pF. The IV converter here is used to convert photocurrents to voltage in our OLED measurements. This is because the lock-in can only receive a voltage input. In addition, by using an IV converter, we eliminate the need to choose a specific load resistance similar to the setups in Fig. 4-5(a) and 4-11. Note that changing R_f and C_f in an op-amp will only change the op-amp's gain factor, but the change itself will not add phase or decrease the input signal. The IV circuit then converts the photodiode current (I_{PD}) into a voltage (V_{out}) and amplify the resulting voltage through $I_{PD} = V_{out}/R_f$. This voltage (V_{out}) is related to the OLED illumination via the photodiode. The V_{out} is given by $V_{out} = V + \Delta V(\omega) \sin(\omega t - \phi(\omega))$, which consists of $\Delta V(\omega)$ and phase $\phi(\omega)$ as a function of ω . Note that the phase response here is negative as we earlier fed the current to the op-amp inverting input. The V_{out} is then fed into the lock-in voltage input. The lock-in will then measure and "pick out" the $\Delta V(\omega)$ by comparing it with the lock-in's ref out voltage frequency ω . As a result, we obtain the

amplitude $\Delta V(\omega)$ and phase $\varphi(\omega)$ of V_{out} and record these parameters as a function of $f = \omega/2\pi$. Later the amplitude $\Delta V(\omega)$ and phase $\varphi(\omega)$ can be plotted as a Bode and Nyquist plot as seen in 1.4.

In Fig. 4-13(b), the new bespoke adder circuit consists of two main parts, one is an AC part, which modulates the OLED with the lock-in's ref out voltage, and represented by the AC voltage source and $Q2$ transistor. While the other is the DC part, that provides a DC bias current to the OLED represented by $Q1$, $Q3$, $Q4$, $Q5$, $Q6$, $Q7$ and one 15 V battery from the circuit's power supplies. So we first apply an AC voltage to the circuit as represented by the AC voltage source in Fig. 4-13(b). In the adder's input, $R6 = 50 \Omega$ is placed in-parallel with $R5 = 4.7 \text{ k}\Omega$ so that we can load the AC voltage branch with $R_T = 50 \Omega$. The purpose of R_T is to produce an AC current I_{BE} (in mA) that will drive/modulate the $Q2$ transistor base with respect to the emitter. The I_{BE} was obtained from $I_{BE} = V_{AC}/R_T$, and $V_{AC} = V_{BE}$ (in V_p), with V_{BE} the applied voltage on $Q2$ base with respect to its emitter. Since we applied an AC voltage or V_{BE} on $Q2$ base, we will also apply this modulation to the node at point B, thus modulating the OLED through $R4$. Hence, the AC modulation current I_{AC} (in mA_p) can be determined from $I_{AC} = V_{BE}/R4$, with $V_{AC} = V_{BE}$. In OLED devices, we also have to account for the OLED's differential resistance R_{diff} in determining I_{AC} , so I_{AC} will then become $I_{AC} = V_{AC}/(R4+R_{diff})$.

For the circuit's DC part, we use the -15 V connection from the supply to add the OLED's DC bias, Thus, the voltage across $R16$, $R2$ potentiometer and $R1 = -15 \text{ V}$. Note also, that the 1 and 10 μF electrolytic and ceramic capacitor pair are connected in-parallel with the power supply to stabilize it at high frequency. Transistors $Q1$, $Q3$, $Q4$, $Q5$, $Q6$, $Q7$ will operate in the same way as the DC transistors in Fig. 4-5(b). However, here we use $R2$ potentiometer = 10 $\text{k}\Omega$ (highlighted in Fig. 4-13(b)) to set $Q5$ V_{BE} and drive it with a base current I_{BE} through $R13 = 1 \text{ k}\Omega$. The $R2$ is used to tune the OLED's DC bias level just like R_{poti} in Fig. 4-5(b). So once we set the V_{BE} on $Q5$, the Darlington pair connection between $Q5$ and $Q3$ will also result in a current gain I_{BE} that will drive the $Q1$ and $Q7$ BC557B PNP transistors. The Darlington is used since $Q1$ and $Q7$ will drive the OLED bias current, hence the need for emitter current I_E from $Q1$ and $Q7$ to be stable at high frequencies. Also, here we use -15 V supply to set a -15 V voltage across $R1$, $R16$, and $R2$. To add, we use a voltage divider setup between $R16$ and $R1$ to apply a base voltage V_{BE} on $Q4$ and $Q6$. The $Q4$ and $Q6$ transistors are also needed to define both $Q3$ and $Q5$ collector currents and their emitter resistances. So now, the $Q1$ and $Q7$ will drive the OLED with a bias current in combination with the modulated current that runs through $R4$. The input voltage applied on the OLED can be measured by measuring the voltage V_E at $Q1$ emitter with respect to ground. While the OLED DC bias voltage V_{DC} can be measured from $V_{DC} = (V_E \text{ at } Q1) - (V_A)$, with V_A the voltage measured at point A in Fig. 4-13(b) circuit with respect to ground. Finally, the OLED bias current I can be determined from $I = V_{R4}/R4$, with $V_{R4} = V_D - V_A$. Here, V_D and V_A are respectively the voltage at points D and A of Fig. 4-13(b) circuit with respect to

ground. To add, we also placed $J1$ 2N3819 JFET parallel to $R4$, with the JFET under a Darlington connection with a $Q8$ BC557C PNP transistor. We placed $J1$ and $Q8$ in the circuit to aid us in monitoring the ref out the voltage and OLED modulation in B from point C. Since doing so directly at B may interfere with OLED modulation. To add, a small capacitance $C7 = 1$ pF is added in-parallel to $R10$ to reduce any parasitic capacitances that can occur at monitoring point C with respect to ground. Also, because we fed the photodiode current into the IV converter inverting input, we will then produce an 180° inverted AC voltage component phase $\phi(\omega)$ from the converter. To account for this in our final voltage and phase results, we modify our IMS software in 4.4 by adding a phase correction algorithm in each of our group frequency VI. This is done by using a formula sub-VI as depicted in Fig. 4-14. The algorithm basically subtracts the resulting phase ϕ with 180° if $\phi \sim 180^\circ$ or lower, and adds 180° to the phase if $\phi \sim -180^\circ$ or higher. The software modification was done by Krisna Adhitya, Department of Physics and Astronomy, The University of Sheffield, UK.

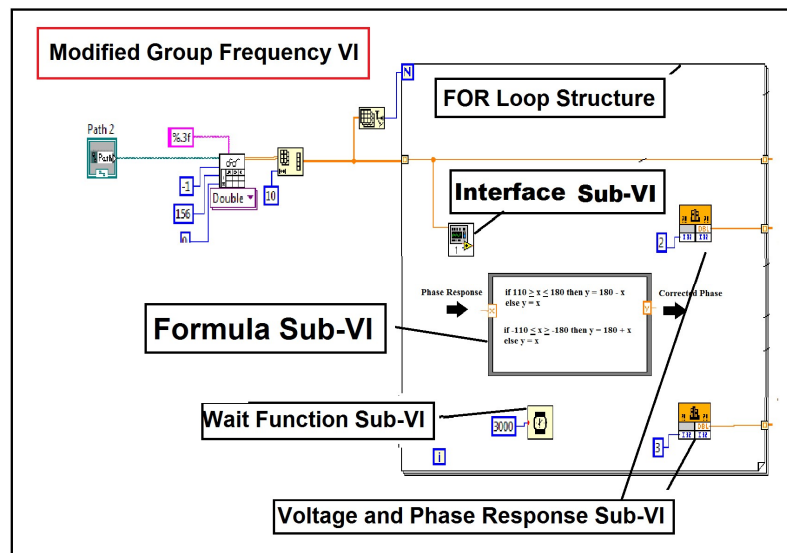


Fig. 4-14. A view of our IMS software modification which employs a formula sub-VI in each group VI, to account for the phase inversion from the IV converter. The formula sub-VI is integrated into the FOR loop structure with its operation limited by the loop iteration number. Note here that the formula sub-VI input and output connection is not connected to the group VI, in practice, the formula input (x) is connected to the phase response sub-VI and its output (y) is connected to the outside of the group VI towards the plotting VI.

In Fig. 4-14, the formula sub-VI is integrated into each group frequency VI, with the remaining group VI unmodified. Here, the formula sub-VI is not connected to anything for illustration purposes. In practice, the formula sub-VI input (x) is connected to the phase response result so we can offset the inverting effect from the converter. While the formula output (y), produced a corrected phase output and is connected to outside towards the final plotting VI. Overall, the bespoke software VI structure remains the same, including its operation and with the lock-in settings that have been described before.

In addition, we have also calibrated Fig. 4-13(a) setup by illuminating the photodiode with the fast red LED and bespoke voltage adder from 4.2. For the calibration, the photodiode is set with a similar setup as in Fig. 4-13(a). Thus, the photodiode is calibrated under a $V_{REV} = -13.2$ V and connected to the LM6171 op-amp with $R_f = 4.7$ k Ω and $C_f = 4.7$ pF. We found that the resulting voltage phase φ from the setup = 5.6° at 250 kHz with respect to the reference output voltage. Hence, the setup in Fig. 4-13 does not add significant phase to the measured signal. To add, we can also use this calibration result as a baseline measurement. So real system results from this setup can be corrected with the setup calibration results. Also, the LM6171 op-amp with the previous R_f and C_f will theoretically give us an RC time constant or $\tau_{RC} = R_f C_f = 22$ ns, which corresponds to a corner frequency $f_c = 45$ MHz from $\tau_{RC} = 2\pi/\omega = 1/f_c$. This means that the op-amp maximum frequency bandwidth (at 45 MHz) is much higher than the maximum scanning frequency at 250 kHz, thus making our IMS frequency range well within the op-amp (frequency) bandwidth [137].

4.7 Intensity-Modulated Spectroscopy (IMS) Instrument Setup for Light-Dependent Resistor (LDR) Characterization

In addition to IMS on organic semiconductor devices, we can also adapt our instrument to characterize a light-dependent resistor (LDR), i.e. a commercial cadmium sulfide (CdS)-based LDR. For IMS on LDR, we use the same setup as in Fig. 4-13(a) but by using a green LED as the IMS source and the bespoke voltage adder in Fig. 4-5(b). The green LED is used since a commercial LDR is typically made from cadmium sulfide (CdS) which has a band gap (E_g) of 2.42, thus corresponding to the region of green wavelength (512 nm) [138]. Here, we use a green LED (peak wavelength $\lambda_p = 516$ nm) model HLMP-CM3A-Z10DD, from Avago Technologies [138]. The green LED rise time is not known but it is slower than the fast red LED in 4.2. The evidence for this is from the green LED calibration results, which we perform by using the LED to illuminate the fast photodiode in 4.5 with the LDR setup. We found that the photodiode's resulting voltage phase under green LED with respect to the lock-in ref out voltage, i.e. $\varphi = 8^\circ$ at a frequency (f) = 250 kHz, which is the highest scanning frequency. This phase is 4° higher than the red LED phase calibration results in 4.5 at the same frequency. The reason for this is due to the different design parameters of the LED, which is optimized for green emission instead of red [139]. The IV converter here is used to convert the modulated current into a voltage signal since the lock-in can only receive voltage input. Also, the IV converter uses $R_f = 1$ k Ω and $C_f = 4.7$ pF. The commercial, CdS-based LDR that is characterized here is an NSL-19M51 Silonex from Farnell UK, Ltd. The LDR is sensitive to a peak spectral wavelength = 550 nm and has a rise time $\tau_r = 45$ ms. We also apply a DC Voltage (V_{bias}) to the LDR so that we can measure modulated currents flowing through the LDR due to the change in the LDR's resistance from

modulated light. Note that current flowing in the LDR is not a photocurrent, but it comes from the applied V_{bias} on the LDR. We apply and change the V_{bias} from $V_{bias} = 1, 1.5, 2, 2.5$ and 3 V. An illustration of the IMS on LDR setup and the modified bespoke voltage adder circuit in 4.2 is depicted in Fig. 4-15(a) and (b).

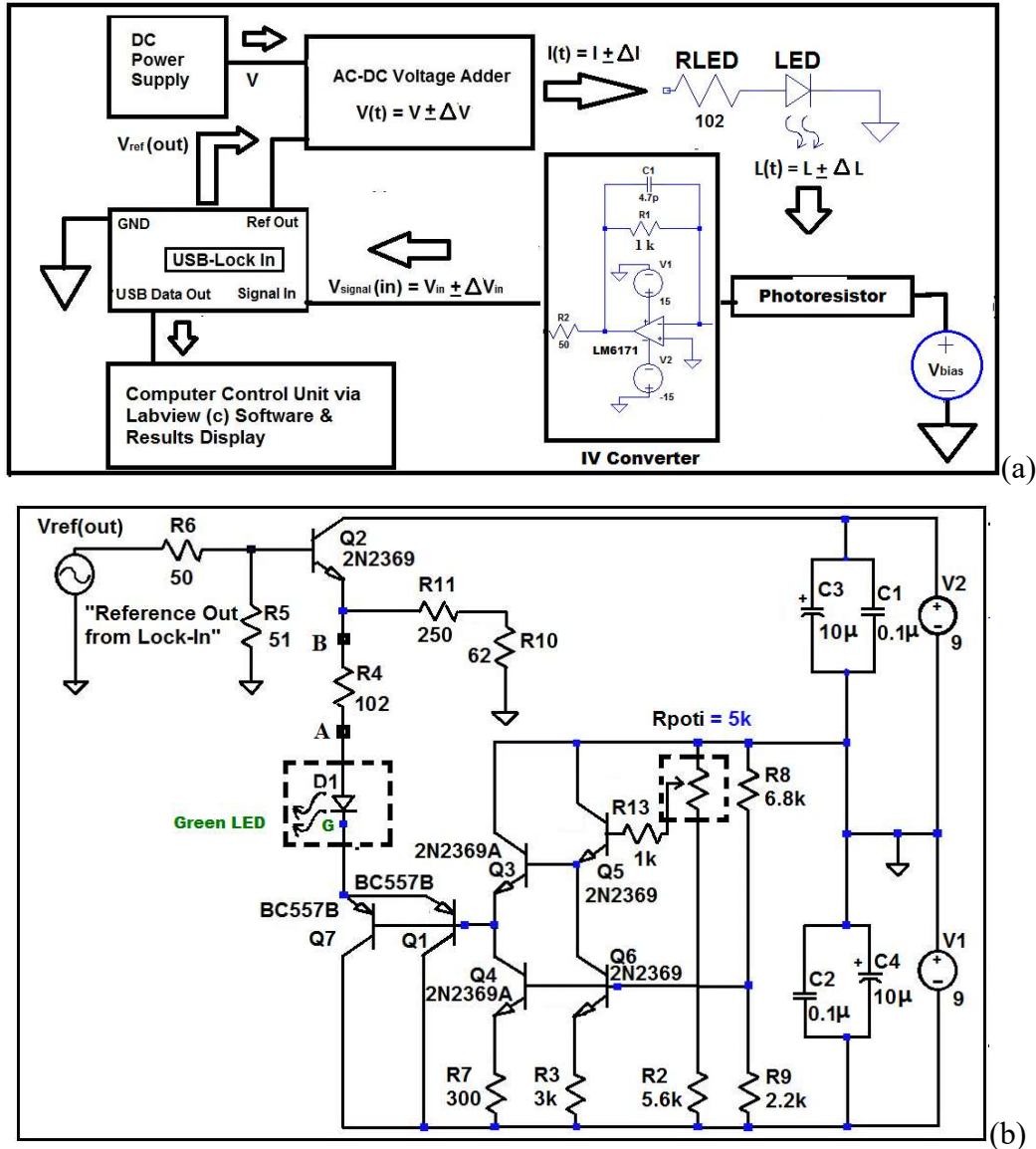


Fig. 4-15 (a). A block diagram of the IMS measurement setup for the CdS-based LDR, shown here are all the same IMS components we see in Fig. 4.6, with the difference that we now use a green LED to do the IMS, and that the LDR is in place of the photodiode in Fig. 4.6. In addition, we also apply a different voltage bias or $V_{bias} = 1, 1.5, 2, 2.5$ and 3 V on the LDR to measure current flow due to V_{bias} . To add, the R_f used in the IV circuit is also different with $R_f = 1$ k Ω . (b). Circuit scheme of modified DC + AC adder circuit used for IMS on LDR. The circuit is the same as those in 4.2, but here we replace the fast red LED with a green LED and the LED resistor $R_{LED} = R4 = 102 \Omega$.

In Fig. 4-15(a), we use V_{AC} from the lock-in's reference output voltage and with the voltage adder from 4.2, combine the V_{AC} with a larger DC bias voltage V from the adder's ± 9 V supply. We then set V_{AC} amplitude by using a modified version of the bespoke software in 4.4. We use the modified version because we will later need to correct the phase results since we fed the resulting signal to an

IV converter inverting input. We then set the lock-in's input coupling to DC, roll-off to 24 dB/oct, dynamic to high, phase offset to 0 and the reference harmonic to 1. The time constants are also set to 5 s at scanning frequency $f = 1\text{-}10$ Hz, 1 s at $f = 10\text{-}100$ Hz, 0.5 s at $f = 10\text{-}1000$ Hz, 0.1 s at $f = 1\text{ kHz}\text{-}10\text{ kHz}$ and 0.05 s at $f > 10$ kHz. As in 4.4, the time constant is set as high as possible at low frequencies and as low as possible at higher frequencies to allow more time for the ΔV output to stabilize and also to eliminate any possible noise. The roll-off is also set to 24 dB/oct with the same reasoning mentioned as in the roll-off setting in 4.4, i.e. to eliminate as much noise/fluctuations as possible. The coupling is set to DC and dynamic to high (input x 1) since a DC coupling will enable us to perform frequency scan in low frequencies that cannot be done under AC coupling. The frequency setting is where we set the starting frequency for our scan, and later shows the frequency where the scan currently operates. The amplitude setting is where we set the ref out voltage amplitude to modulate the green LED. The phase setting is set to 0, as we don't need to correct the voltage phase response to any phase offsets. Finally, the harmonic setting is set to 1, as we usually evaluate the response voltage 1st harmonic.

We then use the voltage adder to apply $V_{LED} = (2.9 \pm 0.9)$ V to the green LED with $R_{LED} = R4 = 102 \Omega$ so that the adder will modulate the LED with $I_{LED} = (19 \pm 9)$ mA. The LED will then produce a light intensity of $L_T = L + \Delta L \sin \omega t$. Here, $L_T \sim I_{LED}$, and $\Delta L/L = \Delta I/I$. We then use the modulated green LED to illuminate the LDR under applied V_{bias} . The LED will then modulate the LDR resistance, and as a result, modulate the current flowing through the LDR. We then use the modified IMS software to perform a frequency scan by varying the lock-in's voltage modulation frequency ω to values between 1 Hz and 250 kHz in 18 steps per decade. Here, a total of 90 frequency points were taken between 1 Hz and 250 kHz, with $\omega = 2\pi f$. The resulting current will be $I = I + \Delta I \sin \omega t$ and we then feed this current into an *IV* converter with $R_f = 1\text{ k}\Omega$ and $C_f = 4.7\text{ pF}$. This current (I) will then be converted and amplified by the *IV* converter into a voltage (V_{out}) through $I = V_{out}/R_f$. Here, I is the resulting current and V_{out} is the converted voltage from the *IV* converter. This voltage (V_{out}) is related to the green LED illumination via the LDR resistance modulation. The V_{out} is given by $V_{out} = V + \Delta V(\omega) \sin(\omega t - \varphi(\omega))$, which consists of $\Delta V(\omega)$ and phase $\varphi(\omega)$ as a function of ω . Here, the phase is negative since we feed the current from the LDR to the op-amp inverting input. This V_{out} is then fed into the lock-in voltage input. The lock-in will measure and "pick out" the modulated voltage component by comparing it with the lock-in's ref out voltage frequency ω . As a result, we obtained the amplitude $\Delta V(\omega)$ and phase $\varphi(\omega)$ of V_{out} and record these parameters as a function of $f = \omega/2\pi$. We then repeat the process for $V_{bias} = 1, 1.5, 2, 2.5$ and 3 V. The amplitude $\Delta V(\omega)$ and phase $\varphi(\omega)$ can then be plotted as a Bode and Nyquist plot as seen in 1.4. In Fig. 4-15(b), we can also see that the

$R4$ resistor has now changed to 102Ω and the D1 LED is now a green LED, otherwise, the remaining parts of the circuit are similar to Fig. 4-5(b).

In addition, we have also calibrated the Fig. 4-15(a) setup by using it to illuminate the fast photodiode from 4.5. For the calibration, the photodiode is under a reverse bias voltage $V_{REV} = -13.2$ V which replace the LDR- V_{bias} connection in Fig. 4-15(a). We apply the same V_{LED} on the green LED and also drive it with the same I_{LED} as before. The photocurrents response (I_{PD}) from the photodiode, where $I_{PD} = I_{PD-DC} + \Delta I_{PD} \sin \omega t$ is then fed into the same IV converter with $R_f = 1 \text{ k}\Omega$ and $C_f = 4.7 \text{ pF}$. The IV converts the photocurrent into a voltage and amplifies the resulting voltage through $I_{PD} = V_{out}/R_f$. The total voltage becomes $V_{out} = V + \Delta V(\omega) \sin(\omega t + \varphi(\omega))$, and this is channeled into the lock-in input. From the lock-in, we then obtain the amplitude $\Delta V(\omega)$ and phase $\varphi(\omega)$ from V_{out} and record these as a function of $f = \omega/2\pi$. The amplitude $\Delta V(\omega)$ and phase $\varphi(\omega)$ from V_{out} were then plotted in a Bode amplitude and phase plot with respect to frequency ω and are shown in Fig. 4-16(a) and (b) respectively.

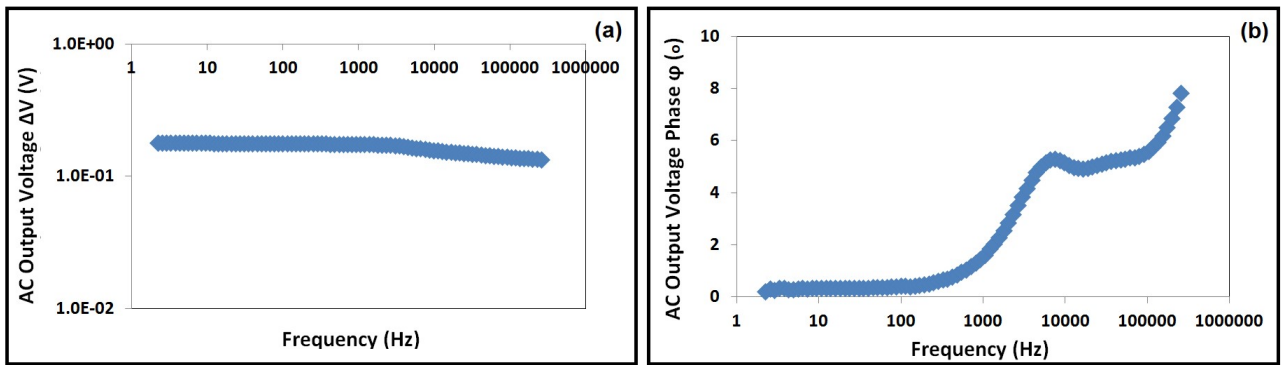


Fig. 4-16 (a). Bode amplitude, and (b) phase plots from OSD5-5T photodiode under green LED and at a reverse-bias voltage $V_{REV} = -13.2$ V. Here, the green LED drive current or $I_{LED} = (19 \pm 9)$ mA.

In Fig. 4-16(a), we see that there is no corner frequency f_c detected between 1 Hz and 250 kHz. However, we also notice a slight ΔV amplitude “fall” at frequency $f \sim 1$ kHz in Fig. 4-16(a). In addition, from the phase plot in Fig. 4-16(b), as mentioned earlier, the phase is $\sim 8^\circ$ at $f = 250$ kHz, which is a rise of 4° compared to φ at $f = 250$ kHz under red LED in 4.5. Also in Fig. 4-16(b), there is an incremental rise in phase, with the rise $\sim 1^\circ$, starting from 100 Hz to 10 kHz similar to the incremental rise in voltage φ under red LED in Fig. 4-12(b). Hence, we conclude that since the calibration of the fast photodiode in 4.5 and the IV converter-based setup in 4.6 will only add respectively as much as 4° and 5.6° in voltage phase, the rise in phase must be caused by a slower LED modulation, or in other words, the green LED is not as fast as the red ones. However, the total voltage phase from the calibration is still small $\sim 8^\circ$, and we can correct this phase addition with the method described in 4.5.

4.8 Intensity-Modulated Spectroscopy (IMS) Instrument Setup for Alkaline Battery Characterization

In addition to IMS on OPV and OLED, another potential use of our instrument/setup are that we can adapt our instrument to conduct IMS on a commercial 1.5 V alkaline battery. We conducted this through load modulation of the 1.5 V battery. So in a load modulation IMS, we take the advantage of using the same fast photodiode (OSD5-5T) in 4.5. and use it as a fast photosensitive device that modulates the battery voltage and load resistance with the setup depicted in Fig. 4-17. In the setup, besides the photodiode, we simply use the IMS instrument from 4.2., a 1.5 V AA-size, Panasonic alkaline battery model LR6APB and a load resistance $R_L = 53 \Omega$.

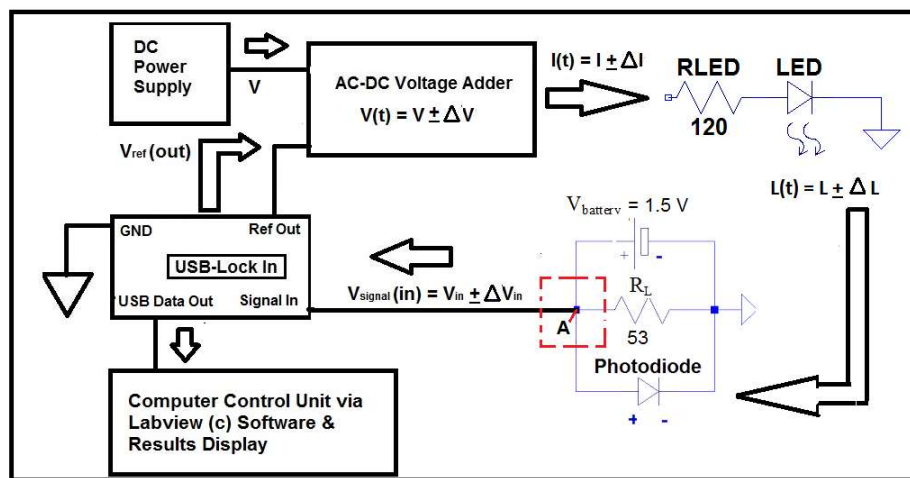


Fig. 4-17. A block diagram of the IMS measurement setup for an alkaline battery load modulation, shown here are all the same IMS components we see in 4.2., but the difference being is that we now have a load modulation circuit, where illumination of the photodiode will modulate the measured voltage in the load branch. This load modulation is measured from point A (highlighted in red) and it lies in the parallel connection between the photodiode, battery and load resistance.

In Fig. 4-17, we have integrated the IMS instrument/setup in 4.2. into a load modulation setup. We have used the fast red LED and the voltage adder in 4.2., with the battery itself, connected in parallel with the OSD5-5T photodiode in 4.5 and a load resistance (R_L) of 53Ω . In the Fig. 4-17 setup, we use the bespoke voltage adder in 4.2. to add a DC voltage (V_{DC}) on top of a small AC voltage (V_{AC}) from the lock-in's ref out voltage, and apply the resultant (DC + AC) voltage to the fast red LED (V_{LED}) in 4.2. with $V_{LED} = (2.2 \pm 1.2) \text{ V}$. The V_{LED} is applied to the red LED with a protective serial resistance (R_{LED}) of 120Ω , thus driving the LED with a current $I_{LED} = (18 \pm 10) \text{ mA}$. The I_{LED} will produce a modulated light intensity (L_T) of $L_T = L \pm \Delta L$. The intensity is not known in absolute terms but $L_T \sim I_{LED}$, so $\Delta L/L = \Delta I/I$.

We then use the red LED with modulated intensity L_T to illuminate the DI photodiode in Fig. 4-17, thus causing the photocurrent from the fast photodiode to modulate the voltage measured at the highlighted point A in Fig. 4-17. In addition, because the illuminated photodiode is also under a

forward bias of the battery voltage ($V_{battery} = 1.5 \text{ V}$), currents from the battery at point A will offset/balance currents flowing out of the photodiode. If the photodiode's current is at the modulation maximum, battery currents will offset the photodiode's current, but if the photodiode current is at its minimum, battery currents will not flow into the photodiode but instead through the load resistance R_L . In other words, at point A we will measure/obtain a load modulation signal in the form of $V + \Delta V(\omega) \sin(\omega t + \varphi(\omega))$. This is what we basically measure in a load modulation IMS, i.e. ΔV at point A because the battery discharges and this discharge is modulated by photocurrents from the photodiode.

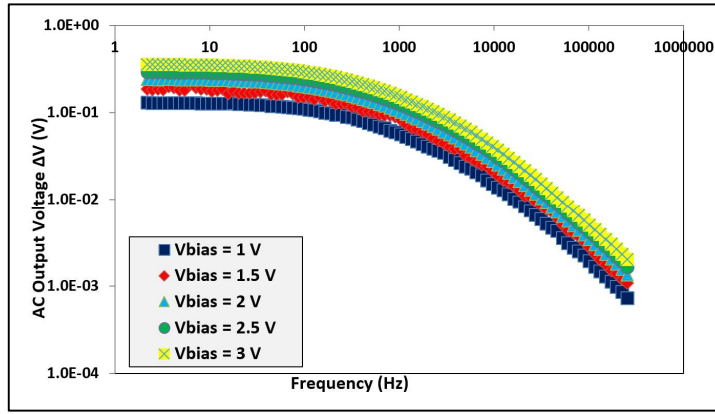
We use the IMS bespoke software in 4.4. to automatically operate a frequency scan by varying the lock-in's reference out voltage or the LED V_{AC} frequency f to values between 1 Hz and 250 kHz in 12 steps per decade of measurement. The software settings used were the same as those in 4.4, i.e. the lock-in's input coupling is set to DC, the roll-off is set to 24 dB/oct, the dynamic is set to high, phase offset to 0 and the reference harmonic to 1. The reasons behind the selected settings are also the same as in 4.4. We then channel the modulated voltage that we obtain at A into the lock-in input. The lock-in will measure the modulated voltage and phase from point A with respect to the ref out voltage. We finally obtain the $\Delta V(\omega)$ and phase $\varphi(\omega)$ from voltage response and recorded these as a function of $f = \omega/2\pi$. We then repeat the entire measurement procedures 1 hour after the first characterization, and then another hour after the second one to observe any change in the load modulation voltage, and thus the battery internal dynamics. The selection of a 1-hour interval in the measurement procedure is because 1 hour is the approximate time a battery discharges.

Chapter 5

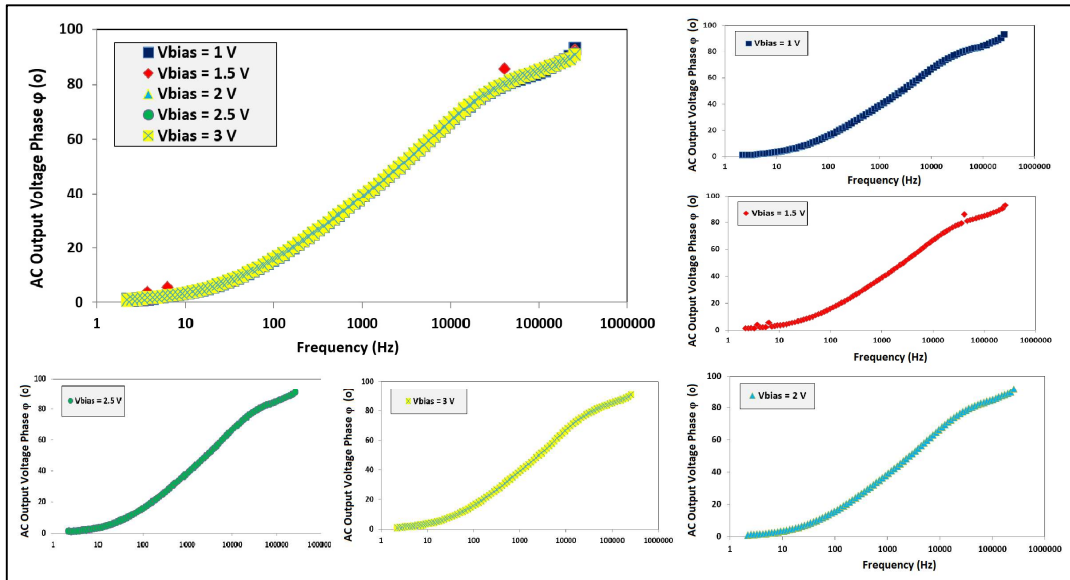
IMS Characterizations of Commercial CdS-Based Light-Dependent Resistor (LDR)

5.1 Results from IMS Characterizations on Commercial CdS-Based Light-Dependent Resistor (LDR)

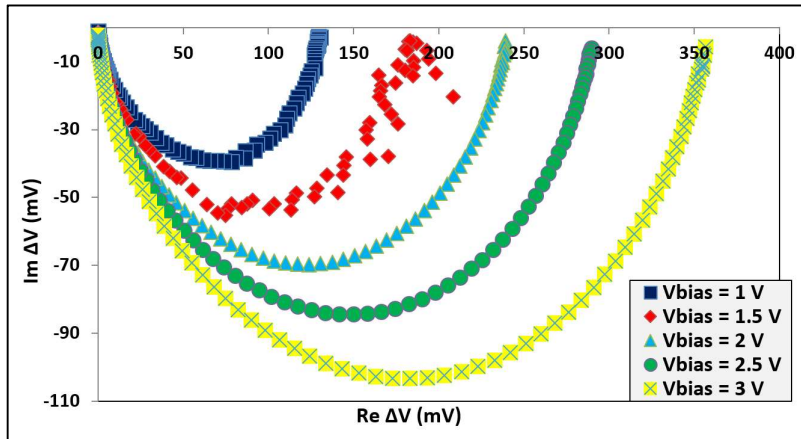
As elaborated in 4.7, for IMS on a light-dependent resistor (LDR), we illuminate a commercial, CdS-based LDR with a modulated green LED (HLMP-CM3A-Z10DD) by using the setup in Fig. 4-15(a). We first apply $V_{LED} = (2.9 \pm 0.9)$ V on the green LED with $R_{LED} = 102 \Omega$. The LED will then be driven by $I_{LED} = (19 \pm 9)$ mA. The modulated LED is then used to illuminate the LDR which is under an applied voltage bias (V_{bias}). We then insert the following lock-in settings into the IMS software in 4.6; first, the input coupling is set to DC, roll-off to 24 dB/oct, dynamic to high, phase offset to 0 and reference harmonic to 1. The time constants are set to 5 s at $f = 1$ -10 Hz, 1 s at $f = 10$ -100 Hz, 0.5 s at $f = 10$ -1000 Hz, 0.1 s at $f = 1$ kHz-10 kHz and 0.05 s at $f > 10$ kHz. The reasoning for these setting has been given in 4.7. We then operate the IMS software to perform a frequency scan at f between 1 Hz and 250 kHz in 18 steps per decade. The resulting currents that flow in the LDR under light modulation are fed into an IV converter with $R_f = 1$ k Ω and $C_f = 4.7$ pF. This current is then converted into a voltage (V_{out}). This voltage is then fed into the lock-in voltage input, and as a result, we obtained $\Delta V(\omega)$ and $\varphi(\omega)$ of V_{out} and record these as a function of $f = \omega/2\pi$. We then repeat the process for $V_{bias} = 1, 1.5, 2, 2.5$ and 3 V. We present our IMS results in the form of Bode amplitude, phase and Nyquist plots of ΔV as shown in Fig. 5-1(a), (b) and (c).



(a)



(b)



(c)

Fig. 5-1 (a). Bode amplitude plot of ΔV , (b) Bode phase plot of ϕ vs frequency f with the plots taken at each V_{bias} depicted separately on the side of the main plot for clarity purposes, and (c) Nyquist plots of ΔV that plots the imaginary ($Im \Delta V = |\Delta V| \sin \phi$) vs. its real part ($Re \Delta V = |\Delta V| \cos \phi$), the spectra being parametric with frequency ω . Here, (a), (b) and (c) are taken at frequencies between 1 Hz and 250 kHz and under LDR-bias voltage $V_{bias} = 1, 1.5, 2, 2.5$ and 3 V (shown colour coded in inset). Note that the Re/Im axis at (c) uses different scales and are not normalized, with the direction of increasing frequency ω given by the blue arrow. For all LDR bias voltages, we use a green LED driven with LED drive current of $I_{LED} = (19 \pm 9)$ mA. This current will then be varied as we varied V_{bias} .

Here, Fig. 5-1(a) and (b) shows the Bode plots of ΔV and phase ϕ with respect to frequency f , at f between 1 Hz and 250 kHz, and also under different LDR V_{bias} with $V_{bias} = 1, 1.5, 2, 2.5$ and 3 V.

While Fig. 5-1(c) shows a set of Nyquist plots measured at all 5 LDR V_{bias} variation. From Fig. 5-1(a), $\Delta V(f \rightarrow 0)$ increases as we increase the LDR V_{bias} . This is because as we increase the LDR V_{bias} , we drive more current through the LDR, thus the increase in ΔV . We also see that the ΔV amplitude plot at LDR $V_{bias} = 1.5$ V is rather noisy, but the general trend of increasing $\Delta V(f \rightarrow 0)$ as we increase LDR V_{bias} is still observed here. All plots in Fig. 5-1(a) also shows corner frequency (f_c) at $f \sim 2$ kHz. In addition, another characteristic of Bode amplitude plots, as shown in Fig. 1-4 and Fig. 5-1(a), is the plot's roll-off. The plot's roll-off is the same as the lock-in filter's roll-off discussed in 4.4. The plot's roll-off is the measure of how steep the plot's attenuation slope immediately after the corner frequency f_c [36]. From Fig. 5-1(a), we found that the Bode plots roll off = -1.1 ± 0.1 . A roll-off ~ -1 indicates the behavior of a first-order system [36]. This means that there would be a single, first-order internal dynamic that occurs in the LDR under the light. This single dynamic is associated with a single time constant τ , and that a single dynamic or time constant will result in an ideal semicircle in the Nyquist plot, as can be seen in Fig. 5-1(c).

From Fig. 5-1(b), ΔV phase ϕ at all LDR V_{bias} are exactly the same, with the phase ϕ reaching 45° at $f \sim 2$ kHz at all V_{bias} . Where f at $\phi = 45^\circ$ being the corner frequency f_c . The corner frequency f_c is linked to a time constant τ through $f_c = 1/2\pi\tau$, where τ represents the LDR's internal dynamic time constant under illumination. Since f_c and τ are the same at all LDR V_{bias} , the same internal dynamic occurs in the LDR at all V_{bias} . The time constant here is most likely the carrier lifetime, this is because τ does not change as we increase the LDR's V_{bias} . Otherwise, τ will not be a carrier lifetime but instead a carrier transit time due to dependency with V_{bias} . There are basically two types of carrier lifetime in an inorganic semiconductor [140, 141]. One is recombination lifetime τ_r , which is the lifetime of extra carriers that is generated in the semiconductor from light absorption. While the other is generation lifetime τ_g , which is the lifetime of small excess carriers that is generated in a reverse-biased semiconductor. The LDR internal dynamic that we measure (corner frequency in Fig. 5-1(a)) originates from current flows in the LDR which was modulated by changing the resistance due to light. Hence, the carrier lifetime here will be the recombination lifetime τ_r . The recombination lifetime is the total of surface and bulk recombination lifetime, and it is defined by the effective recombination lifetime or τ_{eff} in equation 22.

$$\tau_{eff} = \left(\frac{1}{\tau_b} + \frac{1}{\tau_s} \right)^{-1} \quad (22)$$

where τ_b is the bulk recombination lifetime and τ_s is the surface recombination lifetime. Here, the τ_b itself is given by equation 23.

$$\tau_b = \Delta n / R \quad (23)$$

where R is the recombination rate and Δn is the extra carrier density that is present due to light or forward-biasing of a semiconductor. While τ_s is defined in equation 24.

$$\tau_s = \frac{1}{\beta^2 D_n} \quad (24)$$

where D_n is the electron diffusion constant and β is a solution of equation 25.

$$\tan\left(\frac{\beta t}{2}\right) = \frac{s_r}{\beta D_n} \quad (25)$$

where t is the semiconductor's thickness and s_r is the carrier's surface recombination velocity [141]. Note that in eq. (22) to (25), there is no dependence on any external bias voltage for all type of carrier lifetime. If we look at a time-of-flight (TOF) experiment, i.e. where we measure the mobility μ of a carrier traveling in a material under an applied V_{bias} , carrier mobility μ is related to the carrier transit time τ_r through equation (26) [142].

$$\mu = \frac{d^2}{\tau_r V} \quad (26)$$

where μ is in (cm²/V s), d is the material thickness (in cm), V is the applied bias (V) and τ_r is the transit time (s). We can see that a carrier transit time is always dependent on the voltage bias, unlike carrier lifetime which does not, as can be seen in equation (22)-(25). In addition, carrier lifetime dynamic is also the reason why a commercial LDR has an interdigitated track as elaborated in 2.5. Since there is only one carrier dynamic in the LDR, i.e. carrier lifetime, the current path in the interdigitated track has to be designed such that the distance a carrier takes when traveling in the LDR is smaller than its carrier lifetime. Otherwise, a carrier may decay or not flow at all under illumination.

From Fig. 5-1(c), the shape of the Nyquist spectrum at all LDR V_{bias} resembles a semicircle in the 4th quadrant, with the spectrum at $V_{bias} = 1.5$ V being rather noisy, as we can see also in Fig. 5-1(a) and (b). This is because the power supply used for the LDR setup is unstable when we set the power supply voltage setting to $V_{bias} = 1.5$ V. The semicircle increases in size as we increase the

LDR's V_{bias} since the plot's $Re \Delta V (f \rightarrow 0)$ increases in-line with the increase in V_{bias} . This is similar to $\Delta V (f \rightarrow 0)$ in Fig. 5-1(a). Note as well that the Re/Im axis in Fig. 5-1(c) uses different scales. This is also because we drive more current (carriers) through the LDR as we increase the V_{bias} , thus increasing ΔV . To add, the frequency at the semicircle's minimum (or maximum) $Im \Delta V$ value is the corner frequency (f_c) that corresponds to $\varphi = 45^\circ$ in Fig. 5-1(b). The f_c , as said before, is linked to an internal dynamic time constant τ through $f_c = 1/2\pi\tau$. As there is only one semicircle in all Fig. 5-1(c) plots, there will only be one internal relaxation time/time constant τ , that occurs at all V_{bias} conditions. This internal relaxation time is the LDR's carrier lifetime as it (τ) is the same time constant that we get from the corner frequency and phase at the frequency in Fig. 5-1(a) and (b) respectively.

Also from Fig. 5-1(a), (b) and (c), we can extract three characteristic parameters, these are $\Delta V (f \rightarrow 0)$, $Re \Delta V$ at ($f \rightarrow 0$) and corner frequency f_c . In addition, we also derive the time constant τ from all plots with $f_c = 1/2\pi\tau$. All of the characteristics parameters, along with τ and the LDR's V_{bias} , are shown together in Table V.

TABLE V THE LDR V_{bias} , f_c , $\Delta V (f \rightarrow 0)$, $Re \Delta V (f \rightarrow 0)$ AND τ FOR THE SPECTRA SHOWN IN FIG. 5-1(a), (b) AND (c)

LDR V_{bias} [V]	f_c [Hz]	$\Delta V (f \rightarrow 0)$ [V]	$Re \Delta V (f \rightarrow 0)$ [mV]	τ [ms]
1	1800 ± 1	0.132 ± 0.001	132 ± 10	0.0890 ± 0.0001
1.5	1800 ± 1	0.185 ± 0.002	185 ± 20	0.0890 ± 0.0001
2	1800 ± 1	0.240 ± 0.002	240 ± 10	0.0890 ± 0.0001
2.5	1800 ± 1	0.291 ± 0.003	291 ± 10	0.0890 ± 0.0001
3	1800 ± 1	0.360 ± 0.004	360 ± 20	0.0890 ± 0.0001

From Table V, higher LDR V_{bias} will result in more current (carriers) being injected into the LDR, which then result in the increase of (ΔV) flowing in the LDR. We also conclude that the time constant τ is the carrier lifetime since τ here does not change as we change the V_{bias} , or in other words, τ is independent of the LDR V_{bias} . Fermin et al. found from their work on intensity-modulated photocurrent spectroscopy (IMPS) on n-type CdS or n-CdS electrode, that the resulting Nyquist plot also consists of only a single semicircle. Thus, indicating the presence of a single internal dynamic in the LDR under the light. Further, when they perform IMPS on the electrode at different voltage bias, the resulting Nyquist plots still consists of a single semicircle with the plot's peak frequency/corner frequency f_c remaining unchanged similar to f_c results in Table V. Hence, they conclude that this internal dynamic is associated with a certain recombination rate that is independent of bias voltage, or in other words it is a carrier lifetime of the n-CdS under light [92]. Although we cannot compare our results directly to theirs, since the n-CdS in their work is not an LDR and we do not perform IMPS, the comparison is still possible as our LDR is also made of n-CdS. Hence, we conclude that our result, especially the time constant in Table V is consistent with reported CdS behavior under

light at different voltage bias. Finally, we conclude that our instrument/setup works well in terms of consistency of (our) results with previously reported findings on the same material. As such, with this characteristic (results consistency) we can then apply our instrument/setup to perform IMS characterization on research-type materials/devices, where the properties are largely unknown.

5.2 Summary of Results from IMS on Commercial CdS-Based LDR

From IMS characterization on commercial CdS-based LDR, we first conclude that by increasing the LDR's applied V_{bias} , we then increase the current flowing through the LDR and consequently increase the corresponding ΔV ($f \rightarrow 0$) from the converter output. We then found that a single, first-order dynamics dominates the LDR's internal dynamic as indicated by the roll-off magnitude of Bode amplitude plot in Fig. 5-1(a), which is $= -1.1 \pm 0.1$, and also from the single semicircle shape of the Nyquist plots in Fig. 5-1(c) which were obtained from the converter's ΔV output at all applied V_{bias} . We then conclude that the corner frequency f_c and τ that are derived from all the plots in Fig. 5-1(c) is the carrier lifetime of electrons from currents that flows within the LDR, this is because τ (and f_c) does not change at different V_{bias} . If τ changes under different V_{bias} , the τ will then be the carrier transit time based on equation (26), since τ will now be dependent on the applied V_{bias} .

In addition, we also found that the observed single, first-order dynamic found in the CdS-based commercial LDR, i.e. the carrier lifetime, is consistent with the typical dynamic found in an electrode made of an n-type CdS semiconductor, with the electrode under IMPS measurement and an applied voltage bias V_{bias} [92]. From literature, the electrode dynamic was also found to be a carrier lifetime of electrons flowing in the n-CdS under light [92]. Finally, since the observed dynamic in the commercial CdS-based LDR in our research is consistent with those found from an n-type CdS electrode in literature, we can conclude that our instrument/setup works well in determining the dynamics occurring in a widely-known system, and that we can then apply our instrument/measurements to characterize other systems/materials in which the properties/dynamics is not widely-known.

Chapter 6

IMS Characterizations of Organic Photovoltaic (OPV) Devices

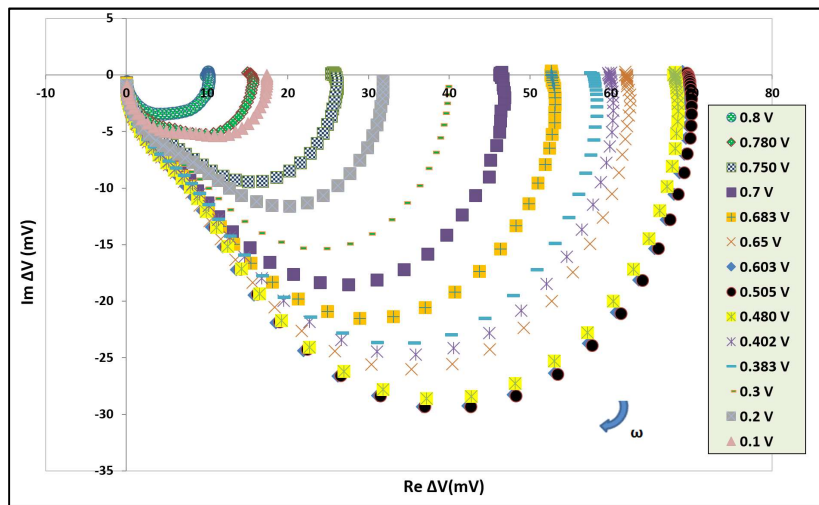
As elaborated in 1.1 and 3.1, we perform IMS characterization on two types of bulk heterojunction (BHJ) OPV, One is a BHJ with PEDOT as its hole extraction layer (HEL), while the other is a BHJ with V_2O_{5-x} as the HEL. Both types of BHJ are made of the same donor and acceptor mixture of PFDT2BT-8 and PC₇₀BM respectively as shown in Fig. 3-1(b). In addition, devices with V_2O_{5-x} HEL were varied by HEL annealing/non-annealing before BHJ layer deposition. Here, we perform IMS on OPV with non-annealed, 100, 200, 300 and 400 °C annealed HEL before BHJ deposition. We first present and discuss IMS characterization results on OPV with PEDOT HEL, where the OPV are externally loaded with different values of finite load resistance R_L , including R_L near the cell's maximum power point (R_{MPP}). We then give and discuss the results of IMS under finite load which was used in the aging study of OPV with PEDOT HEL. Following this, we present and discuss the results of BHJ capacitance determination of OPV with PEDOT HEL by using IMS under finite load. The capacitance determination was done without absolute calibration of the LED intensity. After presenting the results of IMS on OPV with PEDOT HEL, we then give and discuss the result of IMS on OPV with V_2O_{5-x} hole extraction layer (HEL) at a finite load R_L equal to its maximum power point (R_{MPP}). Finally, we present and discuss the result of IMS near R_{MPP} which was used in the aging study of OPV with V_2O_{5-x} HEL.

For IMS characterizations on both types of OPV, we illuminate the OPV with a fast red LED ($\lambda_p = 650$ nm, $\tau = 3$ ns) by using the setup in Fig. 4-5(a). We apply $V_{LED} = (2.2 \pm 0.5)$ V on the red LED with $R_{LED} = 120 \Omega$, hence driving the LED with $I_{LED} = (18 \pm 4)$ mA. We then insert the following lock-in settings into the IMS software in 4.4, first, the input coupling is set to DC, roll-off to 24 dB/oct, dynamic to high, phase offset to 0 and reference harmonic to 1. The time constants are set to 5 s at $f = 1-10$ Hz, 1 s at $f = 10-100$ Hz, 0.5 s at $f = 10-1000$ Hz, 0.1 s at $f = 1$ kHz-10 kHz and 0.05 s at $f > 10$ kHz. The time constants are set to 5 s at $f = 1-10$ Hz, 1 s at $f = 10-100$ Hz, 0.5 s at $f = 10-1000$ Hz, 0.1 s at $f = 1$ kHz-10 kHz and 0.05 s at $f > 10$ kHz. The reasoning behind these lock-in settings has been given in 4.4. We then operate the IMS software to perform a frequency scan at f between 1 Hz and 250 kHz in 12 steps per decade. The OPV is connected to a potentiometer as a variable load resistance R_L , which we later vary to conduct IMS under finite R_L . The OPV photocurrents from illumination are then measured as a voltage drop $V + \Delta V(\omega) \sin(\omega t + \phi(\omega))$ across R_L . The R_L will later be varied in the OPV measurements depending on the experiment. This voltage

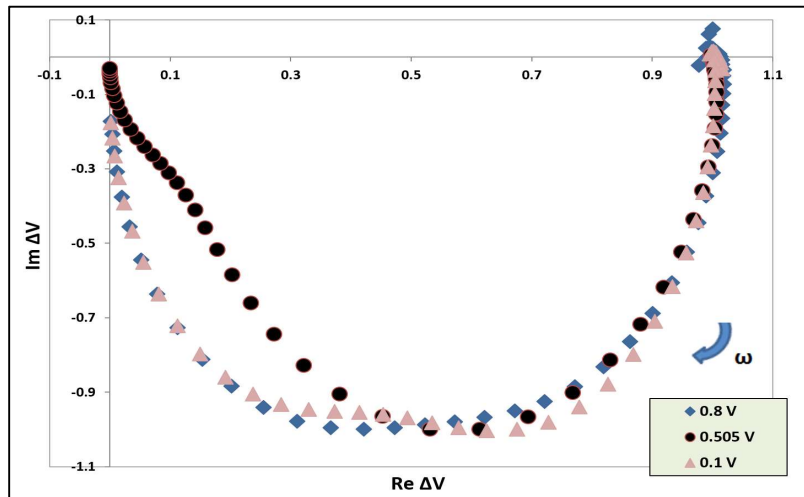
drop is then fed into the lock-in voltage input, without a current-to-voltage converter. As a result, we obtain the amplitude $\Delta V(\omega)$ and phase $\varphi(\omega)$ from the voltage response and record these parameters as a function of $f = \omega/2\pi$. We then present our IMS results in the form of Bode amplitude, phase and Nyquist plots of ΔV as seen in 1.4.

6.1 Results from IMS on OPV with PEDOT Hole Extraction Layer under Finite Load Resistance R_L

We present the IMS results of the OPV with PEDOT HEL under a variation of finite load R_L in Nyquist plot of ΔV , shown in Fig. 6-1.



(a)



(b)

Fig. 6-1 (a). Nyquist plots of ΔV that plots the imaginary part ($Im \Delta V = |\Delta V| \sin \varphi$) vs. its real part ($Re \Delta V = |\Delta V| \cos \varphi$) which is parametric in frequency for IMS spectra taken at different R_L , ranging from near-open circuit (high R_L , or near ‘IMVS’) to near-short circuit (low R_L , or near ‘IMPS’). Spectra are colour coded by their voltage points, V , shown in the right panel, rather than R_L . The LED was driven by $I_{LED} = (18 \pm 4)$ mA. Note Re / Im axis here uses different scales. (b) Normalized Nyquist plots of Fig. 6-1(a) taken at near-open circuit voltage point (0.8 V, $R_L = 476$ k Ω), near maximum power point (0.505 V, $R_L = 36.6$ k Ω) and near-short circuit voltage point (0.1 V, $R_L = 6.8$ k Ω). The direction of increasing frequency is given by the blue arrow. In all plots, $Re \Delta V$ is normalized to its value in the limit of $f \rightarrow 0$ Hz, whilst $Im \Delta V$ is normalized to its minimum magnitude.

Fig. 6-1(a) shows the family of measured IMS spectra as Nyquist plots when R_L is set to a range of different values, giving load lines with a different slope, hence different voltage points. The term voltage point here, as defined in subchapter 4.3, refers to the intersection of a load line with the J/V characteristic in Fig. 4-6(b) that gives the resulting DC voltage V of a solar cell illuminated by a particular light intensity, and loaded with R_L . The resulting DC voltage V here is then called the ‘voltage point’ for R_L , with the load line a representative of load resistor R_L . Here in Fig. 6-1(a), voltage variation starts at voltage point V close to 0 (short circuit, R_L near zero), to V close to the open-circuit voltage/ V_{OC} ($R_L \rightarrow$ infinity). The amplitude and phase of ΔV here, as described in earlier paragraphs, is measured by “locking-in” the ΔV component from the resultant DC + AC voltage across R_L , where ΔV is a function of $f = \omega/2\pi$. In addition, Fig. 6-1(b) shows 3 plots from 6-1(a) (i.e. at near open circuit, near short circuit and near MPP) on a normalized scale to compare their shape. We observe that for all settings of R_L , the general shape of our IMS Nyquist plots is dominated by a semicircle (or semi-ellipse-, note that the scales on the Re / Im axis in Fig. 6-1(a) differ) in the 4th quadrant of the complex plane. However, the characteristic parameters of the semicircles change with R_L , and there is a noticeable ‘shoulder’ feature at high frequencies that deviates from perfect semicircular shape for most choices of load resistance R_L . Further, Fig. 6-1(b) shows that this ‘shoulder’ feature is largely absent in extreme cases, i.e. at high R_L (near open-circuit or at IMVS mode) and low R_L (near short circuit, at IMPS mode). The near- IMPS and IMVS spectra in Fig. 6-1(b) are somewhat flattened compared to a perfect semicircle but without the distinct ‘shoulder’ feature seen at MPP load, which would, therefore, be missed in the traditional IMVS and IMPS modes.

We first investigate and rationalize the dependency of the dominant semicircles’ characteristics with R_L , by using a generic equivalent circuit model that describes the dominant semicircle’s parameters. This was done by simulating the generic circuit with LT SPICE, which is an electronic simulation software from Linear Technology [143]. From Fig. 6-1(a) and (b), we can then extract two characteristic parameters of our Nyquist semicircles, these are their magnitude, characterised by the limit of $Re \Delta V (f \rightarrow 0)$, and the corner frequency f_c , which is given by the frequency where $Im \Delta V$ has its minimum (i.e. maximum magnitude). We then summarize the electrical conditions (i.e. loads R_L , DC voltage points and corresponding DC current densities J under LED) and characteristic parameters f_c and $Re \Delta V (f \rightarrow 0)$ of the IMS spectra in, Fig. 6-1(a) in Table VI, and plot the parameters in Fig. 6-2.

TABLE VI LOAD R_L , DC VOLTAGE POINTS, AND CURRENT DENSITIES J , CORNER FREQUENCIES f_c , AND $Re \Delta V$ FOR $f \rightarrow 0$, FOR THE SPECTRA SHOWN IN FIG. 6-1(a)

R_L [k Ω]	Voltage point [mV]	J [mA/cm ²]	f_c [Hz]	$Re \Delta V (f \rightarrow 0)$ [mV]
6.8	100	0.51	3200 \pm 1	17 \pm 10
13.4	200	0.52	1700 \pm 1	33 \pm 10
19.9	300	0.53	1400 \pm 1	46 \pm 10
26.5	383	0.51	1000 \pm 1	57 \pm 10
27.7	400	0.5	1000 \pm 1	60 \pm 10
34.4	480	0.49	840 \pm 1	68 \pm 10
36.6	505	0.48	750 \pm 1	70 \pm 10
47.6	603	0.44	840 \pm 1	70 \pm 10
54.8	650	0.41	930 \pm 1	62 \pm 10
61.8	683	0.39	1100 \pm 1	53 \pm 10
66.7	700	0.37	1100 \pm 1	46 \pm 10
95.4	750	0.27	2100 \pm 1	25 \pm 10
158	780	0.17	3200 \pm 1	15 \pm 10
476	800	0.06	14000 \pm 1	10 \pm 10

The current density (J) column in Table VI was calculated from the chosen R_L and the DC voltage point, V , from $J = V / (R_L * A)$, with $A =$ device area, $= 2.86 \text{ mm}^2$. The f_c and $Re \Delta V (f \rightarrow 0)$ columns were then used to construct Fig. 6-2, while column J is used to construct Fig. 6-3, which is the OPV J/V characteristic under red LED illumination.

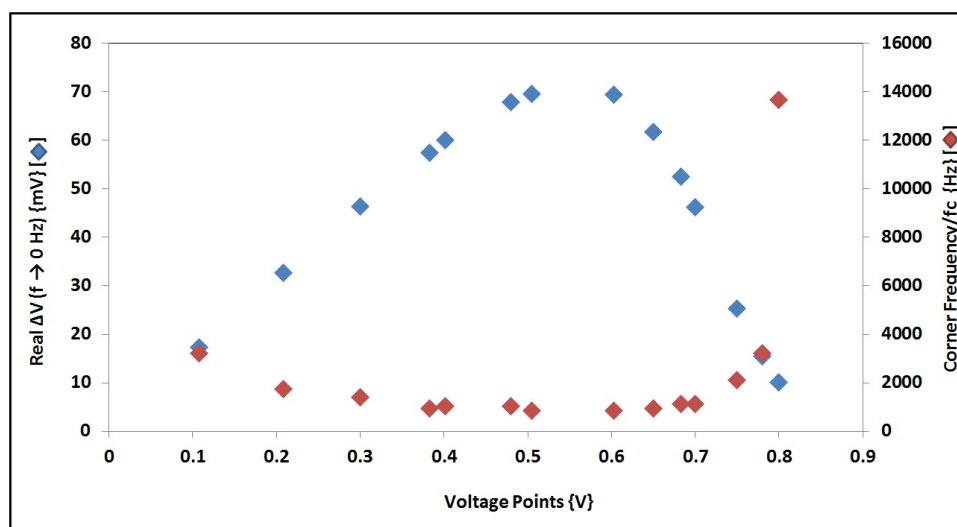


Fig. 6-2. The plot of the dominant Nyquist semicircle characteristic parameters vs DC voltage point, which is set by R_L . Here, the blue plot is $Re \Delta V$ at low-frequency ($f \rightarrow 0$) vs. voltage points. While the red one is corner frequencies, f_c , vs. voltage points.

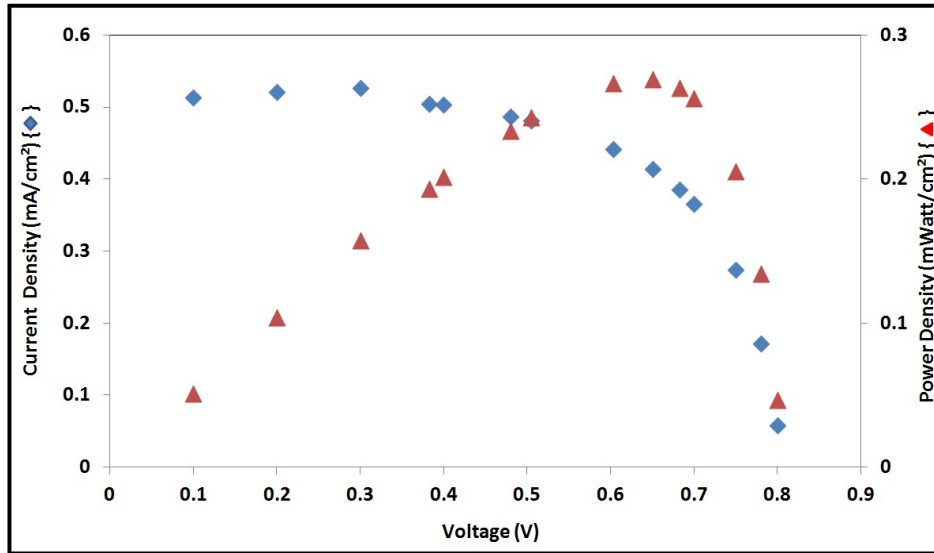


Fig. 6-3. The OPV's J/V characteristics and power profile under red LED illumination, that are constructed from Table VI.

The characteristics of a solar cell, and indeed any extracted (solar cell-) equivalent circuit parameters, depends very much on illumination intensity. Since, we have illuminated the OPV with a red LED with much less intensity than AM 1.5, we have therefore constructed Fig. 6-3 from the J/V data on Table VI due to red LED light, as an alternative DC J/V characteristic of Fig. 3-2 J/V plot under AM 1.5. The result is shown in Fig. 6-3. From Fig. 6-3, we find that $J_{sc} = -0.51 \text{ mA/cm}^2$, $V_{OC} = 800 \text{ mV}$, $V_{MPP} = 650 \text{ mV}$, $J_{MPP} = 0.42 \text{ mA/cm}^2$, $P_{D-MPP} = 270 \text{ } \mu\text{W/cm}^2$ and $FF (\%) = 67$. Also, from the LED J/V plot, we derived specific shunt resistance $R_{sh-spec} = 10000 \text{ } \Omega\text{cm}^2$ and specific serial resistance $R_{s-spec} = 182 \text{ } \Omega\text{cm}^2$, using the same derivation method [144] as in Fig. 3-2. This equates to absolute $R_{sh} = 350 \text{ k}\Omega$ and absolute $R_s = 6.4 \text{ k}\Omega$. However, due to the lower quality of the J/V characteristics under red LED, the latter parameters, in particular, are difficult to extract accurately. If we compare the J/V characteristics in Fig. 6-3 and Fig. 3-2 in 3.1.3, both plots shared a similarity in shape, with the DC current density J being minimum near short-circuit, maximum near V_{OC} and lies in-between maximum and the minimum value at maximum power point (MPP). While the power profile of both Fig. 6-3 and 3-2 also follows the same shape and pattern, i.e. power density will be at a minimum at both short- and open-circuit and (P_D) at a maximum at MPP. The differences of both Fig. 6-3 and 3-2 J/V plot and power profile is the current- and power density magnitude that is much lesser in Fig. 6-3 compared to that in Fig. 3-2, which is due to the much lower LED intensity that was used for Fig. 6-3. In addition, we depict the J/V plot from the red LED illumination (Fig. 6-3) in this subchapter instead of depicting it in 3.1.3 in comparison with the J/V plot under AM 1.5. This is because of the J/V plot in Fig. 6-3 was constructed from a limited set of the OPV's voltage points and current

densities (i.e. from Table VI) as opposed to the J/V plot under AM 1.5 in 3.1.3 which was constructed with a much higher data points (i.e. the OPV's voltage points).

If we return to look at Fig. 6-2, the $Re \Delta V (f \rightarrow 0)$, represented by blue data points, also follows the same shape as the DC J/V characteristics with R_L in Fig. 4-6(b) in 4.3, although $Re \Delta V (f \rightarrow 0)$ here has a different magnitude compared to the DC ΔV in Fig. 4-6(b) due to the much lower LED intensity. By following the same shape, we meant here that the small amplitudes of $Re \Delta V (f \rightarrow 0)$ for both small, and large values of R_L (i.e. voltage point near 0 and V_{OC} , respectively) are easily understandable as low/high R_L that corresponds to a near-vertical, or near-horizontal, load line in Fig. 4-6(b), which then leads to small ΔV at both near 0 and near- V_{OC} voltage point. The $Re \Delta V (f \rightarrow 0)$ profile for intermediate loads, is similar in shape to the power profile in Fig. 3-2 in subchapter 3.1.3. and the profile in Fig. 6-3. In Fig. 6-2, the $Re \Delta V (f \rightarrow 0)$ peaks at voltage point, $V_{MAX} = 550$ mV, somewhat below $V_{MPP} = 650$ mV from the power profile under LED illumination (Fig. 6-3). Also, corner frequencies in Fig. 6-2 are high for both voltage points near short circuit, and voltage points near V_{OC} , with a broad minimum around MPP. Intuitively, f_c can be interpreted as a carrier transit time that is influenced by the screening of the built-in voltage from space charges formation within the bulk BHJ layer [47]. At near open-circuit, built-in voltage screening is weak because very few charge carriers are extracted, with most of the carriers accumulating in the BHJ's donor-acceptor interface. Hence, the significant built-in voltage within the bulk BHJ will result in fast transit time or very high f_c as seen in Fig. 6-2. Whereas in near short-circuit, charge carriers are extracted from the donor-acceptor interface and travel through the bulk BHJ [47], hence the presence of built-in voltage screening. This screening, however, may not be very strong as charge carriers prefer to travel in the bulk layer rather than forming space charges due to the short-circuit condition, thus f_c in short-circuit is also high (or transit time is fast) but not as high as in under open-circuit (Fig. 6-2). However, in-between short- and open-circuit condition, i.e. near or at MPP, space charges will significantly screen the built-in voltage such that when carriers are extracted, the transit time will be much longer due to the influence of the net electric field from screening, hence the observed lower f_c values in Fig. 6-2. In order to rationalize our results we later compared them to LT SPICE simulations on a generic OPV equivalent circuit (e.g. from Narayan et al.) that was loaded externally by R_L [132].

To model BHJ OPV operation and interpret the OPV equivalent circuit in a physical context, we use a theoretical model from Luther et al. that takes into account carrier generation, recombination (i.e. geminate, biomolecular and trap-assisted recombination), and then free carrier trapping in an OPV. This model (Fig. 6-4) is depicted in the form of a simplified diagram of microscopic processes in an OPV [49].

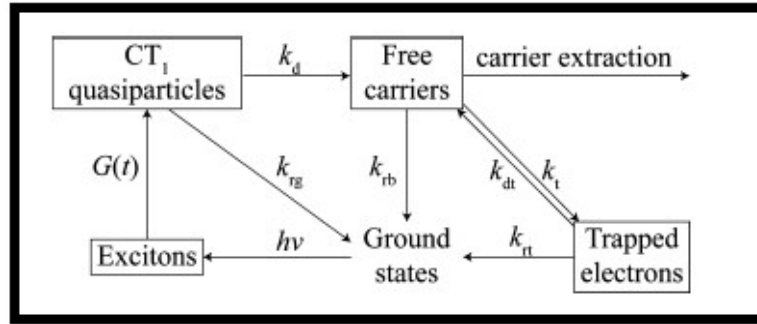


Fig. 6-4. A diagram of microscopic processes that described OPV operation from Luther et.al., The k_d , k_{rg} , k_{rb} , k_{dt} , k_t , and k_{rt} here is the dissociation, geminate recombination, biomolecular recombination, de-trapping, trapping and trap-assisted recombination rate constant respectively. Finally, $G(t)$ is the CT_1 quasiparticle generation rate [49].

In Fig. 6-4, photons are first absorbed in the OPV's donor component almost instantaneously, which then leads to exciton formation from the donor ground state which is called the charge-transfer state 0 or CT_0 . Excitons will then dissociate at the donor-acceptor/D-A interface and becomes a bound electron-hole pair at the interface which is called the charge-transfer state 1 or CT_1 quasiparticles. Here, CT_1 formation is also instantaneous, similar to that of excitons. Now the formation of CT_1 quasiparticles in an IMS must then account for modulated light and the background light bias component, hence the CT_1 quasiparticles generation rate is then given by equation (27).

$$G(t) = G_0 + \Delta G \cos(\omega t) \quad (27)$$

where G_0 is the steady state CT_1 quasiparticles generation rate representing the light bias, ΔG being the magnitude of CT_1 quasiparticles generation rate perturbation which represents the modulated light, ω is the perturbation angular frequency. Once the CT_1 quasiparticles have been formed, two possibilities can happen, one is that CT_1 can dissociate into free carriers/unbound electrons and holes, which is represented by the dissociation rate constant/ k_d (in s^{-1}), while the other is that CT_1 can decay into the ground state (CT_0) or recombine, which is called geminate recombination and represented by the geminate recombination rate constant/ k_{rg} (in s^{-1}). As for free carriers, they can experience three different paths after dissociation, one is that they can decay back into the ground state or recombine, which is called biomolecular recombination, represented by the biomolecular recombination rate constant/ k_{rb} (in s^{-1}), the other path is that carriers can also be trapped or de-trapped due to the presence of electron/hole traps, represented by trapping and de-trapping rate constant/ k_t and k_{dt} (in s^{-1}) respectively. Finally, carriers can also be attracted/pulled by traps such that they will recombine or decay back into the ground state, represented by trap-assisted recombination rate constant/ k_{rt} (in s^{-1}).

Note that de-trapping here means overfilling the traps with electrons, thus pushing back trapped electrons to their unbound/free state [49].

We depict the OPV-equivalent circuit in Fig. 6-5(a). The current source I_L is a frequency-dependent parameter and is used to model free carrier formation from CT₁ quasiparticles in Fig. 6-4 (represented by k_d). So I_L is influenced by both the light bias and modulated light. While the circuit's diode, D is actually a voltage-dependent differential resistance (R_D) that represents geminate recombination from CT₁ to its ground state. Hence D depends on the illumination's DC component. Also in an ideal cell, bigger I_L is better as more carriers will be produced, but for the diode as R_D , its (R_D) magnitude should be smaller to minimize carrier losses due to geminate recombination. Both the shunt resistance (R_{Sh}) and series resistance (R_S) represent resistances faced by free carriers once unbound from CT₁. The R_{Sh} magnitude depends entirely on the OPV's intrinsic properties, while those of R_S depend both on the cell's intrinsic properties and external circuit resistance. In Fig. 62, R_{Sh} and R_S respectively represent the biomolecular recombination (k_{rb}) and electron trap presence (k_t). So ideally, $R_{Sh} \gg R_S$ for the cell to produce more carriers instead of losing them due to recombination. Finally, the BHJ capacitance or C_{BHJ} is a frequency-dependent diffusion capacitance, which is the accumulation of carriers in the BHJ's donor-acceptor interface, once they (carriers) are dissociated from CT₁. Thus, C_{BHJ} magnitude depends entirely on the OPV's intrinsic properties and that it is desirable to have a bigger C_{BHJ} as it increases the active layer area where carriers are generated [49].

As circuit components representing our OPV cells, we selected $R_{Sh} = 100 \text{ k}\Omega$, $R_S = 2 \text{ k}\Omega \ll R_{Sh}$, (Similar to the parameters extracted from Fig. 6-3); $C_{BHJ} = 4 \text{ nF}$ (selection of C_{BHJ} magnitude will be discussed in the next subchapter), and a modified 1N914 diode designated as 1N914_KA. Diode modification consisted of selecting a lower reverse bias saturation current (I_S). In the model, I_S influences the equivalent circuit's V_{OC} and $I_S = 3 \text{ pA}$ was chosen so that the equivalent circuit replicates the observed V_{OC} of our OPV cell. The magnitude of the current source was set to $25 \text{ }\mu\text{A}$ DC with an AC modulation of $5 \text{ }\mu\text{A}$. We then show a simulated 'Nyquist rainbow' in Fig. 6-5(b) under different R_L at the order of $\text{k}\Omega$ ($R_S < R_L < R_{Sh}$), which corresponds to experimental results in Fig. 6-1(a).

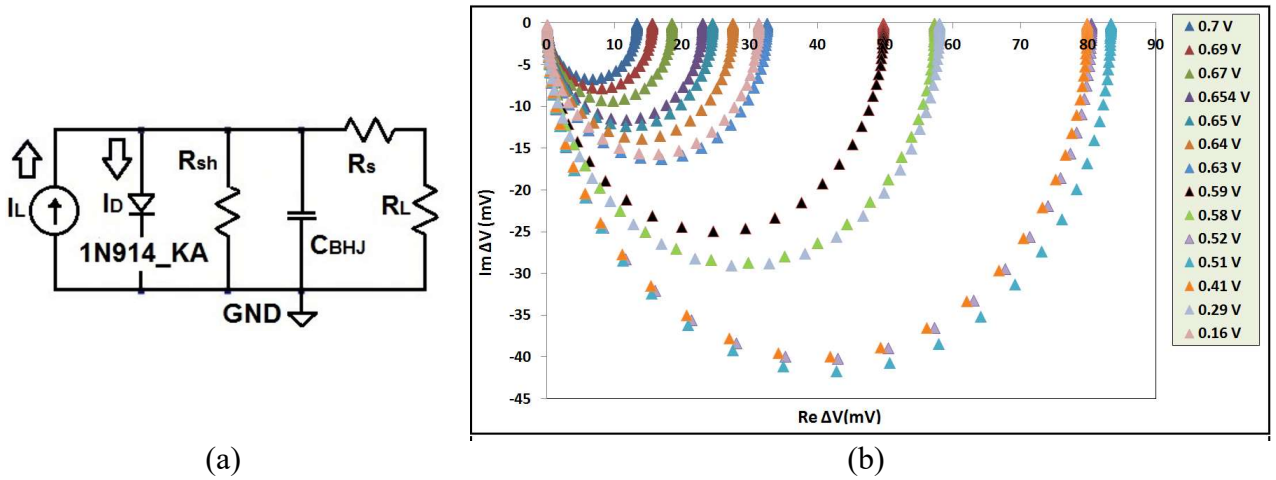


Fig. 6-5 (a). Generic equivalent circuit model for BHJ OPV [132]. I_L here represents the light-driven current source. In IMS, all components apart from R_L are internal to the OPV cell. (b) Simulated ‘Nyquist rainbow’ for the equivalent circuit model, We selected $R_{sh} = 100$ k Ω , $R_s = 2$ k Ω , $C_{BHJ} = 4$ nF, and a customized 1N914 diode (1N914_KA) with the saturation current reduced to 3 pA. The amplitude of the current source modulation was set to 5 μ A and the DC current bias was set to 25 μ A. Here, R_L was varied in the range (6.8-476) k Ω , leading to the voltage points shown in the panel on the right. The largest semicircle (light blue symbols) corresponds to $R_L = 26.5$ k Ω .

In Fig. 6-5(b), we can see that the simulated Nyquist plots of generic OPV equivalent circuit give exact semicircles/ellipses at all voltage points without the presence of a high frequency ‘shoulder’ that is seen in Fig. 6-1(a), even when the simulated cells are loaded to near MPP. Further, the semicircles in Fig. 6-5(b) shows the different magnitude of $\text{Re } \Delta V$ ($f \rightarrow 0$), and corner frequency f_c for different voltage points. For (simulation) comparison to experimental results, we then plot characteristic features of the simulated equivalent circuit in Fig. 6-6, which corresponds to the real results in Fig. 6-2.

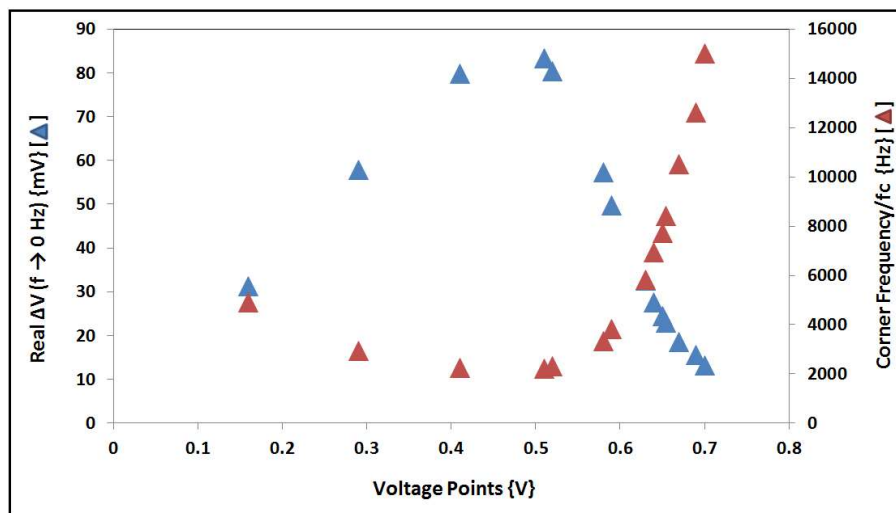


Fig. 6-6. The characteristic parameters of simulated Nyquist semicircle plotted against voltage point V , which is set by R_L . (a) The blue plots indicate $\text{Re } \Delta V$ at low-frequency ($f \rightarrow 0$) vs. voltage points. While at (b) the red plot indicate corner frequencies, f_c , vs. voltage points. Here, $\text{Re } \Delta V$ reaches its maximum for $R_L = 26.5$ k Ω .

For both experimental and simulated spectra, the magnitude of $Re \Delta V (f \rightarrow 0)$ depends very much on the magnitude of R_L , *i.e.* voltage point, V . The experimental (Fig. 6-2) and simulation (Fig. 6-6) $Re \Delta V (f \rightarrow 0)$ vs. voltage point plots are very similar, with both resembling a power profile, with $Re \Delta V (f \rightarrow 0)$ peaking near MPP. The broad and flat minimum of f_c shown in Fig. 6-2 is also replicated by the simulation in Fig. 6-6. In quantitative term, f_c is roughly 3 times higher in the simulation compared to the experimental results. Quantitative differences for f_c probably arise mainly from the difficulties of simulating the nonlinear properties of an organic BHJ diode in the equivalent circuit model with conventional software. Note Gundlach et al. [128] have avoided the use of a diode component in their simulations altogether, linearizing it by an incremental resistor. This is acceptable when a single, fixed voltage point is studied (indeed we also do this ourselves in the next subchapter), but not when we study voltage point dependency of f_c , as the diode incremental resistance changes (non-linearly) with the changes in voltage point. Further, the SPICE software that we use to simulate the circuit offers a selection of stock inorganic diodes, with options for customization. To account for the differences between stock diodes and organic BHJ diodes, we apply two modifications in Fig. 6-5(a) circuit. We do this by setting a significantly smaller saturation current (order pA vs. nA) in Fig. 6-5(a) diode due to lower carrier mobility, and add a 4 nF C_{BHJ} // diode to the (order pF) capacitance of a stock diode, although C_{BHJ} is not voltage- dependent, while diode capacitance is [144]. In addition, a mathematical model that described the diode ideality factor (n) in a one diode model solar cell-equivalent circuit similar to Fig. 6-5(a), has also been reported by Cotfas et al [144]. However, in our simulation, we do not know precisely the ideality factor of our BHJ OPV diode. The observed behavior of $Re \Delta V (f \rightarrow 0)$ (a DC property) under different R_L can, therefore, be understood near-quantitatively by the generic equivalent circuit model in Fig. 6-5(a), but the f_c behavior (AC property) can only be understood qualitatively.

Practically, the increased ΔV , and reduced corner frequency, under load resistances near R_{MPP} are advantageous. This is because increased amplitude improves signal-to-noise ratio, and the reduction in corner frequency effectively extends the instrumental bandwidth to higher frequencies. The latter can be seen in Fig. 6-1(b), where the MPP spectrum approaches the origin more closely than either IMPS or IMVS spectra, although all terminate at the same frequency, *i.e.* 250 kHz. Therefore, we can conclude that conducting IMS in MPP mode, rather than at the established open circuit (IMVS)- and short circuit (IMPS) modes, are both the most realistic and practically most convenient mode of doing IMS. If we now look back at Fig 6-1(a), we observe that at high frequencies, there remains a difference between experiment and generic circuit simulation results, *i.e.* a high frequency ‘shoulder’ in the experimental spectra taken under finite loads, in particular when $R_L \sim R_{MPP}$. This feature is invisible near open circuit (IMVS mode) and near short circuit (IMPS

mode), as seen in Fig. 6-1(b). Qualitatively, in IMPS, most current generated by the cell's current source will flow through the external short circuit. Under open-circuit conditions, the cell's internal diode will be strongly forward biased, resulting in a low resistance internal current path. However, under finite load, both the external current path and internal diode, will display significant resistance, thus forcing more current through the BHJ capacitance path, in particular at high frequencies, when capacitive impedance drops. Hence, IMS under finite load may also reveal the presence of spectral features originating at the BHJ that remain hidden under IMPS and IMVS modes.

As a comparison, Semenekhin et al. previously reported IMPS and IMVS on a similar OPV cell but using a different light absorbing/hole conducting polymer in the BHJ mixture [47]. They observed a marked difference between IMPS and IMVS spectra, which we find to be quite similar as seen in Fig. 6-1(b). However, unlike the results in Fig. 6-1(a), neither their IMPS nor IMVS spectra display a high frequency 'shoulder'. Instead Semenekhin et al. reported a strong '3rd quadrant' (negative $Re \Delta V$) high-frequency feature in IMPS, which is absent in their IMVS spectra [47]. Semenekhin et al. associated negative $Re \Delta V$ with the finite transit time of carriers between exciton splitting at the heterojunction and extraction at the contacts [47]. However, our spectra under all loads, including at near-IMPS, remain in the 4th quadrant, which suggests faster carrier extraction occur in our device.

6.2 Results from Ageing Study on OPV Device with PEDOT Hole Extraction Layer

Besides conducting IMS on the sample under different values of finite load R_L , We also performed an aging study on the same sample with the same IMS mode after 30 days of storage under dark conditions and ambient atmosphere. The study was conducted when the sample was under a load resistance (R_L) = 61 k Ω . The before- and after IMS Nyquist spectra results on R_L = 61 k Ω were then compared and discussed. In addition, from the AM 1.5 characterisation of the stored cell in 3.1.3, we found that J_{SC} has dropped to 3.2 mA/cm², V_{OC} and V_{MPP} dropped to 879 and 620 mV, respectively, and the maximum power to 1.6 mW/cm², with corresponding increase of R_{MPP} compared to when the sample was still fresh. Also, R_{Sh} and R_S under AM 1.5 had increased to 2.4 k Ω and 120 Ω , respectively. We then compared the Nyquist plots of the IMS spectra at the same R_L (61 k Ω) before and after storage in Fig. 6-7.

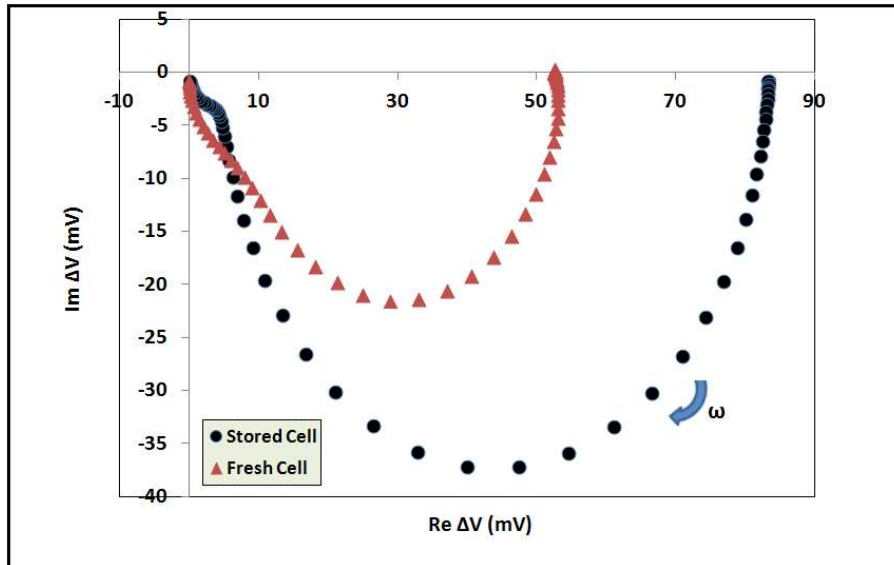


Fig. 6-7. Comparison between the IMS spectra of a freshly prepared sample, and a sample stored for 30 days under air in the dark. $R_L = 61 \text{ k}\Omega$ for both. The corner frequencies (f_c) of the fresh and stored sample are 1140 Hz and 356 Hz respectively.

In Fig. 6-7, we find that the high frequency ‘shoulder’ seen under finite load is exacerbated by the OPV cell aging. In, addition, we can see in the same figure (Fig. 6-7) that the overall larger size of the Nyquist plot indicates that $R_L = 61 \text{ k}\Omega$ leads to a voltage point near to the peak of the $Re \Delta V (f \rightarrow 0)$ vs. voltage point profile for the degraded cell, but not for the fresh cell, where the corresponding voltage point of 683 mV is in the steeply declining flank of the profile as seen in Fig. 6-2. However, the high-frequency feature for the aged cell is now more clearly separated from the dominant semicircle, morphing from ‘shoulder’ to ‘foot’. From previous qualitative reasoning, we suggest that the high-frequency feature seen for loaded cells may originate at the BHJ component. We, therefore, extended the generic equivalent circuit in the SPICE simulation by a resistor parallel to a capacitor ($R // C$) in series with the BHJ capacitance. Fig. 6-8 shows the extended equivalent circuit, and the simulated spectra from the extended circuit, for different magnitudes of the added $R_{ext} // C_{ext}$.

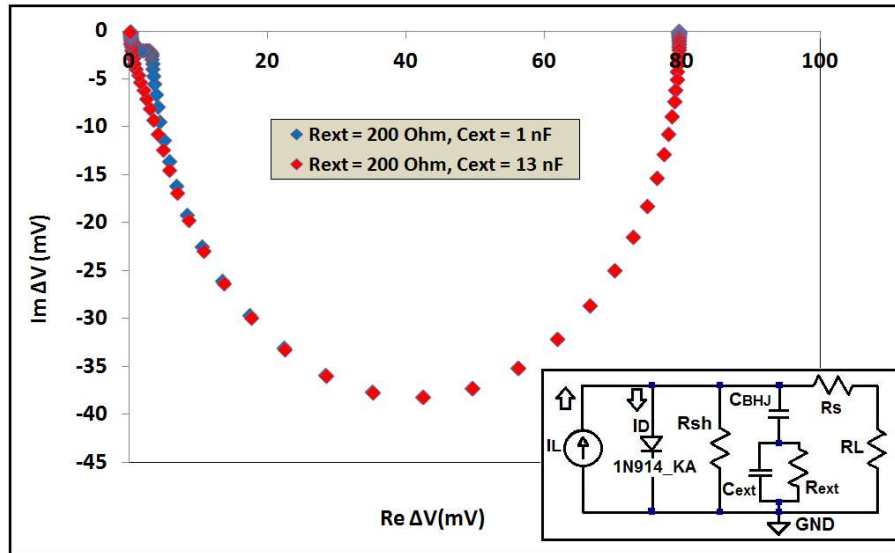


Fig. 6-8. Simulations on an extended equivalent circuit model, shown in the inset. Here, R_L was set to 61 k Ω , while R_{Sh} , R_S , C_{BHJ} were chosen to match the measured values for the stored cell under AM 1.5. (Selection of C_{BHJ} will be discussed in the next subchapter). For simplicity, the diode was represented by a suitable, i.e. 5.5 k Ω differential resistor. Here, the selection of differential resistance magnitude was done similarly with Gundlach et al. and also discussed in the next subchapter. The plot with red symbols was obtained with $C_{ext} = 13$ nF // $R_{ext} = 200$ Ω , while the plot with blue symbols was obtained with $C_{ext} = 1$ nF // $R_{ext} = 200$ Ω .

In Fig. 6-8, when suitable parameters for $R_{ext} // C_{ext}$ are chosen, simulated spectra now include the high frequency ‘shoulder’ or ‘foot’ features, similar to the experimental spectra in Fig. 6-7. The weaker high-frequency feature for a ‘fresh’ sample captures aging at an early stage, note here that a larger value of C_{ext} results in a smaller modification of C_{BHJ} . Modeling thus confirms the origin of the ageing-related high-frequency feature, which is located at the BHJ itself. The aging of the OPV was the subject of detailed recent studies, where a number of different degradation mechanisms were reported as described also in 2.3 [57, 145]. Also from 2.3, an important mechanism that will occur even in dark storage is the etching of the ITO electrodes by the acidic dopant of the PEDOT:PSS hole extraction layer, i.e. polystyrene sulfonic acid (PSS), which liberates indium ions. A Rutherford Backscattering Spectrometry (RBS) study by Janssen et al. [81] and TOF-SIMS studied by Jonkheijm et al. [82], on model devices with PEDOT:PSS hole-extracting layer (HEL) showed that indium will subsequently diffuse across the hole-extracting layer into the BHJ region. The presence of indium will then create instability within the BHJ layer and reduce the OPV’s performance over time [57]. This decrease in performance can be caused by a reduction in the BHJ area size, hence reducing the number of extracted carrier from the BHJ, which is then represented with a R_{ext} in the BHJ branch [57]. At the same time, trap sites can also form in the BHJ due to layer discontinuity caused by Indium penetration, thus creating a capacitance C_{ext} and in turn the $R_{ext} // C_{ext}$ in the C_{BHJ} branch (Fig. 6-8 inset). Hence, from the Fig. 6-8 model, it is likely that $R_{ext} // C_{ext}$ represents the trap-assisted recombination which causes carrier losses in the C_{BHJ} . We can, therefore, as a likely cause, assign the

ageing-related high-frequency feature to the diffusion of indium ions that originate from the etching of ITO by PSS to the BHJ. On the other hand, based only on the simulation results, we cannot conclusively assign the ageing-related high-frequency feature to the diffusion of indium ions and that other causes may have contributed to the appearance of such feature. In order to determine the exact cause of this feature or whether it originated from the diffusion of indium ions into the BHJ, we can perform similar RBS and TOF-SIMS experiments mentioned earlier in this paragraph [81, 82].

6.3 Determination of Bulk Heterojunction (BHJ) Capacitance on OPV Device with PEDOT Hole Extraction Layer

Finally, we also used IMS on another stored OPV sample with the same PEDOT HEL to determine the sample's BHJ capacitance, in the sense of C_{BHJ} within the equivalent circuit model, as seen in Fig. 6-8 inset, at a voltage point near MPP. The C_{BHJ} component itself cannot be derived from DC J/V measurements. Thus here, we added different external capacitive loads, C_L , and connect it in parallel to an already fixed external $R_L = 32.7 \text{ k}\Omega$ ($C_L // R_L$) in Fig. 4-5(a), and identified f_c with IMS by using the setup and procedure described in 4.2. From the resulting Nyquist spectra, we found that the corner frequency dropped with increasing parallel C_L , as shown in Table VII.

TABLE VII Corner Frequency vs. External Load Capacitance, C_L , R_L was fixed at 32.7 k Ω

C_L [nF]	f_c [Hz]
0	2400 \pm 1
0.39	2200 \pm 1
0.47	2100 \pm 1
1	1900 \pm 1
2.2	1600 \pm 1
4.7	1100 \pm 1

In order to evaluate the behaviour of IMS spectra under $C_L // R_L$, we hypothetically replace the diode in the generic equivalent circuit (Fig. 6-5(a)) by its incremental resistor R_D , which is justified for a given voltage point and small modulation amplitudes (i.e. $\Delta L \ll L$; note also that we have dropped ΔI to 1 mA to find f_c under C_L). Also here, R_D replaced the diode in Fig. 6-5(a), hence, the circuit's corner frequency will be given by equation (28).

$$\frac{1}{\omega_c} = \frac{1}{(2\pi f_c)} = C_{BHJ} (R_D // R_{sh} // R_L) \quad (28)$$

Where the '//' symbol stands for the total resistance resulting from parallel resistors. If an external load capacitor C_L is added in parallel to load resistance R_L , the extended circuit corner frequency will then be given by equation (29), with the corner frequency indicated by a prime notation.

$$\frac{1}{\omega_{c'}} = \frac{1}{(2\pi f_{c'})} = (C_{BHI} + C_L)(R_D // R_{Sh} // R_L) \quad (29)$$

Equations (28), (29) rely on two assumptions, one is that $R_S \ll R_L$ and thus R_S can be neglected in the expression for the total effective resistance, i.e. $(R_D // R_{SH} // (R_L + R_S))$, seen by the photocurrent source, I_L . While the other assumption is that $R_S C_L \ll (C_L + C_{BHI})(R_{Sh} // R_D)$. We verified the latter assumption by checking that the two criteria for f_c (i.e. -45° phase shift, -3 dB amplitude drop = drop to 71% w.r.t. low-frequency modulation amplitude) are met simultaneously. This observation also implies that the pole resulting from C_{BHI} is well separated from any higher frequency pole due to C_{ext} (as defined in the inset to Fig. 6-8). This concurs with the previous observation that high frequency 'shoulder' features in Nyquist plots are clearly separated from the dominant, lower frequency corner due to the C_{BHI} component. Hence, high-frequency features related to C_{ext} does not interfere with our determination of C_{BHI} , on the other hand, we can not determine the magnitude of C_{ext} in the way described in equation (29). If we divide equation (28) with equation (29), it will then lead to equation (30a) and (30b), which are mathematically equivalent.

$$C_{BHI} = C_L \left(\frac{f_{c'}}{(f_c - f_{c'})} \right) \quad (30a)$$

$$\frac{f_c}{f_{c'}} = \frac{C_L}{C_{BHI}} + 1 \quad (30b)$$

We can see that equation (30a) relates the unknown BHI capacitance to known C_L , and also measured corner frequencies, without knowledge of ΔL in absolute terms, nor of resistors R_D , R_S , R_{Sh} . Further, equation (30b) suggests a plot of $f_c / f_{c'}$ vs C_L will give a straight line that intercepts the C_L axis at $-C_{BHI}$, thus allowing the determination of C_{BHI} by extrapolation. We show a plot of the data from Table VII in Fig. 6-9, in the form suggested by (30b).

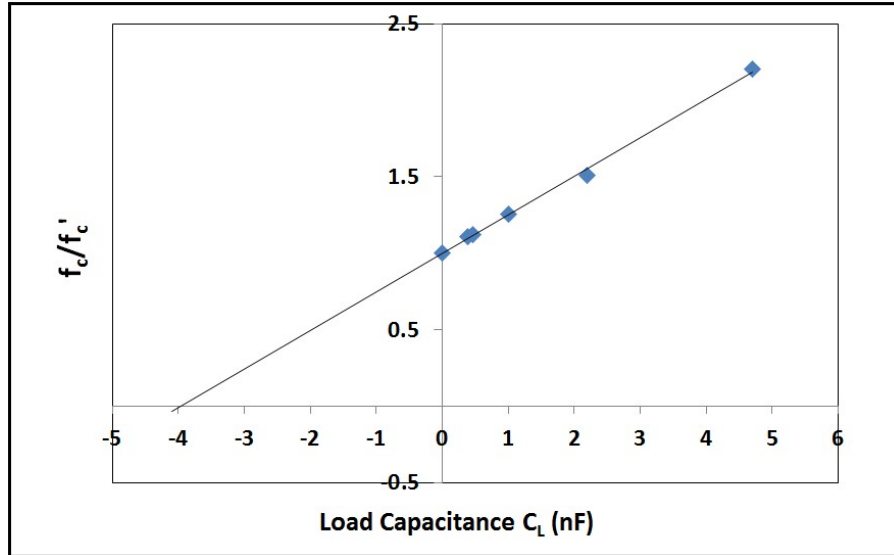


Fig. 6-9. Ratio of corner frequencies for OPV cells not capacitively loaded/loaded with $C_L // R_L = 32.7 \text{ k}\Omega$ vs. magnitude of the capacitive load, C_L . Data from Table VII. The straight line fit intercepts the C_L axis at $-3.9 \pm 0.1 \text{ nF}$.

From Fig. 6-9, we find a good straight line fit which indicates that our underlying assumptions (determination of C_{BHI} from C_L and f_c without knowing ΔL , R_D , R_S , and R_{Sh}) are met. We, therefore, extrapolate a BHI capacitance of 3.9 nF, which corresponds to a specific capacitance of approximately 140 nF/cm^2 . For comparison, we then estimate a hypothetical ‘geometric’ specific capacitance (C_{GEO}), by ‘modeling’ a BHI OPV as a parallel plate capacitor of thickness $d = 100 \text{ nm}$, that is separated by a dielectric medium of dielectric constant $k = 1.5$. This gives a $C_{GEO} = 13.3 \text{ nF/cm}^2$, which is an order of magnitude smaller than the actual BHI capacitance. This significant discrepancy clearly illustrates the inadequacy of approximating a BHI by a parallel plate capacitor, as this ignores the OPV BHI’s large internal interface area. Hence, since maximizing internal interface area is the objective of BHJs, we then propose BHI specific capacitance (C_{BHI}) as an indicator of BHI quality.

6.4 Summary of Results from IMS on OPV with PEDOT:PSS HEL under Finite R_L

From the IMS on OPV with PEDOT HEL under finite R_L , we first found that conducting IMS on the solar cell at finite load resistance R_L values is more advantageous compared to the more established IMPS and IMVS mode as it will reveal more spectral features which would be missed in both the IMPS and IMVS mode. Also, from the Nyquist plot in Fig. 6-1(a) we can derive the $Re \Delta V (f \rightarrow 0)$ and the corner frequency f_c , and construct a plot of $Re \Delta V (f \rightarrow 0)$ vs the voltage point V . We then found that the $Re \Delta V (f \rightarrow 0)$ is similar in shape and pattern to the DC J/V and power profile plots of the OPV under AM 1.5 and under red LED. From the OPV equivalent circuit simulations,

we found that the simulated Nyquist plot and the plot's simulated characteristic feature are very similar to that of the experimental results. The only difference is that the simulated f_c amplitude at voltage point near 0 V and V_{oc} is much higher than that in the experimental results. This is due to the difficulty of simulating an organic diode element with an inorganic ones in the simulation. Also, we found that by conducting IMS at finite R_L , in the context of circuit model, the circuit's R_s , R_L and internal diode, will display significant resistance, thus forcing more current through the BHJ capacitance path, in particular at high frequencies, when capacitive impedance drops. Hence, we conclude that by performing IMS under finite load, we may reveal the presence of spectral features that originated in the cell's BHJ layer, which will not be visible under IMPS and IMVS. In addition, by performing IMS under finite load, we would obtain a much higher ΔV amplitude near the OPV's MPP compared to the ΔV obtained near 0 V and V_{OC} , based on the $Re \Delta V (f \rightarrow 0)$ vs V results. We also conclude that the behaviour of f_c vs voltage point V plot can only be described qualitatively by assuming that f_c corresponds to a time constant that represents the OPV's carrier transit time across the bulk BHJ layer and is influenced by the screening of the built-in voltage from space charges formation within the BHJ layer [47].

We then conducted an aging study on the OPV, by performing IMS on the cell at $R_L = 61 \text{ k}\Omega$ after 30 days of storage under dark and in an ambient atmosphere. We found that the OPV's resulting Nyquist plot semicircle has become larger post-storage and that the high frequency 'shoulder' feature becomes more pronounced and separated from the dominant semicircle post-storage when compared to the 'shoulder' in the fresh cell's Nyquist plot. Therefore, the 'shoulder' feature is aging-related. We also found that if we modify the OPV equivalent circuit [132], by connecting a resistor in-parallel to a capacitor ($R // C$) in series with the BHJ capacitance, with both the resistor and capacitor having a certain magnitude, we can correctly simulate the 'shoulder' feature that appears in Fig. 6-7 Nyquist plot. Hence, we conclude that based solely on the modified circuit simulation, the origin of the high-frequency 'shoulder' feature in the fresh or stored cell Nyquist plot is located in the OPV's BHJ layer. A likely cause of this feature, though not conclusive, is the diffusion of indium ions from the ITO into the BHJ due to the ITO etching by the PSS in PEDOT HEL [81, 82].

We can also determine the OPV's BHJ capacitance (C_{BHJ}) by conducting IMS near MPP on a modified form of Fig. 4-5(a) setup, where we connect external capacitive loads (C_L) of different values in-parallel with the OPV and R_L connection, in which the R_L is set at $32.7 \text{ k}\Omega$. From the resulting Nyquist plot of this IMS, we found that the OPV's f_c dropped with increasing C_L magnitude. In addition, from the f_c results before (f_c) and after (f_c') the addition of C_L , and also equations (28)-(30b), we found that we can construct a plot of f_c / f_c' vs C_L which gives us a straight line that intercepts the C_L axis at $-C_{BHJ}$, thus allowing the determination of C_{BHJ} by extrapolation. From the f_c / f_c' vs C_L

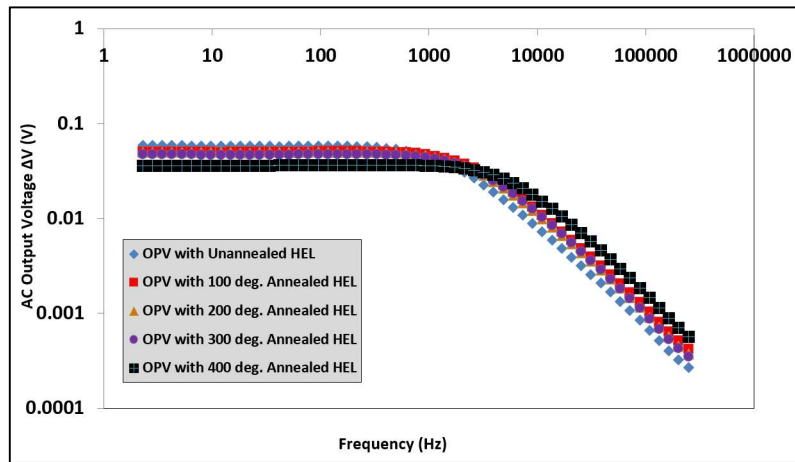
plot's fit, we found a figure of merit for $C_{BHJ} = 3.9$ nF, which corresponds to a specific capacitance of approximately 140 nF/cm².

6.5 Results from IMS on OPV with V₂O_{5-x} Hole Extraction Layer at Maximum Power Point Voltage (V_{MPP})

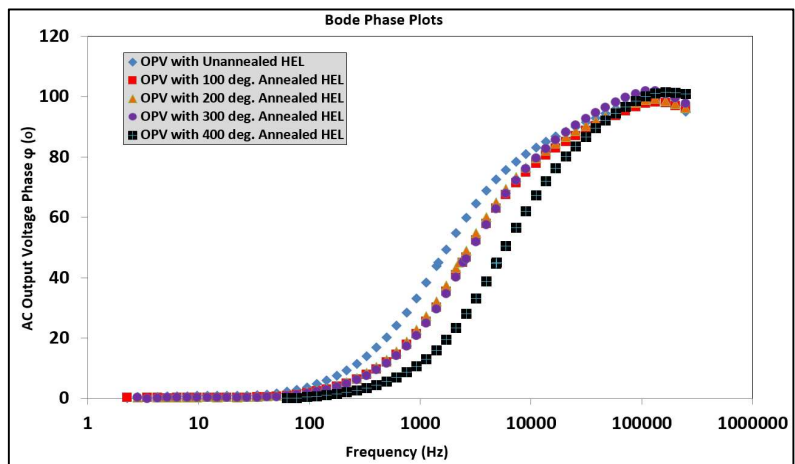
From IMS on OPV with PEDOT results in 6.1 and 6.2, it is clear that an alternative to PEDOT:PSS as a hole extraction layer (HEL) must be used to avoid BHJ degradation due to indium ions diffusion [57]. As described in 2.3, another example of a material that can be used as an HEL material and has been shown to have the same or better performance as HEL compared to PEDOT is vanadium pentoxide or V₂O₅ [83-85]. In addition, V₂O₅ can be deposited on the cell via solution processing, thus enabling a low-temperature OPV fabrication that will not damage the OPV's semiconductor layer [85]. Also from 2.3, Alsulami et al. have recently performed an investigation on the effect of thermal annealing on a solution-processed V₂O_{5-x} as the HEL of a BHJ OPV, in which the structure has been described in 3.1.2 [86]. Among the purpose of their research are also similar to the beginning of this paragraph, i.e. to find an alternative HEL that would not degrade the OPV and its organic semiconductor layer, adaptable to the different type of solar cells and has similar or even better performances compared to PEDOT HEL in an OPV. In their research, they compare the performances (in terms of J/V data) of BHJ OPVs with their V₂O_{5-x} HEL annealed at 100, 200, 300 and 400 °C before the BHJ layer deposition with an OPV in which the V₂O_{5-x} HEL is unannealed. In addition, they also utilize a number of different techniques, i.e. absorption spectroscopy, X-ray photoelectron spectroscopy (XPS) and ultraviolet photoelectron spectroscopy (UPS), to analyze and explain the resulting OPVs J/V characteristics [86]. Most importantly, they found that the thermal annealing of V₂O_{5-x} HEL in the OPV does not improve performance significantly in terms of PCE when compared to the unannealed devices. Further, based on the OPVs J/V characteristics, they found that there are no significant PCE differences between the unannealed OPV and those with their V₂O_{5-x} HEL annealed at 100 and 200 °C before the BHJ layer deposition. While for OPV with their V₂O_{5-x} HEL annealed at 300 and 400 °C before BHJ deposition, their PCE decreases based on the J/V characteristics. Also, based on their absorption spectroscopy results, they have established that there are no relationship at all between the OPVs performance and the band gap variations between the OPV with unannealed and annealed V₂O_{5-x} HEL. While from XPS results, they found that heating the V₂O_{5-x} at 300 and 400 °C will generate oxygen vacancies in the V₂O_{5-x} thus resulting in the reduction of the V₂O_{5-x} layer from V₂O_{4.93} to V₆O₁₄. The presence of additional oxygen vacancies due to heating in the V₂O_{5-x} will then result in the decrease of the respective OPVs V_{oc} , and consequently the reduction of their PCE . Finally, from the UPS results, they conclude that annealing the V₂O_{5-x}

HEL at 300 and 400 °C would shift the V_2O_{5-x} Fermi level much nearer to its conduction band, which as a result, would fill the states within the V_2O_{5-x} band gap and thus decreasing its work function which then results in the decrease of the respective devices (300 and 400 °C annealed V_2O_{5-x} HEL) *PCE* [86].

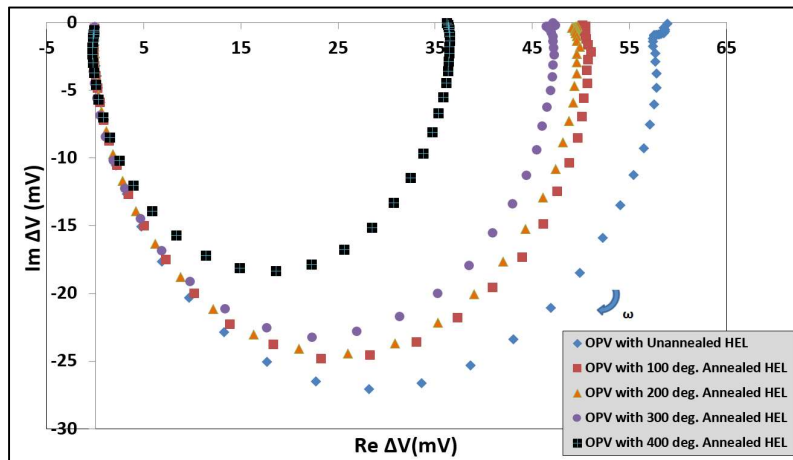
Based on previous research on finding alternative HEL to replace PEDOT and this recent research from Alsulami et al. [86], we then use our IMS instrument and method to investigate the dynamics of the BHJ OPV described in 3.1.2, which has the same OPV structure and types as the ones fabricated and characterized by Alsulami et al. Thus, the characterized cell consists of an OPV with non-annealed V_2O_{5-x} HEL, and cells with their HELs annealed at 100, 200, 300 and 400 °C before the deposition of the BHJ layer. In addition, we also investigate the effect of thermal annealing on the previously mentioned OPV with V_2O_{5-x} as the HEL. We then compare the dynamics of OPV with 100, 200, 300 and 400 °C annealed and unannealed V_2O_{5-x} HEL and then investigate how the respective OPVs dynamic changes after 13 days of storage under dark condition. As mentioned earlier in this chapter, we perform IMS with the same setup, instrument settings, and procedure as described in 4.2. However here, we conduct IMS at the respective OPV maximum power point (MPP), or specifically, at its MPP voltage (V_{MPP}). We determine the cells V_{MPP} based on their J/V plots in Fig. 3-4 and as listed in Table III. We then set the OPV's R_L value to obtain the V_{MPP} mentioned before, with R_L being the resistance at MPP (R_{MPP}). From Table III in 3.1.3, the V_{MPP} for the unannealed cell with V_2O_{5-x} HEL, and cells with the V_2O_{5-x} HEL annealed at 100, 200, 300 and 400 °C are respectively 720, 720, 700, 620 and 560 mV. In Fig. 6-10(a), (b) and (c) we present the IMS results of cells with unannealed and annealed cell with V_2O_{5-x} HEL, in the form of Bode amplitude, phase and Nyquist plot of their ΔV at MPP at f between 1 Hz and 250 kHz.



(a)



(b)



(c)

Fig. 6-10 (a). Bode amplitude and (b) phase of ΔV with respect to frequency f , of OPV with non-annealed V_2O_{5-x} HEL (blue plots), followed by cells with their V_2O_{5-x} HEL annealed at 100, 200, 300 and 400 °C pre-BHJ deposition (shown respectively as the red, orange, purple and black colour in the inset). (c). Nyquist plots results of an OPV with non-annealed V_2O_{5-x} HEL (blue plots), followed by cells with their V_2O_{5-x} HEL annealed at 100, 200, 300 and 400 °C pre-BHJ deposition (shown respectively as the red, orange, purple and black colour in the inset). Note the extended semicircles which crossed from the 4th to 3rd quadrant at high f . Here, all spectra were taken at the respective cells V_{MPP} by setting the external R_{MPP} accordingly and at f between 1 Hz and 250 kHz. The LED was driven by $I_{LED} = (18 \pm 4)$ mA. Also, the Re/Im axis at (c) uses different scales and are not normalized, with the direction of increasing frequency given by the blue arrow.

From Fig. 6-10(a), the cell with unannealed V_2O_{5-x} HEL has the highest ΔV at ($f \rightarrow 0$), while ΔV at ($f \rightarrow 0$) is lower for cells with higher HEL annealing temperature. So as the respective cells V_{MPP} decreases, as seen in Fig. 3-4 J/V plots, their (the cells) ΔV ($f \rightarrow 0$) decreases as well. In addition, we also observed that all Fig. 6-10(a) plots have their corner frequencies (f_c) at around 2 kHz. The f_c , as in 5.1, is related to a time constant τ through $f_c = 1/2\pi\tau$. The time constant τ represent a system's internal dynamic time constant. From Fig. 6-10(a), we also observe that as ΔV ($f \rightarrow 0$) decreases from the highest in a cell with unannealed HEL to the lowest in a cell with 400 °C annealed HEL, the respective cells f_c also increases. As f_c is related to an internal dynamic time constant τ , higher f_c means a shorter dynamic time constant τ in the system. Since ΔV ($f \rightarrow 0$) is a near DC quantity, it, cannot directly explain the increase in f_c for cells with higher HEL annealing temperature. A likely explanation is that the time constant τ (from f_c) is actually a carrier transit time. Hence, similar to Alsulami et al. findings, heating the HEL further may generate oxygen vacancies in the V_2O_{5-x} which in turn results in the decrease of the respective OPVs ΔV ($f \rightarrow 0$) in OPV with higher HEL annealing temperature. While at the same time, heating the OPVs HEL further will also remove any possible contaminants or vapours inside the HEL, thus carrier transport will happen much faster/at a shorter time in OPVs with higher HEL annealing temperature [86, 146]. Also, all (Fig. 6-10(a)) plots roll off $= -1.0 \pm 0.1$. As elaborated in 5.1, a roll-off ~ -1 in a system indicates that it behaves as a first order system [36]. However, organic photovoltaics hardly behave as a first order system [1, 9], instead of in the context of IMS, roll-off ~ -1 means that there will be a single dynamic that dominates the system under light. This single dynamic, as in 5.1, is represented by a single time constant τ , and that it will appear as a single semicircle in a Nyquist plot [24].

From Fig. 6-10(b), we see that ΔV phase (φ) decreases for cells with higher HEL annealing temperature. This is observed from the increase in frequency where $\varphi = 45^\circ$, in other words, from the increase in corner frequency f_c . From 5.1 and 6.3, the corner frequency f_c is defined as the frequency where $\varphi = 45^\circ$. Thus, the ΔV phase (φ) results in Fig. 6-10(b) are consistent with ΔV results in Fig. 6-10(a), i.e. for cell's with higher HEL annealing temperature, their respective f_c also increases. Also, in all Fig. 6-10(b) plots, the frequencies where $\varphi = 45^\circ$ are at $f \sim 2$ kHz, which are also consistent with the f_c obtained from Fig. 6-10(a), i.e. $f_c \sim 2$ kHz. Further, we also observe a peak in the high-frequency region ($f > 100$ kHz) in all Fig. 6-10(b) plots. Here, the phase peaks at high frequencies can manifest itself in the form of a "3rd quadrant" feature in a Nyquist plot, which is similar to the "3rd quadrant" (negative $Re \Delta V$) feature reported by Semenkikhin et al. in the IMPS result of an OPV with different BHJ mixture [47]. In addition, the same author (Semenikhin et al.), also offered an extensive explanation for the "3rd quadrant" feature in the context of IMPS in their 2008 paper [50]. In that paper, the "3rd quadrant" feature in their IMPS result is associated with the slow transport of

photocurrent, so as the photocurrent increases with time, in a frequency-based measurements, the phase of slow photocurrent will lag behind that of the light intensity, thus producing a negative phase result as seen in Fig. 6-10(b) [50]. Note that the spectra are neither under IMPS or IMVS, but instead under an MPP load or at MPP. In addition, we also found that the phase peaks at high frequencies tend to increase as we annealed the HEL further. A likely explanation for the increase in the phase peak at high frequencies is that in a cell with unannealed V_2O_{5-x} HEL, there will be a higher presence of contaminants and water vapor in the V_2O_{5-x} layer compared to cells with annealed V_2O_{5-x} HEL. So as the V_2O_{5-x} HEL is annealed further, heat may generate oxygen vacancies in the HEL, while also removing possible contaminants within the HEL and improving carrier transport in the process, thus reducing the phase peak or the lag in phase experienced by the photocurrents [86, 146]. This is consistent with Fig. 6-10(b) plots, in that the negative phase is larger in the cell with unannealed V_2O_{5-x} HEL, and that as the V_2O_{5-x} HEL is annealed further, the phase slowly becomes more positive.

From Fig. 6-10(c), we observe that, consistent with Fig. 6-10(a) and (b) results, the general shape of all Nyquist spectra resembles a single semicircle in the complex plane 4th quadrant, with the exception of one result from a cell with unannealed V_2O_{5-x} HEL, where we see the presence of a “foot” feature in the low-frequency region. As this feature occurs in the low-frequency region, it can be associated with traps or parasitic resistances in the cell contacts [21]. Note also that the Re / Im axis in Fig. 6-10(c) uses different scales and are not normalized. The presence of a single semicircle in all plots means that the respective cells internal dynamic will be dominated by a single internal dynamic with a time constant τ . Also, we observe that at high frequency, all semicircles in Fig. 6-10(c) crossed to the 3rd quadrant from the 4th at a certain frequency point. We call this feature a ‘3rd quadrant’ feature and it is characterized by the frequency point where the semicircle crossed to the 3rd quadrant, which is called the 3rd quadrant frequency or f_{3rd} . Here, f_{3rd} represents another internal dynamic besides that of f_c . A magnification of this feature between Fig. 6-10(c) plots 3rd and the 4th quadrant is depicted in Fig. 6-11.

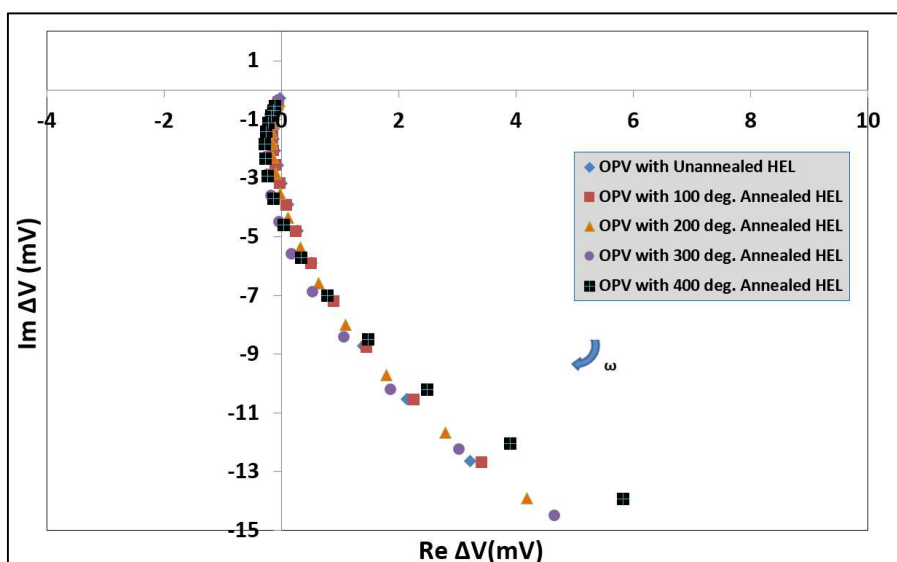


Fig. 6-11. Magnification of the same plots in Fig. 6-10(c) in-between the 3rd and 4th quadrant. Note that here, f_{-3rd} does not change much for cells with higher HEL annealing temperature. Also, the Re/Im axis here also uses different scales and are not normalized, with the direction of increasing frequency given by the blue arrow.

From Fig. 6-11, we can see that f_{-3rd} does not change much in cells with higher HEL annealing temperature. This meant that f_{-3rd} cannot be correlated directly to the change in negative phase as the HEL annealing temperature is increased. In other words, f_{-3rd} is related to the presence of negative phase in Fig. 6-10(b), but the change in that negative phase as the annealing temperature is increased cannot be related directly to f_{-3rd} . A possible explanation for this is that since f_{-3rd} designates the frequency where the phase started to become negative, it is possible that it represents a lagging mechanism or some sort of trap that causes carrier transport to be slower, thus resulting in a negative phase and $Re \Delta V$ [50]. So as the photocurrent increases over time, there will be a trap mechanism that becomes apparent at f_{-3rd} and for the cells in this discussion, it occurs roughly at the same f_{-3rd} .

Overall, the presence of a “3rd quadrant” feature itself is consistent with the presence of negative phases in Fig. 6-10(b) phase plots. The overall cells dynamic, though, are still dominated by f_c , as evident from the general semicircle shape of all plots in Fig. 6-10(c). We also see from Fig. 6-10(c) that the cell with unannealed HEL has the highest $Re \Delta V$ at ($f \rightarrow 0$) and also the largest semicircle. While for cells with higher HEL annealing temperature, their $Re \Delta V$ ($f \rightarrow 0$) are lower along with reductions in semicircle sizes. This is again due to our selection of V_{MPP} that is also related to $Re \Delta V$ ($f \rightarrow 0$) since $Re \Delta V$ ($f \rightarrow 0$) and ΔV at ($f \rightarrow 0$) are basically similar. So as the respective cells V_{MPP} decreases, their (the cells) $Re \Delta V$ ($f \rightarrow 0$), along with their semicircle size, will also decrease. Finally, we also observe that at all plots in Fig. 6-10(c), there is no visible high frequency “shoulder” similar to what we see in Fig. 6-1(a) for OPV with PEDOT HEL. Instead, it is replaced by a “3rd quadrant” feature in the high-frequency region. This shows a possibility that by replacing the OPV HEL with

V_2O_{5-x} , the current cells are able to avoid degradation due to indium diffusion into the BHJ layer that originates from the etching of ITO by PSS.

We can extract four characteristic parameters from Fig's 6-10(a),(b),(c) and 6-11. These parameters are, $Re \Delta V (f \rightarrow 0)$, f_c and f_{-3rd} . The f_c is the frequency where $\varphi = 45^\circ$ and f_{-3rd} is the frequency where the semicircles crosses from the 4th to 3rd quadrant. Also, $\Delta V (f \rightarrow 0)$ in Fig. 6-10(a) is not included, as this parameter is similar to $Re \Delta V (f \rightarrow 0)$ in Fig. 6-10(c). We then list all of the characteristic parameters and OPV types, including the electrical conditions in which we obtain the plots, i.e. V_{MPP} and R_{MPP} , in Table VIII.

TABLE VIII OPV TYPES, V_{MPP} , R_{MPP} , $\Delta V (f \rightarrow 0)$, $Re \Delta V (f \rightarrow 0)$, f_c AND f_{-3rd} FOR THE SPECTRA SHOWN IN FIG. 6-10(a), (b),(c) AND 6-11.

OPV Types	V_{MPP} [mV]	R_{MPP} [k Ω]	$Re \Delta V (f \rightarrow 0)$ [mV]	f_c [Hz]	f_{-3rd} [Hz]
Non Annealed HEL	720	445	59 ± 10	1500 ± 1	25000 ± 1
100 °C Annealed HEL	720	64	51 ± 10	2400 ± 1	39000 ± 1
200 °C Annealed HEL	700	71	50 ± 10	2300 ± 1	31000 ± 1
300 °C Annealed HEL	625	139	47 ± 10	2500 ± 1	25000 ± 1
400 °C Annealed HEL	565	48	36 ± 10	5000 ± 1	39000 ± 1

From Table VIII, we can confirm that the selection of V_{MPP} does determine the $\Delta V (f \rightarrow 0)$ and $Re \Delta V (f \rightarrow 0)$ results as seen in Fig. 6-10(a) and (c). Thus, as the respective cell's V_{MPP} decreases, from the highest in the cell with unannealed V_2O_{5-x} HEL to the lowest in the cell with 400 °C annealed HEL, their $\Delta V (f \rightarrow 0)$, and also the $Re \Delta V (f \rightarrow 0)$ decreases as well. As a proof, the resistance at MPP or R_{MPP} of the respective cells is rather random, since the behavior of both $\Delta V (f \rightarrow 0)$ and $Re \Delta V (f \rightarrow 0)$ are determined only by the selection of V_{MPP} . In addition, we also confirmed that as $\Delta V (f \rightarrow 0)$ decreases from the highest in the cell with unannealed HEL to the lowest in the cell with 400 °C annealed HEL, the respective cells f_c also increases. Hence, as f_c is related to an internal dynamic time constant τ , the dynamic inside cells with higher HEL annealing temperatures occurs much faster (or at a much shorter time) compared to a cell with unannealed HEL or at lower HEL annealing temperature. As such, it is likely that τ is a carrier transit time, and for cells with higher HEL annealing temperature, carrier transport will happen much faster since extra heating may remove any contaminants in the V_2O_{5-x} HEL aside from generating oxygen vacancies in the layer itself. Finally, we can also confirm that f_{-3rd} does not change much for cells with higher HEL annealing temperatures. Hence, as mentioned before, f_{-3rd} represents a lagging mechanism or a trap that causes carrier transport to be slower, thus resulting in a negative phase and $Re \Delta V$ [50]. Therefore, as the photocurrent increases over time, there will be a trap mechanism that becomes apparent at f_{-3rd} and for the cells here, it occurs roughly at the same f_{-3rd} . We investigated the dependency of the characteristics parameters in Table VIII with respect to changes in V_{MPP} , from the highest V_{MPP} in a cell with

unannealed HEL to the lowest V_{MPP} in a cell with 400 °C annealed HEL, by using an equivalent circuit model similar to Fig. 6-5(a) in 6.1. We will also investigate the underlying cause behind the “foot” feature that is visible in the low-frequency region of the cell with unannealed HEL.

From Fig. 6-5(a) circuit in 6.1, we found that the simulated Nyquist plots of the generic OPV equivalent circuit give exact semicircles/ellipses at all voltage points without the presence of any high-frequency feature, even when the simulated cells are loaded to near MPP. If we perform IMS under finite load, or at a cell MPP, where $R_L = R_{MPP}$, the current generated by the cell’s current source I_L in Fig. 6-5(a) will flow through the BHJ capacitance path, especially at high frequencies, when capacitive impedance drops. This is because, under finite load, both the external current path and the internal diode in the Fig. 6-5(a) equivalent circuit will display a significant resistance. Here, we found the presence of a “3rd quadrant feature” in the high-frequency area at all the plots in Fig. 6-10(c). As such, Fig. 6-5(a) circuit has to be modified to account for the mode in which we perform IMS and the “3rd quadrant” feature in our plots. From earlier, we found that f_{-3rd} designates the frequency where the phase started to become negative and that it is possible that f_{-3rd} represents a lagging mechanism or a trap that causes slower carrier transport, which results in a negative phase and $Re \Delta V$. We, therefore, reason that there is a possibility that carriers take a slower path of transport, not through the BHJ capacitance, but through the external current path, such that they will lag behind the light intensity, thus producing the negative phase and $Re \Delta V$. We then extend Fig. 6-5(a) generic equivalent circuit by adding a fixed value capacitor in parallel between R_s and R_L to represent the slower path carriers take to represent the “3rd quadrant” feature. This is because at f_{-3rd} , the photocurrent changes its phase and that the trap mechanism represented by f_{-3rd} will be the same for all cells. We then depict respectively the extended equivalent circuit and simulated spectra from the extended circuit in Fig. 6-12(a), (b) and (c).

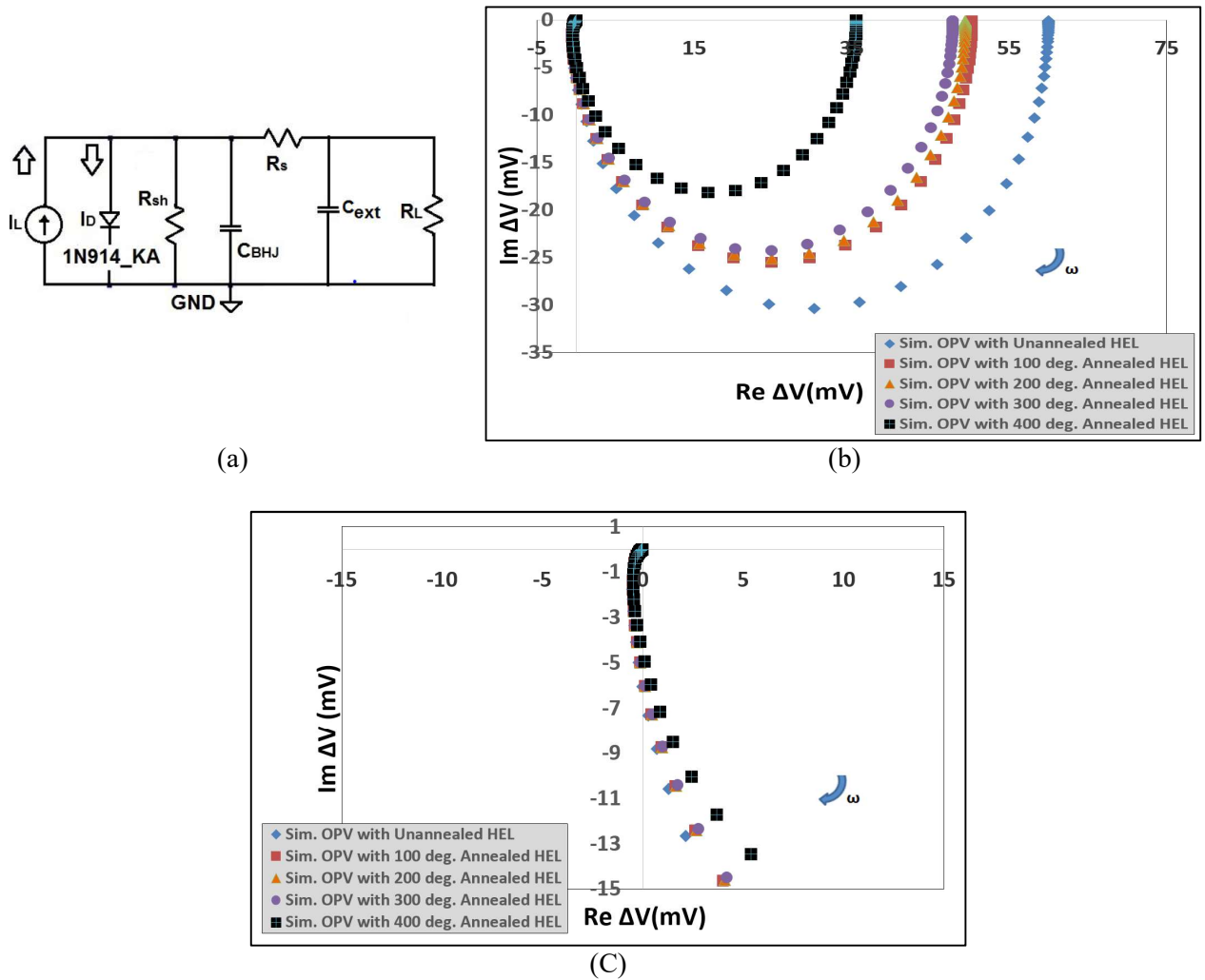


Fig. 6-12 (a). The modified OPV generic equivalent circuit which shows the extended capacitor component (C_{ext}) in parallel between series (R_s) and load resistance (R_L). The C_{ext} component represents the slower carrier path through the cell's external circuit which results in the "3rd quadrant" feature. (b) Simulated Nyquist plot for a cell with unannealed V_2O_{5-x} HEL and cells with its V_2O_{5-x} HEL annealed at 100, 200, 300 and 400 °C (sample types are shown in the colour coded inset). For the simulation, we set the DC current bias (I_{DC}) = 25 μA with current modulation (I_{AC}) = 5 μA_p for all cells. Here, we again use the modified 1N914_KA diode and C_{BJJ} = 4 nF in the circuit. We then set C_{ext} = 2 nF. We also set the shunt resistance (R_{sh}) = 32, 36, 35, 35 and 42 k Ω for cells with unannealed, 100, 200, 300 and 400 °C annealed V_2O_{5-x} HEL respectively. All of the cells series resistances (R_s) are set to R_s = 577 Ω . Also, the R_L magnitudes are set to = 155, 130, 150, 160 and 140 k Ω for cells with unannealed, 100, 200, 300 and 400 °C annealed V_2O_{5-x} HEL respectively. (c) Magnification of the same plots in (a) in-between the 3rd and 4th quadrant. Also here, f_{3rd} does not change much for cells with higher HEL annealing temperature. Finally, the simulation in (b) is set between 1 Hz and 250 kHz, while the Re/Im axis in (b) and (c) uses different scales and are not normalized, with the direction of increasing frequency given by the blue arrow.

For simulation purposes, the DC current bias (I_{DC}) amplitude was set to = 25 μA with current modulation (I_{AC}) = 5 μA_p for all cells. This is because we are simulating the behaviour of the same current source I_L in Fig. 6-5(a), since here, the cells here are also illuminated by the same red LED which has the same LED driving current (I_{LED}) condition, i.e. I_{LED} = (18 \pm 4) mA. We also select C_{BJJ} = 4 nF and the circuit's diode component as the 1N914_KA model, this is because the cell has the same BJJ mixture as in 6.1 and that we assume the BJJ capacitance will also be the same as determined in 6.3. While the 1N914_KA was selected as the diode model with the same reasoning as

in 6.1, i.e. to account for the presence of an organic diode component in the OPV from the modification of stock diodes available in SPICE simulation. We then set the circuit's shunt resistance (R_{sh}) = 32, 36, 35, 35 and 42 k Ω for cells with unannealed, 100, 200, 300 and 400 $^{\circ}\text{C}$ annealed V_2O_{5-x} HEL respectively. Also, all of the cell's series resistances (R_s) are set to $R_s = 577 \Omega$. While the R_L magnitudes are set to = 155, 130, 150, 160 and 140 k Ω for cells with unannealed, 100, 200, 300 and 400 $^{\circ}\text{C}$ annealed V_2O_{5-x} HEL respectively. The R_{sh} and R_s here were based on the cell's J/V characteristics in Table III (in 3.1.3). The values of R_L were an approximation of the real R_L values listed in Table VIII. All three resistance values (R_{sh} , R_s , and R_L) were mainly selected to closely replicate Fig. 6-10(c) $Re \Delta V$ values. Finally, we set the magnitude of the extended capacitor, component (C_{ext}) as $C_{ext} = 2 \text{ nF}$. This is to obtain an identical "3rd quadrant" feature at high frequency. Also, Fig. 6-12(b) simulated plots are taken at f between 1 Hz and 250 kHz.

From Fig. 6-12(b), we see that the simulated plots give the exact single semicircles of Fig. 6-10(c) plots for all types of cells. This means that there is indeed a single internal dynamic that dominates all of the cells under light. In addition, the simulated plots are also able to replicate the $Re \Delta V$ magnitude seen in Fig. 6-10(c) and Table VIII for all cells, together with the decrease in semicircle sizes from the largest for the cell with unannealed V_2O_{5-x} HEL to the lowest for the cell with 400 $^{\circ}\text{C}$ annealed V_2O_{5-x} HEL. In addition, from Fig. 6-12(b) and (c), we can see that the simulated plots also manage to replicate the "3rd quadrant" feature that crosses from the 4th to 3rd quadrant as seen in Fig. 6-11. We also see that, as in Fig. 6-11, the "3rd quadrant" feature does not appear to change much for cells with higher HEL annealing temperatures, thereby confirming our choice of using a fixed value capacitor C_{ext} to simulate the same lagging/trap mechanism that is encountered by carriers for all cells at high frequencies, as represented by the quantity f_{-3rd} . However, as seen in Fig. 6-12(b), we are unable to simulate the "foot" feature in the low-frequency region (Fig. 6-10(c)) based on Fig. 6-12(a) model. This is because the modification that we do to the original equivalent circuit from Narayan et al. [132] only accounts for the high-frequency behaviour of the OPVs at near MPP, i.e. by adding a C_{ext} component in-parallel with R_s and R_L . To account for both the high- and low-frequency behaviour of OPV with unannealed HEL at near MPP (i.e. the 'shoulder' and 'foot' feature respectively), we need to add another component in the circuit besides the C_{ext} . Finally, from simulated results in Fig. 6-12(b) and (c), we derived the same four characteristics parameters as in Table VIII, these are $Re \Delta V$ ($f \rightarrow 0$), f_c and f_{-3rd} . We then list all of the characteristic parameters and OPV types, including the electrical conditions in which we obtain the plots, i.e. V_{MPP} and R_{MPP} , in Table IX. Note that in Fig. 6-12(b) simulations, $R_L = R_{MPP}$ and the DC voltage measured in SPICE in the node between R_s and R_L determines the V_{MPP} .

TABLE IX OPV TYPES, V_{MPP} , R_{MPP} , $\Delta V(f \rightarrow 0)$, $Re \Delta V(f \rightarrow 0)$, f_c AND f_{-3rd} FOR THE SPECTRA SHOWN IN FIG. 6-12 (b) AND (c).

OPV Types	V_{MPP} [mV]	R_{MPP} [k Ω]	$Re \Delta V$ ($f \rightarrow 0$) [mV]	f_c [Hz]	f_{-3rd} [Hz]
Non Annealed HEL	607	155	59	2200	22000
100 °C Annealed HEL	621	130	50	2600	22000
200 °C Annealed HEL	623	150	49	2600	22000
300 °C Annealed HEL	625	160	48	2700	22000
400 °C Annealed HEL	646	140	36	3500	26000

From Table IX, we see that by selecting $R_L = R_{MPP}$, R_{sh} and R_s such that the simulated $Re \Delta V(f \rightarrow 0)$ replicates the $Re \Delta V(f \rightarrow 0)$ in Table VIII, we confirm that the selection of V_{MPP} in the experiment does determine $\Delta V(f \rightarrow 0)$ and $Re \Delta V(f \rightarrow 0)$ results as seen in Fig. 6-10(a) and (c). In the SPICE simulation, since we cannot set the measured voltage point (in this case V_{MPP}) directly, we replicate the $Re \Delta V(f \rightarrow 0)$ by setting the three resistances ($R_L = R_{MPP}$, R_{sh} , and R_s) accordingly in Fig. 6-12(a) circuit, as such, the V_{MPP} obtained from the simulation will also be set based on those three resistances. This is, of course, analogous to setting V_{MPP} first and obtaining R_L at that V_{MPP} point (R_{MPP}), which in turn are the electrical conditions where we obtained $\Delta V(f \rightarrow 0)$ and $Re \Delta V(f \rightarrow 0)$ as seen in Table VIII. Thus, the decrease in $\Delta V(f \rightarrow 0)$ and $Re \Delta V(f \rightarrow 0)$, as seen in Fig. 6-10(a), from the highest in the cell with unannealed V_2O_{5-x} HEL to the lowest in a cell with 400 °C annealed HEL, are attributable to our selection of V_{MPP} , and consequently R_{MPP} in this experiment.

In addition, we can confirm that cells with higher HEL annealing temperatures have indeed a higher corner frequency f_c . Thus, as f_c is related to an internal dynamic time constant τ , the dynamic inside cells with higher HEL annealing temperatures occurs much faster compared to a cell with unannealed HEL or at lower HEL annealing temperatures. To add, we also see that the f_c magnitude replicates well in Table IX when compared to Table VIII for real results. While f_{-3rd} is lower in Table IX but not too different compared to f_{-3rd} in real results. From our earlier reasoning, we found that under finite load, carriers normally went through the C_{BHJ} branch in Fig. 6-12(a) as it offers the least amount of resistance. So the Nyquist plots in Fig. 6-12(b) will be dominated by the dynamics of C_{BHJ} in the cell. As such, to determine the internal dynamic that occurs in the cells, we also tried to vary Fig. 6-12(a) circuit C_{BHJ} in the simulations (not shown here), and we found that if we change C_{BHJ} to higher or lower values, the corner frequency (f_c) will also change, but if we only change C_{ext} for example, f_c remains the same. Thus, the internal dynamic, or dynamic time constant that occurs here is the carrier transit time τ , and this transit time dominates the cells dynamic response as seen in Fig. 6-10(c), with the transit time itself much shorter for cells with higher HEL annealing temperature. As for the f_{-3rd} feature, we can physically assign f_{-3rd} to a carrier trap that equally resides at all cells near the cell's series (R_s) and load resistance (R_L) and is not influenced very much by HEL heating, thus f_{-3rd}

f_{3rd} does not change much for cells with higher HEL annealing temperature. Finally, from our IMS results, we conclude that in terms of the cells selected V_{MPP} and resulting $\Delta V (f \rightarrow 0)$ and $Re \Delta V (f \rightarrow 0)$ results, cells with unannealed V_2O_{5-x} HEL, and 100, 200 and 300 °C annealed V_2O_{5-x} HEL are not that much different in their performance as seen in the respective cell's small difference in $\Delta V (f \rightarrow 0)$ and $Re \Delta V (f \rightarrow 0)$ in both simulation and experiment. While the cell with 400 °C annealed V_2O_{5-x} HEL fared worse in terms of performance. In addition, in terms of carrier dynamics/transit times, transit time between cells with unannealed V_2O_{5-x} HEL, and 100, 200 and 300 °C annealed V_2O_{5-x} HEL are relatively similar, while the cell with 400 °C annealed V_2O_{5-x} HEL has the fastest transit time of all the cells characterized. However, due to the low performance of this cell (i.e. lowest V_{MPP} and $Re \Delta V$), the other cells still offer the best results in terms of both DC properties and carrier dynamics.

The near DC results (i.e. $\Delta V (f \rightarrow 0)$ and $Re \Delta V (f \rightarrow 0)$) from the characterized cells are consistent with those from Alsulami et al. in which the thermal annealing of V_2O_{5-x} HEL in the OPV before BHJ deposition does not improve their DC performance significantly compared to the unannealed OPVs/devices [86]. In addition, as with their (Alsulami et al.) other findings, cells with unannealed V_2O_{5-x} HEL, and 100, 200 °C annealed V_2O_{5-x} HEL have similar DC performances, while the OPV with 300 and 400 °C annealed V_2O_{5-x} HEL has lower DC performances (in terms of $Re \Delta V (f \rightarrow 0)$) compared to the other OPVs as seen in Table VIII. Hence, similar to Alsulami et al. findings [86], further heating of the V_2O_{5-x} HEL before BHJ deposition will likely generate oxygen vacancies within the V_2O_{5-x} HEL, which then changes the HEL band gap and its work function as a consequence, thus resulting in the decrease of DC performance in OPV with 300 and 400 °C annealed V_2O_{5-x} HEL when compared to other OPV devices.

In addition to the previous conclusion from the IMS results on OPV with V_2O_{5-x} HEL, we also model the “foot” frequency visible in 6-10(c) for the OPV with an unannealed HEL. From earlier reasoning, we found that one of the possible causes of the “foot” feature is a trap occurring in the low-frequency region. As we perform our IMS under finite load, at low frequencies, carriers will instead travel in the direction of the external current path as seen in Fig. 6-12(a) circuit instead of the C_{BHJ} branch as is the case at high frequencies. As such, we then modify the circuit in Fig. 6-12(a) further, to include a capacitance in series with both R_L and R_s . We call this series capacitance C_{ext} . The circuit in Fig. 6-12(a) is used since we observe both f_{3rd} and the foot frequency occurring at the same time for the cell with the unannealed HEL. We then depict in Fig. 6-13, the new circuit simulation result, together with the circuit itself.

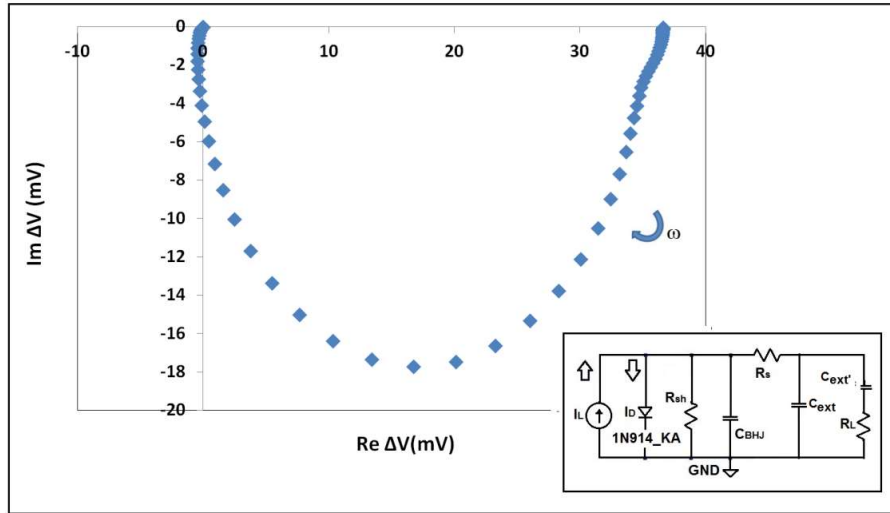


Fig. 6-13. Simulations results from the modified circuit in Fig. 6-12(a) (shown as inset) for the cell with the unannealed HEL. In the circuit inset, I_L ($I_{DC} + I_{AC}$), the 1N914_KA diode, R_{sh} , R_s , C_{ext} , and R_L are chosen to be the same as in Fig. 6-12(a). Here, the trap component at low frequency is represented by a series capacitance C_{ext}' . For this simulation, we set $C_{ext}' = 8$ nF. Finally, the simulation is set between 1 Hz and 250 kHz, where the Re/Im axis uses different scales and are not normalized, with the direction of increasing frequency given by the blue arrow.

As we can see in Fig. 6-13, by selecting a suitable C_{ext}' magnitude, the simulated spectrum for the cell with the unannealed HEL shows both the “3rd quadrant” feature in the high-frequency region and a “foot” feature at low frequency, similar to the plot in Fig. 6-10(c). Physically, we can interpret C_{ext}' as a carrier trap that exists in the cell’s external circuit path, in series with R_s and R_L . As an explanation, it is likely that there are more contaminants and water vapours inside the OPV with unannealed HEL compared to the other type of OPVs. Hence, in cells with higher HEL annealing temperature, further heating may remove some of these contaminants from the HEL while leaving behind a small number of contaminants within the layer, thus the absence of ‘foot’ but the presence of the ‘3rd quadrant’ feature that we see on the OPVs real Nyquist plots.

6.6 Summary of Results from IMS on OPV with V_2O_{5-x} HEL at Maximum Power Point Voltage (V_{MPP})

From the IMS on OPV with V_2O_{5-x} HEL at the respective OPVs V_{MPP} , we first found that the respective OPVs $Re \Delta V$ at ($f \rightarrow 0$) decreases as we increase the OPVs HEL annealing temperature. This is likely due to our selection of V_{MPP} since we determine it based on the J/V data under AM 1.5 in Fig. 3-4. From Fig. 6-10(a) Bode plots, we found that the cells corner frequency f_c increases as we increase the OPV’s HEL annealing temperature. The internal dynamic that f_c and τ represent is likely the carrier transit time. We reason that by annealing the HEL further, we may remove any possible contaminants or vapours inside the HEL, thus making carrier transport occurs much faster (τ is shorter) in OPVs with higher HEL annealing temperature [86, 146].

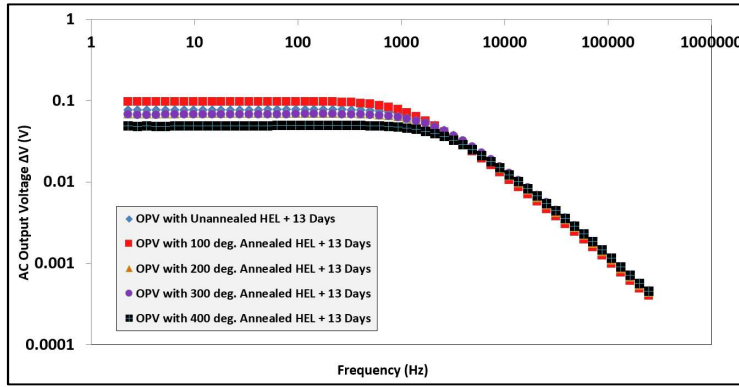
We also observed that there are peaks forming in the high-frequency region in Fig. 6-10(b). Bode phase plot. In addition, we found that the very high-frequency part of the semicircles in Fig. 6-10(c) Nyquist plots have crossed from the 4th quadrant to the 3rd quadrant, forming a ‘3rd quadrant’ feature. It is likely that the high frequency peaks and the ‘3rd quadrant’ feature are related. This feature however, unlike the peaks, does not change much as we increase the HEL annealing temperature. Also, for OPV with unannealed HEL, there is a visible ‘foot’ feature in the low-frequency region besides the ‘3rd quadrant’ feature at high f . The ‘3rd quadrant’ feature and the phase plots high frequency peaks can be simulated by modifying the equivalent circuit in chapter 6 [132]. This is done by connecting an extended capacitor (C_{ext}) with a magnitude of 2 nF in-parallel and between the R_s and R_L in the original model. The C_{ext} represents a lagging mechanism, a capacitive-type trap that start at the same frequency (i.e. f_{-3rd}) and is caused by carriers deviating from the C_{BHJ} due to the presence of another path that has less resistance compared to the C_{BHJ} at $f > 10$ kHz and is located around R_s and R_L . Also, since the lag start at the same frequency, the f_{-3rd} does not change much as we increase the HEL annealing temperature. While both the ‘3rd quadrant’ and ‘foot’ feature in the unannealed OPV can be simulated by adding another capacitance (i.e. C_{ext}') in series with both R_L and R_s , but in-parallel with the previous C_{ext} in the modified model. The C_{ext}' also represents a capacitive-type trap where carriers will travel to in IMS near MPP at low frequency, i.e. towards the circuit’s R_s and R_L , rather than going through the C_{BHJ} or the C_{ext} branch.

We then conclude the OPV with 400 °C annealed HEL has the fastest carrier transit time out of the other OPVs. However, if we compare all the OPVs $Re \Delta V (f \rightarrow 0)$, the OPVs with unannealed V_2O_{5-x} HEL offers the best near DC performance out of the 5 OPV types, while the OPV with 400 °C annealed V_2O_{5-x} HEL has the worst DC performance out of all OPVs. The OPVs near DC (i.e. $Re \Delta V (f \rightarrow 0)$) results are consistent with the results from Alsulami et al. in that there are no significant differences between the DC performance of the unannealed OPV and those with their V_2O_{5-x} HEL annealed at 100 and 200 °C before the BHJ layer deposition, in addition to a decrease in the DC performance of OPV with their V_2O_{5-x} HEL annealed at 300 and 400 °C compared to the other 3 OPVs [86]. Hence, in terms of the OPVs AC (f_c and τ) and near DC ($Re \Delta V (f \rightarrow 0)$) performances, the OPV with 200 °C annealed HEL offers the best performance out of all the OPV types.

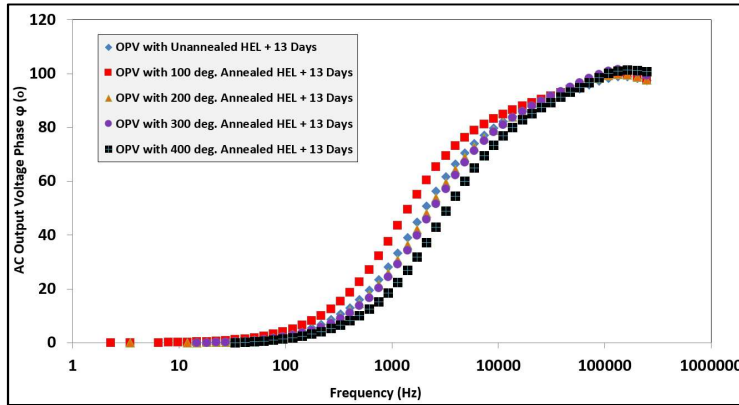
6.7 Results from Ageing Study on OPV with V_2O_{5-x} Hole Extraction Layer

After we performed IMS on OPV with non-annealed V_2O_{5-x} HEL, and with their HELs annealed at 100, 200, 300 and 400 °C before the deposition of BHJ layer, we then proceed to perform ageing study on the same cells at their respective maximum power point voltage (V_{MPP}) after 13 days of storage under dark and ambient atmosphere conditions. Here, we also perform IMS with the same

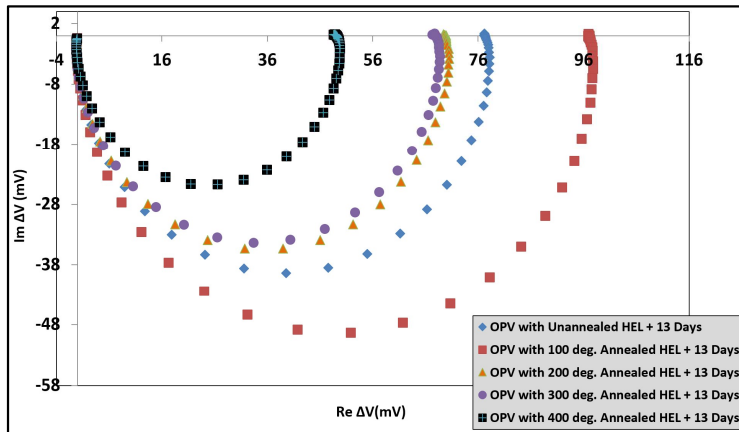
setup, instrument settings, and procedure as described in 4.2, but again the difference is that we conduct IMS at the respective cells V_{MPP} . Also here, unlike in 6.4, we do not determine V_{MPP} post-storage from the J/V characteristics, but we do it by first setting the LED modulation to very low frequency/near DC and then manually tuning the load resistance R_L connected in-parallel with the cell, until we found the highest ΔV readings under that LED illumination (modulated at low frequency). This ΔV reading will then be similar to $\Delta V (f \rightarrow 0)$ and it is the equivalent of the voltage point explained in Fig. 4-6(b) (in 4.3). As the ΔV reading is the highest reading, then that $\Delta V (f \rightarrow 0)$ will be the voltage point at MPP (V_{MPP}) and the resistance at that voltage point is R_{MPP} . This method of finding R_{MPP} is chosen since the determination of V_{MPP} and consequently, R_{MPP} through the J/V characteristics is not very accurate due to the difference between the red LED intensity (used here) and those of an AM 1.5 intensity in J/V characteristics. As a consequence, the aging study results in this subchapter cannot be compared directly to the results in 6.4, as both subchapters use two different methods for determining V_{MPP} . In Fig. 6-14(a), (b) and (c) we present the IMS results of cells with unannealed and annealed cell with V_2O_{5-x} HEL, in the form of Bode amplitude, phase and Nyquist plot of their ΔV at MPP after 13 days of storage under dark and ambient atmosphere conditions.



(a)



(b)



(c)

Fig. 6-14 (a). Bode amplitude and (b). phase of ΔV with respect to frequency f , of OPV with non-annealed V_2O_{5-x} HEL (blue plots), followed by cells with their V_2O_{5-x} HEL annealed at 100, 200, 300 and 400 °C pre-BHJ deposition (shown respectively as the red, orange, purple and black colour in the inset), after 13 days of storage under dark and ambient conditions. (c). Nyquist plots results of an OPV with non-annealed V_2O_{5-x} HEL (blue plots), followed by cells with their V_2O_{5-x} HEL annealed at 100, 200, 300 and 400 °C pre-BHJ deposition (shown respectively as the red, orange, purple and black colour in the inset) also after 13 days of storage under dark and ambient conditions. Note again the “3rd quadrant” feature. Here, all spectra were taken at the respective cells V_{MPP} by setting the external R_{MPP} through manual tuning for the highest ΔV and for f between 1 Hz and 250 kHz. The LED was driven by $I_{LED} = (18 \pm 4)$ mA. Also, the Re/Im axis at (c) uses different scales and are not normalized, with the direction of increasing frequency given by the blue arrow.

From Fig. 6-14(a), the cell with the 100 °C annealed V_2O_{5-x} HEL has the highest ΔV at ($f \rightarrow 0$), while ΔV at ($f \rightarrow 0$) is the lowest for the cell with the 400 °C annealed HEL. Since we do not base our selection of V_{MPP} based on J/V data, but instead based on the cells highest ΔV under red LED modulation at the near-DC condition, we can assume that the V_{MPP} that we obtain from this method is very close/near to the cells MPP. Therefore, we can see that, on average, as the cell’s HEL annealing

temperature is increased, the respective cell's V_{MPP} decreases along with their $\Delta V (f \rightarrow 0)$. Here, the exception is that the cell with unannealed HEL has its V_{MPP} and consequently, its $\Delta V (f \rightarrow 0)$ lower than that of the cell with the 100 °C annealed V_2O_{5-x} HEL. A possible cause of this decrease in $\Delta V (f \rightarrow 0)$ parameter is the annealing of the cell's HEL. This is because annealing will remove any contaminants and vapor that may reside in the HEL layer, thus creating vacant sites where carriers can flow through thereby improving overall carriers transport [146]. In other words, creating a current path which will then lower the $\Delta V (f \rightarrow 0)$ value. As a result, cells with higher HEL annealing temperature have much lower values of $\Delta V (f \rightarrow 0)$. For the cell with unannealed HEL, it is possible that after 16 days of storage more contaminants reside within the HEL such that the overall device $\Delta V (f \rightarrow 0)$ is lower compared to the cell with the 100 °C annealed HEL, though still higher compared to the other cells. On the other hand, excessive annealing, i.e. at a temperature > 600 °C, can also cause structural damage and defects in the V_2O_{5-x} HEL [146]. To add, we also observed that all Fig. 6-10(a) plots have their corner frequencies (f_c) at around 1 kHz. From Fig. 6-14(a), we also observe that as $\Delta V (f \rightarrow 0)$ decreases from the highest in the cell with the 100 °C annealed V_2O_{5-x} HEL to the lowest in the cell with the 400 °C annealed HEL, the respective cell's f_c also increases. As in 6.4, higher f_c means a shorter dynamic time constant τ in the system. Also, it is possible that the time constant τ (from f_c) is actually a carrier transit time. A likely explanation is that the time constant τ (from f_c) is actually a carrier transit time. Hence, as in 6.4, heating the HEL further may generate oxygen vacancies in the V_2O_{5-x} which then results in the decrease of the respective OPVs $\Delta V (f \rightarrow 0)$ in OPV with higher HEL annealing temperature. While at the same time, heating the OPVs HEL further will also remove any possible contaminants or vapours inside the HEL, thus carrier transport will happen much faster in OPVs with higher HEL annealing temperature [86, 146]. Also, all (Fig. 6-14(a)) plots roll off = -1.0 ± 0.1 . As in 6.4, a roll-off ~ -1 indicates that the system behaves as a first order system. This means that there will be a single dynamic that dominates the system under light. This single dynamic will appear as a single semicircle in a Nyquist plot.

From Fig. 6-14(b), we see that ΔV phase (φ) decreases for cells with higher HEL annealing temperature. Again, with the exception of the cell with the unannealed HEL. This can also be ascribed to the same reason that the cell with the unannealed HEL has a lower $\Delta V (f \rightarrow 0)$ compared to the cell with the 100 °C annealed HEL, i.e. the presence of more contaminants in the unannealed HEL. Therefore, the ΔV phase (φ) results in Fig. 6-14(b) are consistent with the ΔV results in Fig. 6-14(a). Also, in all Fig. 6-14(b) plots, $f_c \sim 1$ kHz, which matches the f_c obtained in Fig. 6-14(a). Further, we also observe a peak at the high-frequency region ($f > 100$ kHz) in all Fig. 6-14(b) plots. Here, decreasing/negative φ (after the peak) at high frequencies can again be ascribed to a corresponding “3rd quadrant” feature in a Nyquist plot. Again, this can be ascribed to a lagging or trap mechanism,

since in this feature, cell photocurrents lag behind in phase with respect to LED intensity. As a result, cells with a higher V_2O_{5-x} HEL annealing temperature will have a more positive phase, since any trap mechanism will have been removed by the heating process. The exception here is the phase of the cell with the unannealed HEL which is more positive than the cell with the 100 °C annealed HEL. It is possible that this cell has accumulate more contaminants within the HEL such that there are “active” sites where transport can occur more easily, thus reducing the photocurrent phase more compared to the cell with the 100 °C annealed HEL.

From Fig. 6-14(c), we observe that, consistent with Fig. 6-14(a) and (b) results, the general shape of all plots Nyquist spectra resembles a single semicircle in the complex plane 4th quadrant. Note also that the Re / Im axis in Fig. 6-14(c) uses different scales and are not normalized. In addition, we also observed the ‘3rd quadrant’ feature in-between the 4th and 3rd quadrant. As mentioned before, this feature is characterized by the 3rd quadrant frequency or f_{-3rd} . A magnification of this feature between the Fig. 6-14(c) plots 3rd and 4th quadrant are depicted in Fig. 6-15.

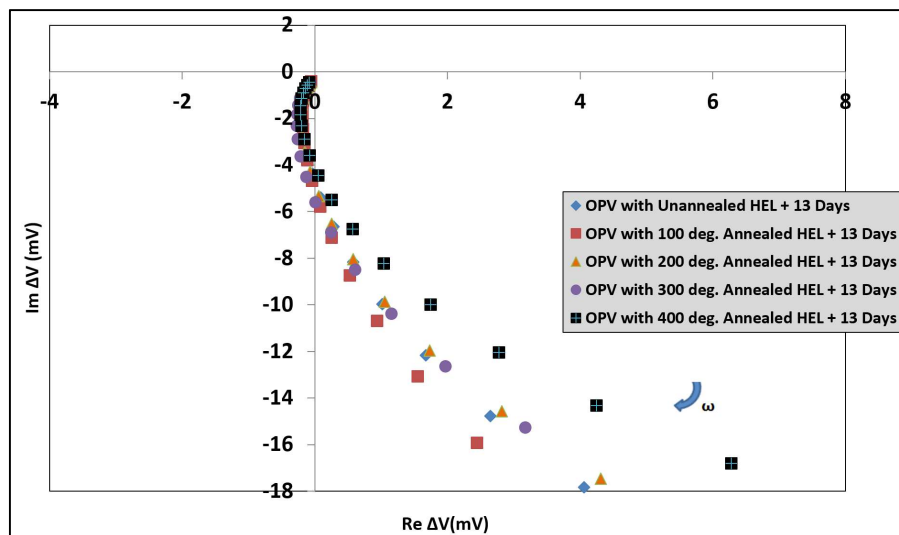


Fig. 6-15. Magnification of the same plots in Fig. 6-14(c) in-between the 3rd and 4th quadrant. Note that f_{-3rd} does not change much for cells with higher HEL annealing temperature. Also, the Re/Im axis here uses different scales and are not normalized, with the direction of increasing frequency given by the blue arrow.

From Fig. 6-15, we can see that f_{-3rd} does not change much for all cells. This again means that f_{-3rd} cannot be correlated directly to the change in negative phase as the HEL annealing temperature is increased. So as photocurrent increases over time, there will be a trap mechanism that becomes apparent at f_{-3rd} and for the cells in this discussion, it occurs roughly at the same f_{-3rd} . Overall, the presence of a “3rd quadrant” feature itself is consistent with the presence of negative phases in Fig. 6-14(b) phase plots. The overall cells dynamic, though, are still dominated by f_c , as evident from the general semicircle shape of all plots in Fig. 6-14(c). We also see from Fig. 6-14(c) that the cell with the 100 °C annealed HEL has the highest $Re \Delta V$ at ($f \rightarrow 0$) and also the largest semicircle. Again, this

follows the same pattern and is caused by the same reasoning as the decrease in the cell's $\Delta V (f \rightarrow 0)$ discussed before. We can now extract four characteristic parameters from Fig's 6-14(a),(b),(c) and 6-15 plots. These parameters are, $Re \Delta V (f \rightarrow 0)$, f_c and f_{-3rd} . We list all of the characteristic parameters and OPV types, including the electric conditions in which we obtain the plots, i.e. V_{MPP} and R_{MPP} , in Table X.

TABLE X OPV TYPES, V_{MPP} , R_{MPP} , $\Delta V (f \rightarrow 0)$, $Re \Delta V (f \rightarrow 0)$, f_c AND f_{-3rd} FOR THE SPECTRA SHOWN IN FIG. 6-14(a), (b),(c) AND 6-15.

OPV Types	V_{MPP} [mV]	R_{MPP} [k Ω]	$Re \Delta V$ ($f \rightarrow 0$) [mV]	f_c [Hz]	f_{-3rd} [Hz]
Non Annealed HEL	532	45	77 ± 10	1700 ± 1	31000 ± 1
100 °C Annealed HEL	585	82	96 ± 10	1200 ± 1	25000 ± 1
200 °C Annealed HEL	605	45	69 ± 10	1900 ± 1	31000 ± 1
300 °C Annealed HEL	505	56	67 ± 10	2100 ± 1	25000 ± 1
400 °C Annealed HEL	425	66	48 ± 10	2800 ± 1	31000 ± 1

From Table X, we can confirm that overall, as the cell's HEL annealing temperature is increased, the respective cells V_{MPP} decreases along with their $\Delta V (f \rightarrow 0)$. Also, it is likely that this decreasing trend is caused by the annealing of the cell's HEL, which can remove any contaminants and vapor that may reside in the HEL layer, thus creating vacant sites where carriers can flow through and improving overall transport. Here, the exception is for the cell with the unannealed HEL. Based on Table X, this is likely because more contaminants or vapor reside within the HEL such that the overall device $\Delta V (f \rightarrow 0)$ is lower compared to the cell with the 100 °C annealed HEL but still higher compared to the other cells. In addition, we also confirm that as $\Delta V (f \rightarrow 0)$ decreases from the highest in the cell with the 100 °C annealed HEL to the lowest in the cell with the 400 °C annealed HEL, the respective cell's f_c also increases in general. Hence, the dynamic inside cells with higher HEL annealing temperatures occurs much faster. So in general, heating the HEL further is likely to generate oxygen vacancies in the V_2O_{5-x} which then decrease of the respective OPVs $\Delta V (f \rightarrow 0)$. At the same time, heating the OPVs HEL further will also remove contaminants inside the HEL, thus carrier transport will happen much faster in OPVs with higher HEL annealing temperature [86, 146]. The one exception is the cell with the unannealed HEL, where the dynamic is instead faster, not longer. This again can be caused by the presence of "active sites" where carrier transport can occur much faster although it is not annealed.

Finally, we can also confirm that f_{-3rd} does not change much for cells with higher HEL annealing temperatures. Hence, as mentioned before, f_{-3rd} represents a lagging mechanism or a trap that causes carrier transport to be slower, thus resulting in a negative phase and $Re \Delta V$. We then investigate the dependency of characteristics parameters in Table X with respect to changes in V_{MPP} , from the cell

with the highest V_{MPP} to the lowest, by using an equivalent circuit model similar to Fig. 6-5(a) in 6.1. So from Fig. 6-5(a) circuit in 6.1, we perform IMS under finite load, or at a cell MPP, where $R_L = R_{MPP}$, the current generated by the cell's current source I_L in Fig. 6-5(a) will flow through the BHJ capacitance path, especially at high frequencies, when capacitive impedance drops. This is because, under finite load, both the external current path and internal diode in Fig. 6-5(a) equivalent circuit will display a significant resistance. Here, we also find the presence of a "3rd quadrant feature" in the high-frequency area at all the plots in Fig. 6-14(c). As such, we then use the same extended circuit in Fig. 6-16(a) and change the circuit's parameter accordingly.

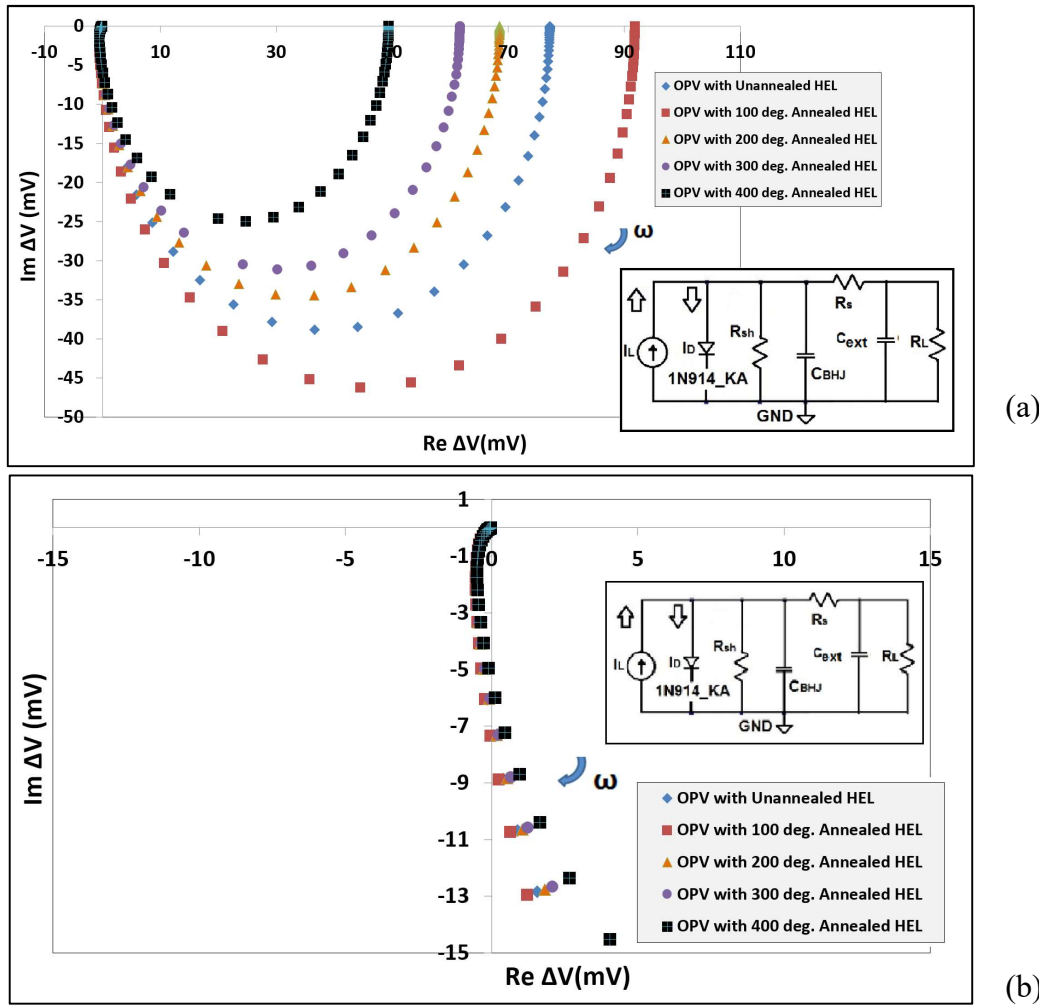


Fig. 6-16 (a). Simulated Nyquist plot for stored cell with unannealed V_2O_{5-x} HEL and cells with its V_2O_{5-x} HEL annealed at 100, 200, 300 and 400 °C after 13 days of storage (sample types are shown in the colour coded inset). Also shown in the circuit inset is the modified OPV generic equivalent circuit which shows the extended capacitor component (C_{ext}) in-parallel between series (R_s) and load resistance (R_L). For the simulation, we set the DC current bias (I_{DC}) = 25 μ A with current modulation (I_{AC}) = 5 μ A_p for all cells. Here, we again use the modified 1N914_KA diode and C_{BHJ} = 4 nF in the circuit. We also set C_{ext} = 2 nF. We also set the shunt resistance (R_{sh}) = 24, 33, 20, 16 and 15 k Ω for stored cells with unannealed, 100, 200, 300 and 400 °C annealed V_2O_{5-x} HEL respectively. All of the cells series resistances (R_s) are set to R_s = 577 Ω . The R_L magnitudes are set to = 45, 50, 45, 56 and 30 k Ω for stored cells with unannealed, 100, 200, 300 and 400 °C annealed V_2O_{5-x} HEL respectively. (b) Magnification of the same plots in (a) in-between the 3rd and 4th quadrant. Here, f_{3rd} does not change much for cells with higher HEL annealing temperature. Finally, the simulation in (b) is set between 1 Hz and 250 kHz, where the Re/Im axis in (b) and (c) uses different scales and are not normalized, with the direction of increasing frequency given by the blue arrow.

For simulation purposes, the DC current bias (I_{DC}) amplitude was set to = 25 μA with current modulation (I_{AC}) = 5 μA_p for all cells. This is because we are simulating the behaviour of the same current source I_L in Fig. 6-5(a) and in Fig. 6-16(b). We also select C_{BHJ} = 4 nF and the circuit's diode component as the 1N914_KA model, this is because the cell has the same BHJ mixture as in 6.1. While the 1N914_KA was selected as the diode model with the same reasoning as in 6.1 and 6.4. We then set the circuit's shunt resistance (R_{sh}) = 24, 33, 20, 16 and 15 k Ω for stored cells with unannealed, 100, 200, 300 and 400 $^{\circ}\text{C}$ annealed V_2O_{5-x} HEL respectively. Also, all of the cell's series resistances (R_s) are set to $R_s = 577 \Omega$. While the R_L magnitudes are set to = 45, 50, 45, 56 and 30 k Ω for stored cells with unannealed, 100, 200, 300 and 400 $^{\circ}\text{C}$ annealed V_2O_{5-x} HEL respectively. All three resistance values (R_{sh} , R_s , and R_L) were adjusted and selected to closely replicate Fig. 6-14(c) $Re \Delta V$ values. Finally, we set the magnitude of the extended capacitor component (C_{ext}) as $C_{ext} = 2$ nF. Again, this is to obtain an identical “3rd quadrant” feature at high frequency. In Fig. 6-16(b) simulated plots are taken at f between 1 Hz and 250 kHz.

From Fig. 6-16(b), we see that the simulated plots gave the exact single semicircles of Fig. 6-14(c) plots for all types of cells. This means that there is indeed a single internal dynamic that dominates all of the cells under light. In addition, the simulated plots are also able to replicate the $Re \Delta V$ magnitude seen in Fig. 6-14(c) and Table X for all cells, together with the decrease in semicircle sizes from the largest for the cell with the 100 $^{\circ}\text{C}$ unannealed HEL to the lowest for the cell with the 400 $^{\circ}\text{C}$ annealed HEL. In addition, from Fig. 6-16(b) and (c), we can see that the simulated plots also manage to replicate the “3rd quadrant” feature as seen in Fig. 6-15. We also see that, as in Fig. 6-15, the “3rd quadrant feature does not appear to change much for cells with higher HEL annealing temperatures, thereby confirming our choice of using a fixed value capacitor C_{ext} to simulate the trap mechanism that is encountered by carriers for all cells at high frequencies and represented by f_{-3rd} . Finally, from simulated results in Fig. 6-16(b) and (c), we derive the same four characteristic parameters as in Table X, these are $Re \Delta V (f \rightarrow 0)$, f_c and f_{-3rd} . We list all of the characteristic parameters and OPV types, including the electric conditions in which we obtain the plots, i.e. V_{MPP} and R_{MPP} , in Table XI.

TABLE XI OPV TYPES, V_{MPP} , R_{MPP} , $\Delta V (f \rightarrow 0)$, $Re \Delta V (f \rightarrow 0)$, f_c AND f_{-3rd} FOR THE SPECTRA SHOWN IN FIG. 6-16 (b) AND (c).

OPV Types	V_{MPP} [mV]	R_{MPP} [k Ω]	$Re \Delta V$ ($f \rightarrow 0$) [mV]	f_c [Hz]	f_{-3rd} [Hz]
Non Annealed HEL	387	45	77	1700	22000
100 $^{\circ}\text{C}$ Annealed HEL	490	50	92	1400	18000
200 $^{\circ}\text{C}$ Annealed HEL	343	45	68	1900	22000
300 $^{\circ}\text{C}$ Annealed HEL	309	56	61	2200	22000
400 $^{\circ}\text{C}$ Annealed HEL	250	30	49	2600	26

From Table XI, we confirm again that as the cell's HEL annealing temperature is increased, the respective cells V_{MPP} decreases along with their $Re \Delta V (f \rightarrow 0)$. Here, the exception is for the cell with the unannealed HEL. Based on Table XI, this exception is again likely due to the presence of more contaminants that reside within the HEL such that the overall device $Re \Delta V (f \rightarrow 0)$ is lower compared to the cell with the 100 °C annealed HEL but still higher compared to the other cells. In addition, we can confirm that cells with a higher HEL annealing temperature have indeed a higher corner frequency f_c , also with the exception of the cell with the unannealed HEL. Thus, as f_c is related to an internal dynamic time constant τ , the dynamic inside cells with a higher HEL annealing temperature occurs much faster compared to a cell with a lower HEL annealing temperature, while the dynamic of cells with an unannealed HEL occur much faster compared to cells with 100 °C annealed HEL but slower with regards to cells with a higher HEL annealing temperature.

In addition, we also see that the f_c magnitude replicates well in Table XI when compared to Table X for real results. While f_{-3rd} is lower in Table XI but not too small compared to f_{-3rd} in real results. We also tried to vary Fig. 6-16(a) circuit C_{BHJ} in the simulations (not shown here), and we found that if C_{BHJ} is changed, the corner frequency (f_c) will also change. Thus, the dynamic time constant here is a carrier transit time τ , and this transit time dominates the cell's dynamic response as seen in Fig. 6-16(c), with the transit time much shorter for cells with higher HEL annealing temperature. As for the f_{-3rd} feature, we can relate f_{-3rd} to a carrier trap that equally resides in all cells near the cells R_s and R_L and is not influenced very much by HEL heating, thus f_{-3rd} does not change much for cells with higher HEL annealing temperature. Finally, from our IMS results, we conclude that in terms of the cell's V_{MPP} and resulting $\Delta V (f \rightarrow 0)$ and $Re \Delta V (f \rightarrow 0)$, cells with unannealed V_2O_{5-x} HEL, and 100, 200 and 300 °C annealed V_2O_{5-x} HEL are not very different in their performance. While the cell with the 400 °C annealed V_2O_{5-x} HEL fared worse in terms of performance. Also, the cell with the unannealed HEL has a lower performance compared to the cell with the 100 °C annealed V_2O_{5-x} HEL, but instead is higher for the other cells. In terms of carrier transit times, transit time between cells with unannealed V_2O_{5-x} HEL, and 100, 200 and 300 °C annealed V_2O_{5-x} HEL are relatively similar, while the cell with the 400 °C annealed V_2O_{5-x} HEL has the fastest transit time out of all cells characterized. However, due to the low performance of the cell (400 °C annealed HEL), the other still offer the best results in terms of both DC properties and carrier dynamics.

6.8 Summary of Ageing Study Results on OPV with V₂O_{5-x} Hole Extraction Layer

From the IMS on the stored OPVs at their V_{MPP} , we first found that based on the OPVs $Re \Delta V$ at ($f \rightarrow 0$) in Fig. 6-14, as we increase the HEL annealing temperature, the OPVs $Re \Delta V$ at ($f \rightarrow 0$) will experience a decrease from the OPV with 100 to 400 °C annealed HEL. Also, we found that the $Re \Delta V$ at ($f \rightarrow 0$) of OPV with 100 °C annealed HEL is higher than that of OPV with unannealed HEL. This decrease in the OPVs $Re \Delta V$ at ($f \rightarrow 0$) can be caused by the increased presence of contaminants or water vapor in the OPVs as we increase the HEL annealing temperature, since heating the HEL further may increase vacant sites within the HEL that can be filled with contaminants/water vapour, thus degrading the OPVs and reducing their $Re \Delta V$ at ($f \rightarrow 0$). Also, it is possible that more contaminants reside in the OPV with unannealed HEL compared to that with 100 °C annealed HEL, hence the lower $Re \Delta V$ at ($f \rightarrow 0$) at OPV with unannealed HEL. From Fig. 6-14(a) Bode plots, we also found that in general, the cells corner frequency f_c increases as we increase the HEL annealing temperature, with the exception of OPV with 100 °C annealed HEL, whose f_c is lower compared to that of OPV with unannealed HEL. The internal dynamic that f_c and τ represent is also likely the carrier transit time. We reason that by annealing the HEL further, we may remove any possible contaminants or vapours inside the HEL, thus making carrier transport occurs much faster (τ is shorter) in OPVs with higher HEL annealing temperature [86, 146]. As for the smaller f_c found in the OPV with unannealed HEL compared to that with 100 °C annealed HEL, it is possibly caused by further device degradation in the former as opposed to the later.

We also observed that there are both high-frequency peaks and ‘3rd quadrant’ feature in the stored OPVs Bode and Nyquist plots. In addition, on all of the OPVs Nyquist plots, there is no presence of ‘foot’ feature in the low-frequency region as in the fresh OPV with unannealed HEL. Also, the high-frequency peaks in OPV with unannealed HEL is lower than the OPV with 100 °C annealed HEL, as opposed to the increase in phase peaks from OPV with 100 to 400 °C annealed HEL. The ‘3rd quadrant’ feature and the phase plots high frequency peaks can be simulated correctly by connecting an extended capacitor (C_{ext}) with a magnitude of 2 nF in-parallel and between the R_s and R_L in the equivalent circuit of chapter 6 [132]. The C_{ext} also represents a lagging mechanism that start at f_{3rd} , and is caused by carriers deviating from the C_{BHJ} due to the presence of other path that has less resistance at $f > 10$ kHz and is located around R_s and R_L . Meanwhile, the lower high-frequency peaks in OPV with unannealed HEL compared to OPV with 100 °C annealed HEL, can be caused by the presence of more contaminants in the former as opposed to the later. We then conclude that the OPV with 400 °C annealed HEL has the fastest carrier transit time out of all OPVs after storage. However, if we compare all the stored OPVs $Re \Delta V$ ($f \rightarrow 0$), the OPVs with 100 °C annealed HEL

offers the best near DC performance out of the 5 OPVs, while the OPV with 400 °C annealed V_2O_{5-x} HEL has the worst DC performance out of all OPVs. Hence, we then conclude that in terms of the OPVs AC (f_c and τ) and near DC ($Re \Delta V (f \rightarrow 0)$) performances, the OPV with 200 °C annealed HEL offers the best performance out of all the OPV types.

Chapter 7

IMS Characterization of Organic Light-Emitting Diodes (OLED) Devices and Alkaline Battery

As elaborated in 1.1 and 3.2, we also perform IMS characterizations on Organic light-emitting diode (OLED) devices. The prepared OLEDs emits white light by using a copolymer, W1100 made by Sumitomo Chemicals Co., Ltd, as the device emissive material. W1100 is a block copolymer that emits white light from the (combination) ratio of red and blue emitter/chromophores within the polymer structure. This was shown in the OLED's electroluminescence spectrum in Fig. 3-8 in 3.2, in that two emission peaks, are observed within the spectrum. The higher peak, with a full width at half maximum (FWHM) = 50 nm, lies between 450-500 nm and represents the emitted blue spectrum from the polymer. The weaker peak, which lies between 560-680 nm with FWHM = 120 nm, represents the polymer's emitted red spectrum. The OLED devices themselves uses PEDOT as the hole injection layer (HIL) and Lithium fluoride (LiF) with calcium (Ca) as the electron injection layer (EIL). For the OLED's cathode, aluminium (Al) was used with the anode being indium tin oxide (ITO). Finally, all OLED devices were prepared and DC-characterized by Mr. Thomas Routledge, University of Sheffield, Sheffield, UK. The OLED's DC characterization results (J/V and L/V plots) are given in 3.2.1.

We first present and discuss the results of intensity-modulated spectroscopy (IMS) characterization of the OLED which was done to determine charge carrier mobility (μ) in the OLED and charge carrier type that is represented by the resulting μ value. We then give and discuss the results of IMS characterization that was conducted to compare different OLED dynamics from different chromophores/colours within the OLED device emissive layer. Finally, we present and discuss the results of IMS characterization which was performed to study the aging of an OLED device. For all IMS on OLED, we perform the characterizations by illuminating a fast photodiode (Centronic OSD5-5T, rise time = 9 ns) with the OLED device by using the setup described in Fig. 4-13(a). We also apply different V_{OLED} and I_{OLED} in each OLED experiments, but in all IMS on OLED, we always apply V_{OLED} on $R_{OLED} = R4 = 2.7 \text{ k}\Omega$ in the modified voltage adder circuit in Fig. 4-13(b). We then insert the following lock-in settings into the modified IMS software in 4.6, the input coupling is set to DC, roll-off to 24 dB/oct, dynamic to high, phase offset to 0 and reference harmonic to 1. The time constants are set to 5 s at $f = 1\text{-}10 \text{ Hz}$, 1 s at $f = 10\text{-}100 \text{ Hz}$, 0.5 s at $f = 10\text{-}1000 \text{ Hz}$, 0.1 s at $f = 1 \text{ kHz}\text{-}10 \text{ kHz}$ and 0.05 s at $f > 10 \text{ kHz}$. The reasoning behind these lock-in settings has been

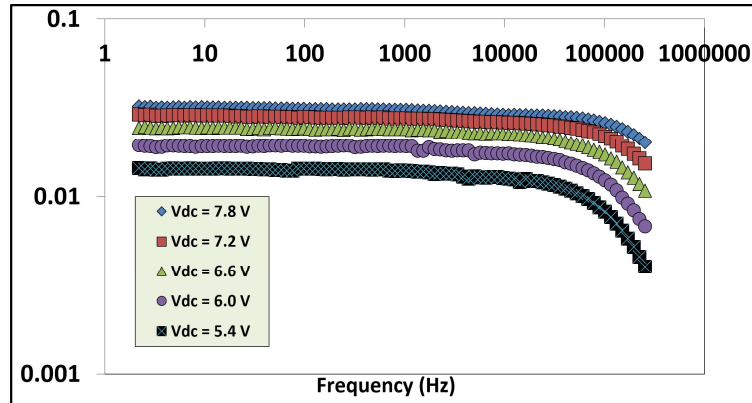
given in 4.4. In addition, we varied the input coupling and dynamic in one of the IMS on OLED experiments. We operate the IMS software to perform a frequency scan at f between 1 Hz and 250 kHz in 18 steps per decade. From the applied V_{OLED} and the resulting I_{OLED} driving current, the OLED will then produce a light intensity $L_T = L + \Delta L \sin \omega t$. We use the modulated OLED intensity to illuminate the fast photodiode which is under a reverse bias voltage (V_{REV}) = -13.2 V. From the OLED illumination, the photodiode will produce a current in the form of $I_{PD} = I_{PD-DC} + \Delta I_{PD}(\omega) \sin(\omega t + \varphi(\omega))$. This photocurrent is fed into an IV converter with $R_f = 4.7 \text{ k}\Omega$ and $C_f = 4.7 \text{ pF}$. Also, in another IMS on OLED experiment, we varied the R_f in the IV converter. The IV circuit converts the photodiode current (I_{PD}) into a voltage (V_{out}) and amplifies the resulting voltage through $I_{PD} = V_{out}/R_f$. V_{out} is related to the OLED illumination via the photodiode. V_{out} is given by $V_{out} = V + \Delta V(\omega) \sin(\omega t - \varphi(\omega))$. V_{out} is fed into the lock-in voltage input. The lock-in will measure and “pick-out” $\Delta V(\omega)$ by comparing it with the lock-in’s ref out voltage frequency ω . As a result, we obtained the amplitude $\Delta V(\omega)$ and phase $\varphi(\omega)$ of V_{out} and recorded these parameters as a function of $f = \omega/2\pi$. Later the amplitude $\Delta V(\omega)$ and phase $\varphi(\omega)$ can be plotted as a Bode and Nyquist plot as seen in 1.4.

7.1 Results from IMS Measurements on OLED Devices with Different DC Voltage Bias

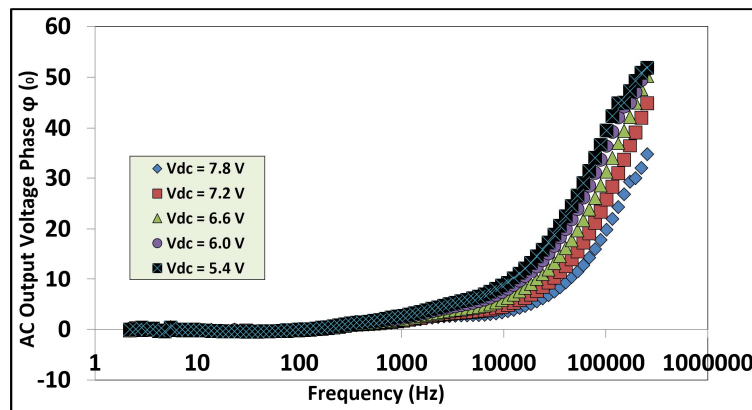
For the IMS characterization of the OLED, which was performed to determine charge carrier mobility (μ) and type, we use different OLED voltage biases V_{DC} , and a fresh OLED sample and using the OLED setup in 4.6. This sample is OLED No. 3 in the OLED J/V characteristics in Fig. 3-10. The V_{DC} condition was varied from 7.8 down to 5.4 V with 0.6 V voltage intervals. From the resulting IMS spectrum at each V_{bias} point, we extract corner frequencies f_c that represent the time constant τ of an internal dynamic in the OLED. We then plot τ with respect to V_{DC} , and from this plot, derived a figure of merit for μ . Note that in an OLED, both carrier’s mobility must be accounted for in the mobility determination [147, 148]. For the IMS, we apply a combination of a large voltage bias and a small sinusoidal AC voltage of $V_{OLED} = (7.8 \pm 0.3) \text{ V}$ on a fresh OLED. Since the OLED is protected by a serial resistor $R_{OLED} = 2.7 \text{ k}\Omega$ in the adder, it will then result in a corresponding $I_{OLED} = (1.9 \pm 0.09) \text{ mA}$. The bias component in V_{OLED} , i.e. $V_{DC} = 7.8 \text{ V}$ was obtained by measuring the voltage drop across the OLED as mentioned in 4.6. While the DC drive current in I_{OLED} , i.e. $I_{DC} = 1.9 \text{ mA}$, was obtained from the equation $I_{DC} = V_{R4}/R_{OLED}$, with V_{R4} being the voltage drop across the R_{OLED} as elaborated in 4.6. The modulating current in the I_{OLED} , i.e. $I_{AC} = 0.09 \text{ mA}_p$ was obtained through the equation $I_{AC} = V_{AC}/(R_{OLED} + R_{diff})$, with $V_{AC} = 0.3 \text{ V}_p$ from the lock-in ref out and differential resistance or $R_{diff} = 588 \text{ }\Omega$ as determined from the OLED No. 3 J/V characteristics in Fig. 3-10. The IMS software settings used for this experiment were the same as that mentioned earlier. Here, the IV

converter used to convert photodiode current into voltage has a feedback resistor $R_f = 4.7 \text{ k}\Omega$ and feedback capacitor $C_f = 4.7 \text{ pF}$.

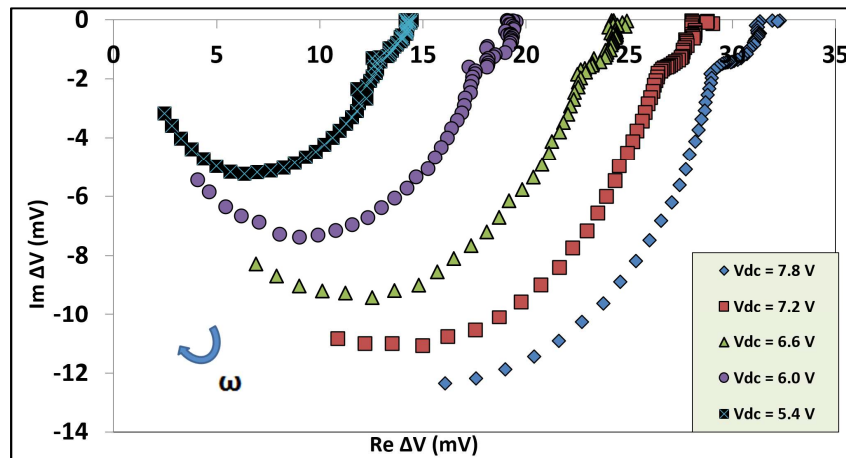
In Fig. 7-1, we present the IMS results of OLED No. 3 in the form of a Bode amplitude, phase and Nyquist plot of ΔV .



(a)



(b)



(c)

Fig. 7-1 (a). Bode amplitude plot of the OLED's ΔV , (b) Bode phase plot of ΔV phase φ with respect to frequency f and (c) Nyquist plots of ΔV that plots the imaginary part ($Im \Delta V = |\Delta V| \sin \varphi$) vs. real part ($Re \Delta V = |\Delta V| \cos \varphi$) which is parametric in frequency for the IMS spectra. Here, (a), (b) and (c) are taken at frequencies between 1 Hz and 250 kHz and at different OLED V_{bias} (shown in the respective plots inset), from 7.8 V down to 5.4 V with 0.6 V intervals, V_{AC} and I_{AC} are kept constant. Note that the Re/Im axis at (c) uses different scales and are not normalized, with the direction of increasing frequency given by the blue arrow.

Fig. 7-1(a) and (b) shows the Bode plots of the OLED's ΔV amplitude and phase φ with respect to f between 1 Hz and 250 kHz and taken at different OLED V_{DC} , from $V_{DC} = 7.8 \text{ V}$ down to 5.4 V

with a 0.6 V interval. While Fig. 7-1(c) shows a set of Nyquist spectra that are also taken at different OLED V_{DC} , i.e. at $V_{DC}=7.8$ V to 5.4 V. From Fig. 7-1(a), $\Delta V(f \rightarrow 0)$ decreases as we decrease V_{DC} , which means that as V_{DC} is reduced, the OLED brightness will also be reduced. While from Fig. 7-1(b), the ΔV phase φ also increases as V_{DC} decreases. Of course, as we change V_{DC} , we also change the OLED's internal dynamic. Also from the same plot (Fig. 7-1(b)), we see that φ does not reach 45° at the highest frequency f for $V_{DC}=7.8$ and 7.2 V in Fig. 7-1(b). In other words, at those OLED voltage biases, we cannot determine any corner frequency f_c . In Fig. 7-1(c), the general shape of the OLED's Nyquist spectra resembles an incomplete semi-ellipse in the 4th quadrant of the complex plane that gets smaller in size with lower V_{DC} , though note that the Re/Im axis in Fig. 7-1(c) uses different scales. In addition, we also observed a "hook" feature at $f \sim 5$ kHz in Fig. 7-1(c) for $V_{DC}=7.2, 6.6, 6$ and 5.4 V, while at $V_{DC}=7.8$ V the "hook" occurs at $f \sim 9$ kHz. Finally, the "hook" feature itself seems to increase in size as V_{DC} is reduced.

From Fig. 7-1(a), (b) and (c), we can extract two characteristic parameters, these are $Re \Delta V$ at ($f \rightarrow 0$) and corner frequency f_c . From 5.1, f_c is the frequency where the ΔV phase $\varphi = 45^\circ$, and is connected to a time constant τ of the system's internal dynamic through $f_c = 1/2\pi\tau$. Also, for Fig. 7-1(b) and (c) plots at $V_{DC}=7.8$ and 7.2 V we determined/approximate f_c with the first order phase shift equation, in which $f_c = f_o/\tan \varphi_o$, where φ_o is the output voltage phase at frequency f_o [36]. Here, we use $f_o = f$ at (ΔV phase) $\varphi_o = 30^\circ$ to approximate f_c or corner frequency at $\varphi = 45^\circ$. The OLED's electrical condition (V_{DC}), $Re \Delta V(f \rightarrow 0)$ and f_c obtained from Fig. 7-1(a), (b) and (c) are shown in Table XII.

TABLE XII OLED V_{DC} , $Re \Delta V(f \rightarrow 0)$ AND f_c FOR THE SPECTRA SHOWN IN FIG. 7-1(a), (b) and (c)

OLED V_{DC} [V]	$Re \Delta V(f \rightarrow 0)$ [mV]	f_c [Hz]
7.8	32 ± 10	310000 ± 1
7.2	29 ± 10	230000 ± 1
6.6	25 ± 10	200000 ± 1
6.2	20 ± 10	160000 ± 1
5.4	19 ± 10	130000 ± 1

From Table XII, it is confirmed that as V_{DC} is reduced, the OLED becomes less bright (reduced $\Delta V(f \rightarrow 0)$ and $Re \Delta V(f \rightarrow 0)$). While the decrease of f_c ($f_c = 1/2\pi\tau$) as V_{DC} is reduced in Fig. 7-1(a) and (c) spectra, indicates that τ is the carrier(s) transit time dynamic within the OLED. In an OLED, as elaborated in 2.4, two opposite carriers (electrons and holes) are needed for electroluminescence. These carriers will first be injected from the OLED's cathode and anode, by the applied OLED V_{DC} . Carriers will then travel across the OLED into the emissive layer, where they will form excitons, decay and emit light as the carriers recombine [103]. As such, we first look at a mathematical model of two carrier transport in an OLED and construct a physical model.

Blom and de Jong proposed a theoretical model, the double-carrier model, that takes into account the effects of holes and electrons transport in an OLED polymer. In addition, the model also accounts for the presence of traps within the polymer and the field-dependent nature of both carrier mobilities. Two important phenomena are also included in the model, one is biomolecular recombination and the other is charge neutralization. Biomolecular recombination is the recombination of both carriers within the OLED polymer that can either lead to light generation or nonradiative recombination, whilst charge neutralization is simply the total charge of both charge carrier within the polymer. So in this model, the total current density from both carriers J (in A/m^2) is given by equation (31) [147].

$$J = J_p + J_n = e\mu_p [E(x)]p(x)E(x) + e\mu_n [E(x)]n(x)E(x) \quad (31)$$

with J_p and J_n being the current density of holes and electron respectively (in A/m^2), and are also described by equation (32).

$$\frac{1}{e} \frac{dJ_n}{dx} = -\frac{1}{e} \frac{dJ_p}{dx} = Bp(x)n(x) \quad (32)$$

also, $E(x)$ in equation (31) is the electric field as a function of position x (in V/m), and can be defined by equation 33 below:

$$\frac{\epsilon_0 \epsilon_r}{e} \frac{dE(x)}{dx} = p(x) - n(x) - n_t(x) \quad (33)$$

where μ_p and μ_n are respectively the hole and electron mobility (in m^2/Vs), $p(x)$ and $n(x)$ are the hole and electron density as a function of position x (C/m) respectively, $n_t(x)$ is the density of trapped electrons (in cm^{-3}) and B is the recombination constant (in cm^3/s) [147]. We construct a simplified diagram of microscopic processes that describe OLED operation according to the double-carrier model as described by equation (31)-(33). This physical model is depicted in Fig. 7-2.

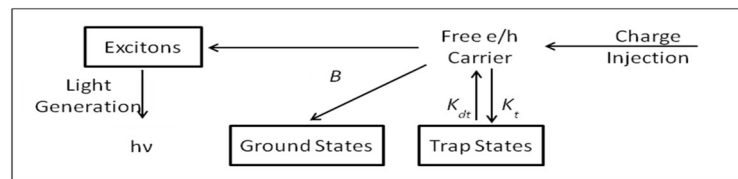


Fig. 7-2. A diagram of the microscopic processes occurring within an OLED according to the double-carrier model by Blom and de Jong. The B , K_{dt} , and K_t here are the recombination, trapping and detrapping constant respectively [147].

In Fig. 7-2, both electron, and holes are injected into the OLED polymer layer through respectively the cathode and anode. Both carriers will be driven towards the OLED's center by the electric field from the applied V_{DC} , from here, three things can happen. One is that electrons can be trapped or detrapped within the bulk polymer, as represented by the constants K_t and K_{dt} respectively. Here, detrapping occurs when traps are overfilled with electrons thus making them inactive. The other is that carriers can recombine without emitting any light (non-radiative recombination) or that carriers will recombine and then emit light, all represented by the constant B [147]. Hence, the time needed for both carriers to recombine within the emissive layer that leads to light emission/luminescence can be represented by a (recombination) transit time. To determine the recombination transit time τ in a double-carrier model, we use an AC impedance approach for a bipolar device where both carriers recombine somewhere within the device. As stated earlier, τ is linked to the corner frequency f_c . In a double-carrier device, τ must also take into account the total mobility from both carriers, which is called the effective mobility μ_{eff} (in cm^2/Vs) and is given by equation (34) [149, 150].

$$\mu_{eff} = \mu_n + \mu_p \quad (34)$$

with μ_n and μ_p being the mobility of electrons and holes respectively (in cm^2/Vs). μ_{eff} here can be considered the mobility average of both carriers in the OLED. Also, a transit time equation must include the potential difference between the work function of an OLED's cathode and anode, i.e. the built-in voltage (V_{bi}). Since we apply V_{DC} to the OLED, a net difference between V_{DC} and V_{bi} will then occur and thus influence both carrier's mobility. Therefore, the (recombination) transit time for both carriers becomes the effective transit time constant τ_{eff} and is given in the AC model by equation (35).

$$\tau_{eff} = \frac{4}{3} \frac{d^2}{(V_{DC} - V_{bi})\mu_{eff}} \quad (35)$$

where d is the emissive layer thickness (in nm), μ_{eff} is the effective mobility (in cm^2/Vs), V_{DC} is the OLED voltage bias (in V), and V_{bi} is the built-in voltage within the OLED (in V) due to the difference in the OLED electrodes work function [149]. The V_{bi} in equation (35) can be determined by using equation (17) in 2.3, in which the respective metal/electrodes work functions can be determined from literature values as a first approximation. Note that since both carriers will meet and recombine in the emissive layer, carriers will not traverse the emissive layer full length (d). This fact has been

accounted for in equation (35), so d here is still the entire layer thickness [149]. Further, from equation (35), it is clear that τ_{eff} will be dominated by the slower mobility between the two carriers. If we return to the Table XII results, it is clear that the decrease of f_c as V_{DC} is reduced means that the time constant τ is indeed a carrier(s) transit time. Therefore, the time constant τ represents both carrier's effective transit time τ_{eff} that leads to OLED light emission, or in another word the time constant $\tau \sim \tau_{eff}$. We investigate the dependence of the characteristic parameters listed in Table XII on the OLED V_{DC} , based on the physical model in Fig. 7-2 along with an OLED-equivalent circuit to explain the experimental results.

So to rationalize Fig. 7-1(a), (b) and (c) results, we performed LT SPICE simulations on a generic OLED equivalent circuit. Here we used a simplified OLED circuit as proposed by Lin et al. in Fig. 7-3(a) [151]. This equivalent circuit was built by using a modified form of the Schottky general diode equation, where the modification was done by using a Taylor-series approximation [151].

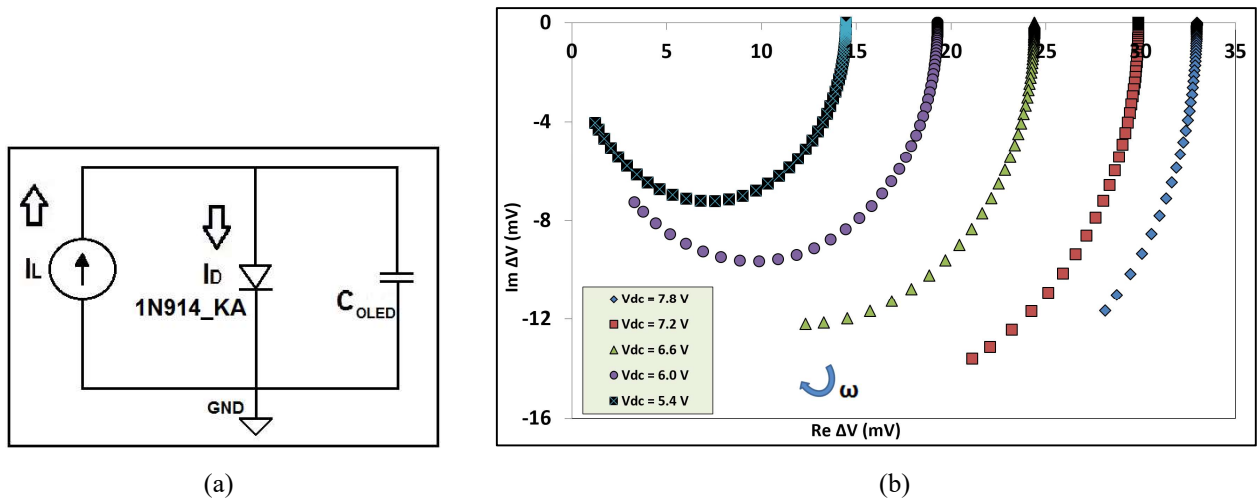


Fig. 7-3 (a). A generic OLED equivalent circuit model [151]. I_L represents the light-driven current source. In IMS, all components are internal to the OLED. (b) Simulated ‘Nyquist rainbow’ for the equivalent circuit model in (a) for f between 1 Hz and 250 kHz and at OLED $V_{DC} = 7.8$ V down to 5.4 V with 0.6 V Fig. interval (inset). Here for (b), we select $C_{OLED} = 13$ nF, and a customized 1N914 diode (1N914_KA) with the saturation current reduced to 3 pA. The DC current bias amplitudes are set at $I_{DC} = 1.9, 1.06, 0.75, 0.33$ and 0.22 mA, these (I_{DC}) corresponds to $DC_s = 7.8, 7.2, 6.6, 6$ and 5.4 V respectively. The current source modulation is set to $I_{AC} = 1.35, 0.69, 0.4, 0.14$ and 0.07 mA for $V_{DC} = 7.8$ and down to 5.4 V respectively. The plots Re/Im axis at (b) uses different scales and are not normalized, with the direction of increasing frequency given by the blue arrow.

For our simulation purposes, the DC current bias amplitude was set at $I_{DC} = 1.9, 1.06, 0.75, 0.33$ and 0.22 mA, which corresponds to $V_{bias} = 7.8, 7.2, 6.6, 6$ and 5.4 V respectively with $R_{OLED} = 2.7$ k Ω . We also varied/decreased the I_{AC} amplitude along with I_{DC} in the simulation, with I_{AC} set to = 1.35, 0.69, 0.4, 0.14 and 0.07 mA for $V_{DC} = 7.8$ and down to 5.4 V respectively. I_{AC} was varied to replicate how the Table XII parameters, especially f_c , changes with respect to V_{DC} . The I_{AC} amplitudes are chosen to replicate the observed $Re \Delta V(f \rightarrow 0)$ in Fig. 7-1(c), since the software will give $Re \Delta V(f \rightarrow$

0) that are in proportion to I_{AC} values (e.g. $I_{AC} \sim \text{mA}$ will give $Re \Delta V (f \rightarrow 0) \sim \text{mV}$) [143]. Also, the Nyquist plot size in Fig. 7-3(b) is smaller at higher I_{DC} as oppose to the real results. This is because, as we decrease the I_{DC} , the relative difference between I_{DC} and I_{AC} becomes smaller, hence the I_{AC} component becomes more significant at low I_{DC} and the Fig. 7-3(b) plot becomes larger at lower I_{DC} . Here, f is set between 1 Hz and 250 kHz. As the circuit components representing our OLED in Fig. 7-3(a), we select $C_{OLED} = 13 \text{ nF}$ and the modified 1N914_KA model from 6.1 as the circuit's diode. The 1N914_KA model was chosen to represent an organic diode due to its smaller saturation current I_S , with $I_S = 3 \text{ pA}$ as oppose to $I_S \sim \text{nA}$ in the LT Spice stock diode. This choice is also to account for lower carrier mobility in the organic diode. Whilst C_{OLED} in Fig. 7-3(a) represents the accumulation of carriers at the interface of the injection and emissive layers, which can be modeled as a capacitor [151]. The C_{OLED} magnitude is chosen to further add the organic diode (order pF) capacitance. Note that as in 6.1, the organic diode capacitance is not voltage-dependent. In addition, we do not know precisely our organic diode's ideality factor (n).

From Fig. 7-3(b), simulated Nyquist plots of the generic OLED equivalent circuit in Fig. 7-3(a) give almost exact semi-ellipses at all V_{DC} without the observed low-frequency 'foot', even at $V_{DC} = 7.8 \text{ V}$. Here, though, the semi-ellipses shows slightly different magnitudes of corner frequency f_c for different V_{DC} . For comparison with experimental results, we deduce the simulated plot's characteristic parameters, i.e. $Re \Delta V (f \rightarrow 0)$ and f_c , and list them in Table XIII.

TABLE XIII OLED V_{DC} , $Re \Delta V (f \rightarrow 0)$ AND f_c FOR THE SIMULATED SPECTRA SHOWN IN FIG. 7-3(b)

OLED V_{DC} [V]	$Re \Delta V (f \rightarrow 0)$ [mV]	f_c [Hz]
7.8	33	472000
7.2	30	273000
6.6	24	195000
6.2	19	90000
5.4	14	59000

From Table XIII, we see again that as V_{DC} is reduced, the OLED becomes less bright (due to reduced $Re \Delta V (f \rightarrow 0)$), consistent with Table XII results. Also, compared to Table XII, f_c are higher for $V_{DC} = 7.2 \text{ V}$ and 7.8 V and lower for $V_{DC} = 5.4$ and 6.2 V . This differences in f_c , as in 6.1, can again be caused by the difficulties of simulating the nonlinear properties of an organic diode in the Fig. 7-3(a) circuit with conventional software. To add, from $Re \Delta V (f \rightarrow 0)$ results in Table XIII, at high V_{DC} more current will be injected into the OLED due to a much stronger electric field and vice versa at lower V_{DC} . So at both high V_{DC} and high f , the field will force more carriers and therefore current to flow into the C_{OLED} due to its lower impedance than through the (organic) diode, while at very low f , currents will flow more into the diode instead of C_{OLED} . At lower V_{DC} and at high frequency, carriers will still flow into the C_{OLED} , but here they can be trapped or forced to recombine before the C_{OLED}

branch due to the weaker electric field. Thus, the smaller f_c results at low V_{DC} . From 5.1, as each simulated plots only forms a single semi-ellipse, each with a minimum peak at a frequency equal to the corner frequency f_c , there will be a single, but dominant internal dynamic that occurs in the simulated cell. This internal dynamic is represented by a time constant τ that can be derived from each plot's f_c . Based on our earlier discussion on carrier transit time, we conclude that the (simulated) time constant τ_{sim} here is the transit time of both carriers that leads to light emission, and is represented by the recombination constant B in Fig. 7-2. This is because τ_{sim} here depends strongly on C_{OLED} while there is no other component in the Fig. 7-3(a) circuit that represent trap dynamics.

However, Fig. 7-3(b) plots remain unable to replicate the “foot” feature that is seen in the low-frequency area of Fig. 7-1(c). From prior discussion, when the Fig. 7-3(a) circuit is at a higher f in the kHz range, carriers may start flowing into the C_{OLED} branch but then become trapped/recombine somewhere in the C_{OLED} branch. We then extend this reasoning to the “hook” feature in Fig. 7-1(c), in that the “hook” is caused by trapped/recombined carriers at f in the kHz range. We model this by placing an extended resistor parallel to an extended capacitor ($R_{ext} // C_{ext}$) in series with the C_{OLED} branch. The simulated spectra from the extended OLED equivalent circuit are shown in Fig. 7-4.

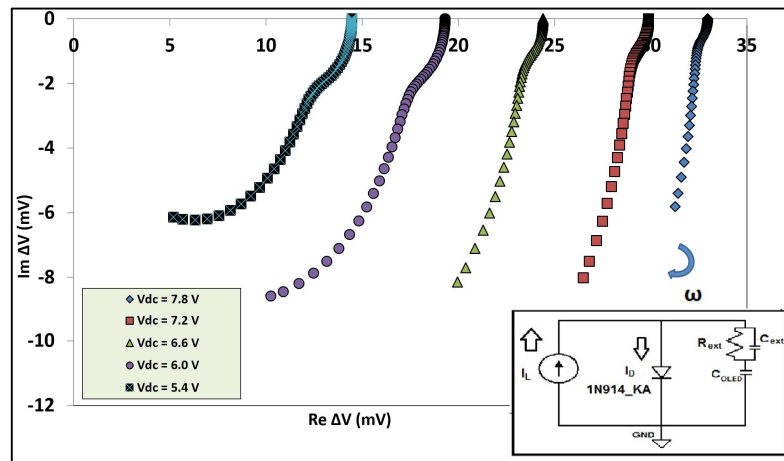


Fig. 7-4. Simulations on the extended equivalent circuit model, shown as an inset. The simulation is performed at f between 1 Hz and 250 kHz and with OLED $V_{DC} = 7.8$ V down to 5.4 V (colour inset). Here, the chosen diode (1N914_KA), the magnitude of C_{OLED} , I_{DC} and I_{AC} are kept to be the same as in Fig. 7-3(a) circuit. Magnitude of $C_{ext} = 6$ nF // $R_{ext} = 600$ Ω . Also, Re/Im axis uses different scales and are not normalized, with the direction of increasing frequency given by the blue, arrow.

In Fig. 7-4, when suitable parameters for $R_{ext} // C_{ext}$ are chosen ($C_{ext} = 6$ nF // $R_{ext} = 600$ Ω), the simulated spectra now include the ‘hook’ feature, similar with the Fig. 7-1(c) experimental spectra. The “hook” here is observed at $f \sim 28$ kHz for $V_{bias} = 7.8$ V, $f \sim 26$ kHz for $V_{DC} = 7.2$ V, and at $f \sim 21$ kHz for $V_{DC} = 6.6, 6$ and 5.4 V, so the decrease in simulated “hook” frequency as we decrease V_{bias} is consistent with the experimental results in Fig. 7-1(c). Also, as we decrease V_{DC} in the Fig. 7-4 simulation, the resulting f_c decreases as well. Modeling thus confirms the origin of the kHz range

“hook” feature in the C_{OLED} branch. We note from OLED preparation in 3.2 that the OLED uses PEDOT as its hole injection layer (HIL). As such, the OLED’s ITO anodes can be etched by the PEDOT’s acidic dopant, i.e. polystyrene sulfonic acid (PSS), which can then liberate indium ions into the injection and emissive layers [57]. Therefore, as in 6.2, the presence of Indium in the injection and emissive layers will create instability in both layers and reduce the OLED’s performance over time. This can be caused by a reduction in the injection layer area size, hence reducing the number of injected carriers, represented by R_{ext} in the C_{OLED} branch. At the same time, trap sites can also form in the injection layer due to a discontinuity caused by Indium penetration. These trap sites thus create a capacitance C_{ext} , and together with R_{ext} forms the R_{ext}/C_{ext} in Fig. 7-4. Hence, we can assign the “hook” feature in Fig. 7-1(c) to the diffusion of indium ions into the C_{OLED} due to ITO etching by PSS. Since we can correctly model our OLED with the Fig. 7-4 extended circuit, the f_c from Fig. 7-1(c) will also depend heavily on C_{OLED} , this is beside the fact that f_c (and τ_{eff}) scales with V_{DC} in Table XII. The C_{OLED} is again the accumulation of carriers at the interface of the injection and emissive layers. Therefore, Table XII f_c corresponds to the effective time constant τ_{eff} , which is the transit time of both carriers before they recombine in the emissive layer which then leads to light emission, as elaborated in the Fig. 7-2 model.

We then convert the f_c in Table XII with $f_c = 1/2\pi\tau_{eff}$ and plot the resulting effective transit time τ_{eff} with respect to $1/(V_{DC} - V_{bi})$ as given by equation (35). For this purpose, the emissive layer thickness is $d = 85$ nm and $V_{bi} = 0.5$ V from equation (17) with the metal/electrode work function values obtained from the literature. Finally, equation (35) predicts a straight line (fit) on τ vs. $1/(V_{DC} - V_{bi})$, from which slope we can derive a figure of merit for the effective mobility μ_{eff} . The resulting plot is depicted in Fig. 7-5.

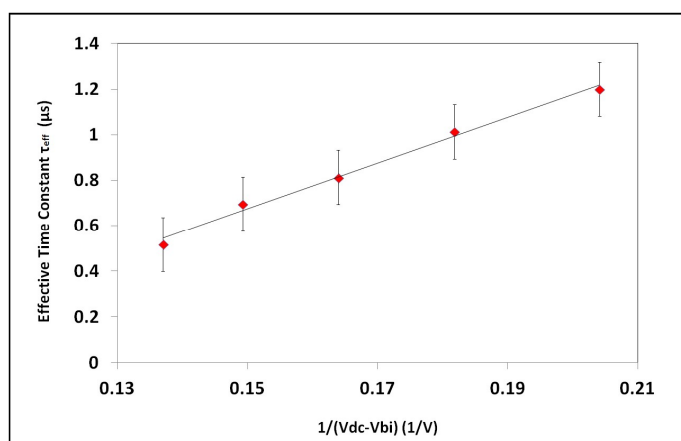


Fig. 7-5 A plot of (transit) time constant τ (μ s) vs $1/(V_{DC}-V_{bi})$ (V^{-1}). Time constant (τ) data were derived from f_c in Table XII.

In Fig. 7-5, we find a straight line fit which indicates that the relationship between τ (μs) vs. $I/(V_{DC}-V_{bi})$ is indeed linear. From the slope, we find that $\mu_{eff} = (9.37 \pm 0.02) \times 10^{-6} \text{ cm}^2/\text{V s}$. On its own, this figure is much larger compared to the hole mobility (μ_h) of poly (*p*-phenylene vinylene) or PPV-based OLED at room temperature [148]. Note, however, that this value is the average mobility of both carriers. Also, from equation (35), as τ_{eff} is influenced more by the slower mobility, μ_{eff} will instead be dominated by the faster ones. From the literature, e.g. for PPV-based devices, the mobility of holes is much higher than those of electrons [148, 152]. Therefore, we estimate that μ_{eff} here is likely to be the OLED's electron mobility or $\mu_{eff} \sim \mu_e$.

7.2 Results from IMS Measurements with Different Optical Filters on OLED Devices

We then proceed to perform IMS characterization in order to compare different OLED dynamics from different chromophores/colours within the OLED device emissive layer. We do this by slightly modifying the IMS setup in Fig. 4-13(a) (in 4.6), i.e. by inserting an optical filter between the OLED and the fast photodiode in the setup. Thus, we can then obtain different light emission from the two-colour OLED that we characterize. To accommodate the filter, we separate the photodiode at a distance away from the OLED. We then use the OLED to illuminate the photodiode. For this characterization, we use OLED No. 2 in the OLED J/V characteristics in Fig. 3-10, filter the OLED's light output with two different filters, where each will result in either red or blue emission being detected. In doing this, we kept the applied V_{DC} and V_{AC} on the OLED to be the same for all (light) filtering conditions. We then compare the resulting IMS spectrum from the red and blue light in the OLED with those from the total (white) emission. We do this by extracting the respective corner frequencies (f_c) from the red, blue and white IMS spectrum. The resulting τ represents the internal dynamics from each of the chromophores as compared to the total white light.

For the IMS, we apply a combination of a large voltage bias and a small sinusoidal AC voltage of $V_{OLED} = (7 \pm 0.6) \text{ V}$ on a fresh OLED. Since the OLED is protected by a serial resistor $R_{OLED} = 2.7 \text{ k}\Omega$ in the adder, it will then result in a corresponding $I_{OLED} = (1.6 \pm 0.2) \text{ mA}$. The bias component in V_{OLED} , i.e. $V_{DC} = 7 \text{ V}$ was obtained by measuring the voltage drop across the OLED as mentioned in 4.6. While the DC drive current in I_{OLED} , i.e. $I_{DC} = 1.6 \text{ mA}$, was obtained from the equation $I_{DC} = V_{RA}/R_{OLED}$, with V_{RA} being the voltage drop across the R_{OLED} as elaborated in 4.6. The modulating current in I_{OLED} , i.e. $I_{AC} = 0.2 \text{ mA}_p$ was obtained through the equation $I_{AC} = V_{AC}/(R_{OLED} + R_{diff})$, with $V_{AC} = 0.6 \text{ V}_p$ from the lock-in ref out and $R_{diff} = 578 \text{ }\Omega$ as determined from the OLED No. 2 J/V characteristics in Fig. 3-10. The IMS software settings used for this experiment are slightly different from the settings mentioned earlier. We set the input coupling to AC and dynamic to low while all

other settings are kept the same. This is because we kept a distance between the OLED and photodiode to accommodate the optical filter. So to anticipate weak photocurrents due to this extra distance, we set the coupling to AC and input amplification to (x 100). As a consequence, we operate the IMS software to perform a frequency scan at f between 33 Hz and 250 kHz in 18 steps per decade, since we cannot perform a low-frequency scan under AC coupling. First, perform the IMS without inserting any filter between the OLED and a reverse-biased ($V_{REV} = -13.2$ V) OSD5-5T silicon photodiode. Later, we repeat the IMS experiment by inserting an optical longpass filter between the OLED and the photodiode. This filter will only pass light with a wavelength (λ) > 550 nm, so only the red part (560-680 nm) of the (OLED's) emissive layer spectrum in Fig. 3-8 (in 3.2) will be passed. After this experiment, we repeat the IMS again by inserting a bandpass filter which will let through light with $320 \leq \lambda \leq 500$ nm, so only the blue part (450-500 nm) of Fig. 3-8 spectrum will be passed. For direct IMS comparison of unfiltered white light with the filtered ones, we maintain a distance $s = 0.6$ cm between the OLED and the photodiode circuit for all cases. Here, the IV converter used to convert photodiode current into voltage has a feedback resistor $R_f = 4.7$ k Ω and feedback capacitor $C_f = 4.7$ pF. In Fig. 7-6, we present the IMS results from the OLED's white, red and blue emission in the form of Bode amplitude, phase and Nyquist plot of ΔV .

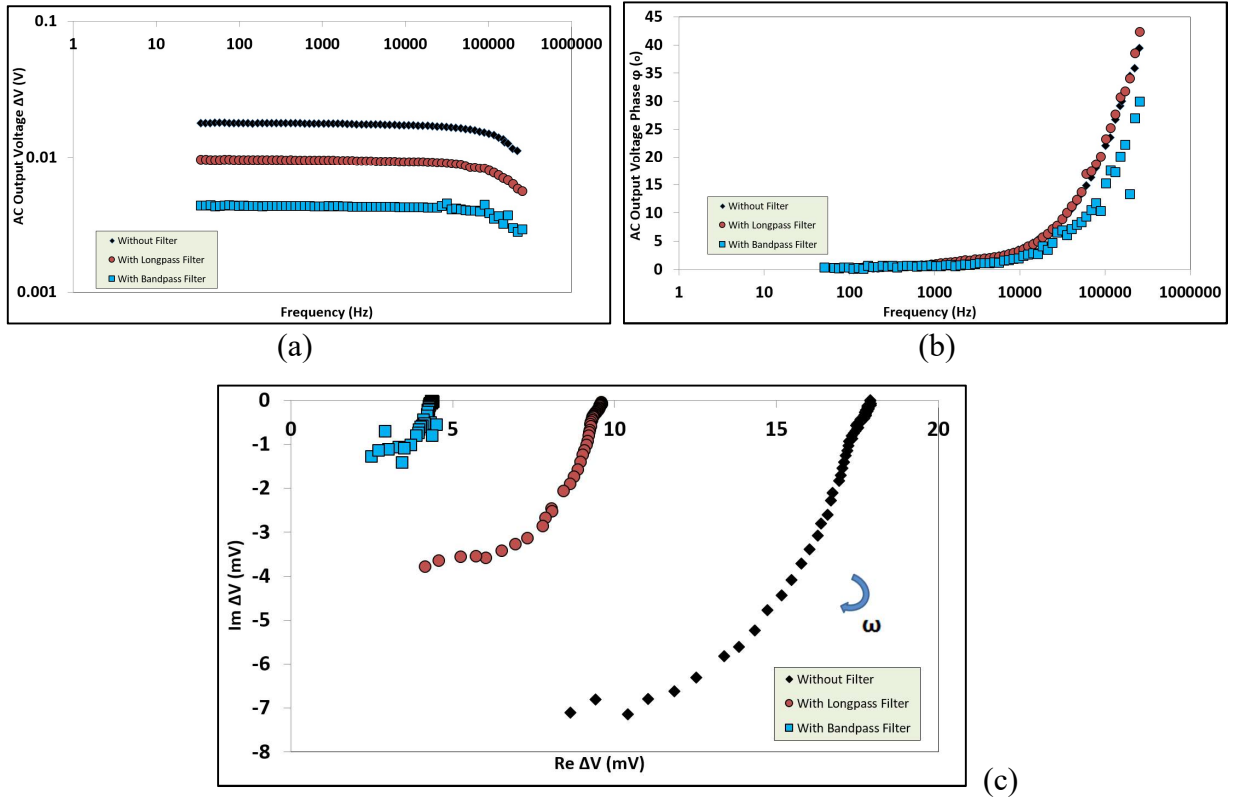


Fig. 7-6 (a). Bode amplitude plot of ΔV , (b) Bode phase plot of ΔV phase ϕ vs frequency f and (c) Nyquist plots of ΔV that plots the imaginary ($Im \Delta V = |\Delta V| \sin \phi$) vs. its real part ($Re \Delta V = |\Delta V| \cos \phi$), the spectra being parametric with frequency. Here, (a), (b) and (c) are taken at frequencies between 30 Hz and 250 kHz and at unfiltered-, longpass and bandpass filtered light (shown as colour coded and in the inset). Note the Re/Im axis at (c) uses different scales and are not normalized, with the direction of increasing frequency given by the blue arrow. For both filtered- and unfiltered light, we applied a voltage $V_{OLED} = (7 \pm 0.6)$ V on the OLED and drive it with a current drive $I_{OLED} = (1.6 \pm 0.2)$ mA.

Fig. 7-6(c) shows a set of Nyquist plot spectra measured for the three light conditions. From Fig. 7-6(a), $\Delta V (f \rightarrow 0)$ is highest for unfiltered light with the smallest being for blue light. Thus, it is clear that white light is the brightest out of the three, followed by red and then blue. From Fig. 7-6(b), ΔV phase ϕ is similar for all three cases, with ϕ never reaching 45° at the highest frequency for both unfiltered- and filtered light. Thus, it is likely that all three lights had a similar internal dynamic. In Fig. 7-6(c), the general shape of the Nyquist spectra for all light emission resembles an incomplete semi-ellipse in the 4th quadrant of the complex plane, with the white light semi-ellipse being the largest in size and the blue the smallest, though note that Re/Im axis in Fig. 7-6(c) uses different scales. We also observe a “bent” feature at $f \sim 6.5$ kHz in Fig. 7-6(c) plot for white light and at $f \sim 3$ kHz for red light. For blue, this “bent” feature is absent, though note that the blue light plots in Fig. 7-6(c) are noisy, especially at $f > 10$ kHz. Finally, the “bent” feature seems to be larger for unfiltered light than for red light in Fig.7-6(c).

From Fig. 7-6(a), (b) and (c), we can extract two characteristic parameters, $Re \Delta V$ at $(f \rightarrow 0)$ and f_c . Note that here, $\Delta V (f \rightarrow 0)$ and $Re \Delta V$ at $(f \rightarrow 0)$ are taken at $f \sim 30$ Hz due to the AC coupling used. In addition, we also approximate f_c for all spectra in Fig. 7-6(c) with $f_c = f_o / \tan \phi_o$, where ϕ_o is

the output voltage phase at frequency f_o [36]. Here, we use $f_o = f$ at $\varphi_o = 30^\circ$ to approximate f_c at $\varphi = 45^\circ$. Also, as f_c is linked to a time constant τ through $f_c = 1/2\pi\tau$, we can derive a time constant τ to compare the dynamics for all three lights. The OLED's electrical condition (V_{DC}), $Re \Delta V (f \rightarrow 0)$ and f_c obtained from Fig. 7-6(a), (b) and (c) are shown in Table XIV.

TABLE XIV THE OLED LIGHT EMISSION, $Re \Delta V (f \rightarrow 0)$ AND f_c FOR THE SPECTRA SHOWN IN FIG. 7-6(a), (b) AND (c)

OLED Light Emission	$Re \Delta V (f \rightarrow 0)$ [mV]	f_c [Hz]
White	18 ± 10	160000 ± 1
Red	10 ± 10	151000 ± 1
Blue	4 ± 10	230000 ± 1

From Table XIV, we can confirm that the white light is brighter than both red and blue, and is consistent with the emissive layer spectrum in Fig. 3-8 as white is a total of both red and blue emission. However, we observe that the red light is much brighter than the blue, while from Fig. 3-8 the opposite is true. This can be caused, among others, by the blue emission's narrow spectrum/FWHM compared to that of the red in Fig. 3-8. However, it is more likely caused by the photodiode's lower responsivity (in A/W) with respect to the resulting blue light wavelength (λ) range (i.e. 450-500 nm) from a bandpass filter when compared to the red ones from the lowpass filter and the total OLED illumination (λ range = 560-680 nm and 450-680 nm respectively). We can observe this from the OSD5-5T photodiode's responsivity plot with respect to an illumination source with a wavelength range ~ 350 -1100 nm, in which the photodiode's responsivity is also compared at both under a 12 V reverse bias (bold spectrum) and without a reverse bias voltage (dotted spectrum) as displayed in Fig. 7-7 from Centronic Ltd. [136].

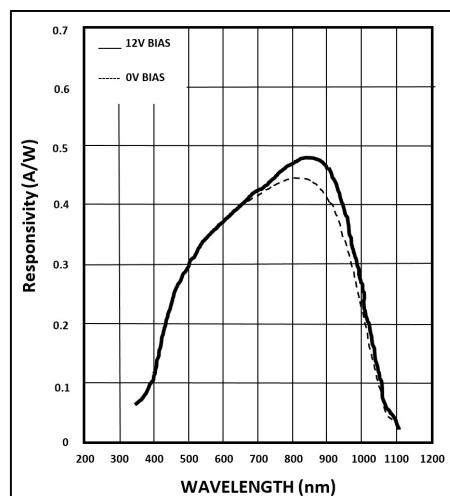


Fig. 7-7. The OSD5-5T responsivity (in A/W) plot under an illumination source with a wavelength range ~ 350 -1100 nm, where the photodiode's responsivity is also compared at both under a 12 V reverse bias (bold spectrum) and at 0 V reverse bias voltage (dotted spectrum), which is taken from Centronic Ltd. [136].

In Fig. 7-7, we can see that at both 12 V and 0 V reverse bias, the photodiode's minimum responsivity in the λ range = 450-500 nm (i.e. responsivity at 450 nm) is roughly 0.15 A/W, which although quite high in terms of responsivity to blue light [136], it is still twice lower compared to its minimum responsivity in the λ range = 560-680 nm, which is ~ 0.35 A/W. As a result, the blue light from the filtered OLED illumination is much less bright compared to the OLED's red light component, as evident from the lower $Re \Delta V$ at ($f \rightarrow 0$) in Fig. 7-6(a) that is obtained under blue illumination when compared to that under red light. Hence, for future work we would recommend the use of a photodiode in which the difference between its blue and red minimum responsivity is not too large as is the case in OSD5-5T. Examples of a photodiode with relatively small difference between their red and blue minimum responsivity are photodiode model S1087 and S1226 from Hamamatsu Photonics K.K. [153, 154]. Returning back to Table XIV, we then conclude that all three lights give similar OLED internal dynamics, as evident from their f_c in Table XIV. Note that though the blue emission's f_c is higher (or its τ is shorter compared to white and red), the ϕ result for blue is still similar to that of the other colours in Fig. 7-6(b). Further, the time constant τ derived from f_c in Table XIV can also be considered as a carrier transit time, i.e. the time needed by both carriers in the OLED to travel and then recombine to emit light in the emissive layer, as elaborated in equation (35). We then investigated how the Table XIV parameters change for all three lights by using an OLED-equivalent circuit model and then elaborate how the changes relate to the OLED's physical processes model in Fig. 7-2.

From 7.1, at a very low f , carriers will prefer to flow through the diode instead of the C_{OLED} in Fig. 7-3(a) OLED equivalent circuit. However, in the kHz range, carriers may start flowing into the C_{OLED} branch but then become trapped/recombine somewhere in the C_{OLED} , thus causing the "bend" to appear. Therefore, we can use the extended equivalent circuit in Fig. 7-4 to both model the "bend" and the dependence of f_c on C_{OLED} at high f . We also modified the circuit parameters accordingly to replicate the experimental results. The resulting spectra and circuit are shown in Fig. 7-8.

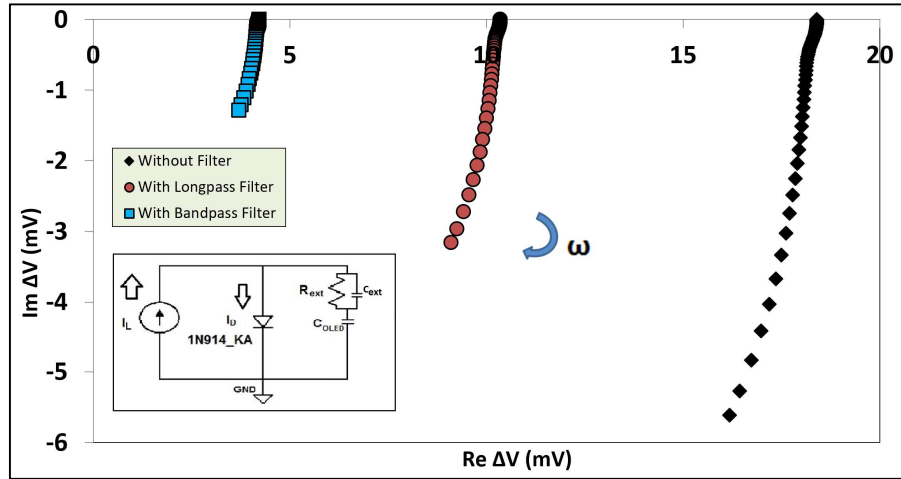


Fig. 7-8. Simulated Nyquist plot of unfiltered- and filtered light (shown as colour-coded) with Fig. 7-4 extended OLED-equivalent circuit model (circuit inset) at f between 30 Hz and 250 kHz. The I_L here represents the light-driven current source in IMS, all components are internal to the OLED. Here, we again select $C_{OLED} = 13$ nF, with the same 1N914_KA diode as in Fig. 7-4. Magnitude of $C_{ext} = 9$ nF // $R_{ext} = 900$ Ω . The DC current bias amplitude (I_{DC}) is set to 1.2 mA for all light, which corresponds to $V_{DC} = 7$ V. Next, the current source modulation is set to $I_{AC} = 0.48, 0.27$ and 0.11 mA for white, red and blue light respectively. The plots Re/Im axis uses different scales and is not normalized, with the direction of increasing frequency given by the blue arrow.

For our simulation, the DC current bias amplitude (I_{DC}) is set at 1.2 mA for all light, which corresponds to $V_{DC} = 7$ V. The current source modulation is set to $I_{AC} = 0.48, 0.27$ and 0.11 mA for white, red and blue light respectively. While the I_{DC} amplitude was constant for all light, the I_{AC} amplitude was varied in the simulation and chosen to replicate the $Re \Delta V(f \rightarrow 0)$ values in Table XIV. Also, for the simulated plots in Fig. 7-8 f is set between 30 Hz and 250 kHz. For the circuit components representing our OLED in Fig. 7-8, we select the same C_{OLED} amplitude of 13 nF and the 1N914_KA diode from 7.1 with the same reasoning. Here, C_{OLED} in Fig. 7-8 represents the accumulation of carriers at the interface of the injection and emissive layers, which is modeled as a capacitor [151]. In addition, the magnitude of the extended resistor (R_{ext}) // extended capacitor (C_{ext}) in Fig. 7-8 is set to 900 Ω and 9 nF respectively. This (R_{ext} // C_{ext}) is set higher than the values in 7.1 to accurately model the “bent” feature shape in Fig. 7-6(c).

We see that the Fig. 7-8 simulated plot roughly resembles the semi-ellipse curve of Fig. 7-6(c) for all three lights. Also, the simulated plot is able to replicate well the low-frequency “bent” feature in Fig. 7-6(c) for all three emissions. Note also that the simulated “bent” feature for blue is barely visible, similar to Fig. 7-6(c). The simulated “bent” feature in Fig. 7-8 occurs at $f \sim 15, 9$ and 4 kHz for white, red and blue light respectively. Now, though this (“bent”) f value is higher than that in Fig. 7-6(c), the trend in f where the “bent” feature occurs (white having the highest f and blue the lowest) is consistent with the experimental results. Further, the simulated “bent” feature size is largest in white and smallest in blue, also similar to Fig. 7-6(c). In addition, the simulated semi-ellipses also

show different f_c magnitudes for all lights compared to the Table XIV values. For comparison with experimental results, we derived characteristic parameters from Fig. 7-8, and list them in Table XV.

TABLE XV THE OLED LIGHT EMISSION, $Re \Delta V(f \rightarrow 0)$ AND f_c FOR THE SPECTRA SHOWN IN FIG. 7-8

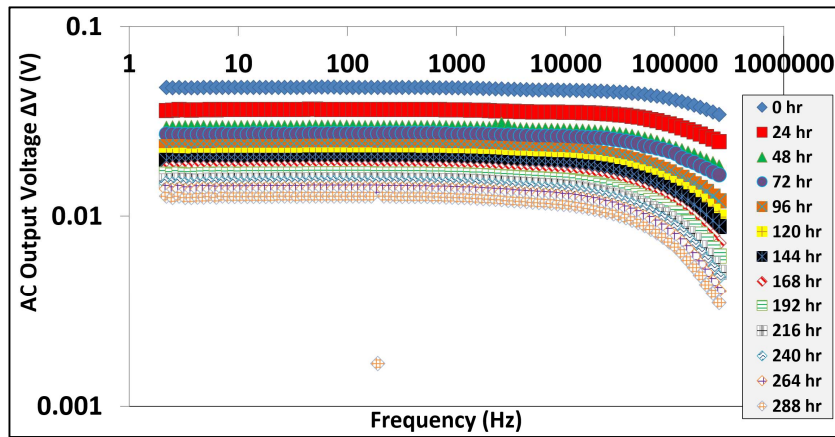
OLED Light Emission	$Re \Delta V(f \rightarrow 0)$ [mV]	f_c [Hz]
White	18	687000
Red	10	687000
Blue	4	687000

From Table XV, the simulated $Re \Delta V(f \rightarrow 0)$ magnitude again depends on I_{AC} as in 7.1 due to the same reasoning, i.e. the $Re \Delta V(f \rightarrow 0)$ magnitude scales linearly with the given I_{AC} in LT Spice. Also, compared to Table XIV, f_c values in Table XV are 5x higher for all three lights. This difference in f_c amplitudes, similar to 7.1, can again be caused by the difficulties in simulating an organic diode in Fig. 7-8 circuit with conventional software. Also, a similar f_c and in turn, similar time constant τ in Table XIV, implies the same internal dynamics occurring within the OLED for all three lights. To further explain the simulated results, at high f , the field from the OLED V_{DC} will force more carriers and therefore current to flow into the $COLED$ due to its lower impedance than through the organic diode in the Fig. 7-8 inset. Thus the high value of f_c in Table XV is due to its dependency on $COLED$. $COLED$ is the accumulation of carriers at the interface of the injection and emissive layer. However, since we kept the OLED V_{DC} to be the same for all three lights, the resulting f_c will also be the same for all lights as is evident in Table XIV and the experimental plot in Fig. 7-6(b). So the only difference between the three will be their respective intensity, i.e. their $Re \Delta V(f \rightarrow 0)$ magnitude, which is reduced due to light filtering for non-white colour. As for the “bent” feature, this can be explained from the prior assumptions of Fig. 7-8, in that in the kHz range, carriers will start flowing into the $COLED$ branch but then become trapped or recombine somewhere. Furthermore, since the OLED also uses PEDOT:PSS as the hole injection layer, the “bent” feature can physically originate from the diffusion of indium ions to the $COLED$ due to ITO etching by PSS [57, 82]. The diffused indium will create instability in both the injection and emissive layers and reduce the OLED’s performance over time. This will be manifested in the presence of a $R_{ext} // C_{ext}$ component similar to that in 7.1. To conclude, since the Fig. 7-6(c) results can be modelled with the extended circuit, f_c will strongly depend on the $COLED$, hence τ from f_c can then be considered as a carrier transit time, i.e. the time needed by both carriers in the OLED to travel and then recombine to emit light in the emissive layer, as in equation (35). Finally, because these IMS results on all type of OLED emission results in the same f_c , we can conclude that all three lights have the same carrier transit time. Also, all three lights showed a fluorescence-type emission.

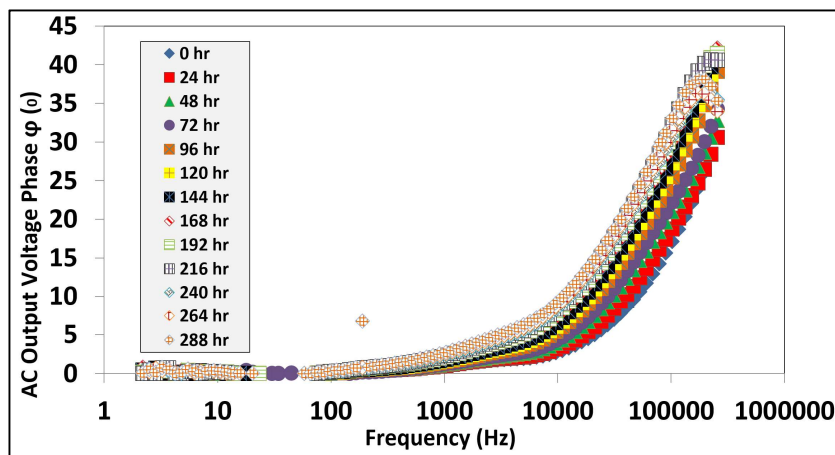
7.3 Results from OLED Device Ageing Study with IMS

Finally, we performed IMS characterization of an OLED for the purpose of conducting an OLED aging study with the same setup as in 4.6. This was done by continually applying a V_{OLED} on a fresh OLED or driving it with an I_{OLED} , i.e. OLED No. 1 in OLED J/V characterization from Fig. 3-10, until the OLED itself, failed, while conducting an (IMS) frequency scan for as much as four times daily, with each scan conducted at 3 hours interval. During the process, we kept V_{OLED} the same for each day of the scan. From the daily IMS spectra, we extract (corner frequencies) f_c that represents the time constant τ of an OLED internal dynamics. We then plot f_c with respect to (IMS) scan hours, in order to observe the changes in the internal dynamics (f_c) with respect to OLED aging.

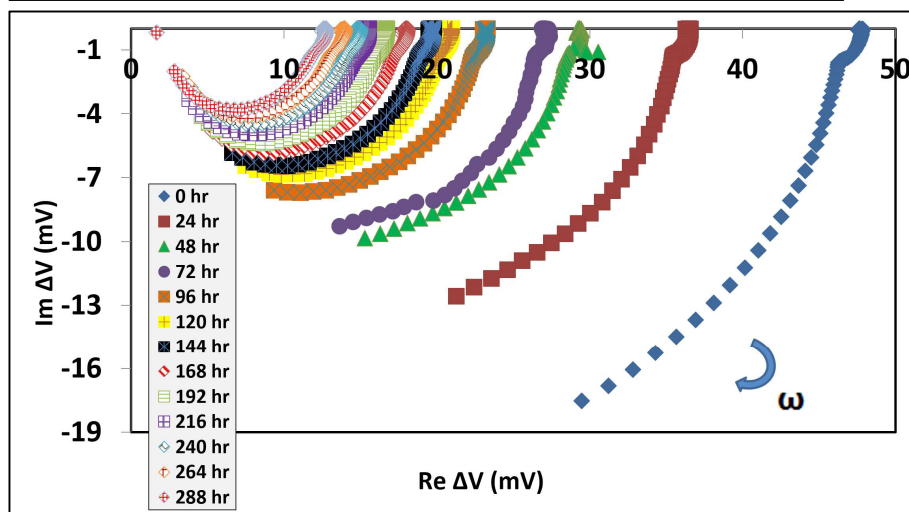
For the IMS, we apply a combination of a large voltage bias and a small sinusoidal AC voltage of $V_{OLED} = (7.1 \pm 1.7)$ V on a fresh OLED. Since the OLED is protected by a serial resistor $R_{OLED} = 2.7$ k Ω in the adder, it will then result in a corresponding $I_{OLED} = (1.6 \pm 0.4)$ mA. The bias component in V_{OLED} , i.e. $V_{DC} = 7.1$ V was obtained by measuring the voltage drop across the OLED as mentioned in 4.6. While the DC drive current in I_{OLED} , i.e. $I_{DC} = 1.6$ mA, was obtained from the equation $I_{DC} = V_{R4}/R_{OLED}$, with V_{R4} being the voltage drop across R_{OLED} as elaborated in 4.6. The modulating current in I_{OLED} , i.e. $I_{AC} = 0.4$ mA_p was obtained through the equation $I_{AC} = V_{AC}/(R_{OLED} + R_{diff})$, with $V_{AC} = 1.7$ V_p from the lock-in ref out and $R_{diff} = 1227$ Ω as determined from the OLED No. 3 J/V characteristics in Fig. 3-10. The IMS software settings used for this experiment are the same as in 7.1. Here, we operate the IMS software to perform a frequency scan at f between 1 Hz and 250 kHz in 18 steps per decade. The IV converter used to convert photodiode current into voltage has a different feedback resistor i.e. $R_f = 1$ k Ω and feedback capacitor $C_f = 4.7$ pF. We also maintain the same V_{OLED} ($V_{DC} + V_{AC}$) and I_{AC} magnitude throughout the experimental duration. However, the OLED I_{DC} amplitude will be reduced later to less than 1.6 mA due to OLED aging. $I_{AC} = 1.6, 1.3, 1, 0.9, 0.7, 0.63, 0.6, 0.5, 0.44, 0.4, 0.4, 0.3$ and 0.3 mA at 0, 24, 48, 72, 96, 120, 144, 168, 192, 216, 240, 264 and 288 hours respectively. In Fig. 7-9, we present the IMS results from the OLED aging study (with respect to aging time) in the form of a Bode amplitude, phase and Nyquist plot of the OLED's ΔV .



(a)



(b)



(c)

Fig. 7-9 (a). Bode amplitude plot of the OLED's ΔV , (b) Bode phase plot of ΔV phase ϕ vs frequency f and (c) Nyquist plots of ΔV that plots the imaginary ($Im \Delta V = |\Delta V| \sin \phi$) vs. the real part ($Re \Delta V = |\Delta V| \cos \phi$), the spectra being parametric with frequency. Here, (a), (b) and (c) are taken from 0 to 288 hours of aging (colour coded in inset), by which time the OLED failed. We summarize the aging results in all plots to a 24-hour measurement interval. In addition, all plots were taken at frequencies between 1 Hz and 250 kHz. Note the Re/Im axis at (c) uses different scales and are not normalized, with increasing frequency direction given by the blue arrow. For this experiment, we applied a voltage $V_{OLED} = (7.1 \pm 1.7)$ V to the OLED.

Fig. 7-9(a) and (b) show the Bode plots of ΔV and ΔV phase ϕ with respect to frequency (f) at f between 1 Hz and 250 kHz and taken from 0 to 288 hours of aging, by which time the OLED failed. Fig. 7-9(c) shows a set of Nyquist plots of the measured Re and $Im \Delta V$ at the same experimental

duration and frequency range. Here, we present the Bode and Nyquist plots results in 24 hours interval to summarize the OLED's aging process. From Fig. 7-9(a), it is clear that as we continually operate the OLED, its performance is reduced as evident from the decrease in $\Delta V(f \rightarrow 0)$. Thus, continued operation leads to OLED degradation which decreases its brightness. From the increase of φ with time in Fig. 7-9(b), we infer that the OLED's internal dynamics, most likely the transit time τ , is influenced by OLED degradation. Further, we also see that a peak starts to appear at $f > 100$ kHz from 216 to 288 hours of aging, with φ having never reach 45° at the highest frequency f throughout aging. This peak is not visible in Fig. 7-9(a) and (c). A possible explanation is that at high f and at later stages of aging, transit time (τ) dynamics occur where τ rises and then decreases due to degradation. The general shape of the Nyquist spectra in Fig. 7-9(c) again resembles an incomplete semi-ellipse in the complex plane's 4th quadrant, though here the Re/Im axis use different scales. We also observe a "hook" feature similar to 7.1 for all aging times. The "hook" occurs at $f \sim 3$ kHz for 0-72 and 264 hours of aging, and at $f \sim 2$ kHz for 96-240 and 288 hours of aging. It is clear that the "hook" dynamics are influenced by OLED degradation, as the frequency where the "hook" feature occurs changes as the OLED is continually kept on.

From Fig. 7-9, we can extract two characteristic parameters, these are $Re \Delta V(f \rightarrow 0)$ and f_c respectively. We approximate f_c for all spectra in Fig. 7-9(c) with $f_c = f_o / \tan \varphi_o$, where φ_o is the output voltage phase at frequency f_o [36]. Here, we again use $f_o = f$ at $\varphi_o = 30^\circ$ to approximate f_c at $\varphi = 45^\circ$. This is because of the majority of the plots in Fig. 7-9(b) never reach 45° at the highest frequency. In addition, we also list changes in OLED I_{DC} with respect to aging time. The OLED's electrical condition (V_{DC}), $Re \Delta V(f \rightarrow 0)$ and f_c obtained from Fig. 7-9(a), (b) and (c) are then shown in Table XVI.

TABLE XVI OLED AGEING TIME, I_{DC} , $Re \Delta V(f \rightarrow 0)$ AND f_c , FOR THE SPECTRA SHOWN IN FIG. 7-9(a), (b) and (c)

OLED Ageing Time [Hours]	I_{DC} [mA]	$Re \Delta V(f \rightarrow 0)$ [mV]	f_c [Hz]
0	1.60	47 ± 10	441000 ± 1
24	1.30	36 ± 10	441000 ± 1
48	1.00	29 ± 10	390000 ± 1
72	0.90	27 ± 10	340000 ± 1
96	0.70	23 ± 10	261000 ± 1
120	0.63	21 ± 10	230000 ± 1
144	0.60	20 ± 10	201000 ± 1
168	0.50	18 ± 10	177000 ± 1
192	0.44	17 ± 10	163000 ± 1
216	0.40	15 ± 10	155000 ± 1
240	0.40	15 ± 10	176000 ± 1
264	0.30	14 ± 10	160000 ± 1
288	0.30	13 ± 10	141000 ± 1

From Table XVI, we confirm that the OLED degrades as it ages, as is evident from the decrease in I_{DC} , and $Re \Delta V (f \rightarrow 0)$ which indicates reduced OLED brightness. From 7.1, we find that f_c is related to a carrier transit time that scales with V_{DC} , I_{DC} . As such, τ here is likely to be a carrier transit time, which gets slower as the device ages. This is consistent with the literature, where a corner frequency (f_c)-equivalent parameter in an impedance measurement also decreases as the OLED ages [155]. We also confirm that the presence of a peak at $f > 100$ kHz in Fig. 7-9(b) corresponds to the slight rise and decrease of f_c (and τ) at 240 to 288 hours of aging. A possible way to explain this peak dynamics is by using the equivalent circuit in Fig. 7-3(a). When the OLED is new, carriers will travel through C_{OLED} due to its lower impedance at high f , thus the absence of a peak in the ΔV phase. At later stages of aging, though carriers will still flow into the OLED, carriers may not travel very far in the C_{OLED} due to OLED degradation. Thus, the presence of a peak in Fig. 7-9(b) plots at later stages of the aging process. We then investigate how the Table XVI parameters change with respect to aging by using an OLED-equivalent circuit model and then elaborate how the changes relate to the OLED's physical model in Fig. 7-2 to explain the experimental results.

Based on the overall results of Fig. 7-9(a), (b) and (c), the “hook” in Fig. 7-9(c), and the trend of the Table XVI parameters, we use the extended equivalent circuit in Fig. 7-4 and modify its parameters accordingly to model the OLED dynamics with respect to aging. The resulting spectra and circuit are shown in Fig. 7-10.

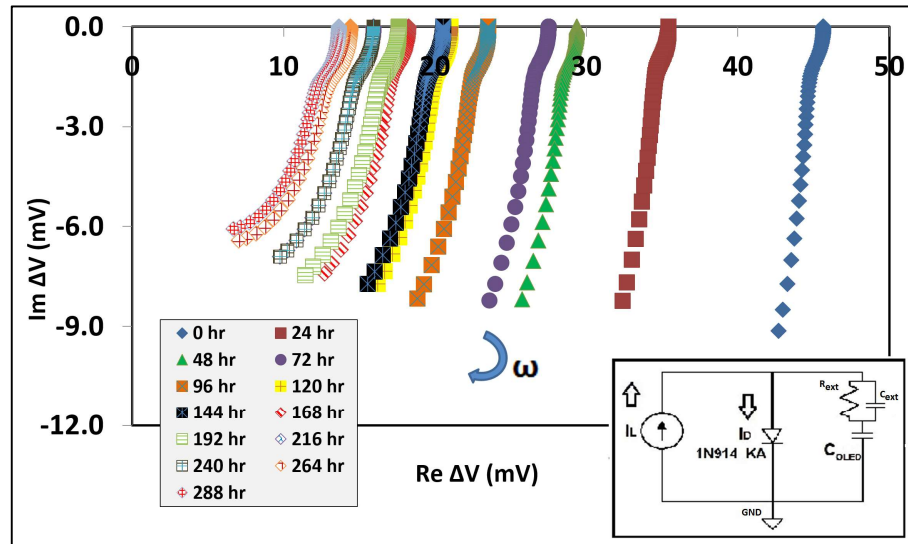


Fig. 7-10. Simulated Nyquist plot for the OLED with respect to OLED ageing hours (colour inset) using the Fig. 7-4. extended circuit (circuit inset) at f between 1 Hz and 250 kHz. For the simulations, we set the DC current bias (I_{bias}) = 1.6, 1.3, 1, 0.9, 0.7, 0.63, 0.6, 0.5, 0.44, 0.4, 0.4, 0.3 and 0.3 mA with current modulation (I_{AC}) = 1.58, 1, 0.64, 0.54, 0.36, 0.29, 0.27, 0.2, 0.19, 0.14, 0.14, 0.095 and 0.09 mA_p for 0-288 ageing hours with 24 hours interval respectively. Here, we again use the modified 1N914_KA diode and set $C_{OLED} = 13$ nF in the circuit. We also set $C_{ext} = 6$ nF // $R_{ext} = 600 \Omega$. Finally, the plots Re/Im axis uses different scales and are not normalized, with the direction of increasing frequency given by the blue arrow.

For our simulations, the DC current bias (I_{DC}) amplitudes were set to = 1.6, 1.3, 1, 0.9, 0.7, 0.63, 0.6, 0.5, 0.44, 0.4, 0.4, 0.3 and 0.3 mA with current modulation (I_{AC}) = 1.58, 1, 0.64, 0.54, 0.36, 0.29, 0.27, 0.2, 0.19, 0.14, 0.14, 0.095 and 0.09 mA_p for 0-288 ageing hours with 24 hours interval respectively. For simulation purposes, we chose the I_{AC} amplitude and then varied/decreased the I_{AC} to replicate how the Table XVI parameters change with respect to aging time. We again select C_{OLED} = 13 nF and the modified 1N914_KA as the circuit's diode with the same reasoning as in 7.1. The C_{OLED} here represents the accumulation of carriers at the interface of the injection and emissive layers. We then set the magnitude of the extended resistor (R_{ext}) // extended capacitor (C_{ext}) in Fig. 7-10 circuit to 600 Ω and 6 nF respectively. Finally, Fig. 7-10 simulated plots are set at f between 30 Hz and 250 kHz.

From Fig. 7-10, we see that the simulated plots roughly resemble the semi-ellipse curve of Fig. 7-9(c) at 0-288 aging hours. Also, the simulated spectra are able to replicate the “hook” feature in Fig. 7-9(c) at all aging time. For comparison with experimental results, we then derived the characteristic parameters of Fig. 7-10, and list them in Table XVII.

TABLE XVII OLED AGEING TIME, I_{DC} , $Re \Delta V(f \rightarrow 0)$ AND f_c FOR FIG. 7-10 SIMULATED SPECTRA.

OLED Ageing Time [Hours]	I_{DC} [mA]	$Re \Delta V(f \rightarrow 0)$ [mV]	f_c [Hz]
0	1.60	46	1200000
24	1.30	35	1100000
48	1.00	29	780000
72	0.90	28	710000
96	0.70	23	570000
120	0.63	21	511000
144	0.60	20	483000
168	0.50	18	420000
192	0.44	17	375000
216	0.40	16	341000
240	0.40	16	341000
264	0.30	14	250000
288	0.30	13	250000

From Table XVII, we see that the extended circuit is able to simulate the decrease in the OLED's brightness with time due to its degradation, as is evident from the decrease in $\Delta V(f \rightarrow 0)$ and $Re \Delta V(f \rightarrow 0)$ as I_{DC} is reduced, which is consistent with the experimental results in Table XVI. We observe that the f_c values in Table XVII are much higher for all aging times compared to the real results in Table XVI. This difference, as in 7.1, can again be caused by the difficulties in simulating the organic diode's nonlinear properties in the Fig. 7-10 circuit inset with conventional simulation software. From Fig. 7-10, we find that the “hook” occurs at f = 19, 15, 13 and 11 kHz for 0, 24-192, 216-264 and 288 aging hours respectively. Thus, the decrease in this “hook” frequency as the OLED ages follows a similar trend in Fig. 7-9(c). Note that here, the simulated “hook” frequency is much

higher compared to those in Fig. 7-9(c), but this can be ascribed as well to the difficulty in simulating an organic diode as mentioned earlier. Since we were able to closely replicate the Fig. 7-9(c) experimental plots, we then conclude that we have correctly modeled the experimental results with the Fig. 7-10 extended circuit. Therefore, the real f_c , and consequently, the τ derived from it, will then depend on the accumulation of carriers at the interface of the injection and emissive layers, as modeled by the C_{OLED} in the extended circuit. This is because, at high f and 0 aging hours, carriers will flow into C_{OLED} due to its lower impedance rather than through the organic diode, as evident from the high f_c value in the experimental results. Therefore, we conclude that the τ derived from f_c , as in 7.1, represents the carrier transit time which is the time needed for both carriers to recombine in the emissive layer and then emits light as depicted in Fig. 7-2. Hence, as the OLED ages, degradation will occur which creates instability in the OLED, and results in reduced carrier flow and the τ that is seen in Table IX at longer aging hours.

In addition, although the high f peak seen in Fig. 7-9(b) at 216-288 hours is not visible on the result's Nyquist plot, we see that the experiment's f_c in Table XVI is the same at 216 and 240 hours, but then starts to decrease at 264 and up to 288 hours of ageing, mimicking at how the peak in phase plot is similar at 216 and 240 hours, followed with a drop at later times. As a result, we can correctly model this peak trend in the phase plot with the extended circuit in the Fig. 7-10 inset. This means that the phase plot peak is also influenced by carrier accumulation between the injection and the emissive layers/ C_{OLED} in the circuit. So at high f and early aging, carriers will flow into the C_{OLED} as before and thus no peak is present at this time. As the OLED ages and degrades, carriers will still flow into C_{OLED} but physically they will not travel far into the emissive layer compared to when the OLED is fresh, hence causing a drop in ϕ and consequently the peak drop in Fig. 7-9(b) at even higher frequencies. Finally, since we can model the "hook" with $R_{ext} // C_{ext}$ in the Fig. 7-10 circuit inset and since the OLED uses PEDOT as its HIL, we can interpret the underlying cause of the "hook" similarly to 7.1. So the "hook" is again a reduction in the injection layer area size that reduces carrier flow (the R_{ext}), accompanied by the formation of trap sites in the same layer (the C_{ext}) due to the diffusion of indium ions into both the injection and emissive layers after ITO etching by PSS [57, 82]. Thus, in terms of the extended circuit, at kHz frequencies, carriers will start flowing into the C_{OLED} branch but then they will recombine or be trapped somewhere in the C_{OLED} branch due to $R_{ext} // C_{ext}$, thus causing the "hook" to appear at that f range. As the OLED ages, carriers can then recombine/trapped much earlier and further away from C_{OLED} due to degradation, thus shifting the "hook" frequency to lower values as we observe in the experimental results in Fig. 7-9(a), (b) and (c).

7.4 Summary of IMS Results on OLED Devices

From the results of IMS on OLED under different applied voltage bias V_{DC} , we found that as the V_{DC} is reduced, the OLED brightness will also be reduced based on the decrease in the IV converter's $Re \Delta V$ ($f \rightarrow 0$). Also, we observed a “hook” feature in the low-frequency region at all OLED V_{DC} . In addition, the “hook” feature itself increases in size as V_{DC} is reduced. We also found that as the OLED's V_{DC} is reduced, the f_c from the converter's ΔV Nyquist spectra is also reduced. Here, f_c corresponds to a time constant τ which is a carrier transit time in the OLED as it changes when we changed the OLED's V_{DC} , based on equation (26) in chapter 5 [142]. Also, τ is the effective transit time constant τ_{eff} as it has to account for the total mobility of both carriers in the OLED, which is called the effective mobility μ_{eff} . We found that we can correctly simulate the ‘hook’ feature, the changes in f_c and the feature itself by modifying the OLED equivalent circuit [151]. This is done by placing an extended resistor in-parallel to an extended capacitor ($R_{ext} // C_{ext}$), with $C_{ext} = 6 \text{ nF} // R_{ext} = 600 \Omega$, in series with the circuit's C_{OLED} branch at $C_{OLED} = 13 \text{ nF}$. We reasoned that at both high V_{DC} and high f , the V_{DC} will force more carriers to flow into the C_{OLED} in the circuit model due to its lower impedance than through the diode, while at very low f , currents will flow more into the diode instead of C_{OLED} . The C_{OLED} is the accumulation of carriers at the interface of the injection and emissive layers, which is modeled as a capacitor [151]. At lower V_{DC} and at high frequency, carriers will still flow into the C_{OLED} , but here they can be trapped or forced to recombine before the C_{OLED} branch due to the weaker electric field. Thus, the smaller f_c results at low V_{DC} . While the ‘hook’ represent a trap mechanism that caused carriers to recombine somewhere within the C_{OLED} branch in the kHz range. Physically, the ‘hook’ can be caused by the diffusion of indium ions into the C_{OLED} to ITO etching by PSS [57, 82]. This is since the OLED uses PEDOT as its HIL, hence the OLED's ITO anodes can be etched by the PSS from the HIL. We then found that the plot of τ or τ_{eff} (from f_c) with respect to $1/(V_{DC} - V_{bi})$ indicates a linear the relationship between τ (μs) vs. $1/(V_{DC} - V_{bi})$. Also, from the plot's slope, we found that the resulting $\mu_{eff} = 9.37 \pm 0.02 \times 10^{-6} \text{ cm}^2/\text{V s}$, which is the average mobility of both carriers. Since τ_{eff} is influenced more by the slower mobility, μ_{eff} will be dominated by the faster ones. Thus μ_{eff} here is likely to be the OLED's electron mobility or $\mu_{eff} \sim \mu_e$.

From IMS on OLED under different optical filter, we found that the OLED's white light has the highest light intensity compared to the other two filtered lights, based on the $Re \Delta V$ ($f \rightarrow 0$) results. Also, we found that the f_c (and τ) under all 3 lights are relatively similar, which indicates similar internal dynamics occurs under all 3 lights. This internal dynamic is the carrier recombination transit time within the emissive layer. Also, we observed a ‘bent’ feature in the low-frequency region under all lights. This feature is larger under white light and is smallest under blue light. We found that we can correctly simulate the ‘bent’ feature and f_c similarities by modifying the OLED equivalent circuit

[151], this is done by placing an extended resistor in-parallel to an extended capacitor (R_{ext}/C_{ext}), with $C_{ext} = 9 \text{ nF} // R_{ext} = 900 \text{ } \Omega$, in series with the $C_{OLED} = 13 \text{ nF}$. We reasoned that as f_c is dependent on the C_{OLED} , and since the OLED V_{DC} and V_{AC} are the same for all three lights, the resulting f_c will also be the same for all 3 lights as seen in the real results. As for the ‘bent’ feature, the reasoning behind it is the same as that to the origin of ‘hook’ feature in OLED under different voltage bias.

From OLED aging study results through IMS, we found that continued OLED operation leads to its degradation which then decreases its brightness, based on the $Re \Delta V (f \rightarrow 0)$ results. Also, we found that in general, the measured corner frequency f_c decreases as we operate the OLED further. The f_c , corresponds to τ , which is the time constant of an OLED internal dynamic. This dynamic is the carrier transit time within the OLED. This is because as the OLED ages, the flow of currents into the OLED will also decrease, therefore since τ is a transit time and will be dependent on the V_{DC} , the flow of carriers in the OLED may take longer thus making τ longer (and f_c lower) in aged cells as opposed to that in fresh cell. Also, we found a ‘hook’ feature in the ΔV Nyquist plot at all stages of aging. In addition, the “hook” feature itself increases in size as the OLED ages. We found that we can again correctly simulate the ‘bent’ feature and changes in f_c by modifying the OLED equivalent circuit [151], this is done by placing an extended resistor in-parallel to an extended capacitor (R_{ext}/C_{ext}), with $C_{ext} = 6 \text{ nF} // R_{ext} = 600 \text{ } \Omega$, in series with the $C_{OLED} = 13 \text{ nF}$. As for the ‘hook’ feature here, the reasoning behind it is the same as that found in IMS on OLED under different voltage bias.

7.5 Results from IMS Characterizations on an Alkaline Battery

Besides performing IMS on OPV and OLED, we also perform IMS characterization on a commercial 1.5 V alkaline battery. As elaborated in 4.8, this was done through load modulation of the 1.5 V battery. So we use the same fast photodiode (OSD5-5T) in 4.5. and use it as a fast photosensitive device that modulates the battery voltage and load resistance with the setup depicted in Fig. 4-17. In the setup, we also use the IMS instrument from 4.2., a 1.5 V AA-size, alkaline battery, and a load resistance $R_L = 53 \text{ } \Omega$. In addition, we also use the bespoke voltage adder in 4.2. to add a DC voltage (V_{DC}) on top of a small AC voltage (V_{AC}) from the lock-in’s ref out voltage, and apply the resultant (DC + AC) voltage to the fast red LED (V_{LED}) in 4.2. with $V_{LED} = (2.2 \pm 1.2) \text{ V}$. The V_{LED} is applied to the red LED with a protective serial resistance (R_{LED}) of $120 \text{ } \Omega$, thus driving the LED with a current $I_{LED} = (18 \pm 10) \text{ mA}$. The I_{LED} will produce a modulated light intensity (L_T) of $L_T = L \pm \Delta L$. The intensity is not known in absolute terms but $L_T \sim I_{LED}$, so $\Delta L/L = \Delta I/I$.

We then use the red LED with modulated intensity L_T to illuminate the DI photodiode in Fig. 4-17, thus causing the photocurrent from the fast photodiode to modulate the voltage measured at the highlighted point A in Fig. 4-17. In addition, because the illuminated photodiode is also under a

forward bias of the battery voltage ($V_{battery} = 1.5 \text{ V}$), currents from the battery at point A will offset/balance currents flowing out of the photodiode. If the photodiode's current is at the modulation maximum, battery currents will offset the photodiode's current, but if the photodiode current is at its minimum, battery currents will not flow into the photodiode but instead through the load resistance R_L . In other words, at point A we will measure/obtain a load modulation signal in the form of $V + \Delta V(\omega) \sin(\omega t + \varphi(\omega))$. This is what we basically measure in a load modulation IMS, i.e. ΔV at point A because the battery discharges and this discharge is modulated by photocurrents from the photodiode.

We use the IMS bespoke software in 4.4. to automatically operate a frequency scan by varying the lock-in's reference out voltage frequency f to values between 1 Hz and 250 kHz in 12 steps per decade of measurement. The software settings were the same with those in 4.4, i.e. the lock-in's input coupling is set to DC, the roll-off is set to 24 dB/oct, the dynamic is set to high, phase offset to 0 and the reference harmonic to 1. The reasoning behind the settings selections is also the same as in 4.4. We then channel the modulated voltage that we obtain at point A in Fig. 4-17 into the lock-in input. The lock-in will measure the modulated voltage and phase from point A with respect to the ref out voltage. We then obtain the $\Delta V(\omega)$ and phase $\varphi(\omega)$ from voltage response and recorded these as a function of $f = \omega/2\pi$. We then repeat the entire measurement procedures 1 hour after the first characterization, and then another hour after the second one to observe any change in the load modulation voltage, and thus the battery internal dynamics. The selection of a 1-hour interval in the measurement procedure is because 1 hour is the approximate time a battery discharges. We then present our IMS results in the form of Bode amplitude and phase of the load modulated voltage ΔV as shown in Fig. 7-11(a) and (b).

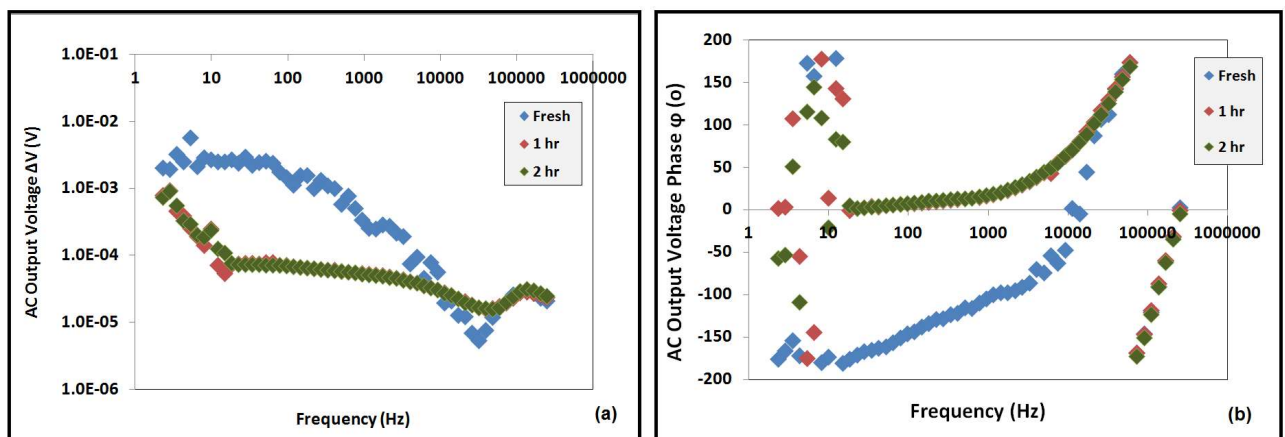


Fig. 7-11 (a). Bode amplitude plot of ΔV and (b) Bode phase plot of ΔV phase φ vs frequency f . Here, (a) and (b) are taken at frequencies between 1 Hz and 250 kHz with each IMS scan taken at a 1-hour interval (shown as colour coded and the in inset) starting from when the battery was new. For all IMS scans, we use a red LED driven with a LED drive current (I_{LED}) of $I_{LED} = (18 \pm 10) \text{ mA}$.

Fig. 7-11(a) and (b) shows the Bode plots of ΔV and ΔV phase ϕ with respect to frequency (f) at f between 1 Hz and 250 kHz and taken at a 1-hour interval, starting from when the battery was new. From both Fig. 7-11(a) and (b) we can see that when the battery was still fresh, the measured load modulation voltage in point A is noisy/unstable, but after 1 hour, and then 2 hours later, the voltage response has become much more stable and relatively constant. In Fig. 7-11(a), at both IMS results after 1 and 2 hours interval, we see that there is a sharp drop in the ΔV amplitude at f between 1 and 10 Hz. This drop is then followed by a stable response up to 10 kHz before a dip for $f > 10$ kHz and then rises again at $f \sim 100$ kHz. We also observe that $\Delta V (f \rightarrow 0)$ in Fig. 7-12(a) decreases 1 hour later, which is most likely caused by the decrease in battery current as the battery discharges. The sharp drop in ΔV amplitude at f between 1 and 10 Hz is most likely caused by the presence of a Warburg element. Our IMS characterizations of organic devices and even inorganic ones, roll-off usually occurs at high frequency but in Fig. 7-11(a) it starts at low frequency, thus there is a possibility that this sharp drop is caused by the Warburg impedance. The Warburg element represents the diffusion process that occurs in the battery, in that it describes the distance traveled by the battery chemical constituents as they diffuse and reacted with each other in operation [156]. The Warburg element usually appears as a 45° slope in a Nyquist/complex plane result, and in the Bode amplitude it usually appears as a sharp low-frequency roll-off similar to the sharp drop that we see in Fig. 7-11(a) [156]. However, a Warburg element rarely appears on its own, and typically it is accompanied or appears together with interface and contact resistances. While the high-frequency dip at $f > 10$ kHz is difficult to explain a possible explanation is that at high frequencies, an electrical resonance occurs in which the ΔV capacitive component is reduced to near zero. We also observed from Fig. 7-11(a) that both the low (Warburg) and high (resonance) frequency dynamics still occur 2 hours after we first perform the load modulation. We observe also that Fig. 7-11(a) corresponds well with 7-11(b), in that the ΔV amplitude is noisy when the battery is still fresh and then stabilizes 1 and 2 hours later. To add, we also observe the same ΔV phase (ϕ) response 1 and 2 hours after we started the load modulation, which indicates that the same internal dynamics occur for load modulation that is done at 1 and 2 hours after the first IMS. The internal dynamics here refer to the possible Warburg and resonance feature seen in the low and high-frequency region in Fig. 7-11(a) respectively. Overall, we have managed to modify, adapt and extend the use of our IMS instrument in 4.2. to perform load modulation IMS on an alkaline battery as seen in Fig. 7-11, and that this setup can be improved further for future measurements.

7.6 Summary of IMS Characterizations on Alkaline Battery

From IMS on a commercial 1.5 V alkaline battery through load modulation, we found that when the battery was still fresh, the measured ΔV is unstable, but it then becomes stable 2 hours after the measurement starts. We also found that there is a sharp drop in the ΔV at f between 1 and 10 Hz, which is then followed by a stable ΔV up to 10 kHz before the ΔV forms a minimum peak at f between 10 and 100 kHz, and then followed by an increase in the ΔV at $f \sim 100$ kHz before then dropping again at $f > 100$ kHz. The drop in measured ΔV at f between 1 and 10 Hz after 1 and 2 hours of IMS is likely caused by the presence of a Warburg element. The Warburg element represents the diffusion process that occurs in the battery, in that it describes the distance traveled by the battery chemical constituents as they diffuse and reacted with each other when the battery is operated [156]. However, since a Warburg element rarely appears on its own, we cannot conclusively assign it as the primary cause of the low-frequency dip in the plot. In addition, the minimum peak formed by the ΔV in the high frequency region in the Bode amplitude plot may be caused by the presence of an electrical resonance that reduces the capacitive component in the ΔV to near zero.

We also found that both the Warburg element and the high-frequency minimum peak still occurs after 2 hours of IMS. Further, from the ΔV Bode phase plot, the ΔV phase (φ) profile from the load modulation is the same after 1 and 2 hours, which indicates that the same internal dynamics occurs in the battery after 1 and 2 hours of IMS. This internal dynamics may correspond to the Warburg element and minimum peak feature seen in the ΔV Bode amplitude plot. Finally, we need to perform further experiments on the battery to determine the exact cause behind the presence of both features (ΔV dip in low and high frequency) in the ΔV Bode amplitude plot. As such, we propose further improvement of the load modulation setup and other experiments in future besides load modulation to determine the battery internal dynamics. Overall, we have managed to modify, adapt and extend the use of our IMS instrument to perform load modulation on a 1.5 V alkaline battery.

Chapter 8

Overall Conclusions and Future Work

8.1 Overall Conclusions

We have successfully built and tested an intensity-modulated spectroscopy (IMS) instrument that is centered around a commercial lock-in amplifier, which can be used to perform intensity-modulated spectroscopy (IMS) up to a frequency of 250 kHz. We have tested our instrument on a commercial CdS-based light dependent resistor (LDR), a device with well-known physical properties. We found that the dynamic characterization results of the CdS-based LDR agrees and are consistent with an already well-established knowledge on its physical properties. We have also performed IMS on a state-of-the-art bulk heterojunction (BHJ) organic photovoltaic (OPV) and introduced a new mode of IMS operation where a photovoltaic cell operates under a finite load, including at its maximum power point. From our IMS results on BHJ OPV, we have established IMS at maximum power point as the optimum operating condition for IMS on photovoltaics, which is a much better alternative to the traditional way of doing IMS, i.e. under intensity-modulated photocurrent spectroscopy (IMPS) and under intensity-modulated photovoltage spectroscopy (IMVS). By using IMS under finite load, we have managed to identify a high-frequency feature that was previously invisible under both IMPS and IMVS. We also found that this feature is ageing-related and is more pronounced after long-term storage. Further, based only on the simulation results of the OPV equivalent circuit, we can, as a likely cause, assign the ageing-related high-frequency feature to the diffusion of indium ions that originate from the etching of ITO by PSS to the BHJ. On the other hand, based only on the simulations, we cannot conclusively assign the ageing-related high-frequency feature to the diffusion of indium ions and that other causes may have contributed to the appearance of such feature. In addition, with IMS, we are also able to determine the BHJ capacitance of a BHJ OPV without absolute calibration of the light intensity.

By using IMS, we have also shown that using V_2O_5 metal oxides as a BHJ OPV hole extraction layer, we can eliminate the problem of indium ions diffusion into the BHJ as was the case in an OPV with PEDOT hole extraction layer. Also by using IMS, we have managed to identify a cell with a 400 °C annealed HEL as having the fastest carrier transit time as compared to a cell with an unannealed HEL, or annealing at 100 °C, 200 and 300 °C, We also managed to show that the origin of the “3rd quadrant” frequency lies in the presence of a lagging/trap mechanism in the OPV external current path, i.e. near the cell’s series and load resistance. We can also show by using IMS that a “foot” feature in the low-frequency region also comes from the presence of traps in series with the series

and load resistance. Also, we have managed to perform IMS on an OLED and have identified the causes of the low-frequency “hook” feature. This feature is attributable to the presence of parallel resistive- and capacitive-like components in the OLED’s emissive layer. The presence of these components is also due to the diffusion of indium ions that originate from the etching of ITO by PSS to the OLED’s emissive layer since PEDOT is used as the HIL in the OLED sample. In addition, by using IMS, we have also managed to determine carrier mobility in an OLED, though only an average mobility is obtained. We found that, from IMS, that the effective mobility of the device will be influenced more by the electron mobility as it is the slowest mobility. We also found that in an OLED, there is an Indium diffusion similar to what we found in the OPV and that it can also degrade the device. Finally, in the aging study of the OLED device, the carrier transit time decreases as the device ages. In addition, we have also managed to adapt our instrument to perform load modulation on an alkaline battery and from preliminary results we found that we have the potential to identify diffusion process that happens in the low-frequency region in the context of an IMS frequency scan.

8.2 Proposed Future Work

In addition to the IMS experiments on OPVs and OLEDs, we also propose further improvements on the IMS characterization on a 1.5 V alkaline battery through load modulation as a possible future work. As elaborated in 4.8 and 7.4, we perform the IMS on 1.5 V alkaline battery by using the setup depicted in Fig. 4-17. In this setup (Fig. 4-17), we use a fast photodiode (the OSD5-5T model) [136] to modulate the voltage at point A in the setup parallel to the battery and load resistance R_L . Hence in Fig. 4-17, we use the bespoke voltage adder in Fig. 4-5(b) to add a DC voltage (V_{DC}) on top of a small AC voltage (V_{AC}) from the lock-in’s ref out voltage, and apply the resultant (DC + AC) voltage to the fast red LED (V_{LED}) in 4.2. with $V_{LED} = (2.2 \pm 1.2)$ V. The V_{LED} is in turn applied to the red LED with a protective serial resistance (R_{LED}) of 120 Ω , thus driving the LED with a current $I_{LED} = (18 \pm 10)$ mA. The I_{LED} will produce a modulated light intensity (L_T) of $L_T = L \pm \Delta L$. The intensity is not known in absolute terms but $L_T \sim I_{LED}$, so $\Delta L/L = \Delta I/I$. We then propose to substitute the red LED with a blue LED that has a higher intensity than the red, but also fast enough that its rise time τ corresponds to a frequency response that is higher than that of our lock-in device maximum scanning frequency, i.e. $f = 250$ kHz. Examples of these types of blue LEDs available in the market today is the HLMP-DB25 and HLMP-KB45 model from Broadcom Ltd., USA [157]. Both models (The HLMP-DB25 and HLMP-KB45) have a higher intensity compared to that of the red LED in terms of their radiant intensity, i.e. 0.7 and 0.5 mW/sr respectively, as opposed to the red LED’s radiant intensity of 0.30 mW/sr. In addition, both models rise time τ also correspond to a frequency value of $f = 2$ MHz via $f = 1/\tau$, which is much higher than the lock-in maximum scanning

frequency of $f = 250$ kHz [133, 157]. Further, we can also use the same applied V_{LED} or resultant (DC + AC) voltage stimulus as in the case of red LED, i.e. $V_{LED} = (2.2 \pm 1.2)$ V. In addition, we also use the same protective serial resistance (R_{LED}) that we use in Fig. 4-17, i.e. $R_{LED} = 120 \Omega$, thus driving the LED with a current $I_{LED} = (18 \pm 10)$ mA.

We then use the blue LED with modulated intensity L_T to illuminate the DI photodiode in Fig. 4-17, thus causing the photocurrent from the fast photodiode to modulate the voltage measured at the highlighted point A in Fig. 4-17. Here, we propose to change the currently use photodiode (The OSD5-5T model [136], to another photodiode that is similarly fast in terms of its rise time τ while also sensitive to blue-wavelength illumination, i.e. at λ range = 450-495 nm [158]. This is because if we change the LED colour from red to blue, then we have to ensure that the photodiode used in the circuit is sensitive to blue illumination. Examples of blue-sensitive photodiode currently available in the market can be found in subchapter 7.2, i.e. the photodiode model S1087 and S1226 from Hamamatsu Photonics K.K. [153, 154]. Both photodiode model (the S1087 and S1226) have a higher responsivity (both model responsivity ~ 0.2 - 0.29 A/W at λ range = 450-495 nm) compared to that of the current photodiode, with responsivity ~ 0.15 - 0.29 A/W at the same wavelength range [153, 154]. In addition, both photodiodes has a rise time of $0.5 \mu\text{s}$ that corresponds to a frequency $f = 2$ MHz under a 0 V applied bias. This frequency value itself is still higher than the lock-in maximum scanning frequency of $f = 250$ kHz, thus the good suitability of both photodiodes as a replacement for the current model. Hence, if we return to the load modulation operation in Fig. 4-17, since the illuminated photodiode is also under a forward bias of the battery voltage ($V_{battery} = 1.5$ V, currents from the battery at point A will offset/balance currents flowing out of the photodiode. If the photodiode's current is at the modulation maximum, battery currents will offset the photodiode's current, but if the photodiode current is at its minimum, battery currents will not flow into the photodiode but instead through the load resistance R_L . We will then measure/obtain a load modulation signal in the form of $V + \Delta V(\omega) \sin(\omega t + \phi(\omega))$ in point A. This is what we basically measure in a load modulation IMS, i.e. ΔV at point A because the battery discharges and this discharge is modulated by photocurrents from the photodiode.

References

- [1] J. Nelson, "Organic Photovoltaics Films," *Current Opinion in Solid State and Materials Science*, no. 6, pp. 87-95, 2002.
- [2] C. Deibel, V. Dyakonov, and C. J. Brabec, "Organic Bulk-Heterojunction Solar Cells," *IEEE Journal of Selected Topics in Quantum Electronics*, vol. 16, no. 6, pp. 1517-1527, 2010.
- [3] C. J. Brabec, S. Gowrisanker, J. J. M. Halls, D. Laird, S. Jia, and S. P. Williams, "Polymer-Fullerene Bulk-Heterojunction Solar Cells," *Advanced Materials*, vol. 22, no. 34, pp. 3839-3856, 2010.
- [4] B. Minaev, G. Baryshnikov, and H. Agren, "Principles of phosphorescent organic light emitting devices," *Physical Chemistry Chemical Physics*, vol. 16, no. 5, pp. 1719-1758, 2014.
- [5] Y. Liu *et al.*, "Aggregation and morphology control enables multiple cases of high-efficiency polymer solar cells," *Nature Communications*, vol. 5, pp. 1-8, 2014.
- [6] K. Masuko *et al.*, "Achievement of More Than 25% Conversion Efficiency With Crystalline Silicon Heterojunction Solar Cell," *IEEE Journal of Photovoltaics*, vol. 4, no. 6, pp. 1433-1435, 2014.
- [7] A. Feldman, R. Ahrenkiel, and J. Lehman, "Degradation of Photovoltaic Devices at High Concentration by Space Charge Limited Currents," *Solar Energy Materials & Solar Cells*, no. 117, pp. 408-411, 2013.
- [8] F. C. Krebs and M. Jorgensen, "Polymer and Organic Solar Cells viewed as Thin Film Technologies : What it Will Take for Them to Become a Success Outside Academia," *Solar Energy Materials & Solar Cells*, no. 119, pp. 73-76, 2013.
- [9] B. Kippelen and J.-L. Bredas, "Organic Photovoltaics," *Energy & Environmental Science*, vol. 2, no. 3, pp. 241-332, 2009.
- [10] S. A. Choulis *et al.*, "High ambipolar and balanced carrier mobility in regioregular poly(3-hexylthiophene)," *Applied Physics Letters*, vol. 85, no. 17, pp. 3890-3892, 2004.
- [11] L. S. Hung and C. H. Chen, "Recent progress of molecular organic electroluminescent materials and devices," *Materials Science and Engineering R-Reports*, vol. 39, no. 5-6, pp. 143-222, 2002.
- [12] M. G. Craford, S. A. Stockman, M. J. Peanasky, and F. A. Kish, "Visible light-emitting diodes," *Electroluminescence I*, vol. 64, pp. 1-47, 2000.
- [13] M. Fujihira, L. M. Do, A. Koike, and E. M. Han, "Growth of dark spots by interdiffusion across organic layers in organic electroluminescent devices," *Applied Physics Letters*, vol. 68, no. 13, pp. 1787-1789, 1996.
- [14] C. W. Tang, "2-Layer organic photovoltaic cell," *Applied Physics Letters*, vol. 48, no. 2, pp. 183-185, 1986.
- [15] J. P. Lu *et al.*, "Synthesis and characterization of a blue light emitting polymer containing both hole and electron transporting units," *Chemistry of Materials*, vol. 11, no. 9, pp. 2501-2507, 1999.
- [16] L. M. Peter, J. Li, and R. Peat, "Frequency Response Analysis of Intensity Modulated Photocurrents at Semiconductor Electrodes," *Electrochimica Acta*, vol. 35, no. 10, pp. 1657-1664, 1990.
- [17] S. Scholz, D. Kondakov, B. Luessem, and K. Leo, "Degradation Mechanisms and Reactions in Organic Light-Emitting Devices," *Chemical Reviews*, vol. 115, no. 16, pp. 8449-8503, 2015.
- [18] H. W. Rhee, K. S. Chin, S. Y. Oh, and J. W. Choi, "Application of impedance technique to OLED," *Thin Solid Films*, vol. 363, no. 1-2, pp. 236-239, 2000.
- [19] J. T. Lim and G. Y. Yeom, "Light-Emitting Characteristics of Organic Light-Emitting Diodes with Ba/Al Cathode and Effect of Ba Thickness by Measuring their Built-in Potential," *Japanese Journal of Applied Physics*, vol. 48, no. 12, 2009.
- [20] M. S. Suresh, "Measurement of solar cell parameters using impedance spectroscopy," *Solar Energy Materials and Solar Cells*, vol. 43, no. 1, pp. 21-28, 1996.
- [21] E. Barsoukov and J. R. Macdonald, Eds. *Impedance Spectroscopy: Theory, Experiment, and Applications*, 2nd ed. New Jersey, USA: Wiley, 2005, pp. 1-595.
- [22] E. A. Ponomarev and L. M. Peter, "A Generalized Theory of Intensity Modulated Photocurrent Spectroscopy (IMPS)," *Journal of Electroanalytical Chemistry*, no. 396, pp. 219-226, 1995.

- [23] N. W. Duffy, L. M. Peter, and K. G. U. Wijayantha, "Characterisation of electron transport and back reaction in dye-sensitised nanocrystalline solar cells by small amplitude laser pulse excitation," *Electrochemistry Communications*, vol. 2, no. 4, pp. 262-266, 2000.
- [24] J. R. Macdonald, "Impedance spectroscopy and its use in analyzing the steady-state AC response of solid and liquid electrolytes," *Journal of Electroanalytical Chemistry*, vol. 223, no. 1-2, pp. 25-50, 1987.
- [25] A. E. Kennelly, "Vector-diagrams of oscillating-current circuits," *Proceedings of the American Academy of Arts and Sciences*, vol. 46, no. 13/24, pp. 373-421, 1911.
- [26] C. P. Steinmetz, "The energy-function of the magnetic circuit," *Science (New York, N.Y.)*, vol. 20, no. 509, pp. 258-259, 1892.
- [27] K. S. Cole and R. H. Cole, "Dispersion and absorption in dielectrics I. Alternating current characteristics," *Journal of Chemical Physics*, vol. 9, no. 4, pp. 341-351, 1941.
- [28] J. E. B. Randles, "Kinetics of rapid electrode reactions," *Discussions of the Faraday Society*, vol. 1, pp. 11-19, 1947.
- [29] G. Jaffe, "Theory of conductivity of semiconductors," *Physical Review*, vol. 85, no. 2, pp. 354-363, 1952.
- [30] H. C. Chang and G. Jaffe, "Polarization in electrolytic solutions .1. Theory," *Journal of Chemical Physics*, vol. 20, no. 7, pp. 1071-1077, 1952.
- [31] J. E. B. Randles, "Kinetics of rapid electrode reactions .2. rate constants and activation energies of electrode reactions," *Transactions of the Faraday Society*, vol. 48, no. 9, pp. 828-832, 1952.
- [32] J. R. Macdonald, "Capacitance and conductance effects in photoconducting alkali halide crystals," *Journal of Chemical Physics*, vol. 23, no. 2, pp. 275-295, 1955.
- [33] P. B. Macedo, C. T. Moynihan, and R. Bose, "Role of ionic diffusion in polarization in vitreous ionic conductors," *Physics and Chemistry of Glasses*, vol. 13, no. 6, pp. 171-179, 1972.
- [34] W. H. Mulder, J. H. Sluyters, T. Pajkossy, and L. Nyikos, "Tafel current at fractal electrodes - connection with admittance spectra," *Journal of Electroanalytical Chemistry*, vol. 285, no. 1-2, pp. 103-115, 1990.
- [35] J. H. Sluyters and J. J. C. Oomen, "On the impedance of galvanic cells .2. experimental verification," *Recueil Des Travaux Chimiques Des Pays-Bas-Journal of the Royal Netherlands Chemical Society*, vol. 79, no. 8, pp. 1101-1110, 1960.
- [36] P. Horowitz and W. Hill, *The Art of Electronics*, 3rd ed. New York, USA: Cambridge University Press, 1990, pp. 1-1219.
- [37] Z. Abedi, M. Janghour, E. Mohajerani, M. Alahbakhshi, A. Azari, and A. Fallahi, "Study of various evaporation rates of the mixture of Alq3: DCM in a single furnace crucible," *Journal of Luminescence*, vol. 147, pp. 9-14, 2014.
- [38] S. M. Park, J. S. Yoo, B. Y. Chang, and E. S. Ahn, "Novel instrumentation in electrochemical impedance spectroscopy and a full description of an electrochemical system," *Pure and Applied Chemistry*, vol. 78, no. 5, pp. 1069-1080, 2006.
- [39] J. Schefold, "Impedance and intensity modulated photocurrent spectroscopy as complementary differential methods in photochemistry.," *J. Electroanal. Chem.*, no. 341, pp. 111-136, 1992.
- [40] G. Schlichthorl, S. Y. Huang, J. Sprague, and A. J. Frank, "Band edge movement and recombination kinetics in dye-sensitized nanocrystalline TiO₂ solar cells: A study by intensity modulated photovoltage spectroscopy," *Journal of Physical Chemistry B*, vol. 101, no. 41, pp. 8141-8155, 1997.
- [41] J. Poppe, S. G. Hickey, and A. Eychmueller, "Photoelectrochemical Investigations of Semiconductor Nanoparticles and Their Application to Solar Cells," *Journal of Physical Chemistry C*, vol. 118, no. 30, pp. 17123-17141, 2014.
- [42] P. D. Foote and F. L. Mohler, "Photo-electric ionization of caesium vapor," (in English), *Physical Review*, vol. 26, no. 2, pp. 0195-0207, 1925.
- [43] R. B. Green, R. A. Keller, G. G. Luther, P. K. Schenck, and J. C. Travis, "Galvanic detection of optical absorptions in a gas-discharge," *Applied Physics Letters*, vol. 29, no. 11, pp. 727-729, 1976.
- [44] C. Stanculescu, R. C. Bobulescu, A. Surmeian, D. Popescu, I. Popescu, and C. B. Collins, "Optical impedance spectroscopy," *Applied Physics Letters*, vol. 37, no. 10, pp. 888-890, 1980.

- [45] H. Oheda, "Phase-shift analysis of modulated photocurrent - its application to the determination of the energetic distribution of gap states," *Journal of Applied Physics*, vol. 52, no. 11, pp. 6693-6700, 1981.
- [46] R. Kern, R. Sastrawan, J. Ferber, R. Stangl, and J. Luther, "Modeling and interpretation of electrical impedance spectra of dye solar cells operated under open-circuit conditions," *Electrochimica Acta*, vol. 47, no. 26, pp. 4213-4225, 2002.
- [47] J. C. Byers, S. Ballantyne, K. Rodionov, A. Mann, and O. A. Semenikhin, "Mechanism of recombination losses in bulk heterojunction P3HT:PCBM solar cells studied using intensity modulated photocurrent spectroscopy," *Applied Materials and Interfaces* 3, vol. 3, pp. 392-401, 2011.
- [48] Metrohm. (2012, 28 March 2012). *Photovoltaics Part 3 – Dye sensitized solar cells, IMVS and IMPS measurements* [Online]. Available: <http://www.ecochemie.nl/download>
- [49] Y. T. Set , M. D. Heinemann, E. Birgersson, and J. Luther, "On The Origin of Quadrant I Semicircle in Intensity-Modulated Photocurrent Spectra of P3HT:PCBM Bulk Heterojunction Solar Cells: Evidence of Degradation-Related Trap-Assisted Recombination," *J. Phys. Chem. C*, vol. 117, pp. 7993-8000, 2013.
- [50] P. M. DiCarmine and O. A. Semenikhin, "Intensity modulated photocurrent spectroscopy (IMPS) of solid-state polybithiophene-based solar cells," *Electrochimica Acta*, vol. 53, pp. 3744-3754, 2008.
- [51] E. A. Ponomarev and L. M. Peter, "A Comparison of Intensity Modulated Photocurrent Spectroscopy and Photoelectrochemical Impedance Spectroscopy in a Study of Photoelectrochemical Hydrogen Evolution at p-InP," *Journal of Electroanalytical Chemistry*, no. 397, pp. 45-52, 1995.
- [52] Z. Li, X. Zhao, X. Li, Z. Gao, B. Mi, and W. Huang, "Organic thin-film solar cells: Devices and materials," *Science China-Chemistry*, vol. 55, no. 4, pp. 553-578, 2012.
- [53] J. Yan and B. R. Saunders, "Third-generation solar cells: a review and comparison of polymer: fullerene, hybrid polymer and perovskite solar cells," *RSC Advances*, vol. 4, no. 82, pp. 43286-43314, 2014.
- [54] C. W. Lee, O. Y. Kim, and J. Y. Lee, "Organic Materials for Organic Electronic Devices," *Journal of Industrial and Engineering Chemistry*, no. 20, pp. 1198-1208, 2014.
- [55] A. J. Heeger, "Synthetic metals with anisotropic structure and properties," *Abstracts of Papers of the American Chemical Society*, vol. 174, pp. 107-107, 1977.
- [56] J. J. M. Halls *et al.*, "Efficient photodiodes from interpenetrating polymer networks," *Nature*, vol. 376, no. 6540, pp. 498-500, 1995.
- [57] N. Grossiord, J. M. Kroon, R. Andriessen, and P. W. M. Blom, "Degradation mechanisms in organic photovoltaic devices," *Organic Electronics*, vol. 13, no. 3, pp. 432-456, 2012.
- [58] L. Pauling, "The shared-electron chemical bond," *Proceedings of the National Academy of Sciences of the United States of America*, vol. 14, pp. 359-362, 1928.
- [59] L. Pauling, "The nature of the chemical bond. IV. The energy of single bonds and the relative electronegativity of atoms," *Journal of the American Chemical Society*, vol. 54, pp. 3570-3582, 1932.
- [60] L. Pauling and G. W. Wheland, "The nature of the chemical bond. V. The quantum-mechanical calculation of the resonance energy of benzene and naphthalene and the hydrocarbon free radicals'," *Journal of Chemical Physics*, vol. 1, no. 6, pp. 362-374, 1933.
- [61] K. Fukui, T. Yonezawa, and H. Shingu, "A molecular orbital theory of reactivity in aromatic hydrocarbons," *Journal of Chemical Physics*, vol. 20, no. 4, pp. 722-725, 1952.
- [62] Z. G. Soos, "Electronic-structure of organic conductors and semiconductors," *Journal of Chemical Education*, vol. 55, no. 9, pp. 546-552, 1978.
- [63] H. Baessler and A. Koehler, R. M. Metzger, Ed. *Unimolecular and Supramolecular Electronics I: Chemistry and Physics Meet at Metal-Molecule Interfaces*. Berlin, Germany: Springer, 2012, pp. 1-320.
- [64] U. Noomnarm and R. M. Clegg, "Fluorescence lifetimes: fundamentals and interpretations," *Photosynthesis Research*, vol. 101, no. 2-3, pp. 181-194, 2009.
- [65] R. M. Hochstrasser, "Luminescence of organic molecular crystals," *Reviews of Modern Physics*, vol. 34, no. 3, pp. 531-550, 1962.

- [66] E. Fron *et al.*, "Photoinduced electron-transfer in perylenediimide triphenylamine-based dendrimers: single photon timing and femtosecond transient absorption spectroscopy," *Photochemical and Photobiological Sciences*, vol. 7, no. 5, pp. 597-604, 2008.
- [67] H. Ishii, K. Sugiyama, E. Ito, and K. Seki, "Energy level alignment and interfacial electronic structures at organic metal and organic organic interfaces," *Advanced Materials*, vol. 11, no. 8, pp. 605-625, 1999.
- [68] J. C. Scott, "Metal-organic interface and charge injection in organic electronic devices," *Journal of Vacuum Science and Technology A*, vol. 21, no. 3, pp. 521-531, 2003.
- [69] V. Coropceanu, J. Cornil, D. A. da Silva Filho, Y. Olivier, R. Silbey, and J.-L. Bredas, "Charge transport in organic semiconductors," *Chemical Reviews*, vol. 107, no. 5, pp. 2165-2165, 2007.
- [70] T. U. Kampen, "Electronic structure of organic interfaces - a case study on perylene derivatives," *Applied Physics a-Materials Science and Processing*, vol. 82, no. 3, pp. 457-470, 2006.
- [71] R. H. Fowler and L. Nordheim, "Electron emission in intense electric fields," *Proceedings of the Royal Society of London Series a-Containing Papers of a Mathematical and Physical Character*, vol. 119, no. 781, pp. 173-181, 1928.
- [72] P. R. Emtage and W. Tantraporn, "Schottky emission through thin insulating films," *Physical Review Letters*, vol. 8, no. 7, pp. 267-268, 1962.
- [73] J. C. Scott and G. G. Malliaras, "Charge injection and recombination at the metal-organic interface," *Chemical Physics Letters*, vol. 299, no. 2, pp. 115-119, 1999.
- [74] N. Karl, "Charge carrier transport in organic semiconductors," *Synthetic Metals*, vol. 133, pp. 649-657, 2003.
- [75] H. Bassler, "Charge transport in disordered organic photoconductors - A Monte-Carlo simulation study," *Physica Status Solidi B-Basic Research*, vol. 175, no. 1, pp. 15-56, 1993.
- [76] W. F. Pasveer *et al.*, "Unified description of charge-carrier mobilities in disordered semiconducting polymers," *Physical Review Letters*, vol. 94, no. 20, 2005.
- [77] C. Tanase, E. J. Meijer, P. W. M. Blom, and D. M. de Leeuw, "Local charge carrier mobility in disordered organic field-effect transistors," *Organic Electronics*, vol. 4, no. 1, pp. 33-37, 2003.
- [78] R. G. Kepler, "Charge carrier production and mobility in anthracene crystals," *Physical Review*, vol. 119, no. 4, pp. 1226-1229, 1960.
- [79] C. D. Child, "Discharge from hot CaO," *Physical Review*, vol. 32, no. 5, pp. 0492-0511, 1911.
- [80] M. Hiramoto, H. Fujiwara, and M. Yokoyama, "p-i-n like behavior in 3-layered organic solar-cells having a co-deposited interlayer of pigments," *Journal of Applied Physics*, vol. 72, no. 8, pp. 3781-3787, 1992.
- [81] J. K. J. van Duren *et al.*, "In-situ compositional and structural analysis of plastic solar cells," *Advanced Functional Materials*, vol. 12, pp. 665-669, 2002.
- [82] C. W. T. Bulle-Lieuwma, W. J. H. van Gennip, J. K. J. van Duren, P. Jonkheijm, R. A. J. Janssen, and J. W. Niemantsverdriet, "Characterization of polymer solar cells by TOF-SIMS depth profiling," *Applied Surface Science*, vol. 203, pp. 547-550, 2003.
- [83] V. Shrotriya, G. Li, Y. Yao, C. W. Chu, and Y. Yang, "Transition metal oxides as the buffer layer for polymer photovoltaic cells," *Applied Physics Letters*, vol. 88, no. 7, 2006.
- [84] J. H. Park, T. W. Lee, B. D. Chin, D. H. Wang, and O. O. Park, "Roles of Interlayers in Efficient Organic Photovoltaic Devices," *Macromolecular Rapid Communications*, vol. 31, no. 24, pp. 2095-2108, 2010.
- [85] P. de Bruyn, D. J. D. Moet, and P. W. M. Blom, "All-solution processed polymer light-emitting diodes with air stable metal-oxide electrodes," *Organic Electronics*, vol. 13, no. 6, pp. 1023-1030, 2012.
- [86] A. Alsulami *et al.*, "Thermally stable solution processed vanadium oxide as a hole extraction layer in organic solar cells," *Materials*, vol. 9, no. 235, 2016.
- [87] P. W. M. Blom, V. D. Mihailechi, L. J. A. Koster, and D. E. Markov, "Device physics of polymer : fullerene bulk heterojunction solar cells," *Advanced Materials*, vol. 19, no. 12, pp. 1551-1566, 2007.
- [88] R. A. Street, "Electronic Structure and Properties of Organic Bulk-Heterojunction Interfaces," *Advanced Materials*, vol. 28, no. 20, pp. 3814-3830, 2016.
- [89] M. Wolf and H. Rauschenbach, "Series resistance effects on solar cell measurements," *Advanced Energy Conversion*, vol. 3, no. 2, pp. 455-479, 1963.

- [90] M. M. Saied, "Matching of DC motors to photovoltaic generators for maximum daily gross mechanical energy," *Energy Conversion, IEEE Transactions on*, vol. 3, no. 3, pp. 465-472, 1988.
- [91] Z. Yaohui, L. Xiaofeng, and L. Yao, "Numerical Simulation of Light- Trapping and Photoelectric Conversion in Single Nanowire Silicon Solar Cells," *IEEE Journal of Selected Topics in Quantum Electronics*, vol. 19, no. 5, pp. 1-8, 2013.
- [92] L. M. Peter, E. A. Ponomarev, and D. J. Fermin, "Intensity-Modulated Photocurrent Spectroscopy : Reconciliation of Phenomenological Analysis with Multistep Electron Transfer Mechanisms," *Journal of Electroanalytical Chemistry*, vol. 427, 1997.
- [93] F. So, J. Kido, and P. Burrows, "Organic Light- Emitting Devices for Solid- State Lighting," *MRS Bulletin*, vol. 33, no. 7, pp. 663-669, 2008.
- [94] J. Lee, Y. Liang, H. Shin, Y. Ma, and J. Park, "White OLED Using Highly Efficient Green Dopant via Solution Process," *Molecular Crystals and Liquid Crystals*, vol. 621, no. 1, pp. 26-30, 2015.
- [95] N. Thejo Kalyani and S. J. Dhoble, "Organic light emitting diodes: Energy saving lighting technology— A review," *Renewable and Sustainable Energy Reviews*, vol. 16, no. 5, pp. 2696-2723, 2012.
- [96] H. Kallmann and M. Pope, "Positive hole injection into organic crystals," *Journal of Chemical Physics*, vol. 32, no. 1, pp. 300-301, 1960.
- [97] J. Dresner, "Photo-hall effect in anthracene," *Physical Review*, vol. 143, no. 2, pp. 558-563, 1966.
- [98] C. W. Tang and S. A. Vanslyke, "Organic electroluminescent diodes," *Applied Physics Letters*, vol. 51, no. 12, pp. 913-915, 1987.
- [99] J. H. Burroughes *et al.*, "Light-emitting diodes based on conjugated polymers," *Nature*, vol. 347, no. 6293, pp. 539-541, 1990.
- [100] J. K. Song, N. K. Lee, and S. K. Kim, "Multiple Ion Cores in Anthracene Anion Clusters," *Angewandte Chemie International Edition*, vol. 42, no. 2, pp. 213-216, 2003.
- [101] Y. Kan, L. Wang, Y. Gao, L. Duan, G. Wu, and Y. Qiu, "Highly efficient blue electroluminescence based on a new anthracene derivative," *Synthetic Metals*, vol. 141, no. 3, pp. 245-249, 2004.
- [102] J. Shinar and R. Shinar, "Organic Light-Emitting Devices (OLEDs) and OLED-based Chemical and Biological Sensors : An Overview," *Journal of Physics D Applied Physics*, vol. 41, no. 13, pp. 1-26, 2008.
- [103] W. Brütting, J. Frischeisen, T. D. Schmidt, B. J. Scholz, and C. Mayr, "Device efficiency of organic light-emitting diodes: Progress by improved light outcoupling," *physica status solidi (a)*, vol. 210, no. 1, pp. 44-65, 2013.
- [104] C. Shallcross. (2016, 1 July). *Organic Light Emitting Diodes : Fluorescent/Phosphorescent Dopants*. [Online]. Available: <http://www.depts.washington.edu/cmditr/modules/oled>
- [105] G. Yu and A. J. Heeger, "Charge separation and photovoltaic conversion in polymer composites with internal donor-acceptor heterojunctions," *Journal of Applied Physics*, vol. 78, no. 7, pp. 4510-4515, 1995.
- [106] J. Chung *et al.*, "Towards highly efficient and highly transparent OLEDs: Advanced considerations for emission zone coupled with capping layer design," *Optics Express*, vol. 23, no. 21, pp. 27306-27314, 2015.
- [107] D. Li, G. Dong, L. Duan, L. Wang, and Y. Qiu, "New method of mobility measurement for organic semiconductors by optoelectronic coupling," *Journal of Physical Chemistry C*, vol. 116, no. 8, pp. 5235-5239, 2012.
- [108] S. Bange *et al.*, "The role of poly(3,4-ethylenedioxythiophene):poly(styrenesulphonate) as a hole injection layer in a blue-emitting polymer light-emitting diode," *J. Appl. Phys.*, vol. 104, no. 10, 2008.
- [109] Y. S. Lee, J.-H. Park, and J. S. Choi, "Frequency-dependent electrical properties of organic light-emitting diodes," *Korean Physical Society*, vol. 42, pp. 294-297, 2003.
- [110] N. Mrmak, P. v. Oorschot, and J.-W. Pustjens. (2016, 12 July). *Resistor Guide : Photo resistor* [Online]. Available: <http://www.resistorguide.com/photoresistor/>
- [111] D. F. Da Silva and D. Acosta-Avalos, "Light dependent resistance as a sensor in spectroscopy setups using pulsed light and compared with electret microphones," *Sensors*, vol. 6, no. 5, pp. 514-525, 2006.
- [112] C. R. Spitzer, Ed. *The Avionics Handbook*, 2nd ed. Boca Raton, USA: CRC Press LLC, 2001, pp. 1-1-1-33.

- [113] L. Urry, "Dry Cell," Patent US2960558 A, 15 November, 1960.
- [114] R. M. Dondelinger, "Batteries: From Alkaline to Zinc-Air," *Biomedical Instrumentation and Technology*, pp. 100-110, March/April 2004.
- [115] S. Donne and J. Kennedy, "Electrochemical impedance spectroscopy of the alkaline manganese dioxide electrode," *Journal of Applied Electrochemistry*, vol. 34, no. 2, pp. 159-168, 2004.
- [116] D. C. Watters, H. Yi, A. J. Pearson, J. Kingsley, A. Iraqi, and D. Lidzey, "Fluorene- Based Co- polymer with High Hole Mobility and Device Performance in Bulk Heterojunction Organic Solar Cells," *Macromolecular Rapid Communications*, vol. 34, no. 14, pp. 1157-1162, 2013.
- [117] J. Griffin, A. J. Pearson, N. W. Scarratt, T. Wang, D. G. Lidzey, and A. R. Buckley, "Organic photovoltaic devices incorporating a molybdenum oxide hole-extraction layer deposited by spray-coating from an ammonium molybdate tetrahydrate precursor," *Organic Electronics*, vol. 15, no. 3, pp. 692-700, 2014.
- [118] R. Kiebooms, A. Aleshin, K. Hutchison, F. Wudl, and A. Heeger, "Doped Poly(3,4-ethylenedioxythiophene) Films: Thermal, Electromagnetical and Morphological Analysis," *Synthetic Metals*, vol. 101, pp. 436-437, 1999.
- [119] R. McGill, J. W. Tukey, and W. A. Larsen, "Variations of Box Plots," *The American Statistician*, vol. 32, no. 1, pp. 12-16, 1978.
- [120] Y. Benjamini, "Opening the Box of a Boxplot," *The American Statistician*, vol. 42, no. 4, pp. 257-262, 1988.
- [121] D. Lind, W. Marchal, and S. Wathen, *Basic Statistics for Business and Economics*, 5th ed. New York, USA: McGraw-Hill Education, 2006, pp. 1-581.
- [122] D. Lane. (2007, 20 August 2016). *Online Statistics Education : A Multimedia Course of Study - Percentiles* [Online]. Available: <http://www.onlinestatbook.com/2/introduction/percentiles.html>
- [123] Microsoft. (2016, 20 August 2016). *Percentile Function* [Online]. Available: <http://www.support.office.com>
- [124] T. J. Pounds, R. J. Wilson, I. Grizzi, and T. Yamada, "Solution processable white pld materials for displays and lighting," *SID Symposium Digest of Technical Papers*, vol. 38, no. 1, pp. 875-878, 2007.
- [125] Ossila. (2016, 21 August 2016). *ZIF Test Board for Pixelated Anode Substrates* [Online]. Available: <http://www.ossila.com/products/oled-test-board-zif>
- [126] F. M. Penning, "Regarding the very small influence on the Admixtures on the ignition voltage of noble gases," *Zeitschrift Fur Physik*, vol. 46, no. 5-6, pp. 335-348, 1928.
- [127] A. I. Carswell and J. I. Wood, "Plasma properties of a CO₂ laser discharge," *Journal of Applied Physics*, vol. 38, no. 7, pp. 3028-3030, 1967.
- [128] B. H. Hamadani, J. Roller, P. Kounavis, N. B. Zhitenev, and D. J. Gundlach, "Modulated photocurrent spectroscopy of CdTe/CdS solar cells-equivalent circuit analysis," *Solar Energy Materials & Solar cells*, vol. 116, pp. 126-134, 2013.
- [129] N. Kavasoglu, A. S. Kavasoglu, O. Birgi, and S. Oktik, "Intensity modulated short circuit current spectroscopy for solar cells," *Solar Energy Materials and Solar Cells*, vol. 95, no. 2, pp. 727-730, 2011.
- [130] Broadcom. (2013, 22 August 2016). *HLMP-Cx1A/1B/2A/2B/3A/3B New 5mm Blue and Green LED Lamps* [Online]. Available: <http://www.docs.avagotech.com/docs/AV02-2228EN>
- [131] S. R. Cowan, J. Wang, J. Yi, Y.-J. Lee, D. C. Olson, and J. W. P. Hsu, "Intensity and wavelength dependence of bimolecular recombination in P3HT:PCBM solar cells: A white-light biased external quantum efficiency study," *Journal of Applied Physics*, vol. 113, no. 15, 2013.
- [132] M. Bag and K. Narayan, "Universality in Intensity Modulated Photocurrent in Bulk-Heterojunction Polymer Solar Cells," *Phys. Rev. B*, vol. 82, pp. 1-4, 2010.
- [133] Roithner. (2013, 22 August 2016). *RC650-TO46FW Resonant Cavity Light-Emitting Diode* [Online]. Available: http://www.roithner-laser.com/datasheets/led_div/rc650-to46fw.pdf
- [134] Anfatec. (2016, 22 August 2016). *USB Lock-In 250 : Lockin Amplifier 10 mHz to 250 kHz* [Online]. Available: http://www.anfatec.net/downloads/USBLockIn/USBLockIn250_Manual.pdf
- [135] K. Adhitya, A. Alsulami, A. Buckley, R. C. Tozer, and M. Grell, "Intensity-Modulated Spectroscopy on Loaded Organic Photovoltaic Cells," *IEEE Journal of Photovoltaics*, vol. 5, no. 5, pp. 1414-1421, 2015.

- [136] Centronic. (2016, 23 August 2016). *OSD5-5T Silicon Photodetector Series 5T : Blue Sensitive For Biased Or Unbiased Operation*. [Online]. Available: <http://www.farnell.com/datasheets/316996.pdf>
- [137] TexasInstruments. (2016, 23 August 2016). *LM6171 High Speed Low Power Low Distortion Voltage Feedback Amplifier* [Online]. Available: <http://www.ti.com/lit/ds/symlink/lm6171.pdf>
- [138] E. Cetinorgu, C. Gumus, and R. Esen, "Effects of deposition time and temperature on the optical properties of air-annealed chemical bath deposited CdS films," *Thin Solid Films*, vol. 515, no. 4, pp. 1688-1693, 2006.
- [139] S. Nakamura, "III-V nitride-based LEDs and lasers: Current status and future opportunities," *International Electron Devices Meeting 2000, Technical Digest*, pp. 9-11, 2000.
- [140] D. Navon, R. Bray, and H. Y. Fan, "Lifetime of injected carriers in Germanium," *Proceedings of the Institute of Radio Engineers*, vol. 40, no. 11, pp. 1342-1347, 1952.
- [141] D. K. Schroder, "Carrier lifetimes in silicon," *IEEE Transactions on Electron Devices*, vol. 44, no. 1, pp. 160-170, 1997.
- [142] W. E. Spear, "Electronic transport in molecular solids and liquids," *Applied optics*, vol. 8, pp. 8-14, 1969.
- [143] LTSpice. (2016, 24 August 2016). *LT Spice IV* [Online]. Available: <http://www.linear.com/designtools/software/#LTspice>
- [144] D. T. Cotfas, P. A. Cotfas, and S. A. Kaplanis, "Methods to Determine DC Parameters of Solar Cells : A Critical Review," *Renewable and Sustainable Energy Reviews*, no. 28, pp. 588-596, 2013.
- [145] C. J. Schaffer *et al.*, "A direct evidence of morphological degradation on a nanometer scale in polymer solar cells," *Advanced Materials*, vol. 25, pp. 6760-6764, 2013.
- [146] R. M. Oksuzoglu, P. Bilgic, M. Yildirim, and O. Deniz, "Influence of post-annealing on electrical, structural and optical properties of vanadium oxide thin films," *Optics and Laser Technology*, vol. 48, pp. 102-109, 2013.
- [147] P. W. M. Blom, M. J. M. de Jong, and S. Breedijk, "Temperature dependent electron-hole recombination in polymer light-emitting diodes," *Applied Physics Letters*, vol. 71, no. 7, pp. 930-932, 1997.
- [148] H. S. Kang *et al.*, "Electrical characteristics of light-emitting diode based on poly(p-phenylenevinylene) derivatives: CzEH-PPV and OxdEH-PPV," *Synthetic Metals*, vol. 130, no. 3, pp. 279-283, 2002.
- [149] Á. Pitarch, G. Garcia-Belmonte, J. Bisquert, and H. J. Bolink, "Impedance of space-charge-limited currents in organic light-emitting diodes with double injection and strong recombination," *J. Appl. Phys.*, vol. 100, no. 8, pp. 084502-1-084502-5, 2006.
- [150] D. Poplavskyy and F. So, "Bipolar carrier transport in a conjugated polymer by complex admittance spectroscopy," *J. Appl. Phys.*, vol. 99, no. 3, pp. 033707-1-033707-9, 2006.
- [151] R.-L. Lin, J.-Y. Tsai, D. Buso, and G. Zissis, "OLED Equivalent Circuit Model With Temperature Coefficient and Intrinsic Capacitor," *Industry Applications, IEEE Transactions on*, vol. 52, no. 1, pp. 493-501, 2016.
- [152] H. C. F. Martens, J. N. Huiberts, and P. W. M. Blom, "Simultaneous measurement of electron and hole mobilities in polymer light-emitting diodes," *Applied Physics Letters*, vol. 77, no. 12, pp. 1852-1854, 2000.
- [153] Hamamatsu. (2016, 24 August 2016). *S1087/S1133 Ceramic Package Photodiodes with Low Dark Current* [Online]. Available: http://www.hamamatsu.com/resources/pdf/ssd/s1087_etc_kspd1039e.pdf
- [154] Hamamatsu. (2016, 24 August 2016). *S1226 Series: For UV to Visible, Precision Photometry; Suppressed Near IR Sensitivity* [Online]. Available: http://www.hamamatsu.com/resources/pdf/ssd/s1226_series_kspd1034e.pdf
- [155] B. C. Krummacher, S. Nowy, J. Frischeisen, M. Klein, and W. Bruetting, "Efficiency analysis of organic light-emitting diodes based on optical simulation," *Organic Electronics*, vol. 10, no. 3, pp. 478-485, 2009.

- [156] J. Song and M. Z. Bazant, "Effects of Nanoparticle Geometry and Size Distribution on Diffusion Impedance of Battery Electrodes," *Journal of the Electrochemical Society*, vol. 160, no. 1, pp. A15-A24, 2013.
- [157] Broadcom. (2016, 24 August 2016). *HLMP-DB25 Blue LED Lamps* [Online]. Available: <http://www.docs.broadcom.com/docs/AV02-2213EN>
- [158] D. Halliday and R. Resnick, *Fundamentals of Physics*, 7th ed. USA: Wiley, 2004, pp. 1-1136.

Note that here the *et al.* abbreviation is used when seven or more names are given.

Lists of Tables

TABLE I. ELECTRON ARRANGEMENTS WITHIN THE ORBITALS OF A CARBON ATOM AT GROUND STATE.....	22
TABLE II. POSSIBLE ELECTRON AND HOLE SPIN COMBINATIONS IN A WAVEFUNCTION IN TERMS OF A KET NOTATION	29
TABLE III OPV Varieties, J_{SC} , V_{OC} , J_{MPP} , V_{MPP} , P_{D-MPP} , R_{s-spec} , $R_{sh-spec}$, R_{Sh} and R_S FROM FIG. 34. AND FIG 35.	67
TABLE IV OLED No., J_{on} , V_{on} , V_{bi} , R_{diff} and L_{on} FROM FIG. 40. AND FIG 41.	75
TABLE V THE LDR V_{bias} , f_c , $\Delta V (f \rightarrow 0)$, $Re \Delta V (f \rightarrow 0)$ AND τ FOR THE SPECTRA SHOWN IN FIG. 5-1(a), (b) AND (c).....	111
TABLE VI LOAD R_L , DC VOLTAGE POINTS, AND CURRENT DENSITIES J , CORNER FREQUENCIES f_c , AND $Re \Delta V$ FOR $f \rightarrow 0$, FOR THE SPECTRA SHOWN IN FIG. 6-1(a).....	116
TABLE VII Corner Frequency vs. External Load Capacitance, C_L , R_L was fixed at 32.7 k Ω	126
TABLE VIII OPV TYPES, V_{MPP} , R_{MPP} , $\Delta V (f \rightarrow 0)$, $Re \Delta V (f \rightarrow 0)$, f_c AND f_{3rd} FOR THE SPECTRA SHOWN IN FIG. 6-10(a), (b),(c) AND 6-11.....	136
TABLE IX OPV TYPES, V_{MPP} , R_{MPP} , $\Delta V (f \rightarrow 0)$, $Re \Delta V (f \rightarrow 0)$, f_c AND f_{3rd} FOR THE SPECTRA SHOWN IN FIG. 6-12 (b) AND (c).....	140
TABLE X OPV TYPES, V_{MPP} , R_{MPP} , $\Delta V (f \rightarrow 0)$, $Re \Delta V (f \rightarrow 0)$, f_c AND f_{3rd} FOR THE SPECTRA SHOWN IN FIG. 6-14(a), (b),(c) AND 6-15.....	148
TABLE XI OPV TYPES, V_{MPP} , R_{MPP} , $\Delta V (f \rightarrow 0)$, $Re \Delta V (f \rightarrow 0)$, f_c AND f_{3rd} FOR THE SPECTRA SHOWN IN FIG. 6-16 (b) AND (c).....	150
TABLE XII OLED V_{DC} , $Re \Delta V (f \rightarrow 0)$ AND f_c FOR THE SPECTRA SHOWN IN FIG. 7-1(a), (b) and (c)	157
TABLE XIII OLED V_{DC} , $Re \Delta V (f \rightarrow 0)$ AND f_c FOR THE SIMULATED SPECTRA SHOWN IN FIG. 7-3(b)	161
TABLE XIV THE OLED LIGHT EMISSION, $Re \Delta V (f \rightarrow 0)$ AND f_c FOR THE SPECTRA SHOWN IN FIG. 7-6(a), (b) AND (c).....	167
TABLE XV THE OLED LIGHT EMISSION, $Re \Delta V (f \rightarrow 0)$ AND f_c FOR THE SPECTRA SHOWN IN FIG. 7-8.....	170
TABLE XVI OLED AGEING TIME, I_{DC} , $Re \Delta V (f \rightarrow 0)$ AND f_c , FOR THE SPECTRA SHOWN IN FIG. 7-9(a), (b) and (c).....	173
TABLE XVII OLED AGEING TIME, I_{DC} , $Re \Delta V (f \rightarrow 0)$ AND f_c FOR FIG. 7-10 SIMULATED SPECTRA.....	175

List of Figures

Fig. 1-1. An Argand diagram of equation (2) taken from Macdonald et al [21].	7
Fig. 1-2. A flow diagram of general characterization procedure in IS taken from Macdonald et al [21].	8
Fig. 1-3. (a) and (b) Examples of two RC circuit with R and C components in parallel and in different configurations, with their respective (c) and (d) Nyquist plot results of $Z(\omega)$. The direction of increasing frequency is from right to left/anti-clockwise, taken from Macdonald et al [21].	10
Fig. 1-4. Example of a Bode amplitude (arrow pointing left and in Ω) and phase (arrow pointing right and in $^\circ$) plot of an impedance measurement with respect to frequency f (in Hz), taken from Macdonald et al [21].	10
Fig. 1-5. An example of a typical impedance spectroscopy setup. Here, $\eta(t)$ is the total voltage applied to the cell, including the modulated component $\Delta\eta$. While $i(t)$ is the total current response from the cell, including the modulated component Δi , taken from Park et al [38].	11
Fig. 1-6. Example of an (a) IMPS (top) and (b) IMVS (bottom) setup. For (a) and (b), transfer function $H(\omega)$, ΔV , Δi and Δi_{LED} is a function of frequency ω . Also the LED DC current is in proportion to the DC light intensity, taken from Metrohm Autolab application note [48].	15
Fig. 1-7. Example of a transfer function Bode amplitude (a) and phase (b) plot with respect to frequency f (in Hz). The transfer function in (a) is represented by Z and the amplitude of Z in units of $A\ m^2/W$. The phase (represented by ψ) plot in (b) presents the transfer function phase difference as a negative value, thus the plot location in the 4 th quadrant. Both plots are taken from Luther et al [49].	16
Fig. 1-8. An example of several $H(\omega)$ Nyquist plot result from a dye-sensitized cell under an IMPS mode of operation. The plot is taken at different DC light intensity ϕ_o^{LED} , with $-H'$ parametric with frequency ω . The $H(\omega)$ plot here is presented as an inverted plot, with the plot's real (H') and an imaginary axis (H'') under a (-) sign. Thus, the plot actually lies in the 4 th quadrant with the extended part running into the 3 rd quadrant, instead of lying in the 1 st quadrant with the extended feature running into the 2 nd quadrant. Note also that H' and H'' are in Ω . Here, the direction of increasing frequency is anti-clockwise, with the units of both H' and H'' in Ω [48].	17
Fig. 1-9. Example of several $H(\omega)$ Nyquist plot result from a dye-sensitized cell under an IMVS mode of operation. The plot is taken at different DC light intensity ϕ_o^{LED} , with $-H'$ parametric with frequency ω . The $H(\omega)$ plot here is also presented as an inverted plot, with the plot's real (H') and imaginary axis (H'') under a (-) sign. Note also that H' and H'' are in Ω . Here, the direction of increasing frequency is anti-clockwise, with the units of both H' and H'' in Ω . [48].	18

- Fig. 2-1. Several examples of organic semiconductors along with their structures and energy gap [54].20
- Fig. 2-2. The three different carbon hybrid orbitals (a) The “sp” hybrid orbitals with 2 “sp” forming a linear structure, (b) The “sp²” hybrid orbitals with 3 “sp²” forming a trigonal-planar structure and (c) The “sp³” hybrid orbitals with 4 “sp³” forming a tetrahedron structure The respective hybrid orbital’s angle is also given in the figure.24
- Fig. 2-3. Three different depictions of the benzene ring structure. These are (a) The benzene ring structure with the complete atomic labels. (b) The alternate single and double bonds depiction of the ring structure and (c) another depiction of the benzene ring structure that shows the influence of 2p orbital’s delocalization within the structure.....25
- Fig. 2-4 (a). Illustration of polaron formation in a PPV structure. Shown here is a hole polaron formation, i.e. when an electron is removed from the molecule’s HOMO. This then results in the molecule’s structure experiencing a deformation due to the strong electron-vibration coupling in an organic semiconductor. After electron removal, the semiconductor’s structure relaxes to the minimum energy position but with different bond lengths and angles due to bond redistributions. (b). In terms of spin, the molecule’s HOMO will be fully occupied with no net spin at the ground state. If an electron is removed, a net spin will be present from an unpaired electron with the electron transitioned to a lower energy level due to strong electron-vibration coupling. On the other hand, if an electron is added, a net spin will be present and the added electron will gain more energy than the LUMO, with the electron transitioning to a lower energy level.26
- Fig. 2-5. Because of the strong electron-vibration coupling in an organic semiconductor, removing an electron from the molecule will cost less in energy than the HOMO level, with the energy needed by the molecule to remove an electron from the HOMO being the ionization potential or I_p (in eV). On the other hand, an electron added into the molecule will gain more energy than the LUMO level, with the energy gained by the molecule called the electron affinity or E_a (in eV).....27
- Fig. 2-6 (a). Exciton formation in a PPV structure. Here, an electron is excited from the molecule’s HOMO into its LUMO which results in the molecule’s structure experiencing a deformation due to strong electron-vibration coupling. Exciton formation usually occurs when a photon is absorbed. After formation, the excited structure will have different bond lengths due to the strong vibration coupling (b). In terms of spin, the molecule’s HOMO will be fully occupied with no net spin in the ground state, which is called the S_0 state. Now if an electron is excited from the HOMO into the LUMO by photon absorption, the S_0 state will be excited into a singlet exciton state or S_1 . At S_1 state, the excited electron transitions to an energy level lower than LUMO while the unpaired ones in the HOMO transition to a higher energy level than the HOMO.....28
- Fig. 2-7. An illustration of fluorescence and phosphorescence processes in an organic semiconductor molecule. First, a photon is absorbed by the molecule which then excites the molecule (electron) from the ground state S_0 with no net spin into (1) the first singlet exciton state S_1 , where there is a net spin, or (2) into a much higher singlet exciton state S_2 which has a net spin at a higher energy state. Once the molecule has been excited into S_2 , it

will always decay to S_1 (3) due to interaction with the outside environment and internal vibrations. When it arrives at S_1 , the molecule can further decay into the ground state S_0 , accompanied by light emission from the semiconductor (4). This process is called fluorescence and the resulting light spectra are broad since the decay from S_1 to S_0 can occur from a lower S_1 energy level to different vibrational levels of S_0 . In addition, if a molecule is excited into an S_1 or S_2 state, it can decay from these states to another energy states which are lower, i.e. the triplet T_1 and a higher T_2 state via intersystem crossing (ISC) mechanism in (5) and (7). However this ISC decay process is very rare and triplet excitons are most commonly found in electrically driven devices. If the molecule transitions to higher T_2 state, the molecule can decay into the lower T_1 state due to internal vibrations (6). Also, photon absorption can occur when the molecule is already in the T_1 state, which can then excite the molecule into the T_2 state (8). When a molecule has already decayed into the T_1 state, two decays pathways are possible, one is that the molecule decays directly into the ground state S_0 , which is called the phosphorescence process (9), in which there must be an interaction/coupling between the singlet and triplet states. While the other decay pathway for T_1 state molecule is through intersystem crossing mechanism to higher S_0 state (10) at which it can then decay into the S_0 state (11) [65].....30

Fig. 2-8. A potential energy diagram that shows transitions and excitations between electronic states in an absorption, fluorescence and phosphorescence process with respect to inter-atomic distance in an organic semiconductor molecule [65].....33

Fig. 2-9. A mirror plot of Anthracene absorption and emission (fluorescence) intensity spectra for an unspecified number of transition states with respect to the states wavelength (in nm) [67].....34

Fig. 2-10. An energy level illustration of an organic semiconductor device, in which the semiconductor is sandwiched between two electrodes, where one is an anode due to its high work function and the other being a cathode due to its low work function. In the above example, PPV is the organic semiconductor, ITO is the anode and the Ca/Al layer is the cathode. In the above illustration, E_g is the energy gap between the semiconductor's HOMO and LUMO, I_p and E_a are respectively the ionization potential and electron affinity of the semiconductor, while Φ_A and Φ_C are respectively the anode and cathode work function. The respective energy levels of the anode, cathode, and the semiconductor's LUMO and HOMO are also given. Finally, the vacuum level in the above is taken at 0 eV.35

Fig. 2-11. An energy level illustration of the sandwiched organic semiconductor device under an applied voltage bias (the bias is not shown here). Here, as in Fig. 2-10, PPV is the organic semiconductor, ITO is the anode and the Ca/Al layer is the cathode. Because of the applied bias, an electric field will be generated in the semiconductor and the energy levels will be tilted. The tilt is uniform since the generated field will be uniform across the semiconductor due to our earlier assumption that there are no carriers beforehand in the semiconductor. Under an applied bias, electrons will be injected from the Ca/Al layer cathode into the LUMO and will encounter an electron injection barrier ΔE_e , while from the opposite side, holes will be injected into the HOMO and will encounter a hole injection barrier ΔE_h . As in Fig. 2-10, E_g is the energy gap between the HOMO and LUMO, I_p is the

ionization potential, E_a is the electron affinity of the semiconductor, while Φ_A and Φ_C are respectively the anode and cathode work function. The vacuum level is taken at 0 eV.36

Fig. 2-12 (a). A typical BHJ OPV structure with a microscopic diagram that describes charge generation/operational process inside the BHJ (b). Energy level diagram of photon absorption, exciton generation and dissociation into free charge carriers inside the OPV's BHJ layer. (c). Chemical structure of a typical donor polymer (P3HT and MEH-PPV), acceptor (PCBM) and hole extraction materials (PEDOT:PSS) used in BHJ OPV [1,2,53].43

Fig. 2-13. An electronic state diagram depicting the BHJ spin states, starting from the ground state (S_0) to the first state after excitation or the exciton state (S_1). This state is then followed by charge-transfer (CT) states, which is where the electron and hole are separated at the donor-acceptor interface. Here, there are multiple CT states that can be formed during charge transfer from donor to acceptor. These possible states are represented by the lowest (CT_1) to the highest (CT_n). These CT states are also an intermediate transition state before the carrier is separated in the final charge-separated state (CS). The different rate constants k_i represents different competing transfer rates in the whole process [9].....45

Fig. 2-14. A solar cell's DC current density-voltage or J/V characteristics under AM 1.5 light that depict several of the cell's DC parameters, i.e. V_{oc} , J_{SC} , V_{MPP} , J_{MPP} and fill factor or FF [58].....47

Fig. 2-15. A solar cell's several DC power density-voltage or P_D/V characteristics under AM 1.5 light, where each P_D/V curve depicts a maximum peak, which is called the maximum power point (MPP), and the voltage and current density at that point being V_{MPP} and J_{MPP} respectively [92].....47

Fig. 2-16 (a). A typical multi-layer OLED structure with (b). an energy level diagram that describes charge generation/operational process inside the OLED's organic materials [104].50

Fig. 2-17. Chemical structure of a typical (a) polymer and small organic molecules fluorescence emitter, and (b) hole injection layer (CuPc) and electron injection layer (TPBI) materials that are used in an OLED. Note that the colour emitted from the polymer and small molecules examples follows the colour spectrum identifier above them, e.g. DPA and DBP are respectively, a blue and red emitter [96,102-104].....51

Fig. 2-18. An OLED can emit white light from (a). the lateral configuration of red, green and blue emitters or (b). stacked configuration of the blue emitter and yellow phosphor in the emissive layer [94].....52

Fig. 2-19. An electronic state diagram depicting OLED operation in terms of carriers spin. To begin with, both carriers started from the excitation/exciton state (1S_1). Then from 1S_1 carriers can decay into the ground state (1S_0) through several pathways, one is through fluorescence (in blue), the other is via phosphorescence (in red) with triplet exciton (3T_1) and intersystem crossing and then finally third, through fluorescence quenching (not shown [105].....53

Fig. 2-20. Example of an OLED's DC current density-voltage or J/V characteristics [107]54

Fig. 2-21. An example of an OLED's DC luminance-voltage or L/V characteristics [37].	54
Fig. 2-22. An example of an OLED's DC J/V and L/V characteristics plot in a semi-log manner. The left-pointing arrow refers to J/V plot, while the right-pointing ones refer to the L/V plot [109].	55
Fig. 2-23. A depiction of (a) LDR device structure, (b) top view and (c) the CdS crystal structure in LDR [111].	56
Fig. 2-24. A cutaway of an alkaline battery [115].	58
Fig. 3-1 (a). A cutaway and top view of the prepared BHJ OPV device, with (b) the BHJ's donor-acceptor and the cell's hole extraction layer material and (c) The energy level diagram of the device constituent layers. Here, PFDT2BT-8 is poly[9,9-dioctylfluorene-4,7-alt-(5,6-bis(octyloxy)-4,7-di(2,2'-bithiophen-5-yl)benzo[c][1,2,5]thiadiazole)-5,5-diyl], PC ₇₀ BM is [6,6]-Phenyl-C71-butyric acid methyl ester and PEDOT:PSS is poly(3,4-ethylenedioxythiophene) polymer doped with poly(styrenesulfonate) [53,117,118].	61
Fig. 3-2. The J/V (in blue) and P _D /V (in red) characteristics of BHJ OPV with PEDOT:PSS HEL. Here the BHJ mixture is PFDT2BT-8:PC ₇₀ BM.	65
Fig. 3-3. The J/V (in blue) and P _D /V (in red) characteristics of BHJ OPV with PEDOT:PSS HEL after 30 days of storage under dark and at ambient conditions.	65
Fig. 3-4. The J/V characteristics of 5 varied OPV with V ₂ O _{5-x} HEL. Here, the OPVs were varied by preparing OPV with unannealed, 100, 200, 300 and 400 °C annealed V ₂ O _{5-x} HEL before BHJ deposition (shown in colour inset).	66
Fig. 3-5. The P _D /V characteristics of 5 varied OPV with V ₂ O _{5-x} HEL. Here, the OPVs were varied by preparing OPV with unannealed, 100, 200, 300 and 400 °C annealed V ₂ O _{5-x} HEL (shown in colour inset).	66
Fig. 3-6. Box plots for OPVs with PEDOT HEL. Here, the PCE statistics are for 9 devices (or 54 pixels in total), in which the average maximum PCE ~ 6%. The PCE is represented by the blue points in the plots.	69
Fig. 3-7. Box plots for OPVs with their V ₂ O _{5-x} HEL (a). unannealed, (b). 100 °C annealed, (c). 200 °C annealed, (d) 300 °C annealed and (e). 400 °C annealed before BHJ deposition. Here, the PCE statistics are for 2 devices (or 12 pixels in total), in which ~ 5.8%. The PCE is represented by the blue points in the plots.	70
Fig. 3-8. Electroluminescence spectrum of a W1100 polymer. The total (white) spectrum is a combination of red and blue emitter/chromophores. Here we can observe two peaks, the highest peak, i.e at the spectrum's blue part, has a full width at half maximum (FWHM) = 50 nm. While the smaller one, i.e. at the red part, has an FWHM = 120 nm [125].	71
Fig. 3-9 (a). The prepared OLED structure and (b). PEDOT:PSS, calcium (Ca) and lithium fluoride (LiF) as the OLED's hole (HIL) and electron injection layer (EIL) respectively [53].	72
Fig. 3-10. The J/V characteristics of all 3 OLEDs. Here, OLED No. 1 to 3 is of the same structure and emissive materials.	74

Fig. 3-11. The L/V characteristics of all 3 OLEDs.	74
Fig. 4-1. A depiction of the “optogalvanic spectroscopy” setup that was used by Green et al. to measure the electrical response from a laser-irradiated gas discharge inside the tube [43].	77
Fig. 4-2. The IMPS setup that was used by Peter et al. to measure photocurrent response of a semiconductor electrode that was illuminated by a modulated laser. Here re, we and se refers to reference, working and standard/counter electrode respectively in a potentiostat three-electrode setup [16].	78
Fig. 4-3. The IMS setup under IMPS used by Kasavoglu et al. to measure photocurrent response from CIGS ($\text{Cu}(\text{In}_x\text{Ga}_{1-x})\text{Se}_2$) and porous Si solar cells. Here, the impedance analyzer controls the current modulation on the LED driver, with the DC current bias provided by the LED driver itself. The LED driver, in turn, modulates the LED group illumination intensity, which is then used to characterize the solar cell sample [131].	80
Fig. 4-4. The IMS setup used by Huang et al. to measure photovoltage response from dye-sensitized nanocrystalline TiO_2 solar cells (DSSC). Here, the setup is under IMVS mode and the lock-in modulates the illumination and measures the photovoltage response from the DSSC. Note that the digital data processing module above does not refer to the analyzer but it refers to further digital data processing from the lock-in [53].	81
Fig. 4-5 (a). A block diagram of our IMS measurement setup, showing the PC running LabView software which controls the USB lock-in, a circuit driving a fast red LED by adding a DC offset voltage to the AC modulation voltage taken from the lock-in’s reference output, the solar cell with its terminals connected via a variable load R_L , and the voltage across the load fed into the lock-in’s measurement input. (b) A circuit schematic of the DC + AC adder circuit, that adds a DC bias to the AC lock-in reference output to drive the LED. The lock-in reference output is represented by a voltage source, top left. DC voltage supply is from 2 x 9 V batteries stabilized by capacitors (right). The level of DC bias is set by a 5 k Ω potentiometer (highlighted). The LED (D1) is also highlighted. As a performance test of the DC + AC adder, we fed the DC + AC signal directly into the lock-in measurement input, and found no measurable drop in AC amplitude, and less than 1° of added phase, up to 250 kHz.	83
Fig. 4-6 (a). The schematic setup for IMS under finite load. R_L represents an external load resistance. (b) DC Current Density-Voltage (J/V) characteristic of a PV cell under modulation, which results in three different light intensities (L (blue); L - ΔL (green); and L + ΔL (red)). The ΔL is the intensity modulation in IMS. Here J_{SC} and V_{OC} are respectively, the cell’s short-circuit current density and open-circuit voltage point. The load line (in black) represents the external load resistance R_L , which intersects the three lines at the characteristic midpoint. This midpoint is the cell’s maximum power point. Also, ΔJ and ΔV are respectively the current density and voltage modulation due to the modulated light [137].	86
Fig. 4-7. A snapshot view of the lock-in’s interface software menu page that shows the lock-in settings. These settings are; ref out voltage amplitude (in V_{rms}), input coupling, roll-off (in dB/oct), frequency f (in Hz), input gain, phase offset (in degrees) and reference harmonic [136].	88

- Fig. 4-8 (a). A snapshot of our frequency scan menu page. Depicted are the file path columns where we insert the frequency group's spreadsheet, the response columns where we display the resulting voltage and phase response, and finally, the Bode plots visualization for the voltage response. (b) depicts the individual group frequency VI enclosed within a FOR loop structure which we use to build our software. Here, we can see the lock-in interface software which is used as a sub-VI in the routine, in addition to a spreadsheet frequency input sub-VI, voltage and phase response sub-VI and wait function sub-VI.91
- Fig. 4-9. A flowchart diagram that describes the frequency scan process in each frequency group VI.92
- Fig. 4-10. An expanded view of our IMS software virtual instrument (VI), which depicts the software process flow, group frequency VIs, FOR loops and interface software together with the sequential structure that is used to build the software. The scanning process starts at (1), where we perform an IMS scan at the first frequency group by using that group VI. After the first group scan is finished, the results will be sent to a plot sub-VI which will then accumulate the results until all frequency groups have been completed. At (2), the sequential structure will continue the scan to the next group VI for the next frequency group. At (3), the scan will continue to the next group and so on, until all frequency groups have been scanned. Finally, at (4), the resulting voltage and phase is accumulated at the plot sub-VI and then at (5), the results are plotted and displayed in the menu page Bode amplitude and phase plots visualization.93
- Fig. 4-11. A block diagram of the IMS calibration setup on the solar cell connections. The diagram along with other instrument setup is similar to 4.2, while also showing the -13.2 V reverse-biased silicon photodiode with voltage measurement at point A in-parallel with measurement resistance $R_1 = 68 \Omega$94
- Fig. 4-12. Bode (a) amplitude, and (b) phase plots from an OSD5-5T photodiode under a red LED and reversed-bias at a reverse-bias voltage $V_{REV} = -13.2 \text{ V}$. Here, the total LED drive current $I_{LED} = (18 + 10) \text{ mA}$95
- Fig. 4-13 (a). A block diagram of our IMS measurement setup, showing the PC running LabView software which controls the USB lock-in, a circuit driving the OLED by adding a DC offset voltage to the AC modulation voltage from the ref out, the OSD5-5T photodiode connected to an LM6171 op-amp with feedback resistor (R_f) = 4.7 k Ω and capacitor (C_f) = 4.7 pF, and the photodiode's current converted into voltage at the op-amp's output. This voltage is then fed into the lock-in's measurement input. (b) A circuit schematic of a modified DC + AC adder circuit in 4.2. which adds a DC bias to the AC ref out to drive the OLED. The lock-in ref out is represented by a voltage source, top left. DC voltage supply is a 9 V and 15 V DC power supply stabilized by capacitors (right). The level of DC bias is set by a 10 k Ω potentiometer (highlighted). The OLED (D1) is also highlighted. As a performance test of the DC + AC adder, we fed the DC + AC signal directly into the lock-in measurement input, and found no measurable drop in AC amplitude, and less than 1° of added phase, up to 250 kHz.97
- Fig. 4-14. A view of our IMS software modification which employs a formula sub-VI in each group VI, to account for the phase inversion from the IV converter. The formula sub-VI is

integrated into the FOR loop structure with its operation limited by the loop iteration number. Note here that the formula sub-VI input and output connection is not connected to the group VI, in practice, the formula input (x) is connected to the phase response sub-VI and its output (y) is connected to the outside of the group VI towards the plotting VI..... 100

Fig. 4-15 (a). A block diagram of the IMS measurement setup for the CdS-based LDR, shown here are all the same IMS components we see in Fig. 4.6, with the difference that we now use a green LED to do the IMS, and that the LDR is in place of the photodiode in Fig. 4.6. In addition, we also apply a different voltage bias or $V_{bias} = 1, 1.5, 2, 2.5$ and 3 V on the LDR to measure current flow due to V_{bias} . To add, the R_f used in the IV circuit is also different with $R_f = 1$ k Ω . (b). Circuit scheme of modified DC + AC adder circuit used for IMS on LDR. The circuit is the same as those in 4.2, but here we replace the fast red LED with a green LED and the LED resistor $R_{LED} = R_4 = 102$ Ω 102

Fig. 4-16 (a). Bode amplitude, and (b) phase plots from OSD5-5T photodiode under green LED and at a reverse-bias voltage $V_{REV} = -13.2$ V. Here, the green LED drive current or $I_{LED} = (19 + 9)$ mA..... 104

Fig. 5-1 (a). Bode amplitude plot of ΔV , (b) Bode phase plot of ϕ vs frequency f with the plots taken at each V_{bias} depicted separately on the side of the main plot for clarity purposes, and (c) Nyquist plots of ΔV that plots the imaginary ($Im \Delta V = |\Delta V| \sin \phi$) vs. its real part ($Re \Delta V = |\Delta V| \cos \phi$), the spectra being parametric with frequency ω . Here, (a), (b) and (c) are taken at frequencies between 1 Hz and 250 kHz and under LDR bias voltage $V_{bias} = 1, 1.5, 2, 2.5$ and 3 V (shown colour coded in inset). Note that the Re/Im axis at (c) uses different scales and are not normalized, with the direction of increasing frequency ω given by the blue arrow. For all LDR bias voltages, we use a green LED driven with LED drive current of $I_{LED} = (19 + 9)$ mA. This current will then be varied as we varied V_{bias} 108

Fig. 6-1 (a). Nyquist plots of ΔV that plots the imaginary part ($Im \Delta V = |\Delta V| \sin \phi$) vs. its real part ($Re \Delta V = |\Delta V| \cos \phi$) which is parametric in frequency for IMS spectra taken at different R_L , ranging from near-open circuit (high R_L , or near ‘IMVS’) to near-short circuit (low R_L , or near ‘IMPS’). Spectra are colour coded by their voltage points, V , shown in the right panel, rather than R_L . The LED was driven by $I_{LED} = (18 \pm 4)$ mA. Note Re / Im axis here uses different scales. (b) Normalized Nyquist plots of Fig. 6-1(a) taken at near-open circuit voltage point (0.8 V, $R_L = 476$ k Ω), near maximum power point (0.505 V, $R_L = 36.6$ k Ω) and near-short circuit voltage point (0.1 V, $R_L = 6.8$ k Ω). The direction of increasing frequency is given by the blue arrow. In all plots, Re ΔV is normalized to its value in the limit of $f \rightarrow 0$ Hz, whilst Im ΔV is normalized to its minimum magnitude..... 114

Fig. 6-2. The plot of the dominant Nyquist semicircle characteristic parameters vs DC voltage point, which is set by R_L . Here, the blue plot is Re ΔV at low-frequency ($f \rightarrow 0$) vs. voltage points. While the red one is corner frequencies, f_c , vs. voltage points. 116

Fig. 6-3. The OPV’s J/V characteristics and power profile under red LED illumination, that are constructed from Table VI. 117

Fig. 6-4. A diagram of microscopic processes that described OPV operation from Luther et.al., The $k_d, k_{rg}, k_{rb}, k_{dt}, k_t,$ and k_{rt} here is the dissociation, geminate recombination,

biomolecular recombination, de-trapping, trapping and trap-assisted recombination rate constant respectively. Finally, $G(t)$ is the CT_1 quasiparticle generation rate [49]..... 119

Fig. 6-5 (a). Generic equivalent circuit model for BHJ OPV [134]. I_L here represents the light-driven current source. In IMS, all components apart from R_L are internal to the OPV cell. (b) Simulated ‘Nyquist rainbow’ for the equivalent circuit model, We selected $R_{Sh} = 100 \text{ k}\Omega$, $R_S = 2 \text{ k}\Omega$, $C_{BHJ} = 4 \text{ nF}$, and a customized 1N914 diode (1N914_KA) with the saturation current reduced to 3 pA. The amplitude of the current source modulation was set to 5 μA and the DC current bias was set to 25 μA . Here, R_L was varied in the range (6.8-476) $\text{k}\Omega$, leading to the voltage points shown in the panel on the right. The largest semicircle (light blue symbols) corresponds to $R_L = 26.5 \text{ k}\Omega$ 121

Fig. 6-6. The characteristic parameters of simulated Nyquist semicircle plotted against voltage point V , which is set by R_L . (a) The blue plots indicate $\text{Re } \Delta V$ at low-frequency ($f \rightarrow 0$) vs. voltage points. While at (b) the red plot indicate corner frequencies, f_c , vs. voltage points. Here, $\text{Re } \Delta V$ reaches its maximum for $R_L = 26.5 \text{ k}\Omega$ 121

Fig. 6-7. Comparison between the IMS spectra of a freshly prepared sample, and a sample stored for 30 days under air in the dark. $R_L = 61 \text{ k}\Omega$ for both. The corner frequencies (f_c) of the fresh and stored sample are 1140 Hz and 356 Hz respectively. 124

Fig. 6-8. Simulations on an extended equivalent circuit model, shown in the inset. Here, R_L was set to 61 $\text{k}\Omega$, while R_{Sh} , R_S , C_{BHJ} were chosen to match the measured values for the stored cell under AM 1.5. (Selection of C_{BHJ} will be discussed in the next subchapter). For simplicity, the diode was represented by a suitable, i.e. 5.5 $\text{k}\Omega$ differential resistor. Here, the selection of differential resistance magnitude was done similarly with Gundlach et al. and also discussed in the next subchapter. The plot with red symbols was obtained with $C_{ext} = 13 \text{ nF} // R_{ext} = 200 \text{ }\Omega$, while the plot with blue symbols was obtained with $C_{ext} = 1 \text{ nF} // R_{ext} = 200 \text{ }\Omega$ 125

Fig. 6-9. Ratio of corner frequencies for OPV cells not capacitively loaded/loaded with $C_L // R_L = 32.7 \text{ k}\Omega$ vs. magnitude of the capacitive load, C_L . Data from Table VII. The straight line fit intercepts the C_L axis at $-3.9 \pm 0.1 \text{ nF}$ 128

Fig. 6-10 (a). Bode amplitude and (b) phase of ΔV with respect to frequency f , of OPV with non-annealed V_2O_{5-x} HEL (blue plots), followed by cells with their V_2O_{5-x} HEL annealed at 100, 200, 300 and 400 $^\circ\text{C}$ pre-BHJ deposition (shown respectively as the red, orange, purple and black colour in the inset). (c). Nyquist plots results of an OPV with non-annealed V_2O_{5-x} HEL (blue plots), followed by cells with their V_2O_{5-x} HEL annealed at 100, 200, 300 and 400 $^\circ\text{C}$ pre-BHJ deposition (shown respectively as the red, orange, purple and black colour in the inset). Note the extended semicircles which crossed from the 4th to 3rd quadrant at high f . Here, all spectra were taken at the respective cells V_{MPP} by setting the external R_{MPP} accordingly and at f between 1 Hz and 250 kHz. The LED was driven by $I_{LED} = (18 \pm 4) \text{ mA}$. Also, the Re/Im axis at (c) uses different scales and are not normalized, with the direction of increasing frequency given by the blue arrow..... 132

Fig. 6-11. Magnification of the same plots in Fig. 6-10(c) in-between the 3rd and 4th quadrant. Note that here, f_{3rd} does not change much for cells with higher HEL annealing

temperature. Also, the Re/Im axis here also uses different scales and are not normalized, with the direction of increasing frequency given by the blue arrow..... 135

Fig. 6-12 (a). The modified OPV generic equivalent circuit which shows the extended capacitor component (C_{ext}) in-parallel between series (R_s) and load resistance (R_L). The C_{ext} component represents the slower carrier path through the cell's external circuit which results in the "3rd quadrant" feature. (b) Simulated Nyquist plot for a cell with unannealed V_2O_{5-x} HEL and cells with its V_2O_{5-x} HEL annealed at 100, 200, 300 and 400 °C (sample types are shown in the colour coded inset). For the simulation, we set the DC current bias (I_{DC}) = 25 μ A with current modulation (I_{AC}) = 5 μ A_p for all cells. Here, we again use the modified 1N914_KA diode and C_{BHJ} = 4 nF in the circuit. We then set C_{ext} = 2 nF. We also set the shunt resistance (R_{sh}) = 32, 36, 35, 35 and 42 k Ω for cells with unannealed, 100, 200, 300 and 400 °C annealed V_2O_{5-x} HEL respectively. All of the cells series resistances (R_s) are set to R_s = 577 Ω . Also, the R_L magnitudes are set to = 155, 130, 150, 160 and 140 k Ω for cells with unannealed, 100, 200, 300 and 400 °C annealed V_2O_{5-x} HEL respectively. (c) Magnification of the same plots in (a) in-between the 3rd and 4th quadrant. Also here, f_{3rd} does not change much for cells with higher HEL annealing temperature. Finally, the simulation in (b) is set between 1 Hz and 250 kHz, while the Re/Im axis in (b) and (c) uses different scales and are not normalized, with the direction of increasing frequency given by the blue arrow. 138

Fig. 6-13. Simulations results from the modified circuit in Fig. 6-12(a) (shown as inset) for the cell with the unannealed HEL. In the circuit inset, I_L ($I_{DC} + I_{AC}$), the 1N914_KA diode, R_{sh} , R_s , C_{ext} , and R_L are chosen to be the same as in Fig. 6-12(a). Here, the trap component at low frequency is represented by a series capacitance C_{ext}' . For this simulation, we set C_{ext}' = 8 nF. Finally, the simulation is set between 1 Hz and 250 kHz, where the Re/Im axis uses different scales and are not normalized, with the direction of increasing frequency given by the blue arrow. 142

Fig. 6-14 (a). Bode amplitude and (b). phase of ΔV with respect to frequency f , of OPV with non-annealed V_2O_{5-x} HEL (blue plots), followed by cells with their V_2O_{5-x} HEL annealed at 100, 200, 300 and 400 °C pre-BHJ deposition (shown respectively as the red, orange, purple and black colour in the inset), after 13 days of storage under dark and ambient conditions. (c). Nyquist plots results of an OPV with non-annealed V_2O_{5-x} HEL (blue plots), followed by cells with their V_2O_{5-x} HEL annealed at 100, 200, 300 and 400 °C pre-BHJ deposition (shown respectively as the red, orange, purple and black colour in the inset) also after 13 days of storage under dark and ambient conditions. Note again the "3rd quadrant" feature. Here, all spectra were taken at the respective cells V_{MPP} by setting the external R_{MPP} through manual tuning for the highest ΔV and for f between 1 Hz and 250 kHz. The LED was driven by I_{LED} = (18 \pm 4) mA. Also, the Re/Im axis at (c) uses different scales and are not normalized, with the direction of increasing frequency given by the blue arrow. 145

Fig. 6-15. Magnification of the same plots in Fig. 6-14(c) in-between the 3rd and 4th quadrant. Note that f_{3rd} does not change much for cells with higher HEL annealing temperature. Also, the Re/Im axis here uses different scales and are not normalized, with the direction of increasing frequency given by the blue arrow. 147

Fig. 6-16 (a). Simulated Nyquist plot for stored cell with unannealed V_2O_{5-x} HEL and cells with its V_2O_{5-x} HEL annealed at 100, 200, 300 and 400 °C after 13 days of storage (sample types are shown in the colour coded inset). Also shown in the circuit inset is the modified OPV generic equivalent circuit which shows the extended capacitor component (C_{ext}) in-parallel between series (R_s) and load resistance (R_L). For the simulation, we set the DC current bias (I_{DC}) = 25 μ A with current modulation (I_{AC}) = 5 μ A_p for all cells. Here, we again use the modified 1N914_KA diode and C_{BHH} = 4 nF in the circuit. We also set C_{ext} = 2 nF. We also set the shunt resistance (R_{sh}) = 24, 33, 20, 16 and 15 k Ω for stored cells with unannealed, 100, 200, 300 and 400 °C annealed V_2O_{5-x} HEL respectively. All of the cells series resistances (R_s) are set to R_s = 577 Ω . The R_L magnitudes are set to = 45, 50, 45, 56 and 30 k Ω for stored cells with unannealed, 100, 200, 300 and 400 °C annealed V_2O_{5-x} HEL respectively. (b) Magnification of the same plots in (a) in-between the 3rd and 4th quadrant. Here, f_{3rd} does not change much for cells with higher HEL annealing temperature. Finally, the simulation in (b) is set between 1 Hz and 250 kHz, where the Re/Im axis in (b) and (c) uses different scales and are not normalized, with the direction of increasing frequency given by the blue arrow..... 149

Fig. 7-1 (a). Bode amplitude plot of the OLED's ΔV , (b) Bode phase plot of ΔV phase ϕ with respect to frequency f and (c) Nyquist plots of ΔV that plots the imaginary part ($Im \Delta V = |\Delta V| \sin \phi$) vs. real part ($Re \Delta V = |\Delta V| \cos \phi$) which is parametric in frequency for the IMS spectra. Here, (a), (b) and (c) are taken at frequencies between 1 Hz and 250 kHz and at different OLED V_{bias} (shown in the respective plots inset), from 7.8 V down to 5.4 V with 0.6 V intervals, V_{AC} and I_{AC} are kept constant. Note that the Re/Im axis at (c) uses different scales and are not normalized, with the direction of increasing frequency given by the blue arrow. 156

Fig. 7-2. A diagram of the microscopic processes occurring within an OLED according to the double-carrier model by Blom and de Jong. The B , K_{dt} , and K_t here are the recombination, trapping and detrapping constant respectively [149]. 158

Fig. 7-3 (a). A generic OLED equivalent circuit model [153]. I_L represents the light-driven current source. In IMS, all components are internal to the OLED. (b) Simulated 'Nyquist rainbow' for the equivalent circuit model in (a) for f between 1 Hz and 250 kHz and at OLED V_{DC} = 7.8 V down to 5.4 V with 0.6 V Fig. interval (inset). Here for (b), we select C_{OLED} = 13 nF, and a customized 1N914 diode (1N914_KA) with the saturation current reduced to 3 pA. The DC current bias amplitudes are set at I_{DC} = 1.9, 1.06, 0.75, 0.33 and 0.22 mA, these (I_{DC}) corresponds to DC_s = 7.8, 7.2, 6.6, 6 and 5.4 V respectively. The current source modulation is set to I_{AC} = 1.35, 0.69, 0.4, 0.14 and 0.07 mA for V_{DC} = 7.8 and down to 5.4 V respectively. The plots Re/Im axis at (b) uses different scales and are not normalized, with the direction of increasing frequency given by the blue arrow. 160

Fig. 7-4. Simulations on the extended equivalent circuit model, shown as an inset. The simulation is performed at f between 1 Hz and 250 kHz and with OLED V_{DC} = 7.8 V down to 5.4 V (colour inset). Here, the chosen diode (1N914_KA), the magnitude of C_{OLED} , I_{DC} and I_{AC} are kept to be the same as in Fig. 7-3(a) circuit. Magnitude of C_{ext} = 6 nF // R_{ext} = 600 Ω . Also, Re/Im axis uses different scales and are not normalized, with the direction of increasing frequency given by the blue, arrow. 162

Fig. 7-5 A plot of (transit) time constant τ (μs) vs $1/(V_{\text{DC}}-V_{\text{bi}})$ (V^{-1}). Time constant (τ) data were derived from f_c in Table XII. 163

Fig. 7-6 (a). Bode amplitude plot of ΔV , (b) Bode phase plot of ΔV phase ϕ vs frequency f and (c) Nyquist plots of ΔV that plots the imaginary ($\text{Im } \Delta V = |\Delta V| \sin \phi$) vs. its real part ($\text{Re } \Delta V = |\Delta V| \cos \phi$), the spectra being parametric with frequency. Here, (a), (b) and (c) are taken at frequencies between 30 Hz and 250 kHz and at unfiltered-, longpass and bandpass filtered light (shown as colour coded and in the inset). Note the Re/Im axis at (c) uses different scales and are not normalized, with the direction of increasing frequency given by the blue arrow. For both filtered- and unfiltered light, we applied a voltage $V_{\text{OLED}} = (7 + 0.6)$ V on the OLED and drive it with a current drive $I_{\text{OLED}} = (1.6 + 0.2)$ mA. 166

List of Abbreviations

AC	Alternative Current
AM	Air Mass
BHJ	Bulk Heterojunction
CB	Conduction Band
CE	Common Electrode
CNLS	Complex Nonlinear Least Square
CS	Charge-Separated
CT	Charge-Transfer
DC	Direct Current
DI	De-Ionized
DSSC	Dye-Sensitized Solar Cells
EEL	Electron Extraction Layer
EIL	Electron Injection Layer
EIS	Electrochemical Impedance Spectroscopy
EL	Electroluminescence
FC	Franck-Condon
FF	Fill Factor
FRA	Frequency Response Analyzer
FWHM	Full Width At Half Maximum
HEL	Hole Extraction Layer
HIL	Hole Injection Layer
HOMO	Highest Occupied Molecular Orbital
IMPS	Intensity-Modulated Photocurrent Spectroscopy
IMPV	Intensity-Modulated Photovoltage Spectroscopy
IMS	Intensity-Modulated Spectroscopy
IS	Impedance Spectroscopy
ISC	Intersystem Crossing
ITO	Indium Tin Oxide
IV	Current-to-voltage
LDR	Light Dependent Resistor
LED	Light-Emitting Diode
LUMO	Lowest Unoccupied Molecular Orbital
MPP	Maximum Power Point
OLED	Organic Light-Emitting Diode
OPV	Organic Photovoltaic
OTFT	Organic Thin Film Transistor
PCE	Power Conversion Efficiency
PDI	Polydispersity Index
PSD	Phase-Sensitive Detector
PV	Photovoltaic
RBS	Rutherford Backscattering Spectrometry
RE	Reference Electrode
SCLC	Space Charge Limited Current
SE	Source Electrode

SE	Standard Electrode
TCO	Transparent Conductive Oxide
TOF	Time-of-Flight
TOF-SIMS	Time-of-Flight Secondary Ion Mass Spectrometry
UPS	Ultraviolet Photoelectron Spectroscopy
UV	Ultraviolet
VB	Valence Band
VI	Virtual Instruments
WE	Working Electrode
XPS	X-Ray Photoelectron Spectroscopy

Publication and Presentation

Journal Publication

K. Adhitya, A. Alsulami, A. Buckley, R. C. Tozer, and M. Grell, Ieee Journal of Photovoltaics **5**, 1414 (2015).

Conference and Meeting Presentations

UK semiconductors 2015 Conference Sheffield: Poster Presentation

2015 Poster Title: “Intensity-Modulated Spectroscopy on Loaded Organic Photovoltaic Cells”; K. Adhitya, A. Alsulami, A. Buckley, Richard C. Tozer, Senior Member, IEEE, M. Grell
